

UCLA

UCLA Electronic Theses and Dissertations

Title

Theoretical Modeling of Highly Dispersed Catalysts under Reactive Gas Environments

Permalink

<https://escholarship.org/uc/item/8r60j0cp>

Author

Yan, George Xu

Publication Date

2022

Peer reviewed|Thesis/dissertation

UNIVERSITY OF CALIFORNIA

Los Angeles

Theoretical Modeling of Highly Dispersed Catalysts under Reactive Gas Environments

A dissertation submitted in partial satisfaction of the
requirements for the degree Doctor of Philosophy
in Chemical Engineering

by

George Xu Yan

2022

ABSTRACT OF THE DISSERTATION

Theoretical Modeling of Highly Dispersed Catalysts under Reactive Gas Environments

by

George Xu Yan

Doctor of Philosophy in Chemical Engineering

University of California, Los Angeles, 2022

Professor Philippe Sautet, Chair

In the past decade, highly dispersed catalysts (HDCs) and more specifically single atom catalysts (SACs) have become popular in the field of heterogeneous catalysis. Although these catalysts efficiently utilize all the active metal in the catalyst, their structure and reactivity are inadequately understood. For the structure and stability of HDCs and SACs on metal oxides, the sensitivity of the very small clusters and single atoms to their surrounding gas/liquid environment results in many accessible states under reaction conditions, rendering simplistic structural models unrealistic. The unique chemical properties of the active sites by their lack of metal-metal coordination or poor mixing of electronic states with the support shift the free energy pathway of catalytic reactions, resulting in nontraditional kinetic behavior. In this dissertation, we use density functional theory (DFT), atomistic thermodynamics, and microkinetic modeling to study several HDCs and SACs to understand their structure, stability, and reactivity under realistic catalytic environments.

DFT-based atomistic thermodynamics were performed to investigate the surface and structure of a highly dispersed Rh/CeO₂ catalyst. We found that the interaction between Rh and the CO gas product induces a counterintuitive redispersion of Rh active sites during the steam reforming of methane, reflecting the sensitivity of the Rh single atoms to their surrounding environment.

We further applied the atomistic thermodynamics approach in the simulation of the surface structure of a dual single-atom Mo₁+Pd₁/Co₃O₄ catalyst. We found that under reducing gas environments containing predominantly H₂ and H₂O, the Co₃O₄(111) surface becomes hydroxylated and Co-enriched. DFT-energetics-based microkinetic modeling of the anisole hydrodeoxygenation (HDO) reaction reveals that the hydroxylated and Co-enriched Co₃O₄(111) surface enables the cooperation between the Mo₁ and Pd₁ sites by allowing the shuttling of H through metastable H₂O intermediates.

Finally, we also applied DFT-energetics-based microkinetic modeling in the modeling of the hydrogenation of 1-hexyne and hydrogenation/isomerization of 1-hexene over a dilute Pd-in-Au catalyst. We found that the large barriers for H₂ dissociation over Pd₁ and for H exchange between individual Pd₁ sites results in the high selectivity of the dilute Pd-in-Au catalyst for 1-hexene in the hydrogenation of 1-hexyne, as well as for 2-hexene in the hydrogenation/isomerization of 1-hexene.

The dissertation of George Xu Yan has been approved.

Anastassia N. Alexandrova

Panagiotis D. Christofides

Dante A. Simonetti

Philippe Sautet, Committee Chair

University of California, Los Angeles

2022

Dedicated to my family.

Table of Contents

List of Figures	xii
List of Tables	xxxii
Acknowledgements	xxxv
Curriculum Vitae	xl
Chapter 1 Research Background	1
1.1 Single Atom Catalysts as the Pinnacle of Highly Dispersed Catalysts	1
1.2 Theoretical Investigations on the Structure and Stability of HDCs	3
1.3 Catalytic Reactivity of SACs and HDCs	7
1.4 Thesis Objectives.....	9
Chapter 2 Reaction Product-Driven Restructuring and Assisted Stabilization of a Highly Dispersed Rh-on-Ceria Catalyst	11
2.1 Introduction	11
2.2 Methods	12
2.2.1 DFT Calculations.....	12
2.2.2 Modeling the Ceria Surface and Rh Active Sites	14
2.3 Results and Discussion	17
2.3.1 Surface Structure of the CeO ₂ Support and Structural Evolution of the Rh/CeO ₂ Catalyst.....	17
2.3.2 Understanding Active Site Stabilization at the Atomic Scale	20
2.3.3 Pressure-Dependent Formation of Rh _m (CO) _n Clusters	25

2.4 Conclusion	27
Chapter 3 The Surface Structure of $\text{Co}_3\text{O}_4(111)$ under Reactive Gas Phase Environments	29
3.1 Introduction	29
3.2 Methods	32
3.2.1 DFT Calculations.....	32
3.2.2 Bulk and Surface Models	34
3.3 Results and Discussion	36
3.3.1 The $\text{Co}_3\text{O}_4(111)$ Surface under Oxidative and Reductive Environmental Conditions.....	36
3.3.2 Comparisons to in situ and ex situ Vibrational Spectroscopy	49
3.3.3 Comparison among $U_{\text{eff}} = 3.5 \text{ eV}$, 2.0 eV , and HSE06	55
3.3.4 Predicted Surface Structure under Various Reaction Conditions.....	58
3.4 Conclusion	63
Chapter 4 Theoretical Simulations of the Hydrodeoxygenation (HDO) of Anisole over a Teamed Single Atom $\text{Mo}_1+\text{Pd}_1/\text{Co}_3\text{O}_4$ Catalyst	65
4.1 Introduction	65
4.2 Methods	66
4.2.1 DFT Calculations.....	66
4.2.2 Microkinetic Simulations	68
4.3 Results and Discussion	69
4.3.1 Structure of the Co_3O_4 Support, Mo_1 and Pd_1 Active Sites	69

4.3.2 The Mechanism of Anisole HDO over Pd ₁ /Co ₃ O ₄ (111).....	71
4.3.3 The Mechanism of Anisole HDO over Mo ₁ +Pd ₁ /Co ₃ O ₄ (111).....	74
4.3.4 Microkinetic Simulations of Pd ₁ /Co ₃ O ₄ and Mo ₁ +Pd ₁ /Co ₃ O ₄	78
4.4 Conclusion	80
Chapter 5 Hydrogen Dissociation and Spillover Control the Selectivity of 1-Hexyne Hydrogenation over Dilute Pd-in-Au Catalysts	82
5.1 Introduction	82
5.2 Methods	86
5.2.1 DFT Calculations.....	86
5.2.2 Microkinetic Simulations	87
5.3 Results	88
5.3.1 H ₂ Dissociation on Pd ₁ Au(111)	88
5.3.2 Hydrogenation Mechanism of 1-Hexyne to 1-Hexene over Pd ₁ Au(111).....	90
5.3.3 Microkinetic Simulations of Catalytic Activity	93
5.3.4 Origin of Improved 1-Hexene Selectivity	102
5.4 Conclusion	106
Chapter 6 1-Hexene Hydrogenation and Isomerization over Dilute Pd-in-Au Catalysts.....	108
6.1 Introduction	108
6.2 Methods	109
6.2.1 DFT Calculations.....	109
6.2.2 Microkinetic Simulations	109

6.3 Results	112
6.3.1 Mechanism of 1-Hexene Hydrogenation and Isomerization over Pd ₁ Au(111)	112
6.3.2 Microkinetic Simulations of 1-Hexene Hydrogenation and Isomerization over Pd ₁ Au(111)	114
6.3.3 Theoretical Assessment of H/D Exchange in 1-Hexene Hydrogenation and Isomerization over Pd ₁ Au(111)	118
6.4 Conclusion	121
Chapter 7 Conclusion	122
Appendix A Supplementary Information for Chapter 2	127
A.1 Formulas for computing the stability of reduced CeO ₂ (111) surfaces and Rh active sites	127
A.2 Vibrational corrections for Gibbs free energy calculations	130
A.3 Configurational entropy of Rh sites	137
A.4 Chemical potential of Rh atoms	139
A.5 CO adsorption energy correction	142
A.6 The structure of the CeO ₂ (111) surface during catalysis	152
A.7 Distribution of Rh active sites during catalysis	156
A.8 DFT-based spectroscopic calculations of simulated Rh active sites	159
Appendix B Supplementary Information for Chapter 3	161
B.1 Procedure for Surface Energy Calculations	161
B.2 Surface energy as functions of H ₂ O/H ₂ /O _{vac} coverage as functions of H ₂ O/H ₂ /O chemical potential and temperature	164

B.3 Fully labeled surface stability diagrams and tabulated top/side/bird's eye view of structures appearing on the diagram	175
B.4 More Details on Frequency Calculations.....	183
B.5 Surface relaxation experienced by the $(\text{Co}^{\text{Oh}}\text{Co}^{\text{Td}})_x$ termination upon reduction, the magnetic structure of the $(\text{Co}^{\text{Oh}}_{0.5}\text{Co}^{\text{Td}})_x$ termination, and isomers of the fully hydroxylated $(\text{Co}^{\text{Td}})_x$ termination.....	185
Appendix C Supplementary Information for Chapter 4	189
C.1 Structure of the $\text{Co}_3\text{O}_4(111)$ surface, Mo_1 , and Pd_1 active sites	189
C.2 Geometry and formal oxidation of all states in the reaction mechanisms	192
C.3 Hydrogen activation and spillover mechanism over the hydroxylated $\text{Co}_3\text{O}_4(111)$ surface.....	195
C.4 Alternative anisole HDO pathway over a grafted Mo_1 site	198
C.5 Estimation of the Gibbs free energy barrier for adsorption	199
C.6 Energetic span assessment of the reaction kinetics	200
C.7 Parameters and additional results of microkinetic simulations	203
Appendix D Supplementary Information for Chapter 5	207
D.1 Supplementary energetics and adsorption configurations	207
D.2 Detailed description of the microkinetic model	211
D.3 Additional results from microkinetic modeling.....	213
D.4 Derived rate laws for the hydrogenation of 1-hexyne	215
D.5 Performance of density functionals for the adsorption energy of 1-hexyne.....	216
D.6 Brønsted-Evans-Polanyi relation of C-H bond formation steps	217
D.7 Electronic structure of $\text{Pd}(111)$ and $\text{Pd}_1\text{Au}(111)$	218

Appendix E Supplementary Information for Chapter 6	219
E.1 Intermediate and transition state geometries in the isomerization/hydrogenation of 1-Hexene over Pd ₁ Au(111)	219
E.2 Additional details and results of microkinetic simulations	220
Bibliography	225

List of Figures

Figure 1.1 Higher catalyst dispersion improves a catalyst's efficiency by exposing more metal sites and improving catalyst activity in structurally insensitive reactions.....1

Figure 2.1 Structure and stability of the CeO₂(111) surface under gas pressure of H₂ and H₂O vapor. (a) Surface structures formed in a gas environment of H₂ and H₂O at different chemical potentials. (b and c) Top and side view of CeO₂(111) passivated with OH groups, corresponding to zone 1C in (a). (a) consists of three main phases, including solely hydroxylated regions (1A, 1B, 1C: 2.54, 5.09, 7.63 OH/nm², beige-colored regions; a coverage of 4.24 OH/nm² is stable in a sliver between regions 1A and 1B), OH/O_{vac} mixed regions (2A: 0.85 O_{vac}/nm² & 1.70 OH/nm², 2B: 0.85 O_{vac}/nm² & 2.54 OH/nm², 2C: 3.39 O_{vac}/nm² & 0.85 OH/nm², magenta-colored regions), and solely O_{vac}-containing regions (3A: 1.91 O_{vac}/nm², 3B: 3.39 O_{vac}/nm², cyan-colored regions). The olive-colored hatched region is associated to possible pressure under which SRM could be performed, from P_i ~ 10⁻² bar to P_i ~ 10¹ bar; the steady state SRM gas environment at 500 °C is marked as a red dot ($\Delta\mu_{\text{H}_2} = -1.17$ eV, $\Delta\mu_{\text{H}_2\text{O}} = -1.65$ eV, calculated using the translational and rotational contributions, assuming P_{H₂} = 0.14 bar and P_{H₂O} = 0.11 bar). The reaction condition falls in the region where the CeO₂(111) surface is hydroxylated.....17

Figure 2.2 Structure and stability of Rh active sites. Theoretical modeling of the evolution of the Rh active site under catalytic conditions as a function of catalysis temperature (T) and CO pressure (P_{CO}) by holding the chemical potentials of gas phase H₂ and H₂O constant as those during SRM at 500 °C (See Figure 2.1). (a) Theoretically proposed stable Rh species; the SRM condition at 500 °C (P_{CO}=0.045 bar) is marked with a green dot with bars representing possible variations in T and P_{CO}. As CO pressure decreases, Rh₃(CO)₃ transforms to Rh₃(CO)₂ and then Rh₃H₁. (b) Gibbs free energy of formation of the most stable Rh-based sites as a function of catalysis temperature (T)

and CO pressure (P_{CO}); the full black line marks the transition between supported Rh nanoparticles and highly dispersed $Rh_m(CO)_n$ clusters, below which the $Rh_m(CO)_n$ species is more stable than the Rh nanoparticle. We find the $Rh_3(CO)_3$ cluster to be close to the Rh nanoparticle in stability under catalytic conditions. For reference, the stability of the $Rh_3(CO)_3$ site is shown in Figure A.17. (c-g) Atomic-scale geometries of Rh sites present in (a). (c) Rh_3H_1 . (d) $Rh_3(CO)_2$, (e) $Rh_3(CO)_3$, (f) $Rh_3(CO)_4$, and (g) $Rh_1(CO)_2$20

Figure 2.3 Relative stability of $Rh_m(CO)_n$ sites in the reaction environment. The ensemble of Rh sites generated during the SRM reaction at 500 °C (see Figure 2.2), ordered by Gibbs free energy of formation relative to the most stable $Rh_3(CO)_3^+$ site (line color/site type: gray/ Rh_3 ; blue/ Rh_2 ; red/ Rh_1). A $3k_B T$ region is shaded in green to indicate the thermally accessible structures. The $Rh_3(CO)_3$ clusters are more stable than $Rh_2(CO)_3$ and $Rh_1(CO)_2$ sites in the reaction environment.22

Figure 2.4 Reversible restructuring of the Rh active sites. CO product pressure-driven restructuring of Rh catalytic sites. (a) Three series of variations of CO pressure at 500 °C marked on the theoretical P_{CO} -T phase diagram (upper portion adopted from Figure 2.2a). (b) DRIFTS spectra (b1-b9) at 500 °C under SRM catalytic condition. Series 1: b1-b9, a transient pulse of CH_4 reactant (equivalent to 0.1 ml CH_4 , STP) composed of 1% CH_4 and 99% Ar was introduced to the catalyst by mixing the pulse with flowing water vapor formed by flowing Ar (99.999%) through water of 25°C. No external CO source was introduced before and during Series 1. Series 2: b10-b14, spectra in a flow of CO (1%) balanced with Ar. Series 3, spectra (b15-b20) being purged with argon as a function of time. The background spectrum for DRIFTS study was collected on the catalyst surface under Ar and water vapor flow at 500 °C. In Series 1, 20 ml/min of water vapor containing 3% vapor was continuously flowing through the reaction cell, CH_4 gas (1% CH_4 in Ar) was pulsed to

mix with water vapor. The DRIFTS spectra were taken as a function of time without CH₄ in the flow. At the t=2 min (b1), the vibrational features in the 2050-1850 cm⁻¹ region, assigned to Rh₃(CO)₃, were clearly observed as CO was generated from SRM at 500°C. These experiments overall show the formation of Rh₃(CO)₃ to be reversible.....25

Figure 3.1 Side view of Co₃O₄ through the [111] direction. From truncating the Co₃O₄ bulk, a total of six possible terminations of the (111) surface can be made. This surface is a type III surface by Tasker’s definitions, where the group of the six labeled layers is stoichiometric when stacked but has a net dipole in the z-direction.....29

Figure 3.2 Top (a, b, c, through the c axis) and side (d, e, f, through the a axis) views of (2x2) cells (area 1.13 nm²) of the three bare Co₃O₄(111) terminations considered in this work, containing (red) O, (green) Co-T_d and (blue) Co-O_h and additional surface Co (gold). a, d: O-rich termination, (Co^{Td})_x, has formula Co₄₄O₆₄, containing four exposed Co in C_{3v} sites on each surface, belonging to bulk T_d sites in the bulk. b, e: Co-rich termination, (Co^{Oh}Co^{Td})_x, has formula Co₅₂O₆₄, containing eight exposed Co in C_{3v} sites on each surface; four originally at bulk T_d sites and four originally at bulk O_h sites. c, f: stoichiometric termination, (Co^{Oh}_{0.5}Co^{Td})_x, has formula Co₄₈O₆₄, containing six exposed C_{3v} Co on each surface; two originally at bulk O_h sites and four at bulk T_d sites.....34

Figure 3.3 Surface stability diagram showing the most stable surface structure as a function of O₂ and H₂O chemical potential and equivalent oxygen/water pressure at 423 K and 873 K. Regions are classified in three ways. (I) By surface Co concentration: blue/grey/white: 3.56 Co/nm²; green: 5.33 Co/nm², and red/brown: 7.11 Co/nm². (II) By general appearance of surface hydroxylation: the bottom bold line separates non-hydroxylated regions and hydroxylated regions, the middle bold line (only the segment running through the blue regions, or when Δμ_O > -1.5 eV) separates isolated hydroxyls and Co(H₂O)₃ (hereby referred to as “triaqua”) surface complexes (with

eventually additional OH groups), and the top bold line separates isolated triqua surface complexes and large OH/H₂O structures. (III) By specific numbered structure (see Table 3.1 for descriptions, Figure B.9 for a fully labeled stability diagram, Figure 3.2 and Table 3.2 for representative geometries, and Table B.10 for all geometries).37

Figure 3.4 Portions of Figure 3.3 showing the H₂O/O₂ surface stability diagram under realistic pressures at (a) 423 K and (b) 873 K. Regions are numbered and colored the same way as Figure 3.3. Only hydroxylated regions can be accessed at 423 K. Higher surface Co concentration can be reached under low P_{O₂}.43

Figure 3.5 Surface stability diagram showing the most stable surface structure as a function of H₂ and H₂O chemical potential and H₂/H₂O pressure at 423 K. The color scheme and numbering are the same as that in Figure 3.3. Regions are again classified in same three ways as those in Figure 3.3. (I) By surface Co concentration: blue: 3.56 Co/nm²; green: 5.33 Co/nm², and red/brown: 7.11 Co/nm². (II) By general appearance of surface hydroxylation: bottom bold line separates non-hydroxylated regions and hydroxylated regions and top bold line separates OH-only regions and molecular H₂O-containing structures. (III) By specific numbered structure (see Table 3.1 for descriptions, Figure B.10 for a fully labeled stability diagram, Table 3.2 for representative geometries, and Table B.11 for all geometries).45

Figure 3.6 Top view of spin density difference on a) bare (Co^{Td})_x, b) bare (Co^{Oh}Co^{Td})_x, and c) (Co^{Oh}_{0.5}Co^{Td})_x, at isosurface level 0.04, where blue represents negative and yellow positive spin density difference. Surface Co (green) on the (Co^{Td})_x termination appear to be slightly more oxidized than bulk Co²⁺, with slightly higher projected magnetic moments. Charge for this off-stoichiometry is compensated by small density differences on surface O. No projected magnetic moments are found on surface O in the (Co^{Oh}Co^{Td})_x termination. All the added Co appears to be

Co^{2+} based on projected magnetic moments, while Co originally on the surface appear slightly reduced. Less Co can be added to the surface to form $(\text{Co}^{\text{Oh}}_{0.5}\text{Co}^{\text{Td}})_x$; these Co also appear to be slightly reduced Co^{2+} and quenches spin differences on some surface O.46

Figure 3.7 Top view of spin density difference on a) $(\text{Co}^{\text{Td}})_x$ with 1.78 OH/nm², b) $(\text{Co}^{\text{Td}})_x$ with 7.11 OH/nm², and c) $(\text{Co}^{\text{Oh}}\text{Co}^{\text{Td}})_x$ with 7.11 OH/nm². Electrons from adsorbing H on $(\text{Co}^{\text{Td}})_x$ are transferred to surface O, subsurface Co^{Oh} , and surface Co^{Td} . On the other hand, electrons from H adsorption on $(\text{Co}^{\text{Oh}}\text{Co}^{\text{Td}})_x$ are transferred mostly to subsurface Co^{Oh}48

Figure 3.8 Gas phase environmental conditions during vibrational characterization by Busca et al. represented as a dashed line on the $\text{H}_2\text{O}/\text{H}_2$ surface stability diagram (Figure 3.5), as H_2O chemical potential is not well-defined. The corresponding termination should contain 7.11 Co/nm² and 7.11 OH/nm² (structure 7a, brown) because an unrealistic high pressure of H_2O must be applied to generate a mixed OH/ H_2O layer (structure 12c, red).51

Figure 3.9 Gas phase environmental conditions during vibrational characterization under $\text{H}_2\text{O}/\text{D}_2\text{O}$ pressure, overlaid with the $\text{H}_2\text{O}/\text{O}$ surface stability diagram of Figure 3.3. These conditions fall under three main regions: $(\text{Co}^{\text{T}})_x$ with triaqua-complex-incorporated OH/ H_2O chains (structure 9b), triaqua surface complex with additional OH (8b) for D_2O dosed at 200 K and 300 K, and $(\text{Co}^{\text{T}})_x$ with isolated OH (structure 5b) for D_2O exposure at 370 K and beyond. Gas phase conditions in characterization experiments are marked as dots with error bars for O chemical potential.52

Figure 3.10 Surface structure as a function of oxygen and water chemical potential calculated using $U_{\text{eff}} = 2.0$ eV. Gas phase conditions observed in vibrational characterization are marked as dots with error bars for O chemical potential. No hydroxylation is predicted to exist in $\text{D}_2\text{O}/\text{H}_2\text{O}$ exposure conditions at 370 K and above when using $U_{\text{eff}} = 2.0$ eV.57

Figure 3.11 Surface stability diagram as a function of O_2 and H_2O chemical potential. Conditions in low temperature CO oxidation, N_2O decomposition, ethane ODH, CH_4 oxidation, and NO reduction with NH_3 are marked on the diagram as yellow triangles if P_{H_2O} is well-defined and dashed lines otherwise.60

Figure 3.12 Surface stability diagram as a function of H_2 and H_2O chemical potential and hydrogen/water pressure at 423 K. Conditions in NO reduction with H_2 found in the literature are marked on the diagram as yellow circles.62

Figure 4.1 The Gibbs free energy pathway for anisole HDO over the Pd_1 site show that the methanol formation controls the energetic span. Anisole HDO over only the Pd_1 site takes advantage of a single O vacancy near the Pd_1 . The energetic span of the reaction mechanism is 1.28 eV, between the PdH_2 intermediate (Pd-6) and the transition state for the desorption of methanol (TS6). See text for description. Geometries of all intermediate and transition states are shown in Figure C.4.71

Figure 4.2 The Gibbs free energy pathway for anisole HDO over the Mo_1+Pd_1 site. (a) Anisole HDO over the Mo_1 site assisted by H spillover formed on Pd_1 site. All structures in the reaction pathway are listed in Figure C.4 and C.5. The energetic span of the reaction mechanism is 1.31 eV under low conversion (1%), between the state Mo-5b and the transition state for the dissociation of the anisole molecule. After dissociation of anisole, a methanol molecule is formed first by reacting OCH_3 with surface OH generated by spillover. The methanol molecule could then desorb (pathway in red) or donate its H to the phenyl group and form benzene (pathway in green). The formation of benzene by reaction between methanol and the phenyl ligand is kinetically preferred over methanol desorption. (b) Gibbs free energy barrier for the dissociation of molecular H_2 on the Pd_1 site.74

Figure 4.3 Microkinetic simulations show that the teamed Mo_1+Pd_1 catalysts is more active than Pd_1 for the HDO of anisole. As the Gibbs free energy spans of anisole HDO over Pd_1 only and Mo_1 assisted by H spillover are similar, microkinetic simulations were performed to compare the HDO activity over only Pd_1 sites and over Mo_1 sites with H provided by Pd_1 . (a) In the temperature range of 50-150 °C and 1% anisole conversion, the $\text{Mo}_1+\text{Pd}_1/\text{Co}_3\text{O}_4$ dual site catalyst is more active than the $\text{Pd}_1/\text{Co}_3\text{O}_4$ single-site catalyst, and (b) the apparent activation energy of the HDO reaction over Mo_1 assisted by H spillover is smaller than that over only Pd_1 in this temperature range as well. The decrease of the apparent activation energy with temperature is due to the depletion of surface intermediates.....78

Figure 5.1 A schematic representation of the course of 1-hexyne hydrogenation. The leftmost pathway shows H_2 dissociation and subsequent migration to supply H atoms for 1-hexyne hydrogenation on another $\text{Pd}_1\text{Au}(111)$ site. 1-Hexyne can be hydrogenated either by fully hydrogenating one of the two unsaturated carbon atoms followed by the remaining one (left), or by alternately hydrogenating the two carbon atoms (right). The former is detrimental to selectivity as it skips 1-hexene formation and produces hexyls directly through 1-hexylidene. Double-headed and single-headed arrows indicate reversibility and irreversibility, respectively, based on experiments and theory in this paper.....84

Figure 5.2 Free energy diagram for 1-hexyne hydrogenation to form 1-hexene on the $\text{Pd}_1\text{Au}(111)$ surface. The butyl group attached to $\text{C}\equiv\text{C}$ bond is abbreviated as R. All species are chemisorbed, unless indicated by (g) for gas phase species. The green and red pathways represent the hydrogenation of the terminal carbon atom (C1) and the carbon atom attached to the butyl group (C2), respectively, in the first reaction step, followed by the hydrogenation of the remaining carbon

atom. The newly added H atoms are indicated in red or in green. Reaction conditions are: $T = 363$ K, $P(\text{H}_2) = 0.2$ bar, $P(\text{C}_6\text{H}_{10}) = 0.01$ bar, $P(\text{C}_6\text{H}_{12}) = P(\text{C}_6\text{H}_{14}) = 0.001$ bar.90

Figure 5.3 Microkinetic simulations of 1-hexyne hydrogenation to 1-hexene and n-hexane under a typical experimental reaction environment corresponding to low (<20%) conversion: $P(\text{H}_2) = 0.2$ bar, $P(1\text{-Hexyne}) = 0.01$ bar, $P(1\text{-Hexene}) = P(\text{n-Hexane}) = 0.001$ bar. (a) rate (s^{-1}) for the conversion of 1-hexyne (blue line) and selectivity for the formation of 1-hexene and n-hexane (red lines) as a function of temperature. The selectivity for 1-hexene was found to be above 98% through the temperature range $T = 313 - 413$ K. (b) Steady state fraction of reactive intermediates on $\text{Pd}_1\text{Au}(111)$ as a function of temperature: adsorbed 1-hexyne (orange line) and 1-hexene (purple line) were found to be the most abundant reactive intermediates until 353 K. (c) Schematics of structures in panel (b).94

Figure 5.4 Analysis of the kinetics for hydrogenation of 1-hexyne shows H_2 dissociation to be the rate-controlling step. (a) Apparent activation enthalpy (blue line) and kinetic orders of H_2 (black solid line), 1-hexyne (dot-dashed line) and 1-hexene (dashed line) for the hydrogenation of 1-hexyne as a function of temperature. The apparent activation enthalpy of the reaction progressively decreases in the temperature range $T = 313 - 413$ K, while the orders of 1-hexyne and 1-hexene increase. (b) Degree of rate control (DRC) of various transition states as a function of temperature. The transition state for H_2 dissociation is the main rate-controlling transition state (red line), while the migration of H from the Pd single atom to the Au substrate (orange line) is second in importance. Importantly, C-H bond formation steps (green and purple lines) do not appear to be rate-controlling. (c) Schematics of the four elementary steps shown in panel (b).96

Figure 5.5 A destabilization of hydrocarbon intermediates and transition states energy by 0.2 eV enables an improved agreement with experiment for the kinetic order of 1-hexyne and the apparent

activation enthalpy. (a) Apparent activation enthalpy (eV) of 1-hexyne hydrogenation as a function of temperature without (full line) and with (dashed line) destabilization of surface C_6H_x intermediates and transition states. Experimental is shown as a green horizontal bar.¹⁸⁶ (b) Orders of reaction of H_2 (blue) and 1-hexyne (red) as a function of temperature without (full line) and with (dashed line) destabilization of surface C_6H_x intermediates and transition states.¹⁸⁶101

Figure 5.6 The degree of selectivity control (DSC), evaluated at $T = 373\text{ K}$, $P(H_2) = 0.2\text{ bar}$, $P(1\text{-Hexyne}) = 0.01\text{ bar}$, $P(1\text{-Hexene}) = 0.001\text{ bar}$, of the TS for H_2 dissociation over Pd_1 ($DSC = -2.75 \times 10^{-3}$), 1-Hexyne hydrogenation to 1-Hexenyl ($DSC = 8.24 \times 10^{-3}$), and 1-Hexyl hydrogenation to n-Hexane ($DSC = -2.46 \times 10^{-3}$). The values were multiplied by 100 in the figure. Decreasing the free energy barrier for 1-hexyne hydrogenation to 1-hexenyl increases the selectivity for 1-hexene, while decreasing the free energy barrier of H_2 dissociation and 1-hexyl hydrogenation to n-hexane decreases the selectivity for 1-hexene.103

Figure 6.1 Free energy profiles for 1-hexene hydrogenation (a) and isomerization to 2-hexene (b) calculated using DFT. The abbreviation R represents the butyl group attached to the $C=C$ bond. Two different hydrogenation pathways are shown in (a): the green pathway hydrogenates first the terminal carbon atom of 1-hexene to form 2-hexyl while the red pathway hydrogenates first the carbon atom which is attached to the butyl group R, to form 1-hexyl. Both pathways finish by hydrogenating the remaining unsaturated carbon atom in the hexyl intermediates. The newly-added H atoms to the unsaturated hydrocarbons are denoted in red or in green. (b) shows the isomerization pathway of the 2-hexyl intermediate to 2-hexene. Reaction conditions are: $T = 363\text{ K}$, $P(H_2) = 0.2\text{ bar}$, $P(1\text{-hexene}) = 0.01\text{ bar}$, $P(2\text{-hexene}) = 0.001\text{ bar}$, and $P(n\text{-hexane}) = 0.001\text{ bar}$112

Figure 6.2 1-Hexene consumption rate, product selectivity and degrees of rate control (DRC) of transition states for 1-hexene consumption evaluated for the Pd₁Au(111) model catalyst at fixed partial pressures. Microkinetic model of 1-hexene reaction with H₂ evaluated at p(H₂) = 0.2 bar, p(1-hexene) = 0.01 bar, and p(2-hexene) = p(n-hexane) = 0.001 bar. (a) Rate of 1-hexene consumption, (b) selectivity of 2-hexene and n-hexane formation, and (c) main rate-controlling transition states (TS) and their DRC for 1-hexene consumption as functions of temperature. (d) Schematic representations of the elementary steps corresponding to the transition states in panel (c). The reaction was found to light off at ~350 K with 2-hexene as the minority product and H₂ dissociation as the main rate-controlling TS.116

Figure 6.3 Product and isotope selectivity of 1-hexene deuteration and isomerization, with the barriers of H₂ dissociation and H-spillover increased by 0.1 eV. (a) 1-hexene conversion and (b) selectivity of 2-hexene and n-hexane as functions of reactor temperature. (c) 1-hexene isotope distribution, (d) 2-hexene isotope distribution, and (e) n-hexane isotope distribution as functions of 1-hexene conversion. The PFR, with 200 mg catalyst loading, was assumed to operate at constant temperature and pressure (1 bar). The 1-hexene conversion and product/isotope selectivity were evaluated under an inlet flow of 50 standard mL/min (corresponding to the standard condition of T = 273.15 K and P = 1 atm), consisting of 1 vol% 1-hexene and 20 vol% D₂ with balance inert.119

Figure A.1 Structures used in the fitting of the ΔG_{vib} of ordinary CO adsorption, where the O end of the CO molecule points away from the surface. The CO molecule accounted in each structure is circled in blue. The arrow in (b) indicates the shift of the H atom's binding site in response to CO adsorption.....132

Figure A.2 Structures used in the fitting of the ΔG_{vib} of tilted CO adsorption, where the O of the CO molecule points towards the surface. The CO molecule accounted in each structure is circled in blue.	133
Figure A.3 Structures used in the fitting of the ΔG_{vib} of H adsorption on Rh. The adsorbed H is circled in blue.	133
Figure A.4 Structures used in the fitting of the ΔG_{vib} of H adsorption on O. The adsorbed H is circled in blue. Arrows indicate H that was moved after the adsorption of the circled H.....	134
Figure A.5 Structures used in the fitting of the ΔG_{vib} of surface O vacancy formation. The formed surface O_{vac} is marked with a blue X.	134
Figure A.6 Structures used in the fitting of the ΔG_{vib} of subsurface O vacancy formation. The formed subsurface O_{vac} is marked with a black X.	135
Figure A.7 Mean absolute errors (MAE) of the six ΔG_{vib} correlations at 200 K and 1000 K.....	137
Figure A.8 Configurational entropy per Rh at 873 K, plotted for Rh_1 , Rh_2 , Rh_3 , and Rh_{13} sites as a function of the surface Rh atomic fraction.	138
Figure A.9 The sampled Rh_{13} clusters ranked by their relative total energy. High symmetry structures from Piotrowski et al. and the Pt_{13} LEME from Sun and Sautet were used as the starting points. ^{58, 102}	139
Figure A.10 The $\Delta\mu_{\text{Rh}}$ plotted against temperature. $\Delta\mu_{\text{Rh}}$ ranges from 1.58 eV to 1.22 eV in the range of 200-1000 K.....	141
Figure A.11 The CO adsorption energy correction developed from Rh carbonyl molecules. The average CO bond length correlates linearly with the computed correction.	145
Figure A.12 The CO adsorption energy correction developed for supported Rh carbonyls. CO bond lengths again correlate linearly with the computed correction.....	148

Figure A.13 Fitted U_{eff} value for H_2 adsorption energy at a full monolayer. A U_{eff} value of 3.771 eV reproduces the H_2 adsorption energy determined through HSE06.152

Figure A.14 Fitted U_{eff} value for average O_{vac} formation energy by H_2 reduction at 1/3 monolayer. A U_{eff} value of 3.829 eV reproduces the vacancy formation energy determined through HSE06.153

Figure A.15 $\text{H}_2\text{O}/\text{H}_2$ 2D stability diagram computed using the major structures appearing on Figure 2.1 and $U_{\text{eff}} = 3.67$ eV. The olive-colored hatched region represents the possible $\text{H}_2\text{O}/\text{H}_2$ chemical potentials encountered by the catalyst under the SRM catalytic conditions.154

Figure A.16 Calculated O 1s core level shift of surface OH groups on $\text{CeO}_2(111)$. The final state approximation is used here with an O ion in the 4th layer beneath the layer of OH groups as the reference. An additional O-Ce-O trilayer was added in these calculations.....155

Figure A.17 The Gibbs free energy of formation of the $\text{Rh}_3(\text{CO})_3$ site as a function of temperature and CO pressure. The solid line between the Salmon and Purple regions demarcates the phase boundary between Rh nanoparticles and $\text{Rh}_3(\text{CO})_3$ sites, above which the Rh NP is the more stable species.....157

Figure A.18 (a) The hydroxylated CeO_2 surface with $5.09 \text{ OH}/\text{nm}^2$ (Region 1B in Figure 2.1) and (b) one with $5.09 \text{ OH}/\text{nm}^2$ and $0.85 \text{ O}_{\text{vac}}/\text{nm}^2$. (c) The geometry a $\text{Rh}_3(\text{CO})_3$ cluster adsorbed on the hydroxylated CeO_2 surface without and (d) with a surface O vacancy.....158

Figure A.19 Principal $\nu(\text{CO})$ vibrational modes of $\text{Rh}_3(\text{CO})_2^+$, $\text{Rh}_3(\text{CO})_3^+$, and $\text{Rh}_3(\text{CO})_4^+$. The vibrational frequency of the principal C-O stretching mode increases with coverage.....159

Figure A.20 (a) Initial state approximation and (b) final state approximation core level shift calculations performed to assess the role of CO on the Rh 3d binding energy. Both approximations

show that the adsorption of CO increases the Rh 3d binding energy of the supported $\text{Rh}_3(\text{CO})_x$ cluster.160

Figure B.1 Hydroxylation of $(\text{Co}^{\text{Td}}\text{Co}^{\text{Oh}})_x$ through H_2O adsorption on the bare surface at oxygen rich conditions ($\Delta\mu_{\text{O}} = 0$ eV). Surface energy of is plotted as (top) $\gamma(\Delta\mu_{\text{H}_2\text{O}})$ and (bottom) $\gamma(\text{T}, P_{\text{H}_2\text{O}}=10^{-5}$ bar). Vertical lines represent surface structure transition points.164

Figure B.2 Hydroxylation of $(\text{Co}^{\text{Td}}\text{Co}^{\text{Oh}_{0.5}})_x$ through H_2O adsorption on the bare surface under oxygen rich conditions ($\Delta\mu_{\text{O}} = 0$ eV). Surface energy of is plotted as (top) $\gamma(\Delta\mu_{\text{H}_2\text{O}})$ and (bottom) $\gamma(\text{T}, P_{\text{H}_2\text{O}}=10^{-5}$ bar).165

Figure B.3 Reduction of $(\text{Co}^{\text{Td}})_x$ through H_2 chemisorption at oxygen rich conditions, $\Delta\mu_{\text{O}} = 0$ eV. Surface energy of is plotted as (top) $\gamma(\Delta\mu_{\text{H}_2})$ and (bottom) $\gamma(\text{T}, P_{\text{H}_2}=10^{-5}$ bar).166

Figure B.4 Reduction of $(\text{Co}^{\text{Td}}\text{Co}^{\text{Oh}})_x$ through H_2 chemisorption at oxygen rich conditions, $\Delta\mu_{\text{O}} = 0$ eV. Surface energy of is plotted as (top) $\gamma(\Delta\mu_{\text{H}_2})$ and (bottom) $\gamma(\text{T}, P_{\text{H}_2}=10^{-5}$ bar).167

Figure B.5 Reduction of $(\text{Co}^{\text{Td}}\text{Co}^{\text{Oh}_{0.5}})_x$ through H_2 chemisorption at oxygen rich conditions, $\Delta\mu_{\text{O}} = 0$ eV. Surface energy of is plotted as (top) $\gamma(\Delta\mu_{\text{H}_2})$ and (bottom) $\gamma(\text{T}, P_{\text{H}_2}=10^{-5}$ bar).168

Figure B.6 Reduction of $(\text{Co}^{\text{Td}})_x$ through O_{vac} formation without consideration of H_2 or H_2O , (top) as $\gamma(\Delta\mu_{\text{O}})$ and (bottom) as $\gamma(\text{T}, P_{\text{O}_2}=10^{-5}$ bar).169

Figure B.7 Reduction of $(\text{Co}^{\text{Td}}\text{Co}^{\text{Oh}})_x$ through O_{vac} formation without consideration of H_2 or H_2O , (top) as $\gamma(\Delta\mu_{\text{O}})$ and (bottom) as $\gamma(\text{T}, P_{\text{O}_2}=10^{-5}$ bar).170

Figure B.8 Reduction of $(\text{Co}^{\text{Td}}\text{Co}^{\text{Oh}_{0.5}})_x$ through O_{vac} formation without consideration of H_2 or H_2O , (top) as $\gamma(\Delta\mu_{\text{O}})$ and (bottom) as $\gamma(\text{T}, P_{\text{O}_2}=10^{-5}$ bar).171

Figure B.9 $\text{O}_2/\text{H}_2\text{O}$ surface stability diagram with all regions labeled.175

Figure B.10 Fully labeled $\text{H}_2/\text{H}_2\text{O}$ surface stability diagram180

Figure B.11 Surface distortion experienced by the Co-rich termination (a) after reduction by (b) adsorption of 7.11 H/nm^2 , (c) formation of $3.56 \text{ O}_{\text{vac}}/\text{nm}^2$, and (d) formation of $7.11 \text{ O}_{\text{vac}}/\text{nm}^2$. After relaxation, Co- O_h , Co- T_d , and surface O, following the arrows, move from their initial positions, denoted by open gold, green, and red circles, to their final positions. Pink circles represent O_{vac} . Two types of surface Co and four types of surface O are indicated as Co_A , Co_B , O_A , O_B , O_C , and O_D185

Figure B.12 Magnetic alignment for the stoichiometric termination in calculations used for this work a) and the ground state b). The energies differ by -0.76 eV/cell in favor of structure (b) and the correction was applied to all structures of this termination in constructing the stability diagrams. The difference at $U_{\text{eff}} = 2 \text{ eV}$ was -1.01 eV/cell187

Figure B.13 The (top two, left: top view, right: side view) pairs (one H_2O molecule-OH pair per surface Co^{2+}) and (bottom two, left: top view, right: side view) hexagonal (OH and H_2O connect to form a hexagonal hydroxyl overlayer) configurations of hydroxyl overlayers on the $(\text{Co}^{\text{Td}})_x$ termination, adapted from ref¹⁴⁵.....187

Figure C.1 Structure of the $\text{Co}_3\text{O}_4(111)$ surface in equilibrium with the gas environment during steady state reaction (adapted from ¹⁷²) and Mo_1 and Pd_1 active sites. The surface (a: top view, b: side view) is Co-enriched and hydroxylated, terminated with 7.11 Co/nm^2 and 7.11 OH/nm^2 . Oxidized $\text{Co}_3\text{O}_4(111)$ films are terminated by O (red) and Co (green). Co (gold) atoms are added to simulate surface reduction without phase-change in the near-surface layers. 2 types of OH exist on the surface: bidentate OH which bridge over surface (gold and green) Co, and tetradentate OH which are bound to 2 subsurface (blue) Co as well as surface (gold and green) Co. (c) The Mo_1 site is constructed by substituting one of the gold Co cations on the surface with Mo and removing one

unit of H ₂ O. (d) The Pd ₁ site is constructed by adsorbing one unit of PdH ₂ and substituting a nearby OH group by OCH ₃	189
Figure C.2 Selected geometries of the Pd ₁ site considered in this work. The relative Gibbs free energy under steady state conditions compared to the most stable configuration is provided for each geometry	190
Figure C.3 Selected geometries of the Mo ₁ site considered in this work. The relative Gibbs free energy under steady state conditions compared to the most stable configuration is provided for each geometry	191
Figure C.4 All intermediate and transition state geometries in the HDO reaction mechanism over Pd ₁ only. Only atoms near the Pd ₁ site and its adjacent Co are shown.	192
Figure C.5 All intermediate and transition state geometries in the HDO reaction mechanism over Mo ₁ assisted by H spillover. Only atoms near the Mo ₁ site and its adjacent Co are shown.....	193
Figure C.6 Hydrogen dissociation over the Co ₃ O ₄ substrate. H ₂ dissociation on the Co ₃ O ₄ (111) substrate requires a rather large free energy barrier of 1.62 eV.	195
Figure C.7 Hydrogen dissociation over the Mo ₁ site. H ₂ dissociates on the Mo ₁ site requires a rather large free energy barrier of 2.39 eV.	196
Figure C.8 Hydrogen spillover pathway across the Co ₃ O ₄ substrate. One additional H on the hydroxylated Co ₃ O ₄ (111) support can migrate across it through a Grotthuss-type mechanism. A metastable H-bonded water intermediate (seen all states beside S-2) facilitates the diffusion of H. The spillover process has an electronic energy barrier of 0.63 eV.....	197
Figure C.9 The HDO of anisole over a grafted Mo ₁ site assisted by H spillover from Pd ₁ . The reaction can proceed through hydrogenation of the methoxy fragment first (black pathway) or the	

phenyl fragment first (red pathway). The overall reaction has a rather high Gibbs free energy span of 1.90 eV and thus is unlikely to be responsible for the reactivity of $\text{Mo}_1+\text{Pd}_1/\text{Co}_3\text{O}_4$198

Figure C.10 The enthalpy pathway for the HDO of anisole over Pd_1 . The structures of the respective intermediates and transition states are shown in Figure C.4.200

Figure C.11 The enthalpy pathway for the HDO of anisole over Mo_1 assisted by H spillover. The structures of the respective intermediates and transition states are shown in Figure C.5.201

Figure C.12 (a) The DRC of key intermediates and transition states in the HDO of anisole over Pd_1 and (b, c) their geometries. The desorption of methanol is the sole rate-controlling transition state, while the PdH_2 is the main rate-controlling intermediate. The DRC of PdH_2 decreases with temperature.204

Figure C.13 (a) The DRC of key intermediates in the HDO of anisole over Mo_1+Pd_1 and (b-f) their geometries. The Mo-OCH_3 species has the lowest DRC in the temperature range studied, but gradually becomes less rate-controlling as temperature increases.205

Figure C.14 (a) The DRC of key transition states in the HDO of anisole over Mo_1+Pd_1 and (b-c) their geometries. The dissociation of anisole has the highest DRC in the temperature range studied, but gradually becomes less rate-controlling as temperature increases.205

Figure D.1 (a) Enthalpy and (b) free energy profiles for hydrogen dissociation and migration on the Pd_1 -in-Au(111) surface. The reaction starts with H_2 molecular adsorption [H_2], followed by the transition state of dissociation [TS-Dis] to form two separated hydrogen atoms [2H]. One of the hydrogen atoms would migrate to the Au surface by going through the transition state for migration [TS-M], reaching the [H(Pd,Au)] state. The H atom at the Pd site would eventually combine with another H atom and desorb while the one at the Au site remains on the surface [H(Au)]. Conditions

used for the free energy profile are: $T = 363 \text{ K}$ and $P(\text{H}_2) = 0.2 \text{ bar}$. (c) Configurations of each of the steps in the energy profiles.207

Figure D.2 Adsorption configuration of the carbonaceous intermediates on $\text{Pd}_1\text{Au}(111)$ for (a) the hydrogenation of the terminal carbon atom (C_1) in the first reaction step, followed by the hydrogenation of the carbon atom attached to the butyl group (C_2) and for (b) the hydrogenation of C_2 in the first step, followed by the hydrogenation of C_1208

Figure D.3 Free energy diagram of 1-hexyl formation via 1-hexylidene on the $\text{Pd}_1\text{Au}(111)$ surface. The C_2 atom was chosen in the first place for the over-hydrogenation as there is electron donation from the carbon chain to help stabilize the transition state. The barrier for the forward hydrogenation of 1-hexylidene (RHHCCCH) is 0.33 eV higher than the reverse barrier. In addition, this side-pathway has an overall free energy barrier (1.09 eV) that is at least 0.26 eV higher than that of the regular pathway to form 1-hexyl via 1-hexene (0.83 eV). Hence, this pathway is energetically unfavorable and is unlikely to deteriorate the selectivity for 1-hexene formation. Conditions are: $T = 363 \text{ K}$, $P(\text{H}_2) = 0.2 \text{ bar}$, $P(\text{C}_6\text{H}_{10}) = 0.01 \text{ bar}$, $P(\text{C}_6\text{H}_{12}) = P(\text{C}_6\text{H}_{14}) = 0.001 \text{ bar}$210

Figure D.4 Microkinetic simulations performed in the temperature range of $323\sim 373 \text{ K}$ at a constant inlet flow rate (50 SCCM , $20\% \text{ H}_2$, $1\% \text{ 1-Hexyne}$, balance inert) and catalyst loading (20 mg). (a) 1-Hexyne conversion (black circles, full line), 1-hexene selectivity (blue triangles, dashed line), and 1-hexyne selectivity (blue squares, dashed line) as a function of reactor temperature. (b) 1-Hexene selectivity plotted against 1-hexyne conversion.213

Figure D.5 Pathway selectivity for (a) the formation of 1-hexene through the hydrogenation of adsorbed 1-hexyne to 1-hexenyl (r_9 , blue) and through the hydrogenation of adsorbed 1-hexyne to 2-hexenyl (r_{14} , orange), and (b) the formation of n-hexane through the hydrogenation of adsorbed

1-hexene to 1-hexyl (r_{16} , blue), through the hydrogenation of adsorbed 1-hexene to 2-hexyl (r_{23} , orange), and through the hydrogenation of 1-hexenyl to 1-hexylidene and then 1-hexyl (r_{27} , green).

.....214

Figure D.6 The degrees of rate control of key intermediate states in the hydrogenation of 1-hexyne to 1-hexene. Adsorbed 1-hexyne (orange line) and 1-hexene (purple line) are the main rate-controlling intermediates until 353 K, largely mirroring the influence of temperature on coverages.

.....214

Figure D.7 The chemical potentials of 1-hexyne (blue) and 1-hexene (red) as functions of temperature at fixed pressures (1 kPa for both 1-hexyne and 1-hexene), compared to their adsorption enthalpies measured by TPD (dashed lines) and their adsorption energies calculated by the optPBE XC functional (dots).....216

Figure D.8 Brønsted-Evans-Polanyi relation between the reaction energies and activation energies of C-H bond formation steps on Pd₁/Au(111).217

Figure D.9 Projected density of states (DOS) onto the Pd 4d orbitals of a single Pd atom on the surface of (a) Pd(111) and (b) Pd₁Au(111). The first moment of the Pd 4d states (d band center) in two situations is not very different, but the 4d band of the Pd single atom is much narrower. ..218

Figure E.1 Adsorption configurations of the reactant, the intermediates and the products on Pd₁Au(111) for hydrogenation of 1-hexene to n-hexane via the 1-hexyl (a) and 2-hexyl (b) intermediate, and (c) isomerization of the 2-hexyl intermediate to 2-hexene.219

Figure E.2 Degree of selectivity control (DSC) for 2-hexene formation of selected TS evaluated at fixed partial pressures. DSC for 2-hexene formation evaluated at T = 373 K, P(H₂) = 0.2 bar, P(1-hexene) = 0.01 bar, and P(2-hexene) = P(n-hexane) = 0.001 bar. The TS of H₂ dissociation (DSC = -0.57) and H spillover to 2-Hexyl (DSC = -0.57) have the most negative impact on the

selectivity of 2-hexene, while the TS of the hydrogenation of 1-hexene to 2-hexyl (DSC = 0.93) and the dehydrogenation of 2-hexyl to 2-hexene (DSC = 0.69) have the most positive impact on the selectivity of 2-hexene.....223

Figure E.3 1-hexene consumption rate and product selectivity evaluated at fixed partial pressures after increasing the barriers of H₂ dissociation and H spillover by 0.1 eV. Microkinetic model of 1-hexene reaction with H₂ evaluated at P(H₂) = 0.2 bar, P(1-hexene) = 0.01 bar, and P(2-hexene) = P(n-hexane) = 0.001 bar. (a) Rate of 1-hexene consumption, (b) selectivity of 2-hexene and n-hexane.....223

Figure E.4 Plug flow reactor (PFR) simulations of product and isotope selectivity of 1-Hexene deuteration and isomerization without shifts to the barrier of H₂ dissociation and spillover. (a) 1-Hexene conversion and (b) selectivity of 2-Hexene and n-Hexane as functions of reactor temperature. (c) 1-Hexene isotope distribution, (d) 2-Hexene isotope distribution, and (e) n-Hexane isotope distribution as functions of 1-Hexene conversion. The same catalyst loading and reaction conditions as (Figure 6.3) were used here.224

List of Tables

Table 3.1 Description of the specific types of surface structures observed in Figure 3.3 and 3.5	38
Table 3.2 Side (through the a axis) and top (through the c axis) views of representative structures in regions 1-12 on the surface stability diagram (see Table 3.1, Figure 3.3, and Figure 3.5). 4 and 9b are adapted from ref. ¹⁴⁵	39
Table 3.3 Gas phase conditions reached in vibrational spectroscopy above 500 K	50
Table 3.4 Comparison of water adsorption energy and energy of vacancy formation calculated using $U_{\text{eff}} = 3.5 \text{ eV}$, 2.0 eV , and HSE06+dDsC (water adsorption data adapted from ¹⁴⁵)	56
Table A.1 Coefficients used in the ΔG_{vib} correlations ($\Delta G_{\text{vib}} = AT^4 + BT^3 + CT^2 + DT + E$)	136
Table A.2 Settings used in developing the extrapolative CO adsorption energy correction at the PBE level	143
Table A.3 The Rh ₁ , Rh ₂ , Rh ₄ , and Rh ₆ carbonyls used in developing the CO adsorption energy correction for Rh carbonyl molecules	144
Table A.4 Extrapolated average CO adsorption energies for the Rh carbonyl molecules	145
Table A.5 Top (2nd row) and side (3rd row) views of supported Rh carbonyl sites used to develop the CO adsorption energy correction	146
Table A.6 Extrapolated average CO adsorption energies of ceria-supported Rh carbonyls	148
Table A.7 Performance of the CO adsorption energy correction in predicting CO adsorption energies in molecular Rh carbonyls compared to those obtained by Fang et al. with CCSD(T). ⁴³	149

Table A.8 Performance of the CO adsorption energy correction in predicting the Rh(CO) ₄ dimerization energy and relative energy of Rh ₂ (CO) ₈ isomers compared to those obtained by Fang et al. with CCSD(T). ⁴³	150
Table A.9 Performance of the CO adsorption energy correction in predicting the relative stability of Rh ₄ (CO) ₁₂ isomers. The result is comparable to those predicted by averaging the energies calculated by MP2 and the ωB97xD functional. ⁴³	151
Table B.1 Energies of H ₂ adsorption on the Co Poor (Co ^{Td}) _x termination	172
Table B.2 Energies of H ₂ adsorption on the stoichiometric (Co ^{Td} Co ^{Oh} _{0.5}) _x termination	172
Table B.3 Energies of H ₂ adsorption on the Co-rich (Co ^{Td} Co ^{Oh}) _x termination	172
Table B.4 Energies of oxygen vacancy (O _{vac}) formation on the Co Poor (Co ^{Td}) _x termination	173
Table B.5 Energies of oxygen vacancy (O _{vac}) formation on the stoichiometric (Co ^{Td} Co ^{Oh} _{0.5}) _x termination.....	173
Table B.6 Energies of oxygen vacancy (O _{vac}) formation on the Co-rich (Co ^{Td} Co ^{Oh}) _x termination	173
Table B.7 Energies of H ₂ O adsorption on the Co Poor (Co ^{Td}) _x termination, retrieved from ref ¹⁴⁵	174
Table B.8 Energies of H ₂ O adsorption on the stoichiometric (Co ^{Td} Co ^{Oh} _{0.5}) _x termination	174
Table B.9 Energies of H ₂ O adsorption on the Co-rich (Co ^{Td} Co ^{Oh}) _x termination	174
Table B.10 Surface structures present on the H ₂ O/O ₂ surface stability diagram. Key: Co ³⁺ : blue, Co ²⁺ on the surface: green, Co ²⁺ added to the surface: gold, O ²⁻ : yellow, H: white.	175
Table B.11 Surface structures present on the H ₂ O/H ₂ surface stability diagram.....	180
Table B.12 ν(O-D) and ν(O-H) vibrational mode calibration for PBE+dDsC, where the ratio between the experimental and calculated average wavenumbers is taken as calibration factor .	183

Table B.13 Side and top views of geometries used in frequency calculations, where the constrained atoms are crossed out. Co: pink, O: red, H: white	184
Table B.14 Displacements of surface Co and O ions upon H adsorption and generation of the structure in Figure B.11b	186
Table B.15 Displacements of surface Co and O ions upon H adsorption and generation of the structure in Figure B.11c	186
Table B.16 Displacements of surface Co and O ions upon H adsorption and generation of the structure in Figure B.11d	186
Table C.1 Bader charges of Pd complexes for assignment of Pd oxidation states.....	193
Table C.2 Bader charges of Mo complexes for assignment of Mo oxidation states.	194
Table C.3 Bader charges of intermediate and transition states along the anisole HDO pathway over Pd ₁	194
Table C.4 Bader charges of intermediate and transition states along the anisole HDO pathway over Mo ₁	195
Table C.5 Elementary steps of the HDO of anisole over Pd ₁ . The rate constants, Gibbs free energies of reaction, and Gibbs free energy are computed at 150 °C and 1 bar. The Gibbs free energy barriers for adsorption steps modelled with collision theory are marked as N/A.	203
Table C.6 Elementary steps of the HDO of anisole over Mo ₁ assisted by H spillover. The rate constants, Gibbs free energies of reaction, and Gibbs free energy are computed at 150 °C and 1 bar. The Gibbs free energy barriers for adsorption steps modelled with collision theory are marked as N/A. Sites on the substrate are denoted as “s”.	203

Table D.1 Free energy values for 1-hexene hydrogenation to form hexane. The same reference for 1-hexyne hydrogenation was used, i.e. 1-hexyne and H ₂ in the gas phase. Conditions are: T = 363 K, P(H ₂) = 0.2 bar, P(C ₆ H ₁₀) = 0.01 bar, P(C ₆ H ₁₂) = P(C ₆ H ₁₄) = 0.001bar.	209
Table D.2 Kinetic parameters, Gibbs free energies of reaction and activation derived from DFT-computed electronic energies evaluated at 363 K and standard pressure (1 bar). The n-butyl tail of gaseous and adsorbed C ₆ species is denoted as “R”. Hydrogen atoms co-adsorbed with carbonaceous intermediates are indicated as (H).	211
Table D.3 Three possible rate laws for the hydrogenation of 1-hexyne, derived by assuming H ₂ dissociation, 1-hexyne hydrogenation to 1-hexenyl, or 1-hexenyl hydrogenation to 1-hexene is the rate-controlling transition state. K _i : equilibrium constant of elementary step i. k _{if} : forward rate constant of elementary step i. P _j : partial pressure of reactant (or product) j. θ _{Pd,0} : fraction of Pd sites on the catalyst surface.	215
Table D.4 The desorption energy of 1-hexyne on Pd ₁ /Au(111) predicted by various density functionals. The desorption energy predicted by optPBE-vdW is the closest to the desorption enthalpy of 1-hexyne reported by Liu et al. ²⁰¹	216
Table E.1 Kinetic rate constants, Gibbs free energies of reaction and of activation derived from DFT-computed electronic energies and evaluated at 373.15 K and standard pressure (1 bar). The n-propyl tail of gaseous and adsorbed C ₆ species is denoted as “R”. Steps in bold indicate those not involving deuterium. No shift was applied to the barriers of H ₂ /D ₂ /HD dissociation or H/D spillover steps.	220

Acknowledgements

First and most importantly, I would like to thank my advisor, Philippe Sautet, for his direction and constant support over the last five years. His wealth of knowledge and patient guidance has made this dissertation possible. I really couldn't have asked for a better advisor.

Additionally, I would like to acknowledge Geng Sun, Tirso López-Ausens, and Yan Tang for their assistance on performing DFT simulations of metal oxides and oxide-supported single atoms, as well as Maarten Sabbe and Tao Wang for their assistance on performing microkinetic simulations. I would like to thank my experimental collaborators in the US and around the world for their contributions to all our research projects.

I would like to acknowledge the member of my dissertation committee, Anastassia Alexandrova for her computational chemistry class where I learned a lot about molecular simulations, Dante Simonetti for his course in kinetics and reaction engineering, and Panagiotis Christofides for his support of the ChBE graduate student committee over the years.

Next, I would like to thank all my colleagues for their help, discussions, and collaborations over the years. I would especially like to acknowledge Ziyang Wei for his help and discussions, and Michael Ngan for our collaboration in performing the DFT calculations of 1-hexyne and 1-hexene hydrogenation over Pd/Au.

Finally, I would like to acknowledge my family and friends for their support.

Several chapters in this dissertation contain material adapted from published, submitted, and unpublished manuscripts with multiple contributing authors, as noted in the following.

Chapter 2 contains figures and text adapted, with permission from Springer Nature, from the article "Reaction product-driven restructuring and assisted stabilization of a highly dispersed Rh-on-ceria catalyst", by George Yan, Yu Tang, Yuting Li, Yixiao Li, Luan Nguyen, Tomohiro

Sakata, Kotaro Higashi, Franklin Feng Tao, and Philippe Sautet, *Nat. Catal.* **2022**, 5(2), 119~127. <https://doi.org/10.1038/s41929-022-00741-2>. PS and FT conceptualized and supervised the work in the article. GY performed the computational studies. YT, Yuting Li, Yixiao Li, and LN performed the experiments. YT, LN, TS and KH contributed to the EXAFS experiments. FT guided the experimental studies. The draft was prepared and edited by GY, YT, FT, and PS. The computational studies carried out in the work was supported by NSF Award no. NSF-CHE-1800601. The calculations in this work used computational and storage services associated with the Hoffman2 shared computational cluster located at University of California Los Angeles. This work also used the Extreme Science and Engineering Discovery Environment, which is supported by National Science Foundation grant no. ACI-1548562. Specifically, the systems Bridges, Bridges-2 and Comet were used. The Bridges system is supported by NSF award no. ACI-1445606, at the Pittsburgh Supercomputing Center.

Chapter 3 contains figures, tables, and text adapted, with permission from the American Chemical Society, from the article “Surface Structure of Co_3O_4 (111) under Reactive Gas-Phase Environments”, by George Yan and Philippe Sautet, *ACS Catal.*, **2019**, 9(7), 6380-6392 (erratum: 10.1021/acscatal.9b03445). <https://doi.org/10.1021/acscatal.9b01485>. PS conceptualized and supervised the work in the article. GY performed the computational studies. The draft was prepared and edited by GY and PS. The computational studies carried out in this work was supported by UCLA startup funding. This work used computational and storage services associated with the Hoffman2 shared computational cluster located at UCLA, provided by UCLA’s Institute for Digital Research and Education Group (IDRE). These works also used the Extreme Science and Engineering Discovery Environment (XSEDE), which is supported by National Science Foundation grant number ACI-1548562. Specifically, they used the Bridges

system, which is supported by NSF award number ACI-1445606, at the Pittsburgh Supercomputing Center (PSC).

Chapter 4 contains unpublished text and figures from a manuscript currently in preparation, by authors Yu Tang, George Yan, Shiran Zhang, Luan Nguyen, Yuting Li, Yasuhiro Iwasawa, Tomohiro Sakata, Christopher Andolina, Judy Yang, Philippe Sautet, and Franklin (Feng) Tao. FT conceived the idea and designed experimental methods of the manuscript. PS designed the computational studies. The manuscript was prepared and edited by YT, GY, PS, and FT. YT, LN, SZ, and YL prepared catalysts, evaluated catalytic performance and characterized catalyst structure. GY performed computational studies. YI and TS performed XAS studies and related analysis. This work was supported by NSF through grants (#1800577 and #180061, and #1462121) and Chemical Sciences, Geosciences and Biosciences Division, Office of Basic Energy Sciences, Office of Science, U.S. Department of Energy, under Grant No. DE-SC0014561. The calculations in this work used computational and storage services associated with the Hoffman2 shared computational cluster located at UCLA. This work also used the Extreme Science and Engineering Discovery Environment (XSEDE), which is supported by National Science Foundation grant number ACI-1548562

Chapters 5 contains text and figures from a manuscript submitted to the American Chemical Society, authored by Hio Tong Ngan, George Yan, Jessi E. S. van der Hoeven, Robert J. Madix, Cynthia M. Friend, and Philippe Sautet. PS, CMF and RJM guided the research in the manuscript. HTN performed the DFT calculations, advised by PS. GY performed the microkinetic modeling. JvdH prepared the catalysts and conducted the catalysis experiments. All authors participated in discussions and have given approval to the final version of the manuscript. This work was supported as part of the Integrated Mesoscale Architectures for Sustainable Catalysis

(IMASC), an Energy Frontier Research Center funded by the U.S. Department of Energy, Office of Science, Basic Energy Sciences under Award # DE-SC0012573. The DFT calculations in this work used computational and storage services associated with the Hoffman2 cluster at the UCLA Institute for Digital Research and Education (IDRE), the National Energy Research Scientific Computing Center (NERSC) of the U.S. Department of Energy, and the Bridges-2 cluster at the Pittsburgh Supercomputing Center (supported by National Science Foundation award number ACI-1928147) through the Extreme Science and Engineering Discovery Environment (supported by National Science Foundation grant number ACI-1548562) grant TG-CHE170060.

Chapter 6 contains text and figures from a manuscript submitted to the American Chemical Society, authored by Jessi E. S. van der Hoeven, Hio Tong Ngan, George Yan, Joanna Aizenberg, Robert J. Madix, Philippe Sautet, and Cynthia M. Friend. CMF, PS and RJM guided the research in the manuscript. JvdH prepared and characterized the catalysts, advised by JA, conducted the catalysis experiments, and developed the quantitative data analysis. HTN performed the DFT calculations. GY performed the microkinetic modeling. All authors participated in discussions and the interpretation of the data. JvdH wrote the manuscript with contributions of all authors. This work was supported as part of the Integrated Mesoscale Architectures for Sustainable Catalysis (IMASC), an Energy Frontier Research Center funded by the U.S. Department of Energy, Office of Science, Basic Energy Sciences under Award # DE-SC0012573. The DFT calculations in this work used computational and storage services associated with the Hoffman2 cluster at the UCLA Institute for Digital Research and Education (IDRE), the National Energy Research Scientific Computing Center (NERSC) of the U.S. Department of Energy, and the Bridges-2 cluster at the Pittsburgh Supercomputing Center (supported by National Science Foundation award number ACI-1928147) through the Extreme Science and Engineering Discovery Environment (supported

by National Science Foundation grant number ACI-1548562) grant TG-CHE170060. The authors thank Dr. M. Luneau and D. Verbart for their initial 1-hexene hydrogenation work, Dr. S. Dussi for writing the python code to deconvolute the GCMS spectra, and Dr. M. Aizenberg for critically reading the manuscript.

Curriculum Vitae

2013 – 2017 B.S. (Chemical Engineering), Lehigh University, Bethlehem, PA

Awards

2021 UCLA Dissertation Fellowship

Publications at UCLA

1. Y. Tang*, G. Yan*, S. Zhang*, L. T. Nguyen*, Y. T. Li, Y. Iwasawa, T. Sakata, C. Andolina, J. Yang, P. Sautet, F. Tao, Revising for Resubmission.
2. J. E. S. van der Hoeven, H. T. Ngan, G. Yan, J. Aizenberg, R. J. Madix, P. Sautet, C. M. Friend, Submitted.
3. H. T. Ngan, G. Yan, J. E. S. van der Hoeven, R. J. Madix, C. M. Friend, P. Sautet, Submitted.
4. N. Marcella*, J. S. Lim*, A. M. Płonka*, G. Yan*, C. J. Owen, J. E. S. van der Hoeven, A. C. Foucher, H. T. Ngan, S. B. Torrisi, N. S. Marinkovic, E. A. Stach, J. F. Weaver, P. Sautet, B. Kozinsky, A. I. Frenkel, *Nat. Commun.*, **2022**, 13 (1), 1-9.
5. G. Yan*, Y. Tang*, Y. T. Li*, Y. X. Li, L. Nguyen, T. Sakata, K. Higashi, F. Tao, P. Sautet, “Reaction product-assisted stabilization of a highly dispersed catalyst”, *Nat. Catal.*, **2022**, 5 (2), 119-127.
6. G. Giannakakis, P. Kress, K. Duanmu, H. T. Ngan, G. Yan, A. S. Hoffman, Z. Qi, A. Trimpalis, L. Annamalai, M. Ouyang, J. Liu, N. Eagan, J. Biener, D. Sokaras, M. Flytzani-Stephanopoulos, S. R. Bare, P. Sautet, E. C. H. Sykes, “Mechanistic and Electronic Insights

- into a Working NiAu Single-Atom Alloy Ethanol Dehydrogenation Catalyst”, J. Am. Chem. Soc., **2021**, 143 (51), 21567-21579
7. T. Zeng, G. Sun, C. Miao, G. Yan, Y. Ye, W. Yang, P. Sautet, “Stabilizing Oxidative Dehydrogenation Active Site at High Temperature with Steam: ZnFe₂O₄ Catalyzed Oxidative Dehydrogenation of 1-Butene to 1,3-butadiene”, ACS Catal., **2020**, 10 (21), 12888-12897.
 8. H. Kersell, Z. Hooshmand, G. Yan, D. Le, H. Nguyen, B. Eren, C. H. Wu, I. Waluyo, A. Hunt, S. Nemsak, G. Somorjai, T. S. Rahman, P. Sautet, M. Salmeron, J. Am. Chem. Soc., **2020**, 142 (18), 8312-8322.
 9. G. Yan, P. Sautet, “The surface chemistry of Co₃O₄(111) under reactive gas phase conditions”, ACS Catal., **2019**, 9 (7), 6380-6392. Erratum: 10.1021/acscatal.9b03445.
 10. G. Yan, T. Waehler, R. Schuster, M. Schwarz, C. Hohner, K. Werner, J. Libuda, P. Sautet, “Water on Oxide Surfaces: A Triqua Surface Coordination Complex on Co₃O₄(111)”, J. Am. Chem. Soc., **2019**, 141 (14), 5623-5627.

*: equal contribution

Chapter 1 Research Background

1.1 Single Atom Catalysts as the Pinnacle of Highly Dispersed Catalysts

Heterogeneous catalysis plays an important role in both the chemical industry and everyday life. From the catalytic converters in our cars to the reforming furnaces in refineries, catalysts change the physical state of chemical mixtures and allow the procession of normally kinetically prohibited chemical reactions. As the world's appetite for fuels and commodity chemicals rapidly grows, the development of better heterogeneous catalysts for sustainable chemical processes is critical.

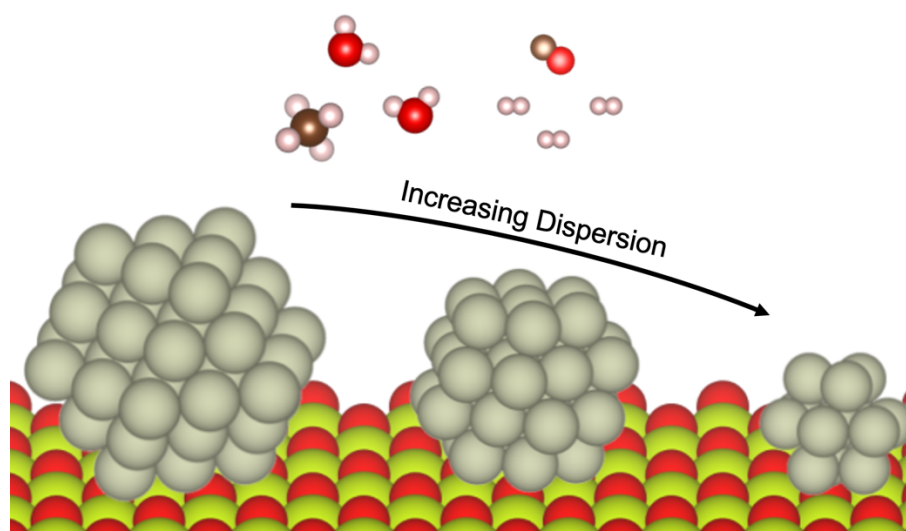


Figure 1.1 Higher catalyst dispersion improves a catalyst's efficiency by exposing more metal sites and improving catalyst activity in structurally insensitive reactions.

Metal oxide supported late TM nanoparticles and sub-nanometer clusters are popular catalysts for the conversion of natural gas and biomass pyrolysis products to commodity chemicals, but the active component of these catalysts is typically expensive. As such, a long-standing goal of metal catalysis research has been to increase catalyst dispersion, defined as the

fraction of exposed metal atoms.¹ Increasing catalyst dispersion and shrinking the particle size improve the catalysts' efficiency; moreover, smaller particles possess a larger fraction of sparsely coordinated catalytic sites, which are highly reactive for structurally insensitive reactions.^{2, 3} Although it appears that shrinking the size of supported metal particles can unilaterally improve a catalyst's efficiency in the usage of its precious component, the electronic structure of metal single atoms and very small clusters deviate from that of extended metal surfaces, which results in drastically different catalytic properties (**Figure 1.1**).⁴

Beyond the electronic structure of the catalytic site, the chemically sensitive nature of single atoms and very small clusters, stemming from their low or lack of metal-metal coordination, results in unique interactions with the support material and gas molecules.⁵⁻¹⁴ On a reducible metal oxide support, single atoms and very small clusters often exhibit oxidation states deviating from the neutral through charge transfer or interaction with surface motifs, such as O vacancies.^{15, 16} Upon reaction with certain gases, such as H₂, O₂, or CO, the supported single atoms or clusters may agglomerate or disperse, changing the active sites' nuclearity.¹⁷⁻¹⁹ These vibrant effects complicate the modeling of the structure and reactivity of dispersed metal catalysts.

Through the recent decades, advancements in synthesis, characterization, and theoretical methods have allowed researchers to fabricate and understand highly dispersed catalysts (HDCs). The most extreme would be the single atom catalyst (SAC), where, at very sparse atomic fractions, single noble metal atoms are grafted on or substituted in some catalyst support. In this sense, SACs represent the pinnacle of HDCs, where every metal atom can participate in a catalytic reaction.²⁰⁻²² Commonly, HDCs and SACs are supported on metal chalcogenides, nitrides, carbides, carbon nitrides, or even other metals. Popular metal oxide supports for such catalysts are CeO₂, Fe₂O₃, Fe₃O₄, Co₃O₄, and others. The continuous development of HDCs and SACs through the past decade

has been accounted in several recent reviews.^{4, 23-25} A brief overview on theoretical studies of the structure, stability, and catalytic reactivity of HDCs and SACs will be presented in the following sections.

1.2 Theoretical Investigations on the Structure and Stability of HDCs

As single metal atoms and very small metal clusters are highly uncoordinated and sensitive to both the environment and various motifs on the support surface, it is vital to address their structure and stability under the various conditions that the catalyst may be subjected. Theoretical investigations have been performed to assess the influence of the support and the environment on the structure and stability of single atoms and very small clusters, as well as the influence of single atoms on the support. By far, density functional theory (DFT) in the general gradient approximation (GGA) is the most prevalently used technique for these investigations as it makes a good compromise between accuracy and cost.

From the computational perspective, the structure of supported single atoms and very small clusters can be addressed by a global optimization. For single atoms and clusters of nuclearity 2~4, possible gas phase cluster configurations and their adsorption geometries on surface sites can be enumerated. For instance, such a comparison has been performed for the adsorption energy of a Pt single atom on the possible binding sites present on a stepped CeO₂(111) surface.²⁶ For larger clusters and complex surfaces, more sophisticated techniques are required (e.g. Genetic Algorithm²⁷, Basin Hopping²⁸, etc.). As a result, the active site may possess many thermally accessible metastable configurations.^{29, 30}

One way to assess the stability of highly dispersed catalysts is by the adsorption energy of their active sites on an idealized support surface and by their diffusional barriers. When the energy

cost for metal-surface bond breaking is high, the diffusional barrier of metal atoms and very small clusters is also high, and the deposited metal atoms and clusters become trapped, making aggregation into larger clusters difficult. A kinetic theory of particle growth based on the surface diffusivity of adsorbed single metal atoms has been proposed to explain the average size, coverage, and distribution of metal particles on oxide surfaces.³¹ Statistical analyses have shown that the diffusional barriers of single metal atoms depend primarily on their binding energies and bulk cohesive energies.³² Aside from single atoms, very small clusters may also be mobile on oxide surfaces and participate in the particle growth process.^{33, 34} More generally, the adhesion energy between metal particles and the support surface has been used to explain the differences in the average particle size and particle density of Ag particles grown on CeO_{2-x}(111) and MgO(100), as well as many other metal/oxide surface combinations.^{35, 36} From the computational perspective, metal particle growth on oxide supports has been studied by both mean-field and kinetic Monte Carlo (kMC) simulations.^{37, 38} Statistical analyses of single atoms on metal oxides show that this binding energy depends on the O vacancy formation energy of the support oxide and the enthalpy of formation of the oxide composed of the supported metal atom.³⁹ This finding points to the chemical picture that as the metal atom-O bond becomes stronger and the support metal-O bond weakens, the bonds between the adsorbed metal atoms and surface O become stronger. The stronger bonding ultimately slows down the agglomeration of the supported metal atoms, retaining single atoms or low nuclearity active sites.

Besides kinetic factors based on the adsorption energy of single atoms and very small clusters and their diffusion barriers, situations also exist where they may be thermodynamically stable. Through scanning tunneling microscopy (STM), Pt atoms deposited on fully oxidized CeO₂(111) were found to diffuse to the step edges on the CeO₂ film upon annealing and localize

at square planar sites.²⁶ DFT calculations found that the adsorption energy at these sites relative to gas phase Pt is higher than the cohesive energy of Pt metal.²⁶ As long as the surface stays oxidized, Pt aggregates cannot form from these isolated Pt ions. Aside from step edges on the CeO₂(111) surface, such square planar sites can also be found on the (100) surface. Although (100) is a minority surface on CeO₂ nanoparticles, it has been found to bind Pt single atoms with a strength greater than the cohesive energy of Pt.^{40, 41}

Besides the proposal of special sites which bind the targeted metal atoms stronger than their cohesive energy, theoretical assessments have also been made to account for the gas environment on the stability of single atoms and very small clusters. In the 1950s, through infrared spectroscopy, it was found that alumina supported Rh catalysts react with CO gas to form single Rh(CO)₂ units.⁴² The phenomenon is not exclusive to Rh/Al₂O₃, as such reactions have also been observed for Rh carbonyl clusters supported on zeolites.⁴³ A thermodynamic argument was developed to explain the propensity for the formation of CO-liganded Rh sites from Rh nanoparticles.⁴⁴ Here, Gibbs free energy of Rh nanoparticle disintegration is computed by subtracting the chemical potential of the gas ligands, the single Rh sites' configurational entropy, and the average energy per atom in the particle from the energy of formation of the monomer Rh(CO)₂. Surface free energy and the enthalpy of adhesion of the particle to the support are used to compute the average energy of an atom in the supported particle. This analysis has been applied to calculate the stability of Rh, Au, and Pt single atoms against nanoparticles under CO pressure.⁴⁴

⁴⁶ The disintegration of Au clusters supported on CeO₂ by adsorbed CO has also been shown by molecular dynamics simulations.⁴⁷ In general, the thermodynamic stability of supported single metal atoms and clusters can be assessed by comparing its free energy of formation to the chemical potential of such atoms on the support surface, considering the influence of the gas environment,

with the absolute lower bound set by the cohesive energy of the corresponding most-stable bulk phase.^{36, 46, 48}

Although the binary pictures are concise approximations of single atoms and very small clusters on model surfaces, their interaction with support surfaces can also change the properties of the supports themselves. Substitution of transition metal cations have been performed on the CeO₂(111) surfaces and their effects on reactivity have been studied.⁴⁹ For the CeO₂(111) surface, it was observed that the substitution of mid and late transition metals on CeO₂ decrease the O_{vac} formation energy. As a direct consequence, the barrier to activate CH₄ is decreased in these situations as it is closely tied to the ease of O_{vac} formation. Besides cation substitutions, small clusters may also influence the properties of support surfaces upon adsorption. For instance, it has been found that Pt particles deposited on CeO₂(111) induces the reverse spillover of O from the CeO₂(111) substrate onto Pt.⁵⁰ Computationally, the reverse spillover of O has also been found to occur from CeO₂(111) onto small Cu clusters.⁵¹ Beyond O, the reverse spillover of H from hydroxylated γ -Al₂O₃ onto Pt and Pd clusters, as well as from hydroxylated zeolites to Rh clusters have been found as well.^{52, 53}

Besides assessing the stability of supported single atoms and clusters just considering the interaction between metal atoms and the support surface, thermodynamic analysis can also be performed to find the most stable configurations of supported or substituted single atoms and clusters across a wide range of temperatures and pressures.⁵⁴⁻⁵⁷ For instance, these studies have been performed on supported and substituted Pd ions on the CeO₂(111) surface.⁵⁵⁻⁵⁷ It was found that the concentration of O around a substituted Pd ion depends on the O₂ chemical potential in the surrounding atmosphere. At P(O₂) = 1 bar at low temperature, one O vacancy surrounds the the substituted Pd site, and the next vacancy is predicted to form above 988 K.⁵⁶ The situation where

three Pd are substituted on the $\text{CeO}_2(111)$ surface is also predicted to be stable against the formation of a grafted Pd trimer under most realistic O_2 pressures.⁵⁵ In both of these situations, the metastable O surrounding the substituted Pd are predicted to be important for the activity of oxidation reactions. As another example, the preferred binding site of Rh single atoms on rutile $\text{TiO}_2(110)$ has been found to change depending on the surrounding environment.¹⁷ Under reducing conditions, Rh single atoms prefer to be grafted on the surface, while under oxidizing conditions, they prefer to reside in Ti cation vacancies. This type of restructuring has been observed by STEM for the Pt atoms on TiO_2 as well.¹⁸

From the theoretical investigations discussed, the interactions between the metal single atoms/small clusters, the support, and the environment appear heavily convoluted. The interaction between metal atoms with support surfaces and the gas environment all affect the stability of the active metal atom, while the grafting and substitution of single atoms on support surfaces can even induce changes in the chemical properties of the support. Theoretical calculations of metal atom adsorption energy, diffusional barrier, and the metal atom's interaction with gases in its environment all contribute to the description of its stability.

1.3 Catalytic Reactivity of SACs and HDCs

The kinetics of catalytic reactions over supported single atoms and very small clusters are best likened to that over homogeneous catalysts and organometallic complexes. For a homogenous catalyst, or a single atom/very small cluster grafted on an inert support, the elementary steps of a catalytic reaction will occur on a single site. More generally, as the structure of the active site can fluctuate among an ensemble of metastable states, the catalyst's overall reactivity can be expressed as a weighted sum of the Boltzmann-weighted activity of each site.^{29,58} For single-site reactions, a

first-order mass action rate law with the rate constants evaluated by transition state theory is written as the rate of an elementary step, and the reaction kinetics of such catalysts are well described by the energetic span approximation.^{59,60} The system of first order rate laws naturally lead to a set of linear algebraic equations for the steady state concentration of intermediate states, which can be solved analytically.⁶¹ Rearranging the determinant definition of the matrix inverse, the steady state reaction rate can be expressed in terms of a summation (1.1) of the individual energetic spans, defined as the difference in Gibbs free energy between intermediate states and transition states:

$$\text{TOF} = \frac{k_{\text{B}}T}{h} \frac{\exp\left(\frac{-\Delta G_{\text{r}}}{RT} - 1\right)}{\sum_{i,j=1}^N \exp\left(\frac{G_{\text{T},i} - G_{i,j} - \delta G'_{i,j}}{RT}\right)} \quad (1.1)$$

From the full expression of the steady state rate, key energetic spans may be extracted to form a simplified and wieldable approximate rate law for the catalytic cycle. The easy interconversion between an analytical rate law written in free energy spans and in rate/equilibrium constants allows the user to directly extract the apparent activation energy, prefactor, and orders of reaction from the energetic span approximation. Overall, the energetic span approximation is a straightforward and powerful visual method to assess the catalytic reactivity of single atoms and very small clusters.

Beyond the energetic span approximation, microkinetic modeling and kMC simulations are two techniques that are also used in assessing the reactivity of SACs. The advantage of the two techniques is that they can be applied in the case where elementary steps can occur on both the SAC and its surroundings support sites. In microkinetic models, the rate of an elementary step is expressed as a mean field rate law, whereas in kMC simulations, the spatial distribution of surface intermediates is directly taken into account.⁶² In microkinetic models, the steady state reaction rate of the catalyst can be found by integrating the time-dependent coverages, by directly solving the system of algebraic equations corresponding to the steady state coverages, or by a combination of

both.⁶³⁻⁶⁵ In the limit of the reaction only occurring on one site, a microkinetic model should yield the same result as the energetic span approximation as they aim to solve the same set of steady state algebraic equations. For example, a microkinetic model was constructed and analyzed to study CO oxidation over Al₂O₃-supported Pd₁.⁶⁶ Importantly, it was found that structure of the active site under steady state reaction differs from that found atomistic thermodynamics. The authors also found, through kMC simulations of the same catalyst, that the oxidation state of the Pd₁ active site fluctuates during reaction. As such, the measured in situ optical spectra of the active site is a weighted average of multiple states of the active site.⁶⁶

1.4 Thesis Objectives

In this dissertation, we seek to investigate both the structure of HDCs and SACs under reactive gas environments and their steady state reactivity using state-of-the-art periodic DFT calculations, atomistic thermodynamics, and microkinetic modeling.

Chapter 2 focuses on the structure of a highly dispersed Rh/CeO₂ catalyst during the steam reforming of methane. The structure and stability of the CeO₂(111) support surface and the Rh active sites were assessed through atomistic thermodynamics and validated by comparison to experimental measurements. Importantly, thermodynamic modeling reveals that CO gas product in the reaction environment is responsible in the re-dispersion of large Rh particles into Rh clusters of 1~3 Rh in size.

Chapters 3 and 4 focus on the structure and reactivity of a dual single-atom Pd₁/Mo₁/Co₃O₄ catalyst in the hydrodeoxygenation (HDO) of anisole. The structure of the Co₃O₄(111) surface was first modeled using atomistic thermodynamics and compared to spectroscopic measurements. Next, the structure of the Pd₁ and Mo₁ active sites and the anisole HDO mechanism over both

active sites were investigated as well. Finally, the catalyst reactivity was assessed using both the energetic span approximation and microkinetic simulations. It was found that the steady state anisole HDO reaction occurs through a H-spillover-mediated mechanism where H_2 dissociates on Pd_1 but the hydrogenation of dissociated anisole occurs on Mo_1 .

Chapters 5 and 6 focus on the reactivity and selectivity of 1-hexyne hydrogenation and 1-hexene hydrogenation/isomerization over a dilute Pd-in-Au alloy catalyst. For the 1-hexyne hydrogenation of $Pd_1Au(111)$, the overall reactivity, product selectivity, orders of reaction, and apparent activation energy were evaluated through microkinetic simulations and compared to experimental observations. For the hydrogenation/isomerization of 1-Hexene, the selectivity and degree of H/D exchange were assessed through microkinetic simulations as well. It was found that the large barriers of H_2 dissociation over Pd_1 ensembles and of H spillover between individual Pd_1 sites are responsible for the selectivity of the dilute Pd-in-Au catalyst.

Chapter 2 Reaction Product-Driven Restructuring and Assisted Stabilization of a Highly Dispersed Rh-on-Ceria Catalyst

2.1 Introduction

Heterogeneous catalysts, commonly formed by particles of active metals deposited on a high surface area support, are of central importance for chemical production and energy transformation. Controlling the structure of a heterogeneous catalyst's active sites is critical to maintaining its activity.^{4,23} The surface composition and morphology of a catalyst can be strongly affected by the reaction environment, such as the change in the reducing or oxidizing capability of a reactant gas or of the temperature.⁶⁷⁻⁶⁹ At high temperature, oxide-supported metal nanoparticles can sinter,^{44,45} and even the oxide support can undergo a phase transition.⁷⁰ At the atomic scale, a catalytic reaction event typically occurs on a specific site, consisting of one or more atoms of the metal particle and potentially involving atoms of the support at the metal particle's periphery, at a given temperature in the gaseous environment. To optimize the use of precious metals, a large effort has been made recently to create highly dispersed supported catalysts, in the form of small clusters.⁴ Downsizing to the single atom extreme has significantly benefited structurally insensitive catalytic reactions that occur on large metal particles;^{3, 4, 23, 71} however, these catalysts can be strongly susceptible to sintering during reaction.⁷² Therefore, understanding the structural dynamics of a highly dispersed supported catalyst under a specific catalytic environment and determining factors that maintain the high dispersion are crucial to the rational design of efficient and robust heterogeneous catalysts.

Here we report the evolution of coordination and chemical environments of initially prepared singly dispersed Rh atoms anchored on CeO₂ (Rh₁/CeO₂) driven by the reduction pretreatment step of the catalyst and then by the catalytic conditions to demonstrate the

predominant impact of the partial pressure of a product gas on the formation and preservation of highly dispersed Rh_m ($m=1-3$) cluster active sites during catalysis. We find that although the freshly prepared Rh_1 single atoms anchored on CeO_2 (Rh_1/CeO_2) transform into Rh nanoparticles ($\text{Rh NP}/\text{CeO}_2$) after H_2 reduction pretreatment, the CO generated by the steam reforming of methane (SRM) reaction ($\text{CH}_4 + \text{H}_2\text{O} \rightarrow \text{CO} + 3\text{H}_2$) breaks down the Rh NPs into highly dispersed sub-nanometer CO-liganded Rh sites, $\text{Rh}_m(\text{CO})_n$ ($m=1-3$, $n=2-4$). The atomistic first principles modelling, addressing the hidden evolution of catalytic sites at atomic scale driven by pressure of product gases.

2.2 Methods

2.2.1 DFT Calculations

Periodic DFT calculations were performed with the Vienna ab-initio simulation package (VASP), version 5.4.1.⁷³⁻⁷⁵ The exchange-correlation energy was calculated using the Perdew-Burke-Ernzerhof functional.⁷⁶ Spin polarization was used in all calculations. A dipole correction in the z direction was used for surface calculations. The projector-augmented wave (PAW) method was used to describe the core electrons.^{77,78} The Kohn-Sham orbitals were expanded using a set of plane waves with kinetic energy up to 600 eV. The electronic structure was considered converged when the electronic energy difference between consecutive SCF steps falls below 10^{-6} eV. The surface and molecular structures were considered converged when the Hellman-Feynman forces on atoms fall below 0.02 eV/Å. To correct for the self-interaction error of the Ce 4f electrons, a Hubbard-like on-site repulsion term was added using the approach of Dudarev et al. (DFT+U), with $U_{\text{eff}} = U - J = 4.5$ eV.^{79,80} Using a parabolic equation of state, the lattice parameter of CeO_2 was found to be 5.502 Å, close to reported values.⁸¹

(2×2) , $(\sqrt{7} \times \sqrt{7})$, (3×3) , $(3 \times \sqrt{7})$ and (4×4) unit cells of $\text{CeO}_2(111)$ containing 3 O-Ce-O tri-layers were used in the calculations.⁸¹⁻⁸³ For these periodicities, the Brillouin zone was sampled using $(3 \times 3 \times 1)$, $(3 \times 3 \times 1)$, $(2 \times 2 \times 1)$, $(2 \times 2 \times 1)$, and $(2 \times 2 \times 1)$ gamma-point-centered k-meshes respectively.⁸⁴ The sensitivity of stable surface structures on the choice of U_{eff} was assessed by calculations using another U_{eff} value (3.67 eV) benchmarked against single point calculations using the HSE06 hybrid functional.^{85, 86} Single point HSE06 calculations were performed from converged PBE+U ($U_{\text{eff}} = 4.5$ eV) geometries. The Brillouin zone was sampled using a 2-fold reduced (VASP commands: $\text{NKREDX} = 2$, $\text{NKREDY} = 2$), gamma point centered $(2 \times 2 \times 1)$ mesh.⁸⁷ The (3×3) cell was used to simulate the Rh active sites. The bottom tri-layer was constrained to bulk positions in structural optimizations.

Vibrational modes were calculated using the finite difference method with a step size of 0.015 Å. Factors of 0.9828 and 1.0086 were multiplied to OH and CO stretching modes respectively when comparing calculated vibrational frequencies to experimental values. Core level shift calculations were performed using both the initial state approximation (ISA) and the final state approximation (FSA). In the ISA, the vacuum-aligned Rh 3d eigen energies are directly compared to each other. Lowering the Rh 3d eigen energy results in a positive CLS. In the FSA, one 3d electron is assumed to be excited by absorption of the incident photon. The core electron binding energy (E_{CL}) is defined as $E_{\text{CL}} = E(N-1) - E(N)$, where $E(N-1)$ is the energy of the assessed structure after excitation, and $E(N)$ is the energy before excitation.⁸⁸ The final state CLS is computed by taking the difference between the E_{CL} of the assessed structure and the E_{CL} of a Rh atom in the 3rd layer below the surface of a 7-layer (3×3) Rh(111) slab. For reference, by the final state approximation, the CLS of a bulk-like Rh^{3+} ion below the $\text{Rh}_2\text{O}_3(0001)$ surface is 0.99 eV.

Structural visualizations were performed using the VESTA program.⁸⁹

2.2.2 Modeling the Ceria Surface and Rh Active Sites

The most stable $\text{CeO}_2(111)$ surface structure under reaction conditions was determined by minimizing surface free energy under the reaction gas environment.^{90, 91} The Ce^{3+} : Ce^{4+} ratio was limited to 1:1 in the two outermost CeO_2 tri-layers to simulate surface reduction. Surface and subsurface O_{vac} and adsorbed H on surface O were included as the possible surface motifs. Bulk CeO_2 , H_2 gas and H_2O gas were used as Ce, H, and O reservoirs in calculating surface free energy (Supplementary Note 6). The simulated Rh active sites were compared to each other by their Gibbs free energies of formation, normalized by each site's Rh nuclearity.^{54, 55} For a given Rh site, the hydroxylated $\text{CeO}_2(111)$ surface, H_2 gas, H_2O gas, CO gas and hypothetical supported Rh_{13} clusters were chosen as the Ce, H, O, C, and Rh reservoirs (**Appendix A.1**).

The thermodynamically controlled assumption of the $\text{CeO}_2(111)$ surface structure was made based on reported experimental observations and reported reaction barriers of elementary redox processes.⁹²⁻⁹⁴ Reduced $\text{CeO}_2(111)$ surfaces in (3×3) periodicity were searched based on rules developed from observations in literature and patterns found for representative surfaces.^{81-83, 95-101} First, using the s-xyz-w notation of Murgida et al., the most stable O_{vac} -containing surfaces should contain minimal $x+y+z$ and w . Second, when OH groups and O_{vac} coexist, the two prefer to segregate. Third, when multiple vacancies are present, Ce^{3+} ions prefer to cluster near a single vacancy. Fourth, Ce^{3+} ions prefer to localize near OH groups. And fifth, Ce^{3+} ions near an O_{vac} prefer to stay out of the O_{vac} 's first coordination shell.

For a given stoichiometry, all structure combinations were first generated without considering the arrangement of Ce^{3+} ions, sorted by rules 1 and 2 and optimized without specification of initial magnetic moments. The most stable structures found using this method were selected, and favorable Ce^{3+} localization patterns were generated and optimized using rules 3, 4,

and 5. In this set of calculations, a set of plane waves with kinetic energy up to 400 eV was used, the Brillouin zone was sampled using only the Gamma point, the electronic energy difference between consecutive SCF steps was converged to 10^{-5} eV, and the forces on atoms were converged to below 0.05 eV/Å.

The Rh active sites were searched by first computing the ligand-free Rh single atom or cluster binding sites on the fully hydroxylated surface, then checking the possible CO/H ligand configurations on the stable Rh sites. A small representative set of OH-liganded Rh₁, Rh₂, and Rh₃ structures were optimized as well, but we did not find them to be as stable as CO or H-liganded Rh single atoms and clusters. In this set of calculations, a set of plane waves with kinetic energy up to 450 eV was used, the electronic energy difference between consecutive SCF steps was converged to 10^{-6} eV, and the forces on atoms were converged to below 0.05 eV/Å.

The surface energy or Gibbs free energy of formation of each structure consists of the translational & rotational components of their gas constituents and vibrational components of the gas constituents and corresponding surface motifs (**Appendix A.2, Figure A.1~A.7, and Table A.1**). For supported Rh sites, the configurational entropy of Rh (**Appendix A.3 and Figure A.8**), the chemical potential of Rh atoms (**Appendix A.4 and Figures A.9~A.10**), and a back bonding-based penalty for the adsorption energy of CO (**Appendix A.5, Figure A.11~A.12, and Tables A.2~A.9**) were included as well.

Vibrational contributions to Gibbs free energy were computed in two ways (**Appendix A.2**). In the screening of CeO₂ surface structures and supported Rh sites and the construction of (**Figures 2.1 and A.15**), vibrational contributions were estimated based on the formation of six types of motifs: surface & subsurface O vacancies, H adsorbed on surface O, H adsorbed on Rh, and CO adsorbed on Rh pointing towards or away from the surface. The average margin of error

of this approach was up to $k_B T$ per motif from the harmonic oscillator approximation (**Figure A.7**). To construct the final T/P_{CO} stability diagram of Rh sites (**Figure 2.2**), the harmonic oscillator approximation was used instead.

Rh_{13} was chosen as the Rh chemical potential reference due its resemblance to the Rh coordination environment found by EXAFS after H_2 pretreatment.¹⁰² The Rh chemical potential was computed based on the cohesive energy of the Rh_{13} cluster, its Gibbs free energy of adsorption, and the configurational entropy of Rh_{13} clusters (**Appendix A.4**).

It is well-known that the PBE functional overpredicts the strength of transition metal d state-CO $2\pi^*$ orbital back bonding.¹⁰³ Many methods have been employed to correct this problem.¹⁰⁴⁻¹⁰⁶ Here, the singlet-triplet transition energy (ΔE_{ST})-based method of Sumaria et al. was developed and employed for the Rh active sites, where a linear trendline was fitted between the CO adsorption energy correction and the relaxed C-O bond length (**Appendix A.5**).¹⁰⁷ The CO adsorption energy correction brings the CO adsorption energy values closer to those obtained from higher level calculations.⁴³

2.3 Results and Discussion

2.3.1 Surface Structure of the CeO₂ Support and Structural Evolution of the Rh/CeO₂ Catalyst

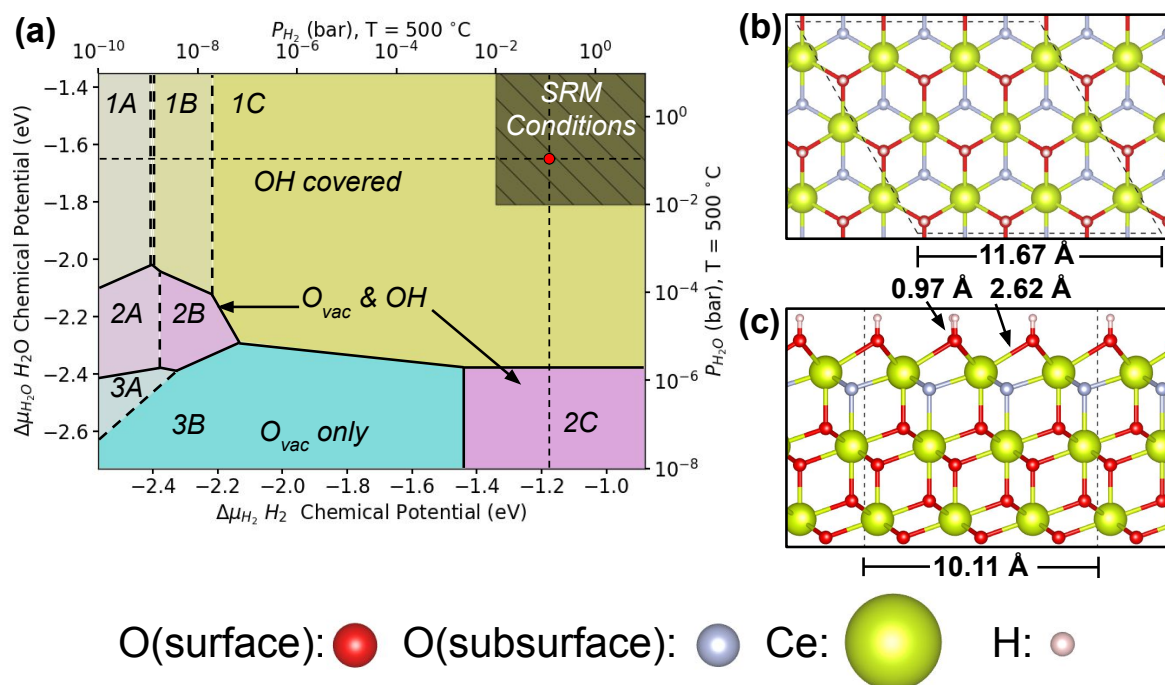


Figure 2.1 Structure and stability of the CeO₂(111) surface under gas pressure of H₂ and H₂O vapor. (a) Surface structures formed in a gas environment of H₂ and H₂O at different chemical potentials. (b and c) Top and side view of CeO₂(111) passivated with OH groups, corresponding to zone 1C in (a). (a) consists of three main phases, including solely hydroxylated regions (1A, 1B, 1C: 2.54, 5.09, 7.63 OH/nm², beige-colored regions; a coverage of 4.24 OH/nm² is stable in a sliver between regions 1A and 1B), OH/ O_{vac} mixed regions (2A: 0.85 O_{vac} /nm² & 1.70 OH/nm², 2B: 0.85 O_{vac} /nm² & 2.54 OH/nm², 2C: 3.39 O_{vac} /nm² & 0.85 OH/nm², magenta-colored regions), and solely O_{vac} -containing regions (3A: 1.91 O_{vac} /nm², 3B: 3.39 O_{vac} /nm², cyan-colored regions). The olive-colored hatched region is associated to possible pressure under which SRM could be

performed, from $P_i \sim 10^{-2}$ bar to $P_i \sim 10^1$ bar; the steady state SRM gas environment at 500 °C is marked as a red dot ($\Delta\mu_{\text{H}_2} = -1.17$ eV, $\Delta\mu_{\text{H}_2\text{O}} = -1.65$ eV, calculated using the translational and rotational contributions, assuming $P_{\text{H}_2} = 0.14$ bar and $P_{\text{H}_2\text{O}} = 0.11$ bar). The reaction condition falls in the region where the $\text{CeO}_2(111)$ surface is hydroxylated.

To model the Rh/ CeO_2 catalyst, we first examined the structure of the $\text{CeO}_2(111)$ surface. In brief, the catalyst was characterized by AP-XPS during pretreatment in 5% H_2 at 500 °C, where a peak at 532.0 eV was observed in the O 1s spectrum and assigned to the O_{surf}^* atom of $\text{H}'\text{-O}_{\text{surf}}^*\text{-Ce}^{3+}\text{-O}$ (O_{surf}^* denotes “host” O originally on the surface, while H' denotes “guest” H). AP-XPS of the catalyst under steam reforming conditions reveal the formation of another type of surface hydroxyl groups: a peak at ~531 eV assigned to O' of $\text{H}'\text{O}'\text{-Ce}^{3+}\text{-O}$. More details can be found in ref¹⁰⁸. These observations are consistent with our thermodynamics calculations based on density functional theory (DFT), which suggest that $\text{CeO}_2(111)$ is hydroxylated during catalysis, and the topmost Ce^{4+} cations of the CeO_2 surface are reduced to Ce^{3+} under the realistic H_2 and H_2O pressures experienced by the catalyst during steady state SRM at 500 °C (**Figure 2.1**). $\text{CeO}_2(111)$ was chosen as the facet to build the structural models for computational studies as the (111) facet is the main surface exposed on CeO_2 nanoparticles. The insensitivity of the predicted surface structure to the choice of U_{eff} as well as DFT-based spectroscopic calculations further support the presence of surface hydroxyls on the CeO_2 support under catalytic conditions (**Section A.6 and Figures A.1~A.16**).

Aside from the structural evolutions of the CeO_2 support, the Rh active sites also experience significant changes during the H_2 pretreatment and steam reforming of methane. The chemical structure of Rh atoms in Rh/ CeO_2 catalyst was primarily characterized by EXAFS and summarized

here.¹⁰⁹ For the as-prepared Rh/CeO₂ catalyst, only one major peak at 2.03 Å was observed in the range of 0-4 Å in the Fourier transformed r-space EXAFS spectrum at the Rh K-edge. On average, a Rh cation in the as-synthesized catalyst was found to only have 6.73±0.4 oxygen atoms in its first shell. Upon reduction in H₂ at 500 °C, a new peak at 2.66 Å, assigned to Rh-Rh bonds forms in the r-space EXAFS spectrum, while the Rh-O peak at 2.05 Å weakens. On average, 5.7±0.7 Rh atoms in the first shell of a Rh atom contribute to the peak at 2.66 Å. Finally, during the steam reforming of methane at 500 °C, the r-space EXAFS spectrum consists of a primary peak at 2.04 Å assigned to Rh-O bonds and a relative weak peak at 2.57 Å assigned to Rh-Rh bonds. The coordination number of Rh to Rh and that of O to Rh under this environment are 1.4 and 5.3 respectively. The distinct differences in CN(Rh-Rh) and CN(O-Rh) between H₂ pretreatment and the steam reforming of methane show that the Rh NPs formed under H₂ reduction are redistributed during reaction. Further analysis by the Wavelet transformation of the EXAFS Rh K-edge spectra suggest that the coordination environment of Rh during catalysis is different from either Rh₂O₃ or Rh metal NPs. Clearly, the chemical and coordination environments of Rh atoms indicate a second restructuring; the Rh NPs re-disperse into smaller Rh clusters which represent the steady state active sites of the catalyst.

2.3.2 Understanding Active Site Stabilization at the Atomic Scale

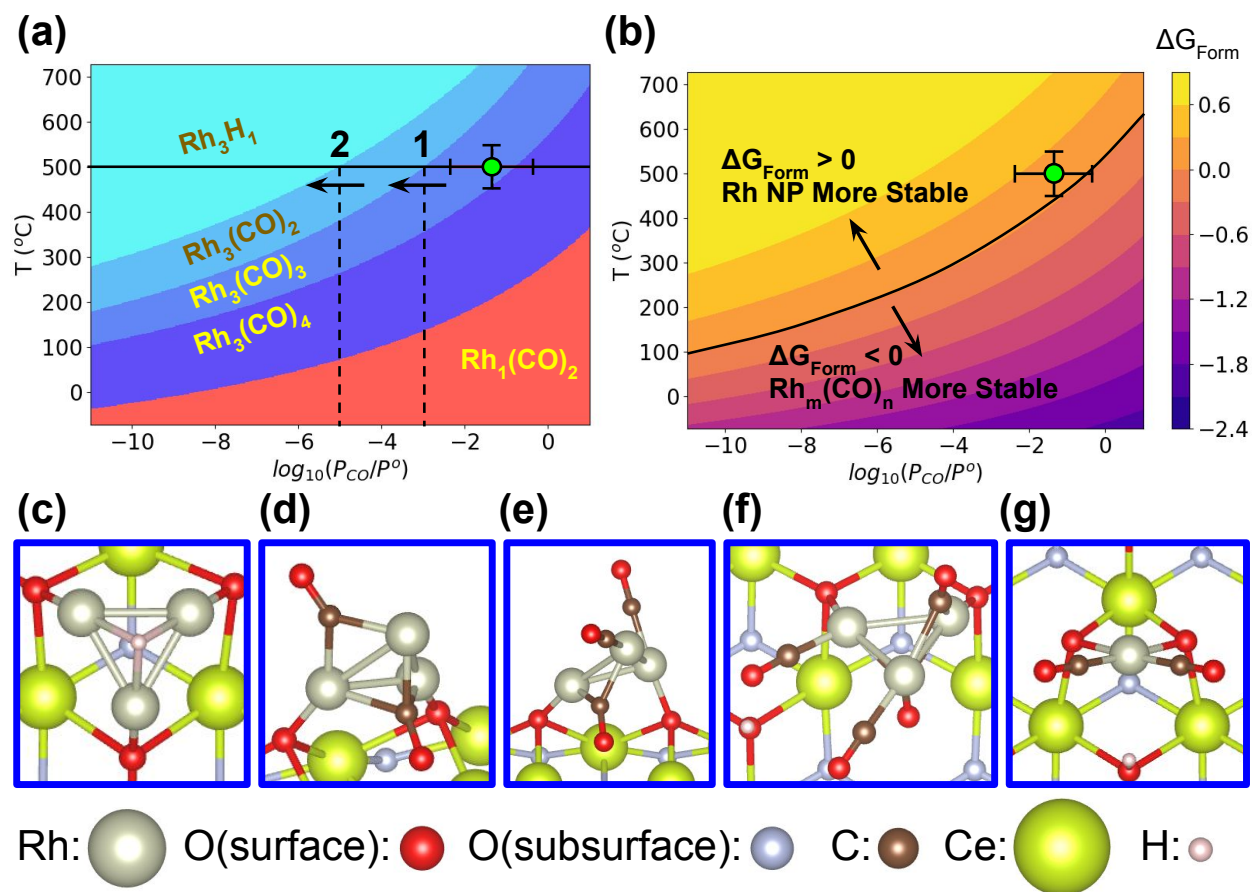


Figure 2.2 Structure and stability of Rh active sites. Theoretical modeling of the evolution of the Rh active site under catalytic conditions as a function of catalysis temperature (T) and CO pressure (P_{CO}) by holding the chemical potentials of gas phase H₂ and H₂O constant as those during SRM at 500 °C (See **Figure 2.1**). (a) Theoretically proposed stable Rh species; the SRM condition at 500 °C (P_{CO}=0.045 bar) is marked with a green dot with bars representing possible variations in T and P_{CO}. As CO pressure decreases, Rh₃(CO)₃ transforms to Rh₃(CO)₂ and then Rh₃H₁. (b) Gibbs free energy of formation of the most stable Rh-based sites as a function of catalysis temperature (T) and CO pressure (P_{CO}); the full black line marks the transition between supported Rh nanoparticles and highly dispersed Rh_m(CO)_n clusters, below which the Rh_m(CO)_n species is more stable than the

Rh nanoparticle. We find the $\text{Rh}_3(\text{CO})_3$ cluster to be close to the Rh nanoparticle in stability under catalytic conditions. For reference, the stability of the $\text{Rh}_3(\text{CO})_3$ site is shown in **Figure A.17**. (c-g) Atomic-scale geometries of Rh sites present in (a). (c) Rh_3H_1 . (d) $\text{Rh}_3(\text{CO})_2$, (e) $\text{Rh}_3(\text{CO})_3$, (f) $\text{Rh}_3(\text{CO})_4$, and (g) $\text{Rh}_1(\text{CO})_2$.

The experimentally observed structural evolution at the atomic scale of Rh-based catalytic sites during catalysis is explained by our atomistic modeling. Using DFT calculations, we computed the structures of Rh_1 , Rh_2 , and Rh_3 active sites, with H, OH and CO as possible ligands generated during catalysis. We considered a large number of liganded cluster structures (more than 500) on the hydroxylated $\text{CeO}_2(111)$ surface, including structures with an O vacancy surrounding the Rh site; we found the formation of such an O vacancy to be exergonic in the presence of Rh. By holding the chemical potentials of H_2 and H_2O constant, the influences of CO pressure (P_{CO}) and temperature on the structure and composition of the clusters were explored through atomistic thermodynamics (**Figure 2.2**).

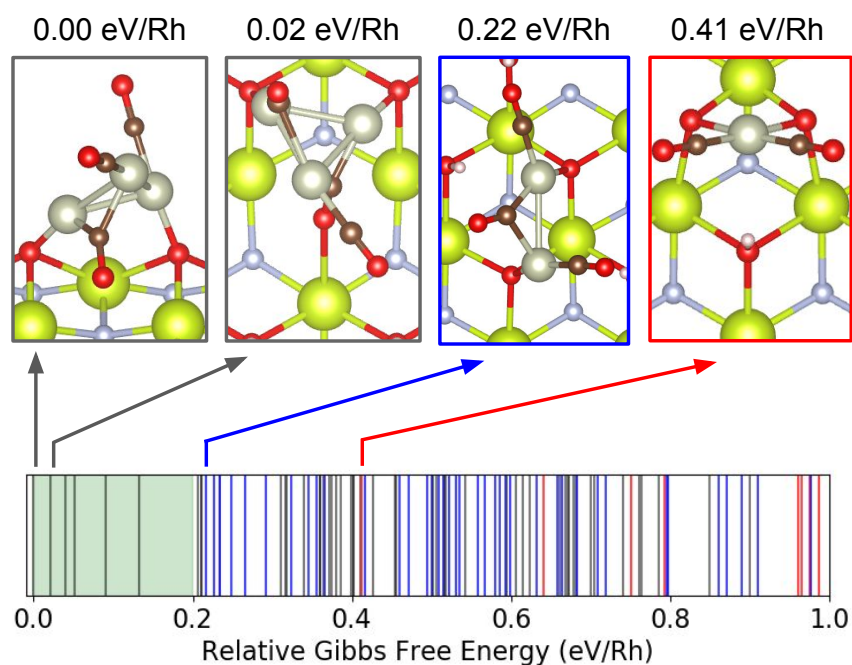


Figure 2.3 Relative stability of $\text{Rh}_m(\text{CO})_n$ sites in the reaction environment. The ensemble of Rh sites generated during the SRM reaction at 500 °C (see **Figure 2.2**), ordered by Gibbs free energy of formation relative to the most stable $\text{Rh}_3(\text{CO})_3^+$ site (line color/site type: gray/ Rh_3 ; blue/ Rh_2 ; red/ Rh_1). A $3k_B T$ region is shaded in green to indicate the thermally accessible structures. The $\text{Rh}_3(\text{CO})_3$ clusters are more stable than $\text{Rh}_2(\text{CO})_3$ and $\text{Rh}_1(\text{CO})_2$ sites in the reaction environment.

Under the steady state catalytic conditions at 500 °C (**Figure 2.2a**), we find that ensembles of distinct CO-liganded Rh clusters are generated, including low energy metastable ones (**Figure 2.3 and Section A.7**).⁵⁸ $\text{Rh}_3(\text{CO})_3$ is the most stable and hence most probable cluster based on our calculations of the Gibbs free energy of formation. In the ensemble of Rh active site structures, the $\text{Rh}_3(\text{CO})_3$ sites are more stable than both $\text{Rh}_2(\text{CO})_3$ and $\text{Rh}_1(\text{CO})_2$ (**Figure 2.3**); thus, the Rh trimers likely make up the majority of the active sites. Consistent with the reaction-driven redispersion of

Rh nanoparticles uncovered experimentally, the thermodynamic calculations suggest that small Rh₂/Rh₃ clusters can be stabilized by interaction with CO, a product of SRM. When comparing the stability of these small trimers to larger Rh nanoparticles (NP), we found that the SRM reaction condition at 500 °C, marked with a green cursor, lies next to the phase boundary between the stability domain of the Rh NPs and of the CO-liganded Rh sites, Rh_m(CO)_n (**Figure 2.2b**).

Although our thermodynamic analyses have identified that the reaction-generated CO are crucial for the stabilization of small Rh clusters, the influence of the CeO₂ support cannot be understated. Numerous studies have shown that the nature of the catalyst support surface in a reactive environment strongly affects the structure of supported metal atoms and nanoparticles.^{17, 18, 35, 48} To assess the role of the support, we calculated the reaction internal energy to form Rh₃(CO)₃ from a free Rh₃ cluster and three CO molecules on one hydroxylated surface containing 5.09 OH/nm² without O_{vac} (**Region 1B in Figure 2.1a, see also Figure A.18a**) and one containing 5.09 OH/nm² with 0.85 O_{vac}/nm² (**Figure A.18b**). The reaction energies for the formation of Rh₃(CO)₃ were found to be -10.58 eV and -10.90 eV, respectively. This difference suggests that the presence of an O vacancy renders the reaction energy for the formation of Rh₃(CO)₃ slightly more favorable by 0.11 eV/Rh. We further compared the interaction energy between the Rh₃(CO)₃ cluster and the support CeO₂(111) surface (**Figure A.18c**), which was found to be -8.03 eV, to the interaction energy between the Rh₃(CO)₃ cluster and the support CeO₂(111) surface with an O vacancy in the Rh₃(CO)₃'s vicinity (**Figure A.18d**), which was found to be -6.63 eV. These interaction energies are calculated by detaching the cluster from the surface without any structural relaxation of the obtained fragments. The existence of an O vacancy hence in contrast weakens the interaction energy by 0.47 eV/Rh atom but allows the cluster and surrounding support atoms to adopt a less deformed, intrinsically more stable, configuration. As a net result, the oxygen vacancies of CeO₂

surface can cooperate with the CO ligands to slightly stabilize the formation of small $\text{Rh}_3(\text{CO})_3$ clusters.

Thermodynamic stability calculations of the Rh active site show that the ligand structure of the Rh active site is sensitive to the CO chemical potential. Starting from the steady state catalytic environment (**Figures 2.2a and 2.2b**) with $\text{Rh}_3(\text{CO})_3$ as the most stable species (**Figure 2.2e**), two ligand restructuring events (labeled 1 and 2 and marked with left pointing arrows in **Figure 2.2a**) may occur when P_{CO} is decreased while the temperature is held constant at 500 °C. In these two events at 500 °C, the active site loses CO ligands. In event 1, one CO ligand is lost when P_{CO} falls below 10^{-3} bar, forming $\text{Rh}_3(\text{CO})_2$ (**Figure 2.2d**). Event 2 occurs when P_{CO} falls below 10^{-5} bar, where the $\text{Rh}_3(\text{CO})_2$ site loses its remaining CO ligands to form the Rh_3H_1 site (**Figure 2.2c**). If the pressure of CO was increased starting from steady state condition, one additional CO is predicted to attach to the $\text{Rh}_3(\text{CO})_3$ site when P_{CO} rises above 10^{-1} bar, forming the $\text{Rh}_3(\text{CO})_4$ site (**Figure 2.2f**). Importantly, both the $\text{Rh}_3(\text{CO})_2$ and Rh_3H_1 sites are metastable compared to the Rh nanoparticle, while the $\text{Rh}_3(\text{CO})_3$ and $\text{Rh}_3(\text{CO})_4$ are similarly stable (**Figure 2.2b**). This difference among thermodynamic stabilities in Figure 4a underlines the key role of CO on the stability of the Rh active site. The predicted P_{CO} -dependent restructuring is consistent with a theoretically predicted decreasing trend in the frequency of the principal CO stretching mode, along the order of $\text{Rh}_3(\text{CO})_4 > \text{Rh}_3(\text{CO})_3 > \text{Rh}_3(\text{CO})_2$ (**Section A.8 and Figure A.19**).

2.3.3 Pressure-Dependent Formation of $\text{Rh}_m(\text{CO})_n$ Clusters

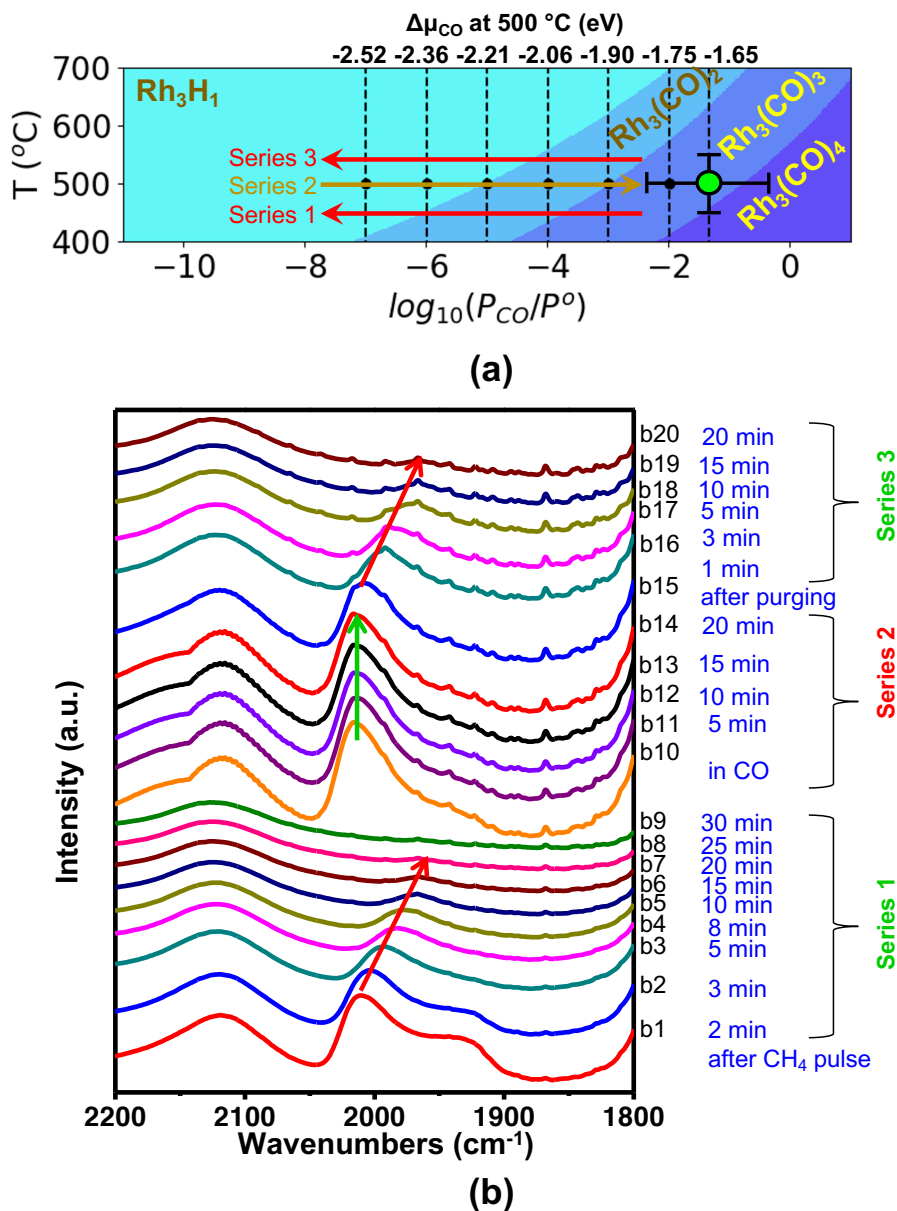


Figure 2.4 Reversible restructuring of the Rh active sites. CO product pressure-driven restructuring of Rh catalytic sites. (a) Three series of variations of CO pressure at 500 °C marked on the theoretical $P_{\text{CO}}-T$ phase diagram (upper portion adopted from **Figure 2.2a**). (b) DRIFTS spectra (b1-b9) at 500 °C under SRM catalytic condition. Series 1: b1-b9, a transient pulse of CH_4

reactant (equivalent to 0.1 ml CH₄, STP) composed of 1% CH₄ and 99% Ar was introduced to the catalyst by mixing the pulse with flowing water vapor formed by flowing Ar (99.999%) through water of 25°C. No external CO source was introduced before and during Series 1. Series 2: b10-b14, spectra in a flow of CO (1%) balanced with Ar. Series 3, spectra (b15-b20) being purged with argon as a function of time. The background spectrum for DRIFTS study was collected on the catalyst surface under Ar and water vapor flow at 500 °C. In Series 1, 20 ml/min of water vapor containing 3% vapor was continuously flowing through the reaction cell, CH₄ gas (1% CH₄ in Ar) was pulsed to mix with water vapor. The DRIFTS spectra were taken as a function of time without CH₄ in the flow. At the t=2 min (b1), the vibrational features in the 2050-1850 cm⁻¹ region, assigned to Rh₃(CO)₃, were clearly observed as CO was generated from SRM at 500°C. These experiments overall show the formation of Rh₃(CO)₃ to be reversible.

The predicted P_{CO}-dependent restructuring of the catalytic sites at 500 °C was also experimentally observed by operando DRIFTS studies, where CO was produced by the reaction between the flowing H₂O vapor and pulsed CH₄ at 500 °C. In series 1 of **Figure 2.4b**, CH₄ was only provided through a pulse; thus, no more CO was continuously produced. Since water vapor was continuously flowing through catalyst, the partial pressure of CO (and the chemical potential of CO) around the catalyst progressively decreased. The time-dependent vibrational signatures show that the Rh₃(CO)₃ clusters progressively restructure to CO-ligand-free Rh clusters as illustrated in **Figure 2.4a** (Series 1). The transformation of Rh₃(CO)₃ to a CO-ligand-free Rh cluster was evidenced by the evolution of CO vibrational feature. The CO stretching frequencies of Rh₃(CO)₃ obviously shift to lower values, and their intensities decrease along the decrease of CO pressure (**Figure 2.4b, b1-b9**), as marked with the red arrows in **Figure 2.4b, b1-b9**.

The key role of CO in maintaining the highly dispersed $\text{Rh}_3(\text{CO})_3$ catalytic sites was further confirmed by the reversible restructuring of the Rh site observed in two additional series of experiments in **Figure 2.4b**. Upon the disappearance of $\nu(\text{CO})$ peaks in the range of 2050-1850 cm^{-1} at 500 °C (**Figure 2.4b, b9**), Rh clusters without CO ligand form at the end of Series 1. Once CO was introduced to the catalyst as a steady flow (at the 31st min, 1% CO), the Rh clusters immediately restructured to $\text{Rh}_3(\text{CO})_3$ (Spectrum b10 in series 2 of **Figure 2.4b**). This restructuring is evidenced by the immediate reappearance of $\nu(\text{CO})$ peaks at 2010 cm^{-1} and 1920 cm^{-1} in Series 2 (**Figure 2.4b, b10**). The produced structure experiences nearly no change as long as CO is continuously flowing through the catalyst (**Figure 2.4b, b10-b14**). Notably, these CO vibrational frequencies are distinct from chemisorbed CO on the (100) or (111) surfaces of Rh.¹¹⁰ At the end of series 2 (the 21st min of the series 2 in **Figure 2.4b**), the flowing CO was replaced with flowing He; the progressive decrease of CO concentration in series 3 resulted in the restructuring of $\text{Rh}_3(\text{CO})_3$ to Rh clusters without CO ligand. The series 1 (under non-steady state catalytic condition) and series 3 (under the same temperature and CO pressure as DFT modelling) exhibit the same evolution of CO vibrational features, suggesting that CO pressure is the main driving force, regardless of CO produced from CH_4 reforming or from external environment. Overall, the formation and restructuring of the Rh active site, $\text{Rh}_3(\text{CO})_n$ can be reversed by changing the chemical potential of CO surrounding the catalytic site.

2.4 Conclusion

In conclusion, this work demonstrated that the structure of the Rh nanoclusters supported on CeO_2 evolves depending on the partial pressure of product CO in the gas environment to which the catalyst is subjected. Beyond the Rh/ CeO_2 catalyst studied in our work, the restructuring

capability of CO on metal catalysts has been shown in systems where CO was a reactant.^{67-69, 111} CO has been found to induce the restructuring of stepped Pt surfaces to CO-covered Pt clusters with size of 2.1-2.2 nm.⁶⁸ For Cu, a metal with a weaker cohesive energy than Pt, CO can even fragment the close-packed Cu(111) surface into nm-sized CO-covered clusters that can activate H₂O.¹¹¹ In our system, the singly dispersed Rh cations in the as-prepared catalyst transform to Rh NPs after reduction by H₂, but CO, a product formed from steam reforming of methane, can re-disperse Rh atoms of the Rh NPs into catalytically active CO liganded Rh₃ clusters during catalysis. As evidenced by first principles atomistic thermodynamic calculations and in situ/operando spectroscopy, the CO product gas produced by the SRM plays a crucial role in inducing and maintaining the highly dispersed active sites, Rh₃(CO)_n of this Rh/CeO₂ catalyst. This work demonstrates the necessity of including product molecules as a factor in identifying the active sites under catalytic conditions.

Chapter 3 The Surface Structure of $\text{Co}_3\text{O}_4(111)$ under Reactive Gas Phase

Environments

3.1 Introduction

Co_3O_4 is a versatile metal oxide capable of being both a catalyst support for single noble metal (NM) atoms, metal clusters, and a catalyst itself.^{112, 113} The catalytic properties of Co_3O_4 have been studied extensively. In thermal catalysis, Co_3O_4 is found to be active for low temperature CO/hydrocarbon oxidation, NO_x reduction, N_2O decomposition, and selective catalytic reduction of NO with NH_3 .^{112, 114} Most groups have attributed the material's extraordinary oxidation activity to its reducibility. On the other hand, NO reduction by H_2 can be performed over various $\text{NM}_1/\text{Co}_3\text{O}_4$ catalysts, where Co_3O_4 acts as the support.¹¹⁵ One promising application of the (111) surface is the oxidative dehydrogenation (ODH) of alkanes.^{116, 117} The (111) surface has recently been shown to have good selectivity for ethane ODH against combustion.¹¹⁸

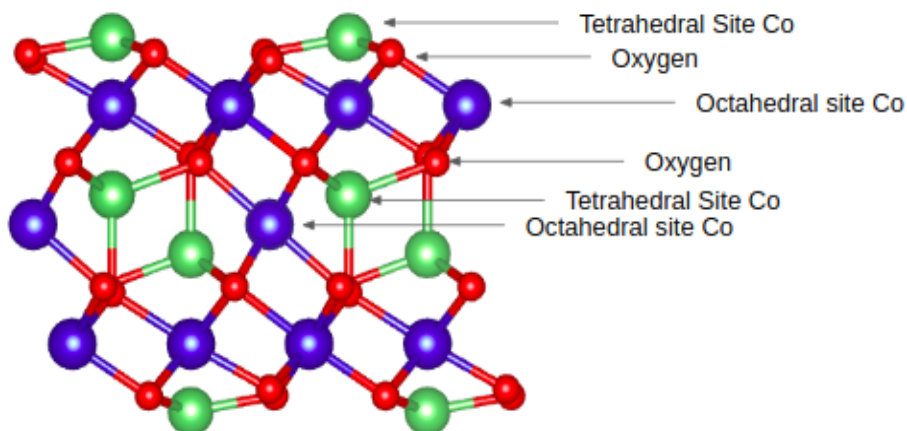


Figure 3.1 Side view of Co_3O_4 through the [111] direction. From truncating the Co_3O_4 bulk, a total of six possible terminations of the (111) surface can be made. This surface is a type III surface by Tasker's definitions, where the group of the six labeled layers is stoichiometric when stacked but has a net dipole in the z-direction.

Bulk Co_3O_4 has the normal spinel structure and an indirect band gap. Co^{2+} in tetrahedral (T_d) sites are in the quadruplet spin state while Co^{3+} in octahedral (O_h) sites are in the singlet spin state.¹¹⁹ Co^{2+} ions aligned on the same (111) plane have the same spin direction, and these (111) planes are antiferromagnetically aligned in the bulk.¹²⁰ Experimentally, Co_3O_4 particles calcined at 673 K expose (100), (110), and (111) surfaces in similar portions.¹²¹ In the case of the (111) surface, it is polar and can be terminated by Co in tetrahedral sites (Co-T_d), octahedral sites (Co-O_h), O^{2-} , or a mix of the three for a total of six unique bulk-truncated terminations (**Figure 3.1**). Thin films exposing O^{2-} and Co-T_d relax inwards to compensate for the surface dipole.^{122, 123} The relative stability of bulk-truncated low miller index Co_3O_4 surfaces have been examined by various studies under purely oxygen-containing environments.^{121, 124-126}

Experimental characterization of the Co_3O_4 surface is a challenging task. Busca et al. obtained IR spectra of the surface after diluting the sample with KBr and activating under vacuum. Vibrational modes in the fingerprint region ($<1000 \text{ cm}^{-1}$) were present, but the overall IR transmission window is severely limited.¹²⁷ High temperature evacuation or H_2 reduction were found to widen this window, but carry the risk of reducing the Co_3O_4 sample to CoO . To mitigate this problem, alternative characterization techniques can be used, but they are generally limited to ultra-high vacuum (UHV).¹²⁸ Although x-ray photoelectron spectroscopy (XPS) can now be performed at ambient pressures, it is still difficult to identify types of surface O because OH^- , CO_3^{2-} and defective O all have similar O 2p binding energy.^{113, 128-131} Petitto et al. used XPS and high-resolution electron energy loss spectroscopy (HREELS) to study surface OH created on (111)-terminated single Co_3O_4 crystals after annealing in H_2O .¹³² Schwarz et al. probed $\text{Co}_3\text{O}_4(111)$ epitaxial films using XPS and infrared reflection absorption spectroscopy (IRAS) after exposing

them first to D₂O or CO.^{133, 134} To summarize, experimental characterization of the Co₃O₄(111) surface can only provide a limited view of the surface at low pressures. These difficulties highlight the importance of theoretical studies for understanding surface structure, especially outside the limits of experimental characterization.

Although many computational studies have been performed on the Co₃O₄(111) surface using density functional theory (DFT), they generally lack three considerations. First, only a few studies regard the magnetic structure, even when it was shown that inconsistent magnetic coupling induces errors in calculated energy.¹³⁵⁻¹³⁷ Second, mechanistic studies of reactions on the (111) surface generally do not consider the role of hydroxyls.^{116, 117, 138} Low pressure H₂O/D₂O exposure experiments have shown that hydroxyls are stable on the surface up to 570 K.¹³⁴ Further, H₂ was also shown to dissociate easily over the (111) termination.¹³⁹ Therefore, any H₂O or H₂ impurity in the gas environment will likely produce hydroxyls. Third, the electronic effects of surface reduction are not addressed in most studies. Early studies used generalized gradient approximation (GGA) exchange correlation functionals but did not include any self-interaction error correction for Co 3d electrons.^{124, 140} Conventional DFT predicts a bulk band gap that is too narrow.^{120, 141} Only a few studies have addressed electron localization upon reduction.¹³⁵⁻¹³⁷ Most often, the Co²⁺ and O²⁻ terminated surface is used as the active site structure for the (111) termination.^{116, 117, 138}

In this study, we seek to provide insight into the structure of this surface under various reaction environments. We examine the structure of the surface in equilibrium with O₂, H₂O, and H₂ to address surface hydroxylation, vacancy formation, and possible change of the Co concentration, while taking a rigorous approach and minding both the bulk magnetic structure and electronic effects that occur through surface modifications.

3.2 Methods

3.2.1 DFT Calculations

Density functional theory (DFT) calculations were performed using the Vienna ab-initio simulation package (VASP), version 5.4.1.⁷³⁻⁷⁵ Exchange-correlation energy was calculated using the Perdew-Burke-Ernzerhof (PBE) functional.⁷⁶ Spin polarization was applied in all calculations unless otherwise specified. Since PBE does not account for van der Waals (vdW) forces, the dDsC dispersion-correction method was used.^{142, 143} The projector-augmented-wave (PAW) method was used to describe the core electrons.^{77, 78} The one-electron wavefunctions are developed on a basis set of plane waves with a 450 eV energy cutoff. To correct for the large self-interaction error of the 3d electrons of Co, a Hubbard-like repulsion term was added using Dudarev's approach (DFT+U), with $U_{\text{eff}} = U - J = 3.5$ eV.⁷⁹ This value of U_{eff} is consistent with those found in literature as a value that properly describes the energy of formation of Co_3O_4 from CoO .¹⁴⁴ Due to the controversy on choosing the appropriate U_{eff} , calculations using $U_{\text{eff}} = 2.0$ eV were also performed starting from $U_{\text{eff}} = 3.5$ eV geometry. Single point calculations using the Heyd-Scuseria-Ernzerhof functional with dispersion (HSE06+dDsC) were also performed using geometry and charge density obtained from $U_{\text{eff}} = 3.5$ eV as benchmarks for vacancy formation energies.^{85, 86} Previously, we benchmarked the energy of water adsorption on 11-layered Co-T_d -terminated slabs at the PBE+U+dDsC level ($U_{\text{eff}} = 3.5$ eV), against HSE06+dDsC and those with 17-layered Co-T_d -terminated slabs.¹⁴⁵ We found that water is under bound by 0.15 eV/ H_2O . This same correction was applied to all water-adsorbed structures to construct the 1-D and 2-D surface stability diagrams in this work.

Since Co^{2+} ions in Co_3O_4 are known to have antiferromagnetic ordering in the bulk, while Co^{3+} ions have no magnetic moment, careful considerations were taken to ensure that the bulk-like

section of the slab retains the correct Co^{2+} magnetic ordering and spin state. Electron localization or delocalization were also properly ensured on the modified surface, so that no electrons were spuriously added to the other side of the slab. Specifically, the occupancy matrix control technique developed by Allen and Watson was used, where a spin-polarized VASP WAVECAR file containing desirable Co 3d projected electron occupations was generated and used as the starting guess for the system.¹⁴⁶

The surface structures considered in this work were compared to each other by their surface Gibbs free energy, under a given temperature and a set of gas pressures (**Section B.1**).^{90, 91} DFT energies used to develop the surface stability diagrams were all computed from structures in (2×2) supercells (a, b, c axes shown on **Figure 3.2**) to ensure proper calculation of vdW contributions to electronic energy with dDsC. At PBE+U+dDsC level, assessing the adsorption energy of water in a (1×1) cell induces an error within 0.025 eV/ H_2O . The outermost layer of O and Co atoms were displaced in the frequency calculations (**Table B.13**). For a (2×2) slab ($a = b = 11.4 \text{ \AA}$, $\gamma = 120^\circ$), the Brillouin zone was sampled using a $3 \times 3 \times 1$ Monkhorst-Pack mesh.⁸⁴ Electronic energy difference between steps in each self-consistent field (SCF) cycle were converged to 10^{-6} eV, and atomic positions were converged until the forces on unconstrained atoms are less than 0.02 eV/\AA . A (1×1) cell was used for HSE06+dDsC calculations, with a $3 \times 3 \times 1$ Monkhorst-Pack mesh. At PBE+U+dDsC level, reducing the k-point mesh from $6 \times 6 \times 1$ to $3 \times 3 \times 1$ in a (1×1) cell only increases the total energy by $<0.1 \text{ meV/atom}$. The lattice parameter and the atomic positions of the bulk cell were relaxed simultaneously. Structural and electron density visualizations were performed using the VESTA program.⁸⁹ Vibrational frequencies were calculated using finite differences with a step size of 0.015 \AA . The calculated $\nu(\text{OH})$ and $\nu(\text{OD})$ modes were rescaled by

factors of 0.9789 and 0.9918 respectively; these factors were calculated using the same scheme as that specified by Freund, Sauer et al.¹⁴⁷

3.2.2 Bulk and Surface Models

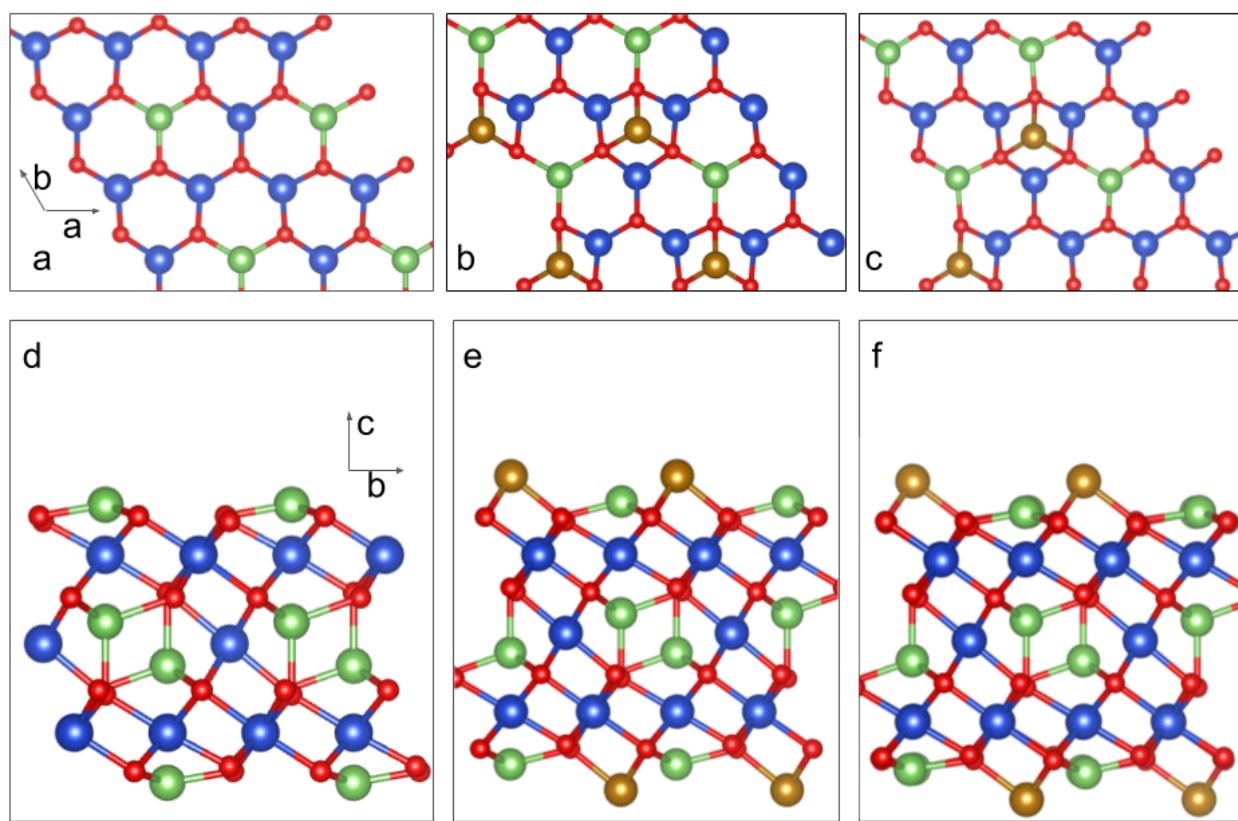


Figure 3.2 Top (a, b, c, through the c axis) and side (d, e, f, through the a axis) views of (2×2) cells (area 1.13 nm^2) of the three bare $\text{Co}_3\text{O}_4(111)$ terminations considered in this work, containing (red) O, (green) Co-T_d and (blue) Co-O_h and additional surface Co (gold). a, d: O-rich termination, $(\text{Co}^{\text{Td}})_x$, has formula $\text{Co}_{44}\text{O}_{64}$, containing four exposed Co in C_{3v} sites on each surface, belonging to bulk T_d sites in the bulk. b, e: Co-rich termination, $(\text{Co}^{\text{Oh}}\text{Co}^{\text{Td}})_x$, has formula $\text{Co}_{52}\text{O}_{64}$, containing eight exposed Co in C_{3v} sites on each surface; four originally at bulk T_d sites and four originally at bulk O_h sites. c, f: stoichiometric termination, $(\text{Co}^{\text{Oh}_{0.5}}\text{Co}^{\text{Td}})_x$, has formula $\text{Co}_{48}\text{O}_{64}$, containing six exposed C_{3v} Co on each surface; two originally at bulk O_h sites and four at bulk T_d sites.

A cubic $\text{Co}_{24}\text{O}_{32}$ cell was used to model the Co_3O_4 bulk. The lattice parameter was found to be 8.06 Å, which matches the experimental lattice parameter, 8.08 Å.¹⁴⁸ A magnetic moment of 2.64 μ_{B} was found on the Co^{2+} ions in the bulk, consistent with values obtained by Selloni et al., but lower than the 3.26 μ_{B} measured by Roth.^{119, 120} As previously mentioned, $\text{Co}_3\text{O}_4(111)$ is a Tasker type III polar surface with six different bulk-truncated terminations. To simulate the surface, three terminations, previously proposed by Zasada et al., were chosen (**Figure 3.2**).¹⁴⁹ $(\text{Co}^{\text{Td}})_x$ and $(\text{Co}^{\text{Oh}}\text{Co}^{\text{Td}})_x$ were cut directly from the bulk and are oxygen-rich and cobalt-rich respectively, while $(\text{Co}^{\text{Oh}}_{0.5}\text{Co}^{\text{Td}})_x$ is stoichiometric.¹⁴⁹ A symmetric 11-layer slab was used to model $(\text{Co}^{\text{Td}})_x$, and symmetric 13 layer slabs were used to model $(\text{Co}^{\text{Oh}}\text{Co}^{\text{Td}})_x$ and $(\text{Co}^{\text{Oh}}_{0.5}\text{Co}^{\text{Td}})_x$. In a (2×2) cell, they have formulas $\text{Co}_{44}\text{O}_{64}$, $\text{Co}_{52}\text{O}_{64}$ and $\text{Co}_{48}\text{O}_{64}$, containing 3.56, 7.11, and 5.33 Co/nm^2 respectively. The $(\text{Co}^{\text{Td}})_x$ surface contains two unique types of surface O: those directly adjacent to surface Co^{Td} (**Figure 3.2a**, red O bonded to 2 blue Co and 1 green Co) and those in isolation (**Figure 3.2a**, bonded to 3 blue Co). To simulate 5.33 Co/nm^2 , Co is added to three-fold adjacent O sites, generating another category of O bonded to both Co^{Td} and Co^{Oh} (**Figure 3.2b**, red O bonded to 2 blue Co, 1 green Co, and 1 gold Co). Finally, when all the three-fold O sites are occupied on the surface by Co at 7.11 Co/nm^2 , two types of O exist on the surface: isolated O and those between Co^{Td} and Co^{Oh} .

The antiferromagnetic alignment of surface Co ions on the $(\text{Co}^{\text{Oh}}_{0.5}\text{Co}^{\text{Td}})_x$ termination was challenging to keep consistent; therefore, they were kept ferromagnetic and shifted by a constant correction per unit cell (see **Figure B.12**). At least 15 Å of vacuum was used to prevent interactions between slabs in the z direction. For a given slab calculation, the five innermost layers were fixed to their bulk positions and all other atoms were relaxed. Adsorption of atoms and molecules were performed on only one side of the slab to prevent surface-surface interactions

through the slab. Dipole corrections were applied in all slab calculations. H adsorption, H₂O adsorption, and oxygen vacancy formation were considered separately on all three surfaces, and the combination of up to 1.78 H₂/nm² (up to 4 H added per unit cell) and 2.78 H₂O/nm² (up to 3 H₂O added per unit cell) on the (Co^{Td})_x termination as a simplified case of H/H₂O co-adsorption. At given set of temperature and partial pressure, surfaces are compared to each other through approximate surface energy (see **section B.1**).

3.3 Results and Discussion

3.3.1 The Co₃O₄(111) Surface under Oxidative and Reductive Environmental Conditions

For oxidative reactions, we consider the surface to be in equilibrium with O₂ and H₂O. The surface stability diagram under realistic O₂ and H₂O chemical potentials ($\Delta\mu_{\text{H}_2\text{O}} > -2.5$ eV, $\Delta\mu_{\text{O}} > -2.5$ eV) is shown below:

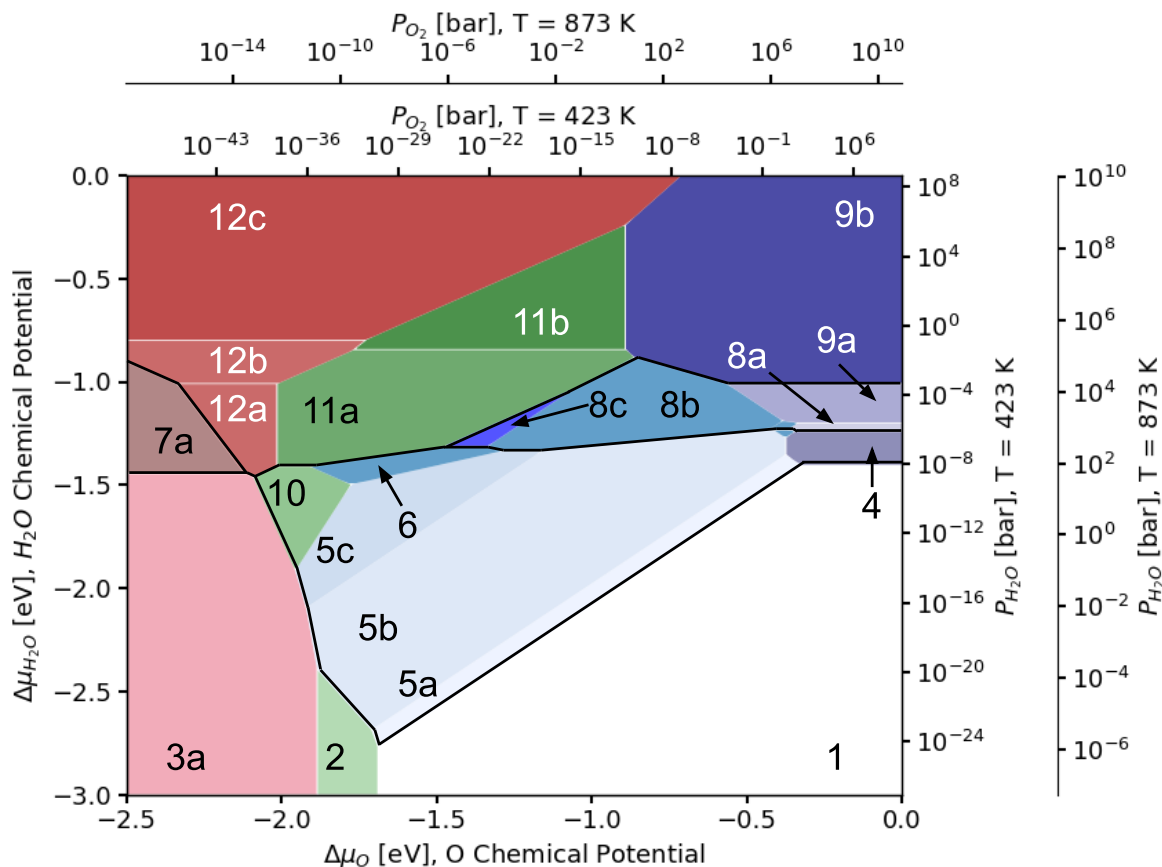
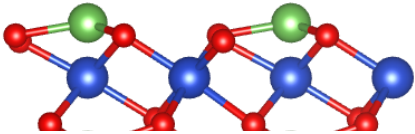
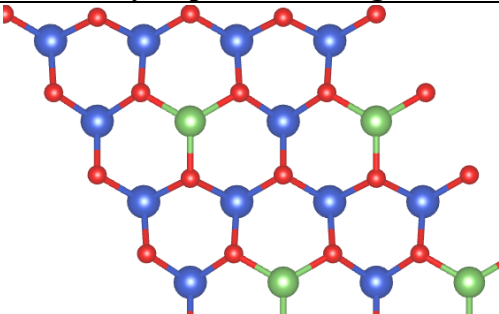
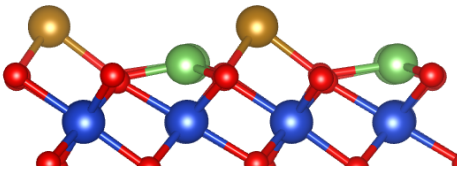
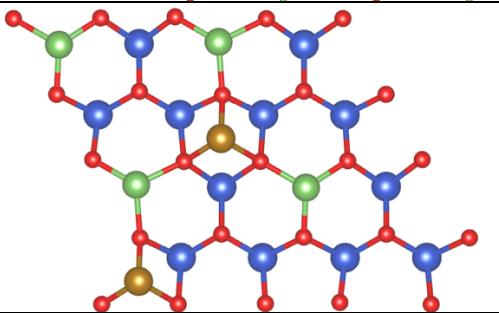
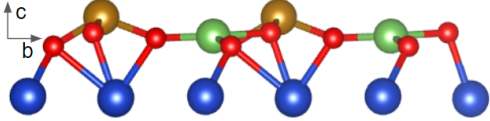
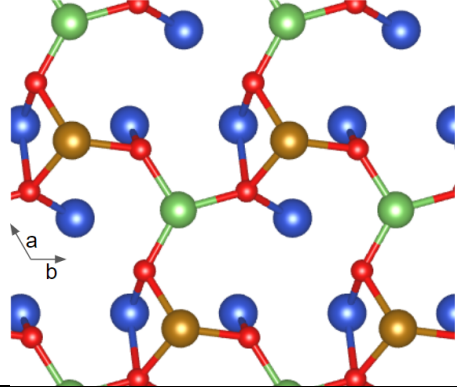
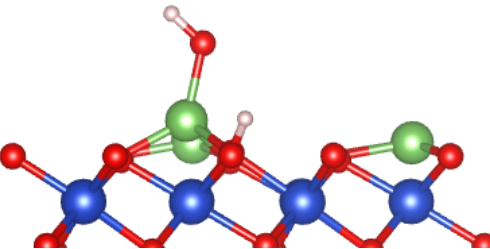
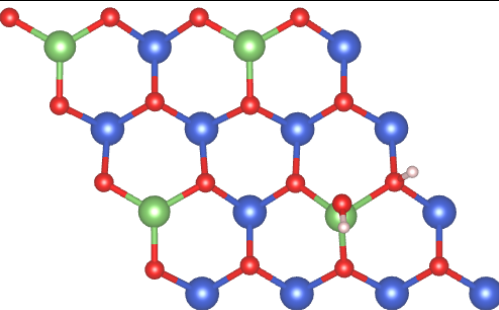


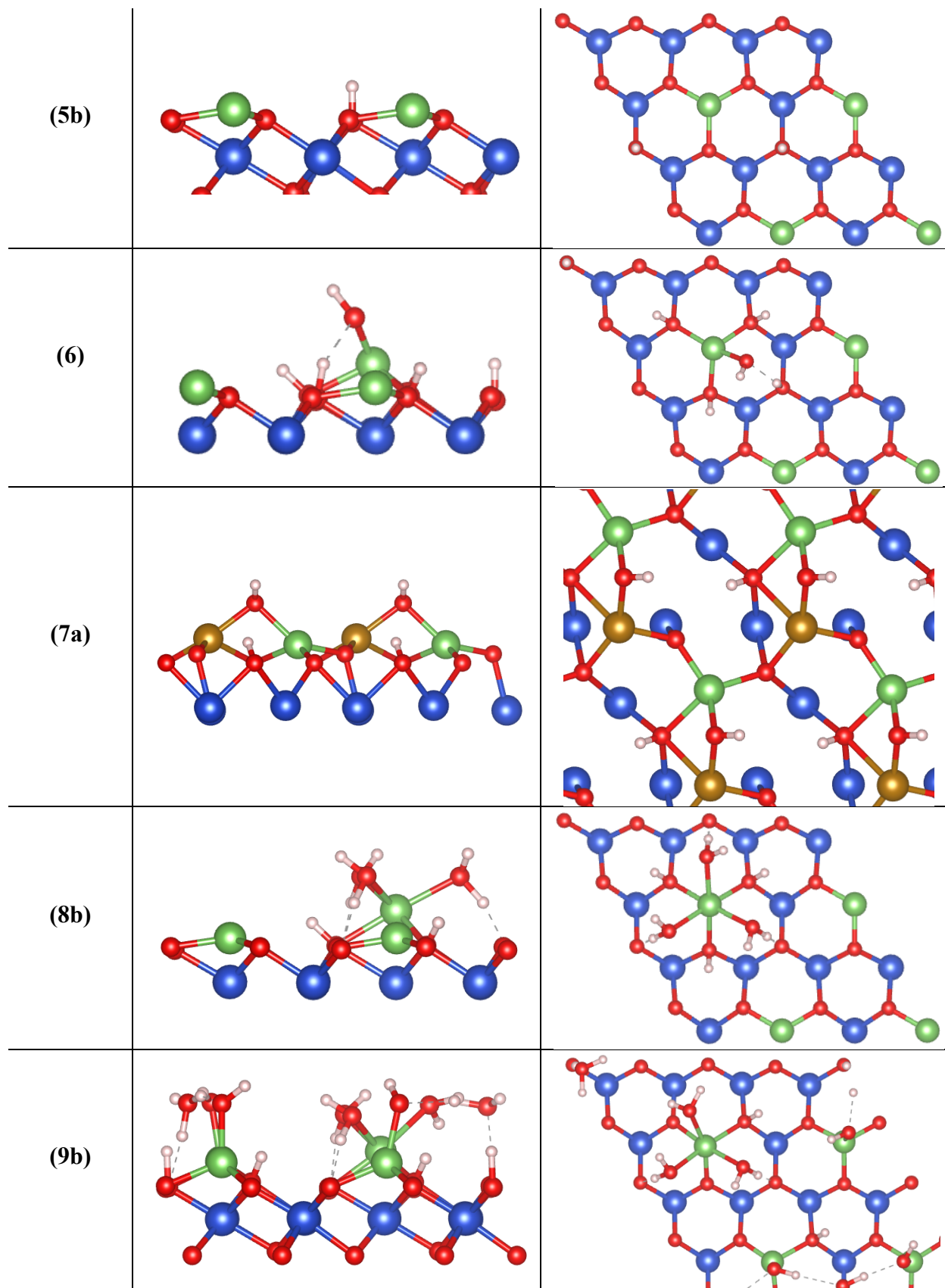
Figure 3.3 Surface stability diagram showing the most stable surface structure as a function of O_2 and H_2O chemical potential and equivalent oxygen/water pressure at 423 K and 873 K. Regions are classified in three ways. (I) By surface Co concentration: blue/grey/white: 3.56 Co/nm^2 ; green: 5.33 Co/nm^2 , and red/brown: 7.11 Co/nm^2 . (II) By general appearance of surface hydroxylation: the bottom bold line separates non-hydroxylated regions and hydroxylated regions, the middle bold line (only the segment running through the blue regions, or when $\Delta\mu_{\text{O}} > -1.5 \text{ eV}$) separates isolated hydroxyls and $\text{Co}(\text{H}_2\text{O})_3$ (hereby referred to as “triaqua”) surface complexes (with eventually additional OH groups), and the top bold line separates isolated triaqua surface complexes and large OH/ H_2O structures. (III) By specific numbered structure (see **Table 3.1** for descriptions, **Figure B.9** for a fully labeled stability diagram, **Figure 3.2** and **Table 3.2** for representative geometries, and **Table B.10** for all geometries).

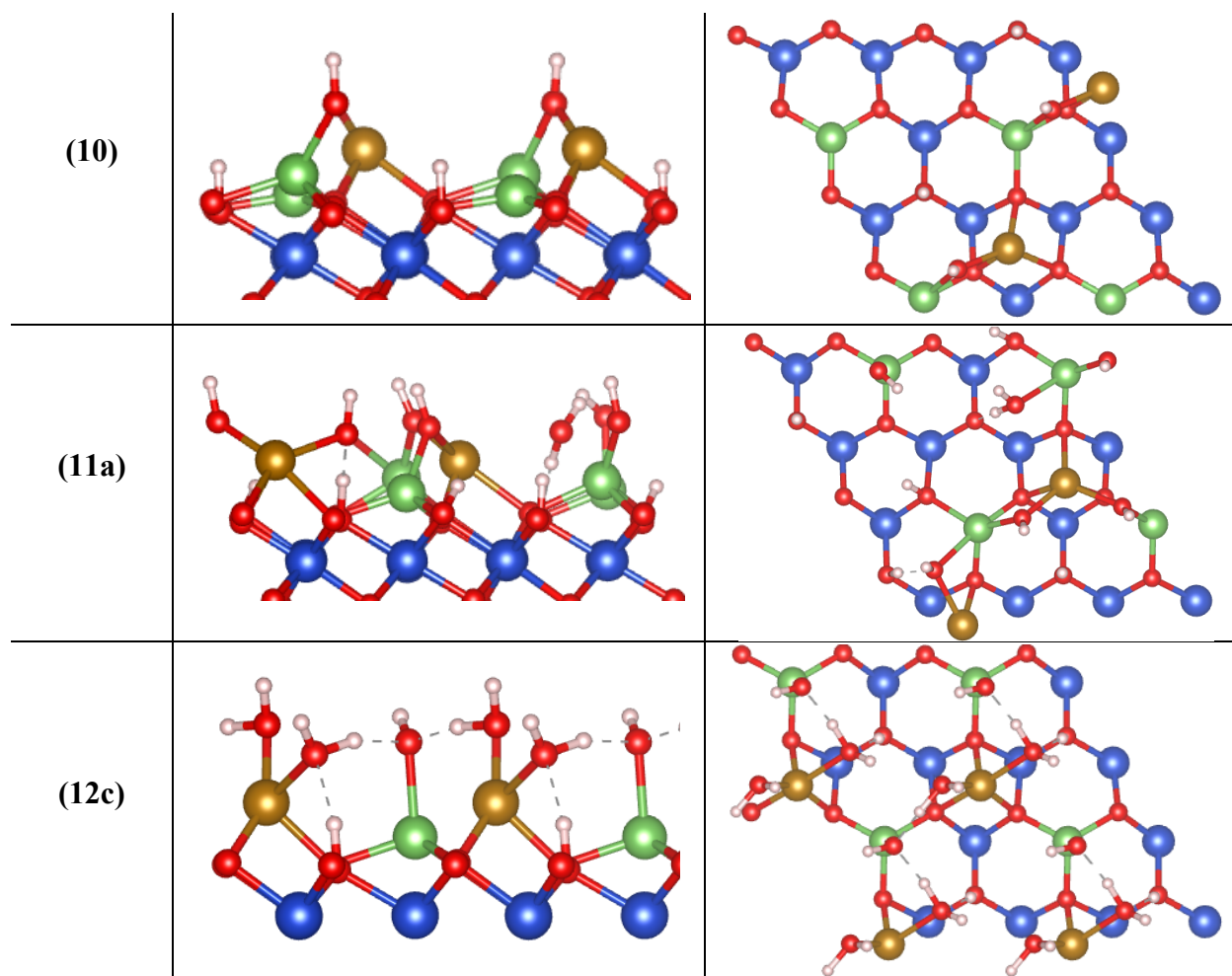
Table 3.1 Description of the specific types of surface structures observed in **Figure 3.3** and **3.5**

Label(s) on Figure 3.3 and/or Figure 3.5	Termination, coverage, and appearance
1	Bare $(\text{Co}^{\text{Td}})_x$ surface
2	Bare $(\text{Co}^{\text{Oh}}_{0.5}\text{Co}^{\text{Td}})_x$ surface
3 a, b	$(\text{Co}^{\text{Oh}}\text{Co}^{\text{Td}})_x$ surface with: a) $3.56 \text{ O}_{\text{vac}}/\text{nm}^2$ and b) $7.11 \text{ O}_{\text{vac}}/\text{nm}^2$
4	$(\text{Co}^{\text{Td}})_x$ with $1.78 \text{ OH}/\text{nm}^2$, appearing as 1 dissociated H_2O
5 a-c	$(\text{Co}^{\text{Td}})_x$ with: a) 0.89 , b) 1.78 , c) $2.67 \text{ OH}/\text{nm}^2$, appearing as adsorbed H
6	$(\text{Co}^{\text{Td}})_x$ with $5.33 \text{ OH}/\text{nm}^2$, appearing as 4 adsorbed H and 1 dissociated H_2O
7 a-e	$(\text{Co}^{\text{Oh}}\text{Co}^{\text{Td}})_x$ with: a) $7.11 \text{ OH}/\text{nm}^2$, b) $8.00 \text{ OH}/\text{nm}^2$, c) $8.89 \text{ OH}/\text{nm}^2$, d) $9.78 \text{ OH}/\text{nm}^2$, e) $10.67 \text{ OH}/\text{nm}^2$, appearing as dissociated H_2
8 a-c	$(\text{Co}^{\text{Td}})_x$ with: a) $0 \text{ OH}/\text{nm}^2$ and $2.67 \text{ H}_2\text{O}/\text{nm}^2$ b) $2.67 \text{ OH}/\text{nm}^2$ and $2.67 \text{ H}_2\text{O}/\text{nm}^2$, c) $2.67 \text{ H}_2\text{O}/\text{nm}^2$ and $3.56 \text{ OH}/\text{nm}^2$, appearing as one triaqua surface complex eventually surrounded by adsorbed H
9 a, b	$(\text{Co}^{\text{Td}})_x$ with: a) $3.56 \text{ H}_2\text{O}/\text{nm}^2$, $3.56 \text{ OH}/\text{nm}^2$ and b) $5.33 \text{ OH}/\text{nm}^2$, $4.44 \text{ H}_2\text{O}/\text{nm}^2$, each containing one triaqua surface complex and H-bonded OH/ H_2O chain. The triaqua complex is incorporated into the chain in structure 9b
10	$(\text{Co}^{\text{Oh}}_{0.5}\text{Co}^{\text{Td}})_x$ with $3.56 \text{ OH}/\text{nm}^2$, appearing as dissociated H_2O
11 a, b	$(\text{Co}^{\text{Oh}}_{0.5}\text{Co}^{\text{Td}})_x$ with: a) $8.89 \text{ OH}/\text{nm}^2$ and $0.89 \text{ H}_2\text{O}/\text{nm}^2$, b) $10.67 \text{ OH}/\text{nm}^2$ and $1.78 \text{ H}_2\text{O}/\text{nm}^2$, appearing as dissociated and molecular H_2O
12 a-c	$(\text{Co}^{\text{Oh}}\text{Co}^{\text{Td}})_x$ with: a) $8.89 \text{ OH}/\text{nm}^2$, $0.89 \text{ H}_2\text{O}/\text{nm}^2$, b) $7.11 \text{ OH}/\text{nm}^2$ and $5.33 \text{ H}_2\text{O}/\text{nm}^2$, c) $7.11 \text{ OH}/\text{nm}^2$ and $7.11 \text{ H}_2\text{O}/\text{nm}^2$, appearing as dissociated and molecular H_2O linked by H bonds.

Table 3.2 Side (through the a axis) and top (through the c axis) views of representative structures in regions 1-12 on the surface stability diagram (see **Table 3.1**, **Figure 3.3**, and **Figure 3.5**). 4 and 9b are adapted from ref.¹⁴⁵

Number	Geometry, side view, through a axis	Geometry, top view, through c axis
(1)		
(2)		
(3)		
(4)		





While in equilibrium with O_2 and H_2O , the surface stability diagram is dominated by the $(Co^{Td})_x$ termination. Only considering the $(Co^{Td})_x$ regions, the diagram can be drawn into four sections based on the type of surface hydroxyls present. It should be noted that the structures listed in **Table 3.1** are representatives of the various macroscopic regions on the stability diagram; it is possible that there are more stable isomers. These four regions are separated by bold black lines (**Figure 3.3**). The lowest line separates the non-hydroxylated regions below the line from strong surface hydroxyl groups. Under H_2O and O_2 pressure, these regions can be interpreted as the equilibrated states of H_2O adsorption on surface vacancies. The coverage of isolated OH should be 2~4 OH/nm² (**Table 3.1**, **Table 3.2** and **Table B.1**). As mentioned in **Section 3.2.2**, two types

of O exist on the $(\text{Co}^{\text{Td}})_x$ surface, ones adjacent to surface Co^{Td} , coordinated to the surface Co^{Td} and to subsurface Co^{Oh} , and ones in isolation, coordinated to 3 subsurface Co^{Oh} . It is more favorable to populate isolated O first. The line second-to-the-bottom, running across at roughly -1.3 eV, separates the isolated OH region to the one containing triaqua surface complexes, surrounded by OH groups coming from adsorbed H atoms. Structure 8b (**Table 3.2**, row 6) can serve as a representative for such OH-surrounded triaqua surface complexes, where one surface Co^{Td} is coordinated to three molecular H_2O and adjacent to three surface OH. Finally, the upper line, running across at roughly -1.1 eV, divides the triaqua surface complex-containing region below and the fully wetted region, containing extended H-bonded OH/ H_2O structures. On the other hand, the diagram can also be divided by surface Co concentration. Regions in shades of blue/grey and white are Co poor (3.56 Co/nm^2), regions in green are stoichiometric (5.33 Co/nm^2), and regions in red and brown are Co-rich (7.11 Co/nm^2). As expected, surface Co concentration increases as $\Delta\mu_{\text{O}}$ decreases through all the major zones, i.e. when the gas environment shifts towards O poor conditions.

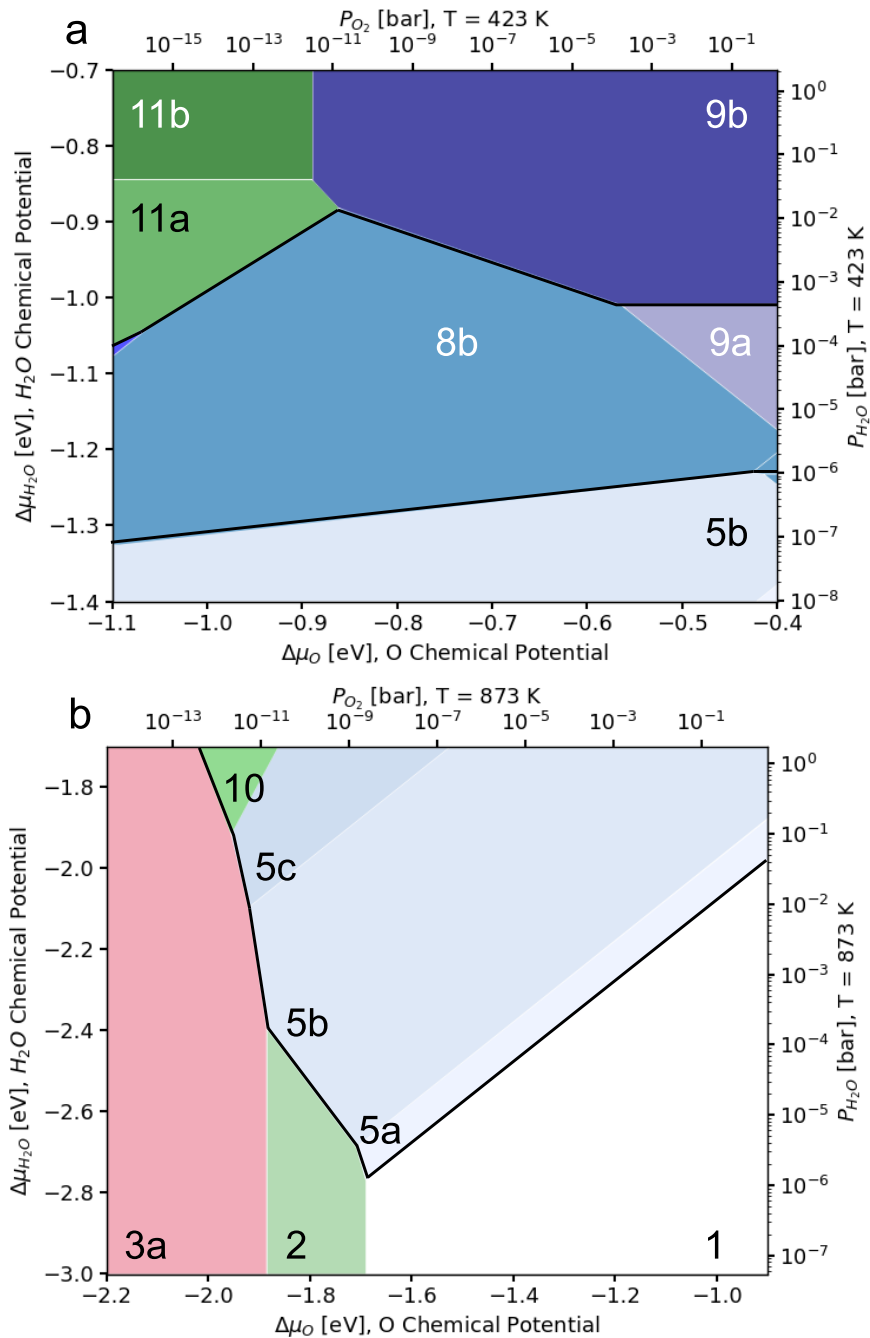


Figure 3.4 Portions of **Figure 3.3** showing the H₂O/O₂ surface stability diagram under realistic pressures at (a) 423 K and (b) 873 K. Regions are numbered and colored the same way as **Figure 3.3**. Only hydroxylated regions can be accessed at 423 K. Higher surface Co concentration can be reached under low P_{O₂}.

Although many possible terminations of this surface exist in theory, not all terminations can be accessed under realistic pressure and temperature. At 423 K (**Figure 3.4, top**), only a fraction of the hydroxylated regions (structures 5b, 8b, 9a,b, and 11a,b) can be visited at equilibrium; however, clear separations among isolated OH, triqua complexes, and hydroxyl networks can still be observed when $P_{\text{H}_2\text{O}}$ is increased. When the O_2 pressure is between 1 bar and 10^{-4} bar and the H_2O pressure is above 10^{-4} bar, the surface is predicted to be heavily hydroxylated, with a triqua complex incorporated into the OH/ H_2O chain (9b). Triqua complexes are predicted to be separated from the chain below $P_{\text{H}_2\text{O}} = 10^{-4}$ bar (8b, 9a), and only isolated hydroxyls (5b) are stable below $P_{\text{H}_2\text{O}} = 10^{-7}$ bar. Overall, at 423 K, the surface stability diagram is dominated by triqua complex regions with various amounts of additional $\text{H}_2\text{O}/\text{OH}$ groups. On the other hand, if the temperature is increased to 873 K (**Figure 3.4, bottom**), isolated hydroxyls will be exposed under 10^{-2} bar. We note that, for the surface Co concentration to increase to above $3.56 \text{ Co}/\text{nm}^2$, P_{O_2} needs to be reduced to below 10^{-11} bar while $P_{\text{H}_2\text{O}}$ is kept below 10^{-5} bar, i.e. in UHV conditions.

Finally, for reductive reactions involving H_2 , we consider the surface to be in equilibrium with H_2 and H_2O . Under these conditions, the system temperature must be kept low, so that kinetics for bulk reduction is slow enough, and the near-surface region is kinetically trapped to retain structure like bulk Co_3O_4 . By monitoring the surface oxidation state of $\text{NM}_1/\text{Co}_3\text{O}_4$ catalysts under NO/H_2 environments via ambient pressure (AP) XPS, Nguyen et al. observed that the near-surface regions generally do not fully reduce to CoO until above 500~600 K.¹¹⁵ Under $\text{H}_2/\text{H}_2\text{O}$ pressure, the surface stability diagram is as follows:

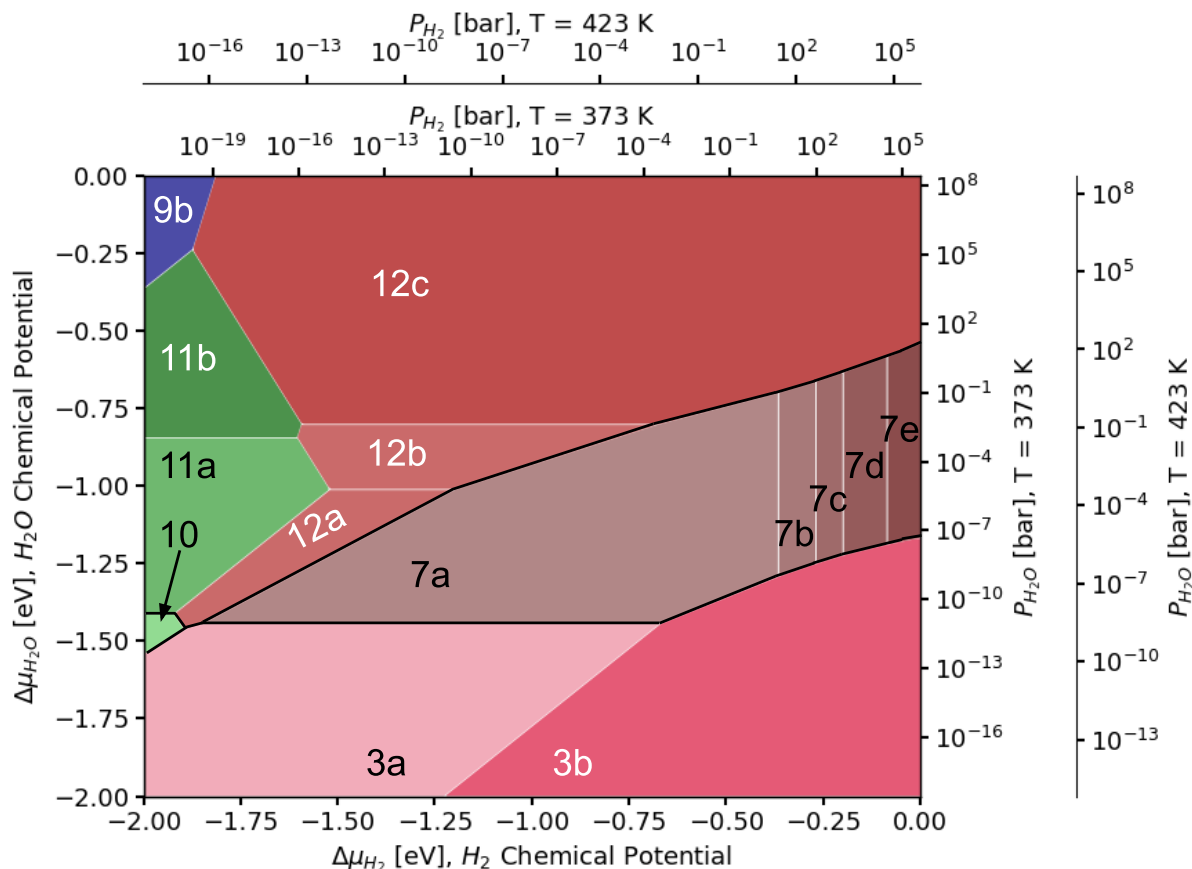


Figure 3.5 Surface stability diagram showing the most stable surface structure as a function of H_2 and H_2O chemical potential and H_2/H_2O pressure at 423 K. The color scheme and numbering are the same as that in **Figure 3.3**. Regions are again classified in same three ways as those in **Figure 3.3**. (I) By surface Co concentration: blue: 3.56 Co/nm²; green: 5.33 Co/nm², and red/brown: 7.11 Co/nm². (II) By general appearance of surface hydroxylation: bottom bold line separates non-hydroxylated regions and hydroxylated regions and top bold line separates OH-only regions and molecular H_2O -containing structures. (III) By specific numbered structure (see **Table 3.1** for descriptions, **Figure B.10** for a fully labeled stability diagram, **Table 3.2** for representative geometries, and **Table B.11** for all geometries).

Under H_2 and H_2O pressure, separation of non-hydroxylated, hydroxylated, and hydrated regions under H_2/H_2O is also very apparent. When the H_2O chemical potential increases above -1.5 eV, the surface transitions from a vacancy-covered state (representative structure: region 3a, see **Table 3.2**, row 1) to a hydroxylated state (representative structure: region 7a, see **Table 3.2**, row 5). When H_2O chemical potential increases to above roughly -0.75 ~ -1.00 eV, the surface transitions to a fully hydrated state (representative structure: region 12c, see **Table 3.2**, row 10). We note that the bare $(Co^{Oh}Co^{Td})_x$ termination does not appear on the stability diagram. Upon reduction by H adsorption or O_{vac} formation, the surface undergoes a large relaxation (**Figure B.11**, **Table B.14~B.16**). This relaxation makes vacancy formation much easier than on $(Co^{Oh}Co^{Td})_x$ (**Table B.4~B.6**), and H adsorption strong as well (**Table B.1~B.3**), but not as strong as that on $(Co^{Td})_x$, which is expected, as the $(Co^{Td})_x$ termination appears overly oxidized. If we again only consider realistic H_2 and H_2O pressures, the surface is dominated by this heavily relaxed hydroxylated region (region 7a in **Figure 3.5**, see also **Table 3.2** for structure).

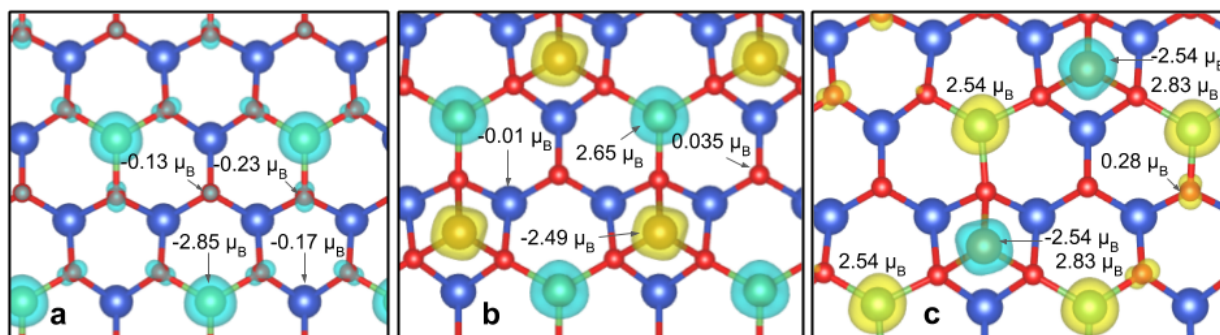


Figure 3.6 Top view of spin density difference on a) bare $(Co^{Td})_x$, b) bare $(Co^{Oh}Co^{Td})_x$, and c) $(Co^{Oh}_{0.5}Co^{Td})_x$, at isosurface level 0.04, where blue represents negative and yellow positive spin

density difference. Surface Co (green) on the $(\text{Co}^{\text{Td}})_x$ termination appear to be slightly more oxidized than bulk Co^{2+} , with slightly higher projected magnetic moments. Charge for this off-stoichiometry is compensated by small density differences on surface O. No projected magnetic moments are found on surface O in the $(\text{Co}^{\text{Oh}}\text{Co}^{\text{Td}})_x$ termination. All the added Co appears to be Co^{2+} based on projected magnetic moments, while Co originally on the surface appear slightly reduced. Less Co can be added to the surface to form $(\text{Co}^{\text{Oh}_{0.5}}\text{Co}^{\text{Td}})_x$; these Co also appear to be slightly reduced Co^{2+} and quenches spin differences on some surface O.

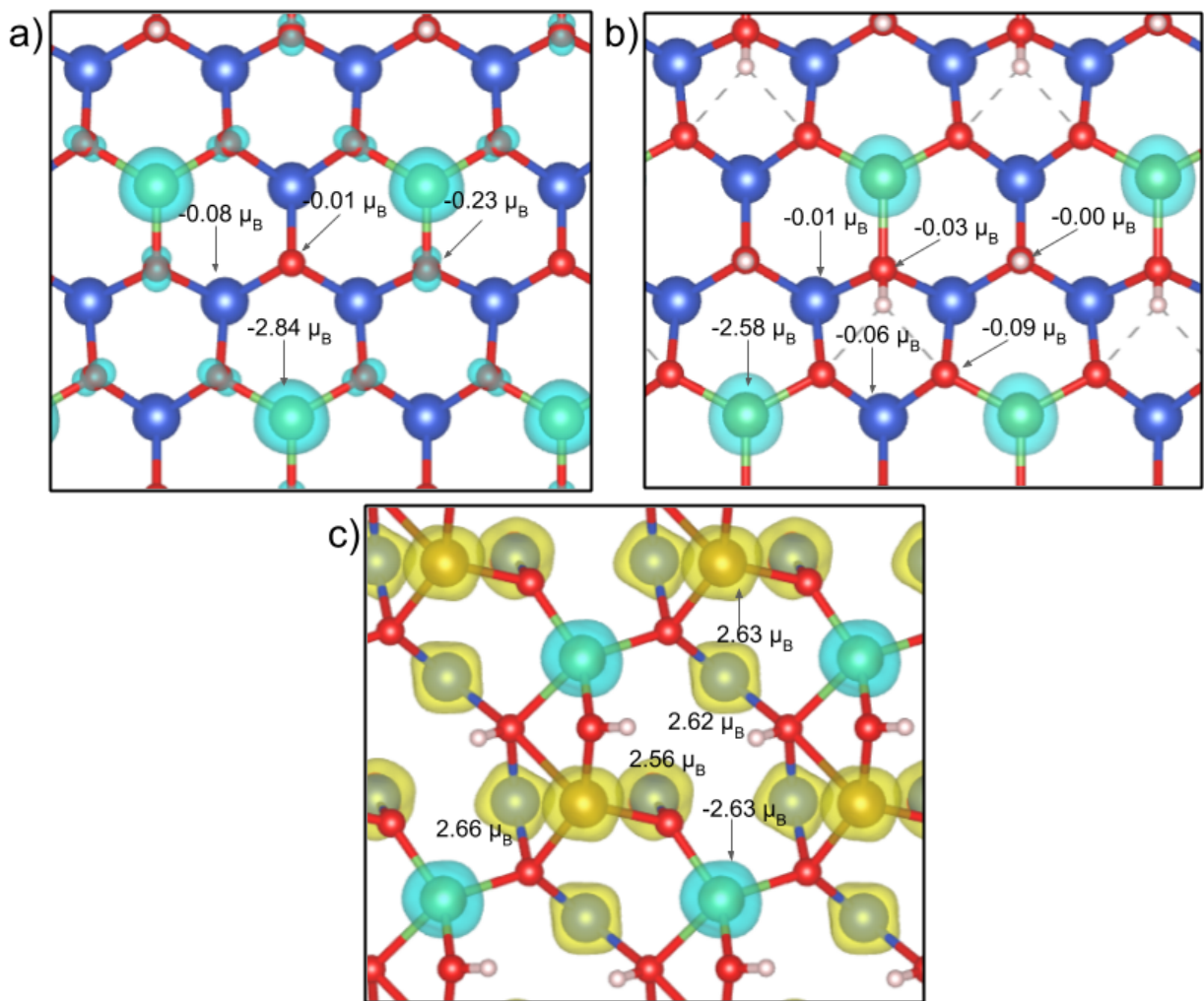


Figure 3.7 Top view of spin density difference on a) $(\text{Co}^{\text{Td}})_x$ with $1.78 \text{ OH}/\text{nm}^2$, b) $(\text{Co}^{\text{Td}})_x$ with $7.11 \text{ OH}/\text{nm}^2$, and c) $(\text{Co}^{\text{Oh}}\text{Co}^{\text{Td}})_x$ with $7.11 \text{ OH}/\text{nm}^2$. Electrons from adsorbing H on $(\text{Co}^{\text{Td}})_x$ are transferred to surface O, subsurface Co^{Oh} , and surface Co^{Td} . On the other hand, electrons from H adsorption on $(\text{Co}^{\text{Oh}}\text{Co}^{\text{Td}})_x$ are transferred mostly to subsurface Co^{Oh} .

Besides surface relaxation, adsorbate-induced charge transfer is very different on the bare Co-rich $(\text{Co}^{\text{Oh}}\text{Co}^{\text{Td}})_x$ as well, relative to Co-poor $(\text{Co}^{\text{Td}})_x$. On $(\text{Co}^{\text{Td}})_x$, initial H_2 adsorption results in delocalization of charge onto surface O directly below and subsurface Co; the small projected magnetic moments on surface O disappear (**Figure 3.6a, 3.7a**), while subsurface Co's projected

magnetic moments decrease in absolute value (from $-0.177 \mu_B$ to $-0.088 \mu_B$, **Figure 3.6a, 3.7a**). At a higher OH concentration on $(\text{Co}^{\text{Td}})_x$, charge is added to surface Co^{T} , surface O, and subsurface Co^{Oh} as well (**Figure 3.6a, 3.7b**). On the other hand, on the $(\text{Co}^{\text{Oh}}\text{Co}^{\text{Td}})_x$ surface, the charge is almost entirely transferred to subsurface Co^{Oh} (**Figure 3.6b, 3.7c**). This result can be rationalized by again considering the overall surface stoichiometry; due to the overoxidized state of the $(\text{Co}^{\text{Td}})_x$ termination, H_2 adsorbs strongly to balance the stoichiometry. Further, the $(\text{Co}^{\text{Oh}}\text{Co}^{\text{Td}})_x$ slab is closer to that of CoO , whereas the $(\text{Co}^{\text{Td}})_x$ is closer to Co_2O_3 , making near-surface Co atoms in the $(\text{Co}^{\text{Td}})_x$ slab closer to Co^{3+} , and near-surface Co in $(\text{Co}^{\text{Oh}}\text{Co}^{\text{Td}})_x$ closer to Co^{2+} . By the spectrochemical series, Co^{2+} induces a much smaller crystal field splitting than Co^{3+} , and as a result, subsurface Co on reduced $(\text{Co}^{\text{Td}})_x$ have magnetic moment smaller than $1 \mu_B$, while those on $(\text{Co}^{\text{Oh}}\text{Co}^{\text{Td}})_x$ have magnetic moment closer to $2.6 \mu_B$ (**Figure 3.7b, 3.7c**).

3.3.2 Comparisons to in situ and ex situ Vibrational Spectroscopy

Experimental characterization of surface hydroxyls on Co_3O_4 by vibrational spectroscopy is difficult, but not impossible. In Busca et al.'s ex situ IR investigation of air-calcined, then reduced Co_3O_4 , the $\nu(\text{OH})$ IR window was open when the surface is reduced in 200 Torr of H_2 at 523 K.¹²⁷ Upon evacuation at 373 K, $\nu(\text{OH})$ on the reduced Co_3O_4 were observed at 3680, 3658, 3630, and $\sim 3580 \text{ cm}^{-1}$, with an additional broad band centered at 3330 cm^{-1} . Assuming the particle did not reshape during the H_2 treatment, some OH modes remaining after evacuation should correspond to those observed on the equilibrated reduced (111) surface.

Vibrational spectroscopy after treatment only by water has also been performed by various groups on this surface. Petitto et al. performed ex situ HREELS on a single (111) terminated Co_3O_4 crystal after annealing at 623 K under $6.6 \times 10^{-5} \text{ Pa}$ H_2O , cooling down to 110 K, and flashing to

400 K to remove molecular water, all in the absence of H₂ reduction.¹³² They observed a single $\nu(\text{OH})$ peak located at 3650 cm⁻¹. Through in situ IRAS at 500 K under 3.0×10^{-7} mbar D₂O, Schwarz et al. reached a similar result on Co²⁺ and O²⁻ terminated Co₃O₄(111) thin films.^{133, 134} They found a single $\nu(\text{OD})$ peak at 2650 cm⁻¹. They also observed the surface's hydroxylation behavior changing drastically in the interval of 200 K – 500 K under the same pressure. Two broad hydroxyl peaks appear at 2715 cm⁻¹ and 2550 cm⁻¹ at 200 K, while an array of sharp, discrete peaks of variable intensity appear in the range 2730 cm⁻¹ to 2500 cm⁻¹ between 300 K and 400 K.

Table 3.3 Gas phase conditions reached in vibrational spectroscopy above 500 K

Reference	Conditions: T [K] and P _i [bar]	Conditions: $\Delta\mu_i$ [eV]
Busca et al. ¹²⁷	T = 523 K, P _{H2} = 0.27 bar	$\Delta\mu_{\text{H2}} = -0.70$ eV
Petitto et al. ¹³²	T = 623 K, P _{H2O} = 6.6×10^{-10} bar P _{O2} = $4 \times 10^{-10} \sim 4 \times 10^{-16}$ bar	$\Delta\mu_{\text{H2O}} = -2.30$ eV $\Delta\mu_{\text{O}} = -1.22 \sim -1.60$ eV
Schwarz et al. ^{133, 134}	T = 200 K, P _{D2O} = 3×10^{-11} bar P _{O2} = $10^{-10} \sim 10^{-16}$ bar T = 300 K, P _{D2O} = 3×10^{-11} bar P _{O2} = $10^{-10} \sim 10^{-16}$ bar T = 370 K, P _{D2O} = 3×10^{-11} bar P _{O2} = $10^{-10} \sim 10^{-16}$ bar T = 500 K, P _{D2O} = 3×10^{-11} bar P _{O2} = $10^{-10} \sim 10^{-16}$ bar	$\Delta\mu_{\text{D2O}} = -0.74$ eV $\Delta\mu_{\text{O}} = -0.37 \sim -0.49$ eV $\Delta\mu_{\text{D2O}} = -1.14$ eV $\Delta\mu_{\text{O}} = -0.57 \sim -0.75$ eV $\Delta\mu_{\text{D2O}} = -1.43$ eV $\Delta\mu_{\text{O}} = -0.71 \sim -0.93$ eV $\Delta\mu_{\text{D2O}} = -1.98$ eV $\Delta\mu_{\text{O}} = -0.99 \sim -1.29$ eV

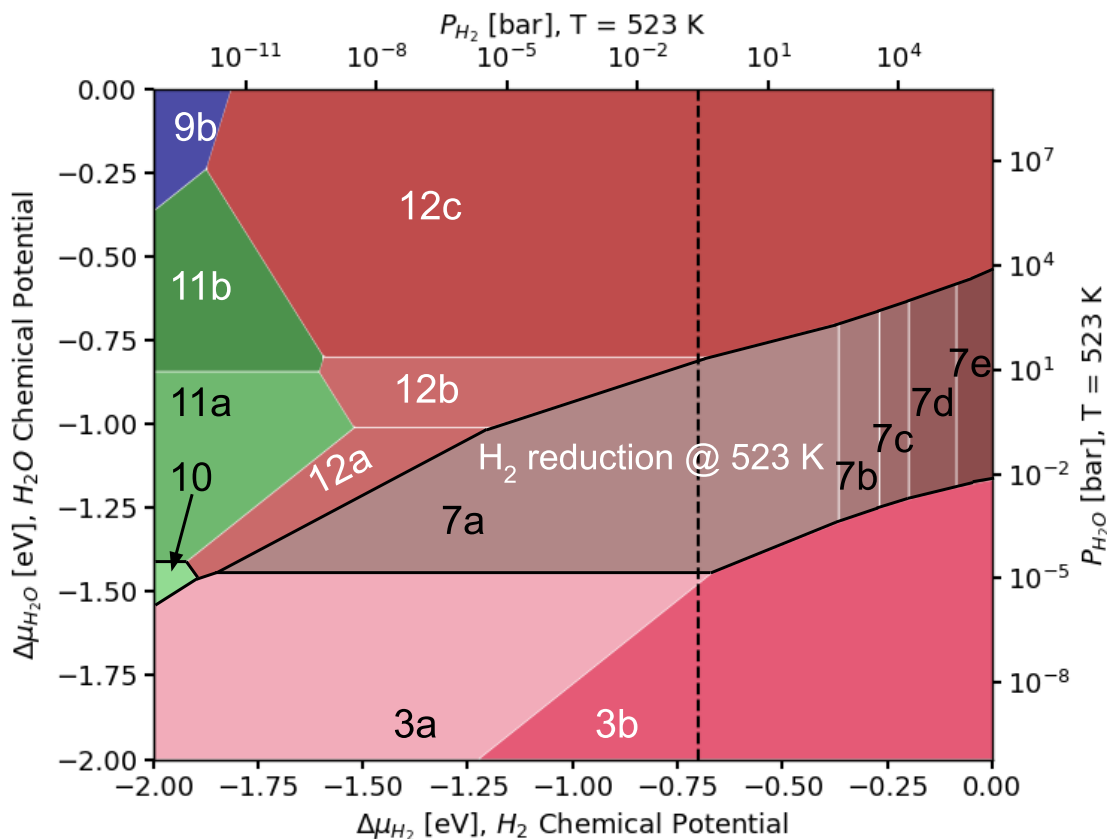


Figure 3.8 Gas phase environmental conditions during vibrational characterization by Busca et al. represented as a dashed line on the H₂O/H₂ surface stability diagram (**Figure 3.5**), as H₂O chemical potential is not well-defined. The corresponding termination should contain 7.11 Co/nm² and 7.11 OH/nm² (structure 7a, brown) because an unrealistic high pressure of H₂O must be applied to generate a mixed OH/H₂O layer (structure 12c, red).

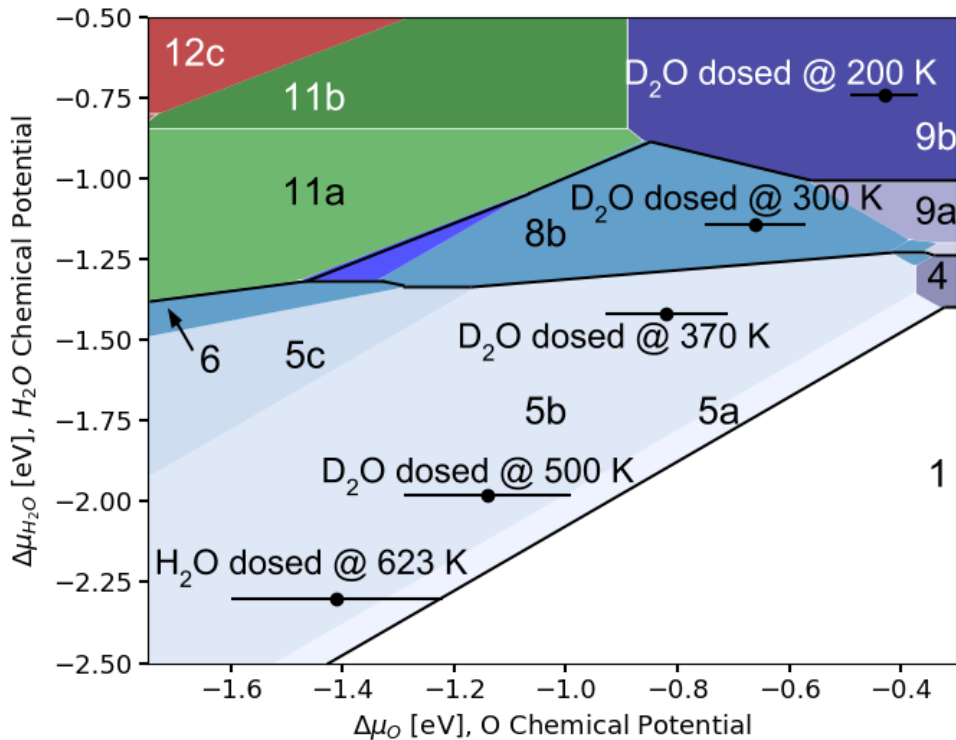


Figure 3.9 Gas phase environmental conditions during vibrational characterization under H₂O/D₂O pressure, overlaid with the H₂O/O surface stability diagram of **Figure 3.3**. These conditions fall under three main regions: (Co^T)_x with triaqua-complex-incorporated OH/H₂O chains (structure 9b), triaqua surface complex with additional OH (8b) for D₂O dosed at 200 K and 300 K, and (Co^T)_x with isolated OH (structure 5b) for D₂O exposure at 370 K and beyond. Gas phase conditions in characterization experiments are marked as dots with error bars for O chemical potential.

While considering only D₂O adsorption on Co₃O₄(111), we identified three main structures observed on (Co^{Td})_x surface upon exposure to 3 × 10⁻⁸ mbar D₂O at 300 K, without considering any surface reduction. The three motifs are: i) isolated hydroxyls, ii) surface Co(H₂O)₃ complexes, and iii) extended hydroxyl networks.¹⁴⁵ Here, accounting for the effect of O₂ in the atmosphere, we provide an O₂-equilibrated view of the hydroxylation behavior observed on Co₃O₄(111) films

during and after the experiments described. Through interpolation of experimental thermochemistry data, the conditions produced by the H₂, H₂O, and D₂O treatments can be converted to a set of water and hydrogen or oxygen chemical potentials (**Table 3.3**) and overlaid on the stability diagrams (**Figure 3.8, 3.9**). Since no in situ spectra are available under the conditions of Busca et al.'s and Petitto et al.'s experiments, we assume that cooling and evacuation does not disrupt the surface structures generated during H₂ and H₂O treatments. To approximate the oxygen content in the atmosphere observed in the water exposure experiments, we consider three magnitudes above and below the vacuum level in the experiments to calculate a possible range of chemical potentials for the conditions. For the H₂-exposure experiment, we consider the range of water pressures that can be realistically reached to set a possible range of water chemical potentials.

In ex situ IR after H₂ reduction and evacuation, multiple types of hydroxyl groups remain on the surface.¹²⁷ This result can be attributed to the large variation of exposed surfaces on a Co₃O₄ particle.¹²¹ Our calculations show that for the (111) surface, the (Co^{Oh}Co^{Td})_x termination (7.11 Co/nm²) with 7.11 OH/nm² (structure 7a) is most likely exposed (**Figure 3.8**). Two types of OH groups can be found on this surface: a bidentate OH group and a tetradentate OH group (see **Table 3.2**), which we found to exhibit 3667~3668 cm⁻¹ and 3527~3528 cm⁻¹ v(OH) modes respectively. These modes are close to two reported values (3680 cm⁻¹ and 3580 cm⁻¹) out of many modes found by Busca et al. It is suggested that other modes are associated with other terminations of Co₃O₄. We did not consider the hydroxyl overlayer structure (structure 12c) in our assessment because P_{H₂O} must be unrealistically high at 523 K for the fully hydroxylated structure to exist.

Since no H₂ is present in the gas phase in the preparation of Co₃O₄(111) films and D₂O/H₂O exposure experiments of Schwarz et al., we considered the surfaces to be in equilibrium with an

oxygen pressure 3 magnitudes about the vacuum level. With P_{O_2} in consideration, we predict the following structures. D_2O exposure at 200 K, compared to our previous investigation, still corresponds to a hydrogen bonded hydroxyl network containing a triaqua complex (structure 9b). Next, D_2O exposure at 300 K corresponds to triaqua complexes immediately surrounded by OD (structure 8b). The $Co(D_2O)_3+OD$ structure shows modes in the range $2715\sim 2723\text{ cm}^{-1}$, belonging to the $\nu(OD)$ modes of the triaqua surface complex, and modes in the range $2547\sim 2551\text{ cm}^{-1}$ belonging to OD surrounding the complex. This result shows that the triaqua surface complex is robust and insensitive to surrounding OH. Finally, the conditions obtained by H_2O or D_2O adsorption experiments 370 K and above by Petitto et al. and Schwarz et al. fall under the sparsely hydroxylated region (structure 5b). Surface tridentate modes are located at $2684\text{ cm}^{-1}/2681\text{ cm}^{-1}$ for OD and $3637\text{ cm}^{-1}/3633\text{ cm}^{-1}$ for OH. These results match those obtained by Petitto et al. after purging physisorbed water (3645 cm^{-1}) and the OD bands are $25\text{-}35\text{ cm}^{-1}$ away from D_2O adsorption modes found by Schwarz et al. (2657 cm^{-1}).¹³²⁻¹³⁴

Previously, through a comparison between $D_2^{18}O$ and $D_2^{16}O$ exposure IRAS, it was shown that O of isolated surface OD generated through D_2O exposure above 500 K originate from the surface, since the $\nu(OD)$ modes are not modified upon change of O isotope in water. Here, since we assume that no H_2 is present in the atmosphere, the only way to generate only these hydroxyls is through vacancy re-filling by D_2O , and diffusion of the proton to surface O atoms. Upon $D_2^{18}O$ dissociation at vacancy, one ^{18}OD and one ^{16}OD are generated, but since the surface is still rich in ^{16}O , $\nu(^{16}OD)$ will be the predominant peaks in the IR spectrum. Another hypothesis is that eventual OD groups from water have low intensity in the spectrum.¹⁴⁵

3.3.3 Comparison among $U_{\text{eff}} = 3.5 \text{ eV}$, 2.0 eV , and HSE06

The DFT+U approach is a very popular method used to describe strongly correlated systems as it makes a good compromise between accuracy and feasibility. The most popular adaptation is the rotationally-invariant method of Dudarev et al., where only one quadratic on-site self-interaction penalty is added to the DFT energy to enforce integer occupancies in each spin orbital of the orbitals of interest.⁷⁹ Choosing an appropriate U_{eff} value to use is a very controversial topic in DFT modeling of strongly correlated systems.¹⁵⁰

Approaches taken in literature can be divided to two categories: directly computing U_{eff} through linear response to correct DFT's unphysical energy response to addition and removal of fractional numbers of electrons and 2) fitting some empirical properties of the system. Studies using both approaches have been performed for the Co_3O_4 bulk and surfaces. Chen et al. calculated U_{eff} of Co^{2+} and Co^{3+} in bulk Co_3O_4 and used the weighted average, 5.9 eV , to study bulk properties; however, the approach predicted the ferromagnetic ground state being more favorable.¹²⁰ The approach also does not predict well surface and bulk redox properties.^{137, 151} The U_{eff} determined through this approach is also unique to the calculation method; a later study performed using PAW pseudopotentials in VASP, instead of Troullier-Martins pseudopotentials in Quantum Espresso found U_{eff} of Co^{2+} and Co^{3+} at bulk sites to be 4.3 eV and 5.02 eV .¹³⁶

Since the Co linear response U_{eff} does not predict well redox properties, authors interested in reactive properties tend to choose smaller values. Bajdich et al. and Chen et al. have noted that $U_{\text{eff}} \sim 3 \text{ eV}$ is optimal to properly describe reactivity.^{151, 152} Jiang et al. used $U_{\text{eff}} = 2.0 \text{ eV}$ to match bulk band gap with experiment.¹⁴¹ Recently, Hu et al., using results obtained from RPA as benchmarks, proposed the usage of two different values of U_{eff} , applied to the Co and surface Co atoms respectively, to examine the reactivity of oxygen-rich $\text{Co}_3\text{O}_4(110)$.¹⁵³ To ensure that our

choice of $U_{\text{eff}} = 3.5$ eV is appropriate for $\text{Co}_3\text{O}_4(111)$, we compared energies of water adsorption and O vacancy formation generated at this U_{eff} to those obtained using $U_{\text{eff}} = 2.0$ eV and HSE06+dDsC. We chose the value of $U_{\text{eff}} = 2.0$ eV in addition to our initial choice $U_{\text{eff}} = 3.5$ eV, as it is a very popular value used in many DFT studies on the reactivity of Co_3O_4 surfaces. Table 4 compares energy of vacancy formation, for $O_{\text{vac}} = 3.56 \text{ nm}^{-2}$ and energy of adsorption of water at $3.56 \text{ H}_2\text{O}/\text{nm}^2$ and $7.11 \text{ OH}/\text{nm}^2$, reached using the three methods on the $(\text{Co}^{\text{Td}})_x$ termination of Co_3O_4 .

Table 3.4 Comparison of water adsorption energy and energy of vacancy formation calculated using $U_{\text{eff}} = 3.5$ eV, 2.0 eV, and HSE06+dDsC (water adsorption data adapted from¹⁴⁵)

Description	Energy [eV], $U_{\text{eff}}=3.5$ eV	Energy [eV], $U_{\text{eff}}=2.0$ eV	Energy [eV], HSE06+dDsC
Vacancy formation, $(\text{Co}^{\text{Td}})_x$ with $3.56 O_{\text{vac}}/\text{nm}^2$, energy of O_{vac} formation, E_{form} per O_{vac}	2.07	3.01	2.31
Water adsorption, $(\text{Co}^{\text{Td}})_x$ with $7.11 \text{ OH}/\text{nm}^2$ and $3.56 \text{ H}_2\text{O}/\text{nm}^2$ in the “pair” configuration (see SI, Figure B.13, top), E_{ads} per H_2O molecule	-1.02	-0.91	-1.08
Water adsorption, $(\text{Co}^{\text{Td}})_x$ with $7.11 \text{ OH}/\text{nm}^2$ and $3.56 \text{ H}_2\text{O}/\text{nm}^2$ in the “hexagonal” configuration (see SI, Figure B.13, bottom), E_{ads} per H_2O molecule	-1.00	-0.96	-1.10

As seen in the table above, the energy of vacancy formation decreases as U_{eff} increases. Upon generation of a single O_{vac} on this termination, electrons are transferred to the Co atoms immediately surrounding the vacancy. Increasing U_{eff} increases the penalty placed on delocalization while facilitating electron localization. Selcuk and Selloni also observed that O vacancy formation energy on the (110) surface, in the case where electrons are localized, heavily

depends on U_{eff} .¹³⁷ On the other hand, the adsorption of water is an electron-neutral process, which explains why the change in E_{ads} is not very significant. These adsorption results obtained from $U_{\text{eff}} = 3.5$ eV do not strongly differ from those at $U_{\text{eff}} = 2$ eV but agree better with results from HSE06.

For further confirmation, we recalculated using $U_{\text{eff}} = 2.0$ eV the surface energy of structures shown in **Figure 3.9** and **Table 3.4** and constructed an analogous surface stability diagram combined shown on **Figure 3.10**.

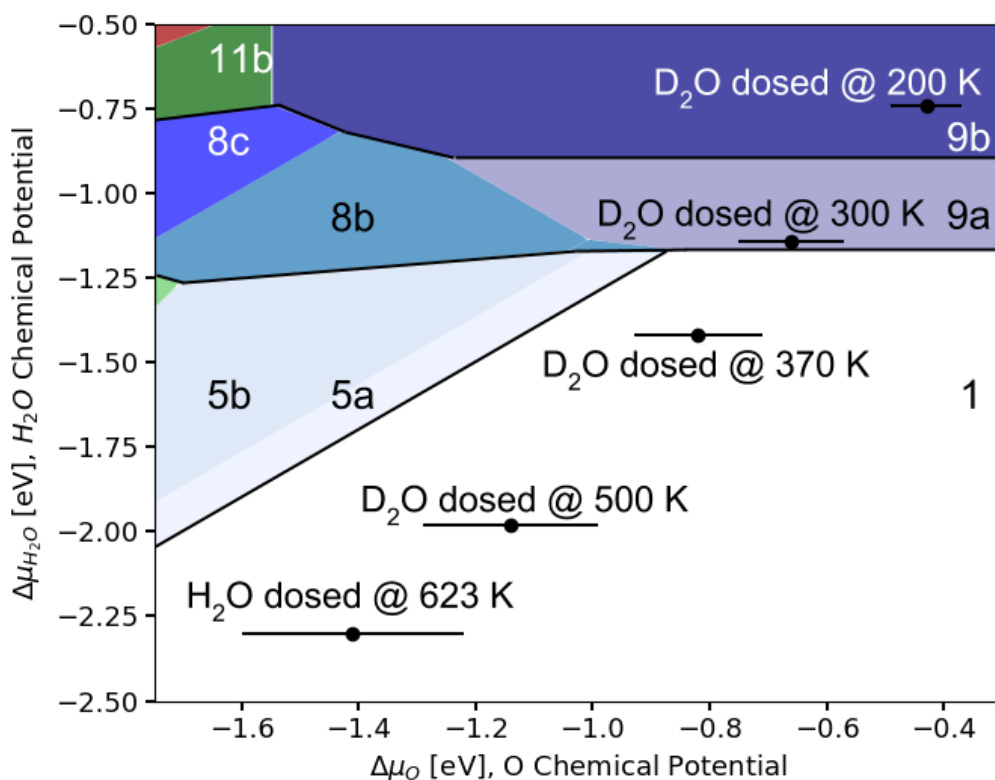


Figure 3.10 Surface structure as a function of oxygen and water chemical potential calculated using $U_{\text{eff}} = 2.0$ eV. Gas phase conditions observed in vibrational characterization are marked as dots with error bars for O chemical potential. No hydroxylation is predicted to exist in $\text{D}_2\text{O}/\text{H}_2\text{O}$ exposure conditions at 370 K and above when using $U_{\text{eff}} = 2.0$ eV.

The lower U_{eff} value heavily decreases the energy of adsorption of hydrogen and weakens slightly water adsorption. Interestingly, the stability diagram reached from $U_{\text{eff}} = 2.0$ eV does not predict hydroxylation through D_2O exposure or annealing in H_2O , in contrast with experiments. The value $U_{\text{eff}} = 3.5$ eV hence produces results that match much better the spectroscopic experiments. Like vacancy formation, H adsorption adds electrons to the surface and becomes expectedly more favorable with increasing U_{eff} . Altogether, these test results validate the theoretical method used in the present paper.

3.3.4 Predicted Surface Structure under Various Reaction Conditions

Co_3O_4 's applications in thermal catalysis can be divided into three categories. First, Co_3O_4 has been known as an effective CO and hydrocarbon oxidation catalyst.^{112, 154-156} Xie et al. found that CO oxidation can occur over Co_3O_4 nanorods at a temperature as low as -77 °C, but is easily poisoned by water.^{154, 157} The activity appears to depend on the exposed surfaces and catalyst shape.¹⁵⁶ Second, Co_3O_4 can also be used as a catalyst or support for NO_x reduction.^{112, 114, 115, 158, 159} N_2O decomposition to N_2 and O_2 over Co_3O_4 was found to occur at 873 K, and selective catalytic reduction (SCR) reaction of NO with NH_3 and O_2 was found to occur over Co_3O_4 at 423 K.^{114, 158} NO reduction with H_2 can also be performed over single noble metal (NM) atoms anchored on Co_3O_4 to produce N_2 or N_2O .^{115, 160} Third, one promising application of the (111) surface is the oxidative dehydrogenation (ODH) of alkanes. This reaction was explored by Tyo et al., Liu et al, and Fung et al.¹¹⁶⁻¹¹⁸ It was found that the alkane activation occurs over one isolated surface O and one O adjacent to surface Co (see **Section 3.2.2**), and that substitution of surface Co- T_d with other metals lowers the activation barrier of alkanes by increasing surface reducibility.¹³⁸ Liu et al.

showed that Co_3O_4 particles primarily exposing the (111) facet have higher conversion and selectivity for ethane ODH than particles that expose higher miller index surfaces such as (311).¹¹⁸ Overall, reactions using Co_3O_4 as a catalyst or support and containing O_2 in the atmosphere are performed below 900 K, and reactions using $\text{H}_2/\text{H}_2\text{O}$ as reactant/product are performed below 500-600 K.

Table 5. Gas phase conditions observed in catalytic reactions

Reaction	Conditions: T [K] and P_i [bar]	Conditions: $\Delta\mu_i$ [eV]
$2\text{CO} + \text{O}_2 \rightarrow 2\text{CO}_2$ ¹⁵⁷	T = 196 K, $P_{\text{O}_2} = 0.02$ bar	$\Delta\mu_{\text{O}} = -0.20$ eV
$2\text{N}_2\text{O} \rightarrow 2\text{N}_2 + \text{O}_2$ ¹⁵⁸	T = 873 K, $P_{\text{O}_2} = 2 \times 10^{-3}$ bar	$\Delta\mu_{\text{O}} = -1.17$ eV
$2\text{C}_2\text{H}_6 + \text{O}_2 \rightarrow 2\text{C}_2\text{H}_4 + 2\text{H}_2\text{O}$ ¹¹⁸ $2\text{C}_2\text{H}_6 + 7\text{O}_2 \rightarrow 4\text{CO}_2 + 6\text{H}_2\text{O}$	T = 873 K, $P_{\text{O}_2} = 0.018$ bar $P_{\text{H}_2\text{O}} = 0.033$ bar	$\Delta\mu_{\text{O}} = -1.09$ eV $\Delta\mu_{\text{H}_2\text{O}} = -2.00$ eV
$\text{CH}_4 + 2\text{O}_2 \rightarrow \text{CO}_2 + 2\text{H}_2\text{O}$ ¹⁶¹ $2\text{CH}_4 + 3\text{O}_2 \rightarrow 2\text{CO} + 4\text{H}_2\text{O}$	T = 873 K, $P_{\text{O}_2} = 0.0017$ bar $P_{\text{H}_2\text{O}} = 0.0050$ bar	$\Delta\mu_{\text{O}} = -1.18$ eV $\Delta\mu_{\text{H}_2\text{O}} = -2.14$ eV
$2\text{NO} + 2\text{H}_2 \rightarrow \text{N}_2 + 2\text{H}_2\text{O}$ ¹¹⁵ $2\text{NO} + \text{H}_2 \rightarrow \text{N}_2\text{O} + \text{H}_2\text{O}$	T = 423 K, $P_{\text{H}_2} = 0.0095$ bar $P_{\text{H}_2\text{O}} = 0.040$ bar	$\Delta\mu_{\text{H}_2} = -0.66$ eV $\Delta\mu_{\text{H}_2\text{O}} = -0.85$ eV
	T = 523 K, $P_{\text{H}_2} = 0.00049$ bar $P_{\text{H}_2\text{O}} = 0.0483$ bar	$\Delta\mu_{\text{H}_2} = -0.98$ eV $\Delta\mu_{\text{H}_2\text{O}} = -1.08$ eV
$4\text{NO} + 4\text{NH}_3 + \text{O}_2 \rightarrow 4\text{N}_2 + 6\text{H}_2\text{O}$ ¹¹⁴	T = 423 K, $P_{\text{O}_2} = 0.020$ bar $P_{\text{H}_2\text{O}} = 6 \times 10^{-4}$ bar	$\Delta\mu_{\text{O}} = -0.48$ eV $\Delta\mu_{\text{H}_2\text{O}} = -1.00$ eV

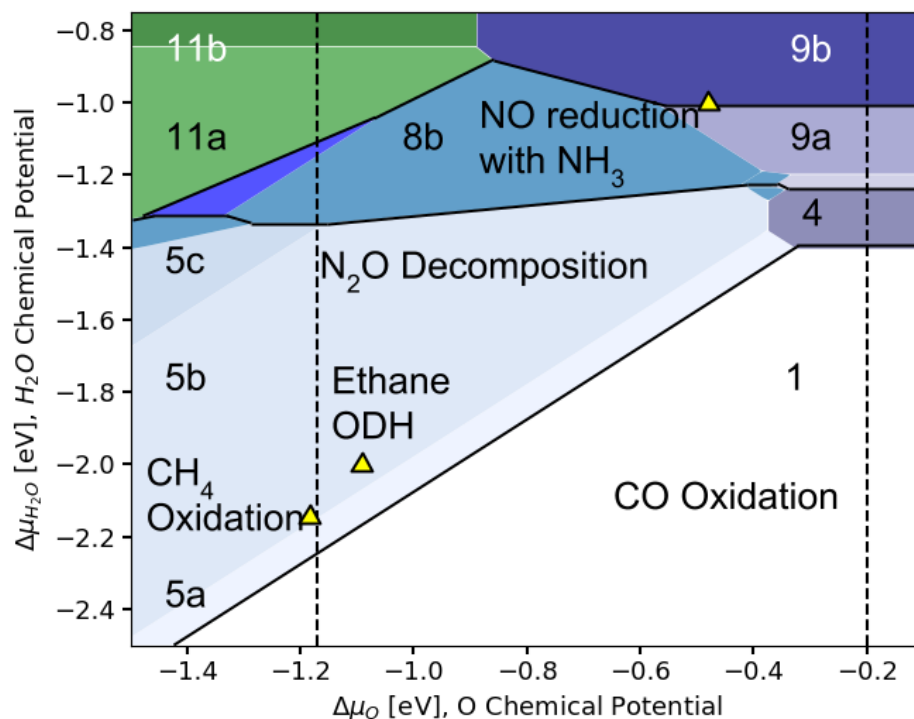


Figure 3.11 Surface stability diagram as a function of O_2 and H_2O chemical potential. Conditions in low temperature CO oxidation, N_2O decomposition, ethane ODH, CH_4 oxidation, and NO reduction with NH_3 are marked on the diagram as yellow triangles if P_{H_2O} is well-defined and dashed lines otherwise.

Reactive conditions considered in this work are listed on Table 5. H_2 , O_2 , and H_2O are assumed to be ideal gases, and their partial pressures are estimated using the reported reaction conversion and selectivity, assuming the reactions take place isobarically at 1 bar. Co_3O_4 is most commonly used for oxidative reactions without H_2 ; therefore, in most gas phase reactions, the Co_3O_4 surfaces are in equilibrium with H_2O and O_2 . Let us start this discussion with low temperature CO oxidation. Since the water chemical potential is not clearly defined for that reaction, conditions are indicated as a dashed vertical line on the right side of **Figure 3.11**. However, the nature of the $Co_3O_4(111)$ surface can change quite drastically when water is present.

In these conditions, from our calculations (**Figure 3.11**), hydroxyls will populate the surface when water chemical potential is greater than -1.45 eV, which, at 196 K, corresponds roughly to a pressure higher than 10^{-30} bar; in other words, any water present will contaminate the surface. As the reaction temperature increases at the same O_2 pressure, the surface becomes less susceptible to hydroxylation. CO TPD studies have also shown that lattice oxygen does not appear to be reactive; therefore, it is crucial for surface Co^{2+} to be exposed during CO oxidation to adsorb reactants.¹⁶² At 196 K, under the O_2 pressure applied in the CO oxidation reaction, the surface already becomes covered with an triaqua-complex-containing H_2O/OH overlayer (structure 9b) when P_{H_2O} is in the order of 10^{-15} bar. Both experimentally determined and calculated energy of CO adsorption falls far above -1.1 eV, indicating that any water impurities will completely block the reaction, in agreement with experiments.^{162, 163} Conditions for N_2O decomposition also correspond to a line on **Figure 3.11**, but at a lower O chemical potential, mainly from the much higher temperature. The surface structure during N_2O decomposition is also dependent on the amount of H_2O impurities in the gas phase; though, the only accessible regions, i.e. $P_{H_2O} > 10^{-12}$ bar and above, are the bare $(Co^{Td})_x$ and $(Co^{Td})_x$ terminations with ≤ 1.78 OH/nm² (5a, 5b). The transition from bare to hydroxylated can occur very easily, but no hydroxyl cluster or overlayer can form.

Reactions that generate H_2O , as a product or side product, also carry the threat that the Co_3O_4 surface will hydroxylate. In the conditions associated to the ODH of ethane, the surface is found to be slightly hydroxylated, with 1.78 OH/nm² (structure 5b). CH_4 oxidation would also fall under the same region on the phase diagram. Both reactions occur at high temperatures, so it is reasonable to expect the surfaces to have low degrees of hydroxylation. It can be inferred from trends developed for CH_4 activation that surface O's affinity for H directly correlates to its alkane activation barrier.⁴⁹ Considering that surface O is the first recipient of charge transfer upon H_2

adsorption (**Figure 3.7a**), it is then important to control moisture content in the environment to ensure that alkane activation activity is not hampered by hydroxyls. Finally, for NO reduction with NH_3 , the conditions for this reaction fall at the boundary between the zone of triqua-complex-containing OH/ H_2O chains (9b) and triqua complex/OH/ H_2O chain existing separately (8b). In other words, surface Co is unlikely to be exposed during this reaction.

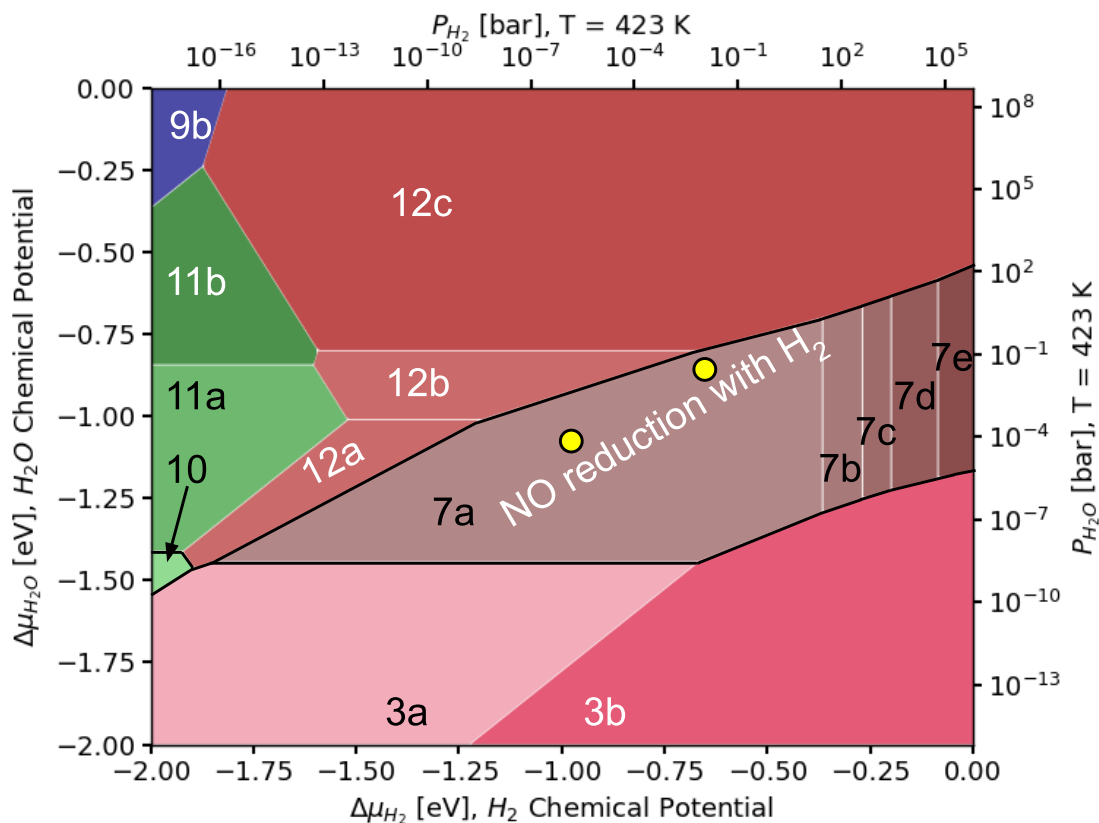


Figure 3.12 Surface stability diagram as a function of H_2 and H_2O chemical potential and hydrogen/water pressure at 423 K. Conditions in NO reduction with H_2 found in the literature are marked on the diagram as yellow circles.

On the other hand, the environment during NO reduction with H_2 equilibrates the surface with H_2O and H_2 (**Figure 3.12**). In this reaction, the Co_3O_4 plays the role of support for noble metal

atoms (Pd, Pt, and Rh; the conditions here refer to NO reduction over Pd/ Co₃O₄), and it was observed through AP-XPS that when the temperature is moderate enough, surface transition to CoO is inhibited.^{115, 160} In these conditions, the (Co^{Oh}Co^{Td})_x surface with 7.11 OH/nm² (structure 7a) would be exposed. The high coverage of hydroxyl groups present might, however, play a major role in modifying the catalysts support interaction and the nature of the charge transfer between the support and the metallic nanoparticle.⁵³

3.4 Conclusion

In this study, we investigated the surface structure of three terminations of Co₃O₄(111) in equilibrium with a wide range of gas environments and mapped out detailed surface stability diagrams with respect to vacancy formation and hydroxylation of the surface either from hydrogen or water adsorption. We found that all three terminations are accessible, but the Co-poor ((Co^{Td})_x, 3.56 Co/nm²) and Co-rich ((Co^{Oh}Co^{Td})_x, 7.11 Co/nm²) terminations are the most prevalent. When equilibrated with oxygen and water, we found that the Co-poor termination exhibits three stages of hydroxylation – formation of isolated OH at low $\Delta\mu_{\text{H}_2\text{O}}$, transition to isolated OH/H₂O clusters when $\Delta\mu_{\text{H}_2\text{O}} > -1.3$ eV, and finally to a fully hydrated state when $\Delta\mu_{\text{H}_2\text{O}} > -1.0$ eV.

We found that if the surface is in equilibrium with oxygen, the Co-poor/O-rich surface (Co^{Td})_x is predominantly exposed, and it is very difficult to produce the stoichiometric (Co^{Oh_{0.5}}Co^{Td})_x or the Co-enriched (Co^{Oh}Co^{Td})_x termination. Since we found it to be very easy to populate the (Co^{Td})_x surface with hydroxyls through H₂ adsorption or H₂O dissociation over a vacancy, we predict that hydroxyls will appear during oxidative reactions that produce water or even when water is present as an impurity at low partial pressure. We compared the calculations results concerning hydroxylation of (Co^{Td})_x to those obtained from vibrational spectroscopy on

Co₃O₄ single crystals and Co₃O₄(111) films and conclude that at low and medium temperature triqua surface complexes surrounded by OH/H₂O groups are observed, while only isolated OH are present at higher temperature. In a similar way, unless the environment contains very little water, the O-poor termination (Co^{Oh}Co^{Td})_x is predicted also be hydroxylated.

We found that stabilization of the stoichiometric termination (Co^{Oh}_{0.5}Co^{Td})_x and Co-rich termination (Co^{Oh}Co^{Td})_x is only possible under vacuum at high temperature and in hydrogen and water at low temperatures. The H₂/H₂O conditions are the most important for catalytic applications. We found that reduction of this Co-rich termination through H adsorption and O_{vac} formation is easy due to the large relaxation observed at 7.11 OH/nm² or 3.56 O_{vac}/nm². At 423 K and below and under realistic H₂/H₂O pressure, the (Co^{Oh}Co^{Td})_x termination with 7.11 OH/nm² is highly stable. The OH groups on that termination exhibit vibrational frequencies that fall under the range observed in ex situ IR experiments. We believe that this termination should be considered when modeling reactions over Co₃O₄ in low temperature reducing environments.

We validated our results through changing the U_{eff} value and comparing with results reached through hybrid functionals. We found good agreement with both macroscopic experimental observations and HSE06+dDsC calculations using U_{eff} = 3.5 eV. Hence, the various terminations of Co₃O₄ should be hydroxylated under a large range of conditions. It is therefore of high importance to include a correct coverage in hydroxyl groups for a realistic modelling of the Co₃O₄ surface in calculations; the bare surface model usually used in reaction pathway calculations might not be adequate. The effect of hydroxyls in the modification of reaction mechanisms and their interactions with supported metal atoms/clusters must also be considered. Further studies will focus on the interaction among various surface features discussed in this work, and the implications of these structures on the surface's reactivity and properties of the supported active sites.

Chapter 4 Theoretical Simulations of the Hydrodeoxygenation (HDO) of Anisole over a Teamed Single Atom $\text{Mo}_1+\text{Pd}_1/\text{Co}_3\text{O}_4$ Catalyst

4.1 Introduction

Metal nanoparticles form one of the major types of catalysts, active for numerous reactions.⁴ Many of these catalytic reactions involve two reactants A and B [$\text{A}+\text{B}\rightarrow\text{target product(s)}$] and follow the Langmuir-Hinshelwood mechanism. Under this mechanism, the first step is the chemisorption of reactants A and B on the surface of the metallic nanoparticles. In most cases reactants A and B have different adsorption energies and, at a low reaction temperature, if reactant A is preferentially adsorbed, the high coverage of A limits the access of B to the catalyst surface, slowing down the reaction or even preventing it from occurring at this low temperature. For example, computational studies of furfural hydrogenation on Pd(111) showed that the high coverage of adsorbed H only allows furfural to adsorb on Pd(111) through a tilted vertical binding configuration by the O atom of its -CHO functional group¹⁶⁴. This binding mode, arising from the preferential chemisorption of H, makes the catalyst inactive in furfural decarbonylation to form furan, since the C-C bond is too far from the metal surface¹⁶⁴

Here, to realize catalysis along a demanded reaction channel at a low temperature where a supported metal nanoparticle catalyst, of element X, is not active, we propose teaming two single-atom sites, X_1 , responsible for chemisorbing and activating molecule A, and Y_1 for molecule B, respectively, at low temperature. Y is another metal element. Here the subscript “1” was added to refer the single-atom site. Typically, single-atom sites are formed by immobilization of an isolated metal cation on an oxide support and have a chemical state and coordination environment markedly different from that of the surface site of a nanoparticle of the considered metal.⁴ To explore the hypothesis of realizing low-temperature catalysis through teaming single-atom sites,

hydrodeoxygenation (HDO) of anisole was chosen as a probe reaction. Single-atom Pd₁ and Mo₁ sites were chosen to activate H₂ and anisole, respectively.

Kinetic tests show that the teamed Pd₁ and Mo₁ single-atom catalyst is highly active for HDO of anisole at a temperature as low as 100 °C. Although Pd₁/Co₃O₄ can also catalyse the HDO of anisole, the selectivity is worse than that of Mo₁+Pd₁/Co₃O₄; on the other hand, the Mo₁/Co₃O₄ catalyst is inactive for anisole HDO. DFT calculations and microkinetic modelling show that, while the reaction can take place over Pd₁, H on the hydroxylated Co₃O₄ support can spill over to Mo₁ sites to enable the HDO reaction to occur cooperatively on a teamed Mo₁+Pd₁/Co₃O₄ catalyst at a higher overall rate than on a single-site Pd₁/Co₃O₄ catalyst. This work demonstrates that teaming single-atom catalytic sites is an efficient approach for designing catalysts active and selective at low-temperature.

4.2 Methods

4.2.1 DFT Calculations

Density functional theory (DFT) calculations were performed using the Vienna Ab-initio Simulation Package (VASP).⁷³⁻⁷⁵ Exchange-correlation energy was calculated using the Perdew-Burke-Erzenhof (PBE) functional.⁷⁶ Since the PBE functional does not account for van der Waals (vdW) forces, the dDsC dispersion-correction method was used.^{142, 143} The projector-augmented-wave (PAW) method was used to describe core electrons, while valence one-electron wavefunctions were developed using a set of plane waves with kinetic energy up to 500 eV.⁷⁸ To correct for the self-interaction error of the 3d electrons of Co, a Hubbard-like repulsion term was added using Dudarev's approach (DFT+U), with $U_{\text{eff}} = U - J = 3.50$ eV.⁷⁹ Value of U_{eff} near 3.50 eV was shown to reproduce correct CoO_xH_y bulk redox properties.¹⁵² A U_{eff} value of 4.00 eV was

used for the 4d electrons of Mo, motivated by PBE's underestimation of MoO_3 's reducibility compared to HSE06.¹⁶⁵

The (2×2) supercell of a bulk-truncated 13-layer $\text{Co}_3\text{O}_4(111)$ slab was used for calculations, with the top 4 layers relaxed during structural optimization. The surface model contains 7.11 $\text{Co}^{2+}/\text{nm}^2$ and 7.11 OH/nm^2 . The Brillouin zone was sampled using a $3 \times 3 \times 1$ Monkhorst-Pack mesh.⁸⁴ Atomic positions were relaxed until forces on unconstrained atoms fall below $0.04 \text{ eV}/\text{\AA}$. Transition states were calculated by first performing a nudged elastic band (NEB) calculation with 4~12 images for at least 50 steps, followed a climbing image (CI) NEB calculation.^{166, 167} In this stage, only the Gamma point was sampled in the Brillouin zone. Then, the highest energy image of the CI-NEB trajectory was optimized using the dimer and quasi-Newton algorithms until forces on unconstrained atoms fall below $0.04 \text{ eV}/\text{\AA}$.¹⁶⁸ Here, the Brillouin zone was sampled using a $3 \times 3 \times 1$ Monkhorst-Pack mesh. Frequency calculations were performed using the finite difference approximation. After decreasing the electronic convergence criterion to 10^{-8} eV , some transition states were still found to contain soft imaginary modes of the aromatic ring or on the weakly bound CH_3 group in addition to the reaction coordinate. The soft modes likely arose from numerical inaccuracies, and thus they were rounded up to 50 cm^{-1} . Co_3O_4 's antiferromagnetic structure among parallel (111) planes of Co^{2+} ions was kept in all calculations using the occupancy matrix control method.¹⁴⁶ Gibbs free energies of gases were approximated using the rotational, translational, and vibrational degrees of freedom, while only the vibrational degrees of freedom were considered for surface intermediates and transition states.¹⁶⁹

4.2.2 Microkinetic Simulations

For quantitative comparisons between computational results and experimental measurements beyond the energetic span approximation, we performed microkinetic simulations using kinetic rate parameters computed from the DFT energetics. The forward and reverse rate constants of surface reactions were computed using transition state theory:

$$k_i = \frac{k_B T}{h} \exp\left(\frac{-\Delta G_{\text{act}}^\circ}{RT}\right) \quad (4.1)$$

The rate constants for adsorption were computed with collision theory for some steps (**Equation C.1 and C.2**). σ , the sticking coefficient, was set to 1, and A_{site} , the area of a single active site, was set to $3.72 \times 10^{-20} \text{ m}^2$. The corresponding rate constants of desorption were computed using the equilibrium constants of adsorption:

$$k_{\text{des},i} = \frac{k_{\text{ads},i}}{K_{\text{ads},i}} \quad (4.2)$$

$$K_{\text{ads},i} = \exp\left(-\frac{\Delta G_{\text{ads},i}^\circ}{k_B T}\right) \quad (4.3)$$

The rate of elementary step j was computed using the following equation:

$$r_j = k_j^{\text{fwd}} \prod_i \alpha_{i,\text{IS}}^{v_{ij}^{\text{fwd}}} \prod_i \alpha_{i,\text{gas}}^{v_{ij}^{\text{fwd}}} - k_j^{\text{rev}} \prod_i \alpha_{i,\text{IS}}^{v_{ij}^{\text{rev}}} \prod_i \alpha_{i,\text{gas}}^{v_{ij}^{\text{rev}}} \quad (4.4)$$

where k_j^{fwd} and k_j^{rev} are the forward and reverse rate constants, and v_{ij}^{fwd} and v_{ij}^{rev} are the stoichiometric coefficients of reactant i in the forward and reverse directions. The activity α_i is taken as the surface coverage fraction θ_i for surface intermediates (including bare sites) and as the ratio of the partial pressure to the standard pressure, P_i/P° , for gaseous species.¹⁷⁰ To model the spillover of H from the substrate to the Mo_1 site, the coverage of H on the support surface was assumed to be equilibrated with the pressure of H_2 . The steady state coverages of intermediates were found by solving the following system of equations:

$$0 = -\sum_j v_{ij}^{\text{fwd}} r_j + \sum_j v_{ij}^{\text{rev}} r_j \quad (4.5)$$

$$\theta_{\text{site}}(t = 0) = \sum_i \theta_{\text{site},i} \quad (4.6)$$

Here, $\theta_{\text{site},i}$ are the surface coverages of species i , including the bare site.

The steady state intermediate coverages and rates of reaction were computed in the temperature range of 50~150 °C. The partial pressures of H₂, anisole, benzene, and methanol were set to 0.995 bars, 4.67×10^{-3} bars, 4.72×10^{-5} bars, and 4.72×10^{-5} bars, respectively. The reaction pathways were analysed by computing the apparent activation energies and the degrees of rate control (DRC) of surface intermediates and transition states.¹⁷¹ The derivatives are evaluated numerically using step sizes of 10^{-3} °C and 10^{-4} eV for the apparent activation energy and the degree of rate control, respectively.

4.3 Results and Discussion

4.3.1 Structure of the Co₃O₄ Support, Mo₁ and Pd₁ Active Sites

Experimentally, the single-atom dispersion of Pd₁ and Mo₁ sites were confirmed by in situ EXAFS during anisole HDO at 150 °C. Upon deconvoluting the Fourier-transformed r -space spectra of EXAFS, Pd cations were found to have 2.09 ± 0.28 O atoms in their first shell at 2.23 ± 0.02 Å, and Mo cations were found to have 3.20 ± 0.71 O atoms in their first shell at 1.72 ± 0.01 Å. The crystallinity of the Co₃O₄ support was confirmed by x-ray diffraction (XRD) as well as ex situ TEM of the spent catalyst.

To simulate the HDO of anisole over the Mo₁+Pd₁/Co₃O₄ catalyst, we first optimized the active site geometries. Due to the low surface atomic fractions of both Mo₁ and Pd₁ in this catalyst, we modelled the two sites separately on Co₃O₄. As TEM images of the spent Mo₁+ Pd₁/Co₃O₄

catalyst showed that the (111) surface is the most prevalently exposed termination, the (111) surface of Co_3O_4 was chosen to represent the support. In the previous chapter, we constructed a thermodynamic model for the structure of the $\text{Co}_3\text{O}_4(111)$ surface under both reducing and oxidizing conditions, validated our models by comparing the calculated surface O-H vibrations to those measured by in situ and ex situ IR spectroscopy of Co_3O_4 , and predicted the surface structure of $\text{Co}_3\text{O}_4(111)$ under typical reactive gas environments.¹⁷² Under the catalytic conditions of anisole HDO, the $\text{Co}_3\text{O}_4(111)$ surface was found to be heavily hydroxylated (7.11 OH/nm^2 , see **Figure C.1**). A series of Pd_1 and Mo_1 were simulated and compared (**Figure C.2 and C.3**). In these conditions, the Pd_1 active site is formally in a (+II) oxidation state, coordinated to two hydride ligands and two surface O atoms in a square planar geometry (See **Table C.1** and **Section C.2** for the assignment of formal oxidation states). For the Mo_1 site, although the mono-oxo-molybdenum site is the most stable configuration, we selected a 3-fold coordinated substituted Mo site as the starting point because it is only mildly metastable by 0.27 eV under low anisole conversion, and the highly coordinated Mo sites are rather inert as shown in studies on the activation of CH_4 over $\text{MoO}_3/\text{SiO}_2$.¹⁷³ This Mo_1 site was generated by replacing one surface Co with Mo and removing one lattice OH plus one H from another adjacent OH (**Section C.1**).

4.3.2 The Mechanism of Anisole HDO over Pd₁/Co₃O₄(111)

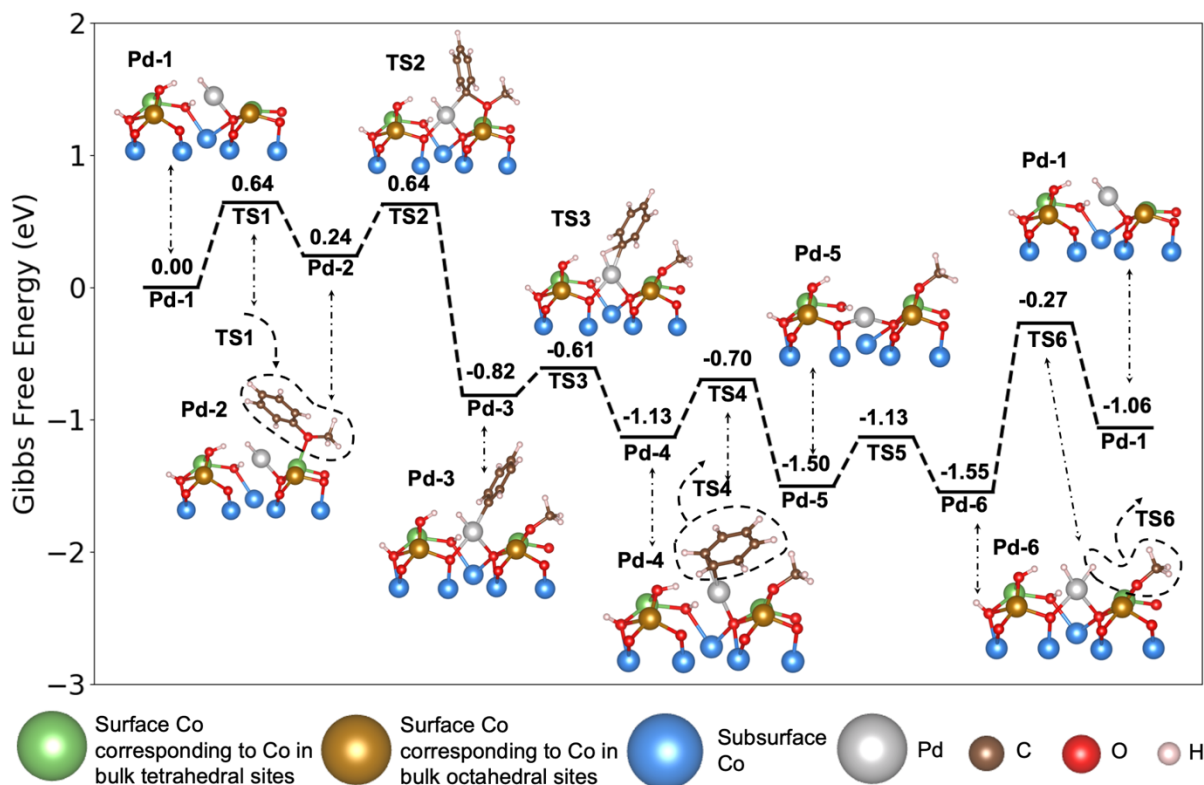


Figure 4.1 The Gibbs free energy pathway for anisole HDO over the Pd₁ site show that the methanol formation controls the energetic span. Anisole HDO over only the Pd₁ site takes advantage of a single O vacancy near the Pd₁. The energetic span of the reaction mechanism is 1.28 eV, between the PdH₂ intermediate (Pd-6) and the transition state for the desorption of methanol (TS6). See text for description. Geometries of all intermediate and transition states are shown in **Figure C.4**.

Next, to compare the anisole HDO activity of the catalysts, we first examined the reaction mechanism over the Pd₁ site alone. We found the HDO of anisole to occur at the interface between the Pd₁H₂ site and the hydroxylated Co₃O₄(111) support (**Figure 4.1**). Similar to some reported reaction mechanisms on metal oxide-containing catalysts, the mechanism over Pd₁ leverages an O

vacancy in Pd₁'s surrounding.¹⁷⁴⁻¹⁷⁶ We start the cycle not at the most stable and abundant Pd₁-H₂ structure, but with a Pd₁ site containing a single hydride (H) ligand and an O vacancy (O_v) in the vicinity of the Pd₁ active site, generated from the recombination of a hydride ligand and a hydroxyl or alkoxy species on the support (Pd-1 on **Figure 4.1**). Formally, the Pd₁H₁ complex is closest to an oxidation state of (-I) (**Table C.1 and C.3**). The more stable Pd₁H₂ site is formed later in the catalytic cycle. In the first step, the anisole reactant is adsorbed at the O vacancy near Pd₁ (Pd-2). The activation Gibbs free energy of this step (0.64 eV) is estimated from the kinetic theory of gases (see **Section C.5** for derivation. Note that a similar derivation was also performed by Cohen and Vlachos⁶²). By crossing a 0.40 eV barrier from Pd-2 to TS2 in **Figure 4.1**, the adsorbed anisole dissociates by breaking its C₆H₅-OCH₃ to form a phenyl (C₆H₅) ligand on Pd₁H₁ and a methoxy (OCH₃) group (Pd-3 in **Figure 4.1**). The key C-O cleavage hence occurs at the interface between the single atom and the oxide, the C atom going to Pd₁ and the O atom filling the nearby vacancy on the support. In other words, the support plays a major role to complement the reactivity of the Pd cation in the C-O cleavage transition state (TS2). The Pd centre is oxidized in this step from Pd₁H₁ (-I) to Pd (+II).

The intramolecular hydrogenation of the C₆H₅ group by the H ligand is expectedly easy, requiring only 0.21 eV from Pd-3 to TS3, reducing the Pd (+II) centre to Pd (0). After the desorption of benzene, H₂ replenishes the H ligands on the Pd₁ site, oxidizing the Pd (0) centre back to Pd (+II). The formation of PdH₂ proceeds with a small barrier of 0.37 eV from Pd-5 to TS5. Since no potential energy barrier was found for the dissociation of H₂, the free energy barrier for this step is purely comprised of entropy losses corresponding to a collision theory adsorption rate. Clearly, as anticipated, H₂ dissociation (Pd-5 to Pd-6) is easy on the Pd₁ site and is not a rate determining step at all. Pd₁H₂ (Pd-6) is the square-planar Pd₁ active site mentioned previously.

Finally, one H ligand reacts with the adjacent OCH₃ group through the transition state (TS6) to form methanol and restore the formally (-I) Pd₁H₁ site, closing the catalytic cycle. No potential energy barrier was found for this step, and the barrier was estimated using collision theory. Notably, the formation and desorption of methanol from Pd₁H₂ and a nearby OCH₃ group through TS6 requires a rather large Gibbs free energy barrier of 1.28 eV.

4.3.3 The Mechanism of Anisole HDO over $\text{Mo}_1+\text{Pd}_1/\text{Co}_3\text{O}_4(111)$

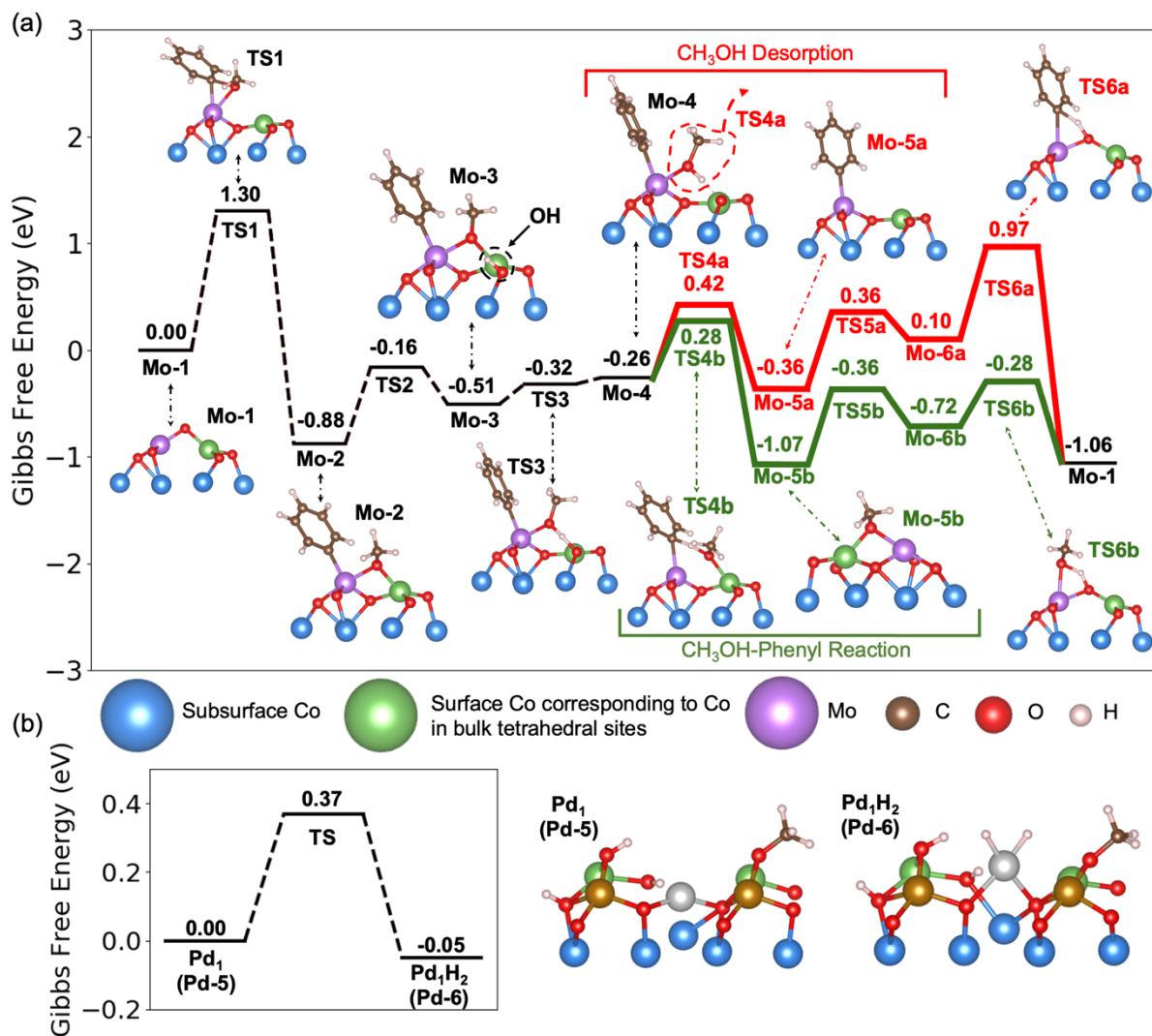


Figure 4.2 The Gibbs free energy pathway for anisole HDO over the Mo_1+Pd_1 site. (a) Anisole HDO over the Mo_1 site assisted by H spillover formed on Pd_1 site. All structures in the reaction pathway are listed in Figure C.4 and C.5. The energetic span of the reaction mechanism is 1.31 eV under low conversion (1%), between the state Mo-5b and the transition state for the dissociation of the anisole molecule. After dissociation of anisole, a methanol molecule is formed first by reacting OCH_3 with surface OH generated by spillover. The methanol molecule could then desorb (pathway in red) or donate its H to the phenyl group and form benzene (pathway in green). The

formation of benzene by reaction between methanol and the phenyl ligand is kinetically preferred over methanol desorption. (b) Gibbs free energy barrier for the dissociation of molecular H₂ on the Pd₁ site.

We explored next the HDO of anisole over the teamed single-atom Pd₁+Mo₁/Co₃O₄ catalyst, where reactivity on the Mo₁ site is assisted by the Pd₁ site for H₂ dissociation and H spillover on the support (**Figure 4.2**). Since this sub-coordinated Mo₁ site appears to have very little steric hindrance, we found that the C_{ring}-O bond is cleaved through oxidative addition. In the transition state (TS1), the C_{ring}-O bond is stretched to 1.76 Å and forms a triangle with the Mo₁ centre. This step produces a C₆H₅ fragment whose carbon atom binds to a Mo₁ and an OCH₃ fragment whose O atom bridges over Mo₁ and its neighbouring Co (Mo-2). In combination, this step raises Mo's formal oxidation state from (+III) to (+IV) (see **Table C.3 and C.5** for assignment). The activation Gibbs free energy to break the C_{ring}-O bond in the oxidative addition step is 1.30 eV (TS1), accounting for the loss of gas-phase entropy upon adsorption. Here again the Co atoms on the support play a role, although not in the C-O bond cleavage TS1 but rather in the stabilization of the product. To continue the reaction, the C₆H₅ and OCH₃ fragments must be hydrogenated. The dissociation of H₂ over Pd₁ only requires crossing a Gibbs free energy barrier of 0.37 eV (**Figure 4.1 and 4.2b**). Other sites present on the catalyst were also considered for the dissociation of H₂, but they were found to be much less active than the Pd₁ site. Accounting for the translational and rotational degrees of freedom, the dissociation of H₂ on the hydroxylated Co₃O₄(111) substrate is estimated to have a 1.62 eV Gibbs free energy barrier, while the barrier is 2.39 eV over the Mo₁ site (**Figures C.6 and C.7**). Hence, for the teamed Pd₁+Mo₁ catalyst,

dissociation of H_2 must happen on Pd_1 , while the hydroxylated $Co_3O_4(111)$ substrate acts as a H adsorbate reservoir, where surface H is in equilibrium with H_2 gas (**Figure 4.2b**).

Spillover of H across the Co_3O_4 support surface occurs through a Grotthuss type motion involving metastable water intermediates and the Co_3O_4 surface itself as an electron reservoir.¹⁷⁷ The H spillover event on $Co_3O_4(111)$ presents an electronic energy barrier of 0.63 eV (**Figure C.8**) which is markedly lower than that of the C-O bond cleavage at Mo_1 (**Figure 4.2a**). In our pathway in **Figure 4.1a**, the whole process of H_2 adsorption and spillover is lumped in a single effective step where a proton and electron are brought close to the Mo_1 site (forming Mo-3), with a net Gibbs free energy barrier of 0.72 eV and a Gibbs free energy of reaction of +0.37 eV. A detailed description of the H spillover mechanism on the catalyst surface is presented in **Figure C.8 and Section C.3**.

After the transfer of H, the OCH_3 group bridging over Mo and Co reacts with the transferred H to produce a methanol molecule. The methanol molecule can either desorb or further react with the C_6H_5 ligand. Let us first explore the steps following the desorption of methanol (pathway in red in **Figure 4.2**). From collision theory rate of adsorption/desorption, methanol can be desorbed by crossing a 0.68 eV Gibbs free energy barrier (TS4a, see **Section C.5** for derivation). Then one more H may be transferred to the O bridging between Mo and Co to continue the reaction (Mo-6a). In this step, the Mo is reduced from (+IV) to (+III). By crossing a 0.87 eV Gibbs free energy barrier (TS6a), this bridging OH group reacts with the C_6H_5 ligand to form a free benzene molecule, storing the Mo_1 active site (Mo-1, most-right side of **Figure 4.2**). This step couples a proton transfer from the OH group and an electron transfer from the substrate.

In another sub-pathway (in green) starting from Mo-4, the methanol formed by TS3 may rotate and react with the C_6H_5 ligand to form a benzene molecule and a bridging OCH_3 group, with

a 0.54 eV barrier, which is slightly smaller than the desorption barrier of methanol (0.68 eV from Mo-4 to TS4a). The Mo₁ centre is formally reduced in this step from (+IV) to (+III). The near-linear configuration of the C_{ring}, H, and O atoms in this transition state (TS4b in **Figure 4.2**) resembles that for σ bond metathesis.¹⁷⁸ The methoxy group acts as a relay for the proton from the oxide surface to the phenyl fragment. Due to the thermodynamic stability of the bridging OCH₃ group in TS4b, the formation and desorption of a free benzene molecule is much more exergonic than the desorption of methanol (Mo-5b versus Mo-5a). After desorption of benzene at Mo-5b, to close the catalytic cycle, one more H is brought to Mo₁ by spillover. The bridging OCH₃ group (Mo-6b) is re-hydrogenated by crossing a 0.44 eV barrier (TS6b) to methanol which desorbs and restores the Mo-1 site. Interestingly, the net free energy barrier to hydrogenate OCH₃ on the Mo₁ site (0.79 eV, from Mo-5b to TS-6b), teamed with Pd₁ to supply the H adsorbate reactant, is much smaller than the barrier on Pd₁ alone in **Figure 4.1** (1.28 eV). Overall, this second sub-pathway is kinetically preferred as the relay role of the methoxy group offers a lower barrier for the formation of benzene. In addition to this pathway over the substituted Mo₁ site, the reactivity of a grafted Mo₁ site was also explored (**Figure C.9**). The energetic span over this active site was found to be 1.90 eV, making it rather unreactive.

4.3.4 Microkinetic Simulations of Pd₁/Co₃O₄ and Mo₁+Pd₁/Co₃O₄

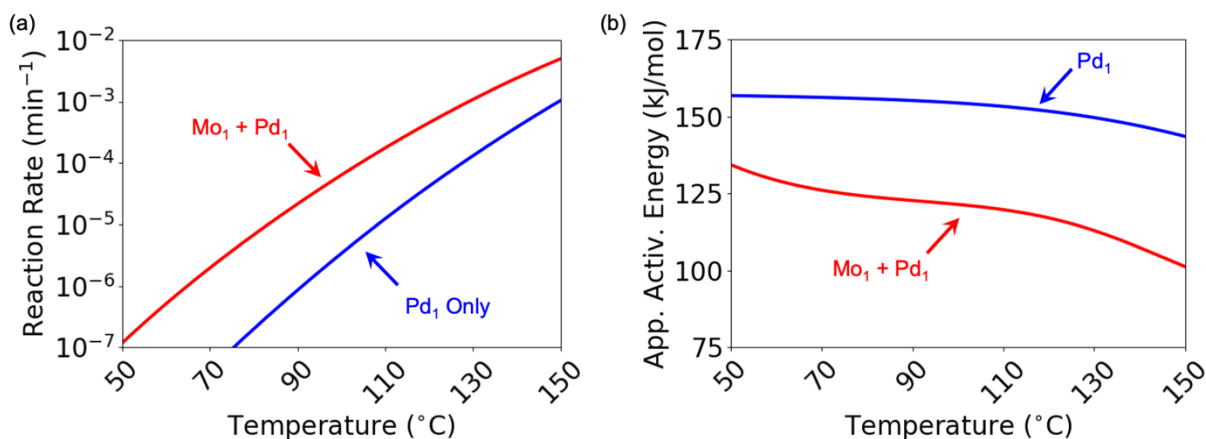


Figure 4.3 Microkinetic simulations show that the teamed Mo₁+Pd₁ catalysts is more active than Pd₁ for the HDO of anisole. As the Gibbs free energy spans of anisole HDO over Pd₁ only and Mo₁ assisted by H spillover are similar, microkinetic simulations were performed to compare the HDO activity over only Pd₁ sites and over Mo₁ sites with H provided by Pd₁. (a) In the temperature range of 50-150 °C and 1% anisole conversion, the Mo₁+Pd₁/Co₃O₄ dual site catalyst is more active than the Pd₁/Co₃O₄ single-site catalyst, and (b) the apparent activation energy of the HDO reaction over Mo₁ assisted by H spillover is smaller than that over only Pd₁ in this temperature range as well. The decrease of the apparent activation energy with temperature is due to the depletion of surface intermediates.

Experimentally, kinetic tests found that Mo₁+Pd₁/Co₃O₄, exhibits nearly 100% conversion of anisole at 150 °C, with an 83% selectivity for benzene. For compositions where Pd atoms in Mo₁+Pd₁/Co₃O₄ are singly dispersed (0.01~0.25 wt% Pd), the anisole conversion and benzene selectivity at were found to be insensitive to Pd loading. Without Pd, the Mo₁/Co₃O₄ catalyst was found to be nearly inactive for anisole HDO. At 150 °C, the conversion was found to be below

10% with a selectivity of about 40% for benzene. Finally, the Pd₁/Co₃O₄ catalyst was found to perform better than Mo₁/Co₃O₄ but worse than Mo₁+Pd₁/Co₃O₄. At 150 °C, the conversion of anisole was found to be 88 % at 150 °C, with a 40% selectivity for benzene.

To establish the link between the DFT-calculated energy profiles and the catalysis experiments, the reactivity of Mo₁+Pd₁/Co₃O₄ over Pd₁/Co₃O₄ and Mo₁/Co₃O₄ was investigated by microkinetic simulations of the HDO of anisole. As the Gibbs free energy barriers of H₂ dissociation over the Co₃O₄(111) substrate and the Mo₁ site are 1.62 eV and higher, the Mo₁/Co₃O₄ catalyst is obviously less active than the Pd₁/Co₃O₄ catalyst, where the Gibbs free energy span of the whole reaction is 1.28 eV.⁵⁹ To quantitatively compare the Pd₁/Co₃O₄ and Mo₁+Pd₁/Co₃O₄ catalysts, we developed microkinetic models for the proposed reaction mechanisms to quantify the rates of anisole HDO (**Sections C.7**).^{65, 171} These simulations show that the Mo₁ site on the Pd₁+Mo₁/Co₃O₄ catalyst is the main contributor to the overall catalytic activity with the assistance of the Pd₁ site to activate H₂ molecules (**Figure 4.3a**). The rate of anisole HDO over Mo₁+Pd₁/Co₃O₄ was found to be higher than that over Pd₁/Co₃O₄ by ~one order of magnitude in the temperature range 50-150 °C (**Figure 4.3a**). The energetic spans of the two catalysts are very similar, but the number of Mo sites on Mo₁+Pd₁/Co₃O₄ is much larger than the number of Pd sites on Pd₁/Co₃O₄, making the Mo₁+Pd₁/Co₃O₄ catalyst more reactive overall (see also **Section C.6**). Correspondingly, the apparent activation energy E_a(app) over Mo₁+Pd₁/Co₃O₄ is markedly lower than that over Pd₁/Co₃O₄, in qualitative agreement with the experimental measurements (**Figure 4.3a**). Experimentally, the apparent activation energy of anisole HDO over Pd₁/Co₃O₄ was found to be 79±5 kJ/mol, while that over Mo₁+Pd₁/Co₃O₄ was found to be 69±6 kJ/mol. Further, during steady state reaction, we note that the most abundant configurations of the Mo₁ and Pd₁ sites on Mo₁+Pd₁/Co₃O₄ (Mo-5b with a bridging OCH₃ and Pd-6 with two adsorbed H in **Figure 4.1**) agree

with the coordination environment of Mo₁ and Pd₁ sites measured by EXAFS. Finally, the link between the active site coverage and catalyst reactivity is also revealed. In the catalytic tests, we found that when both Mo₁ and Pd₁ sites are present on the Co₃O₄ support, the catalyst reactivity is not sensitive to the amount of Pd₁ sites. If Pd₁ sites are present on the same catalyst particle to generate surface H, the Mo₁ sites will have H to perform the reaction, with little dependence on the concentration of Pd₁ sites since H₂ dissociation on these sites is not the rate determining process.

4.4 Conclusion

In summary, we have demonstrated that low-temperature catalysis can be realized by teaming two different single-atom sites which can temporally simultaneously but spatially separately activate two reactants A and B of a reaction [A+B→target product(s)] where an ordinary metal nanoparticle catalyst cannot. The catalyst consisting of teamed single-atom sites, Mo₁+Pd₁/Co₃O₄ was synthesized through two consecutive preparation steps. The Mo₁+Pd₁/Co₃O₄ catalyst is highly active and selective in producing benzene through HDO of anisole at 150°C while supported metal Pd nanoparticle catalysts are inactive at this temperature.

Computational studies uncovered the Gibbs free energy pathways of HDO of anisole on dual site Mo₁+Pd₁/Co₃O₄, and single site Pd₁/Co₃O₄ and Mo₁/Co₃O₄ catalysts. For the teamed single-atom site catalyst, Pd₁ activates H₂ with a barrier of only 0.37 eV while Mo₁ cleaves the C-O bond of anisole. The hydroxylated Co₃O₄ support plays the crucial role of conducting H atoms from the Pd₁ to the Mo₁ site, where the hydrogenation of OCH₃ could be performed with only a net free energy barrier of 0.79 eV instead of 1.28 eV over Pd₁. The analysis of microkinetic models built from proposed reaction mechanisms found that the Mo₁+Pd₁/Co₃O₄ catalyst has both a higher

reactivity and lower apparent activation energy than the Pd₁/Co₃O₄ catalyst. The difference in reactivity also reflects the Mo₁+Pd₁/Co₃O₄ catalyst's insensitivity to the Pd₁ mass fraction, where a small amount of Pd₁ sites is enough to provide a source of atomic hydrogen for the HDO of anisole.

Chapter 5 Hydrogen Dissociation and Spillover Control the Selectivity of 1-Hexyne Hydrogenation over Dilute Pd-in-Au Catalysts

5.1 Introduction

Selective hydrogenation of specific functional groups, such as $-C\equiv C$, $-C=O$, $-NO_2$ and $-COOH(R)$, is an essential process in the petrochemical industries as well as for the production of fine chemicals.¹⁷⁹ Selective hydrogenation of $-C\equiv C-$ is critical in the removal of alkynes from alkene streams, which poison catalysts for downstream polymerization in the petrochemical industry.¹⁸⁰

The partial hydrogenation of alkynes to selectively form alkenes with high conversion is a long-standing challenge in heterogeneous catalysis. Ideally, 100% conversion with 100% selectivity for alkene formation would be achieved. The Lindlar catalyst, which has a high concentration of Pd and is supported on $CaCO_3$ (5 w/w% Pd/ $CaCO_3$), is now widely used for alkyne hydrogenation; however, the selectivity for alkene formation is insufficient.¹⁸¹ The selectivity of the hydrogenation of 2-hexyne to 2-hexene on this catalyst, for example, is only ~88% at ~25% conversion.¹⁸² Alkynes have a stronger binding to the Pd catalyst surface than alkenes; hence, most of the active sites of the catalyst are occupied by the alkyne molecules when the conversion is low.¹⁸³⁻¹⁸⁶ The strong adsorption of alkynes eliminates the alkene molecules from the catalyst surface and prevents over-hydrogenation, which enhances the selectivity.¹⁸⁷ However, when the conversion is high, the selectivity deteriorates. Quinoline and lead are added to the Lindlar catalyst to improve both activity and selectivity.¹⁸² Because lead is extremely toxic, there is a drive to develop a more selective and environmentally-friendly catalyst.

An alternative approach to increase selectivity is to employ dilute alloy catalysts in which an active element, such as Pd, is diluted in a less active metal, such as Cu, Ag or Au.^{22, 188-190} The

concept is that the active metal will initiate the catalytic cycle — H_2 dissociation in the case of hydrogenation — whereas the majority, less reactive metal imparts the selectivity by electronically modifying the dilute dopant, compared to its bulk state. In the single-atom limit, the reactive dopant element Pd in the surface layer of Au(111) or Ag(111) has a narrow d-band due to the poor orbital mixing between the two different species.^{191, 192} This unique electronic structure decreases the covalent binding strength of molecules on the catalyst surface, which could be utilized to facilitate alkene desorption over further reaction for selective alkyne hydrogenation.^{193, 194} Side reactions, such as oligomerization, require a larger ensemble of active metals, and can also be prevented when using dilute alloy catalysts.¹⁹⁵ Thus, by careful tuning, dilute alloys can enhance catalytic performance if these various factors can be understood and related to changes in activity and selectivity.

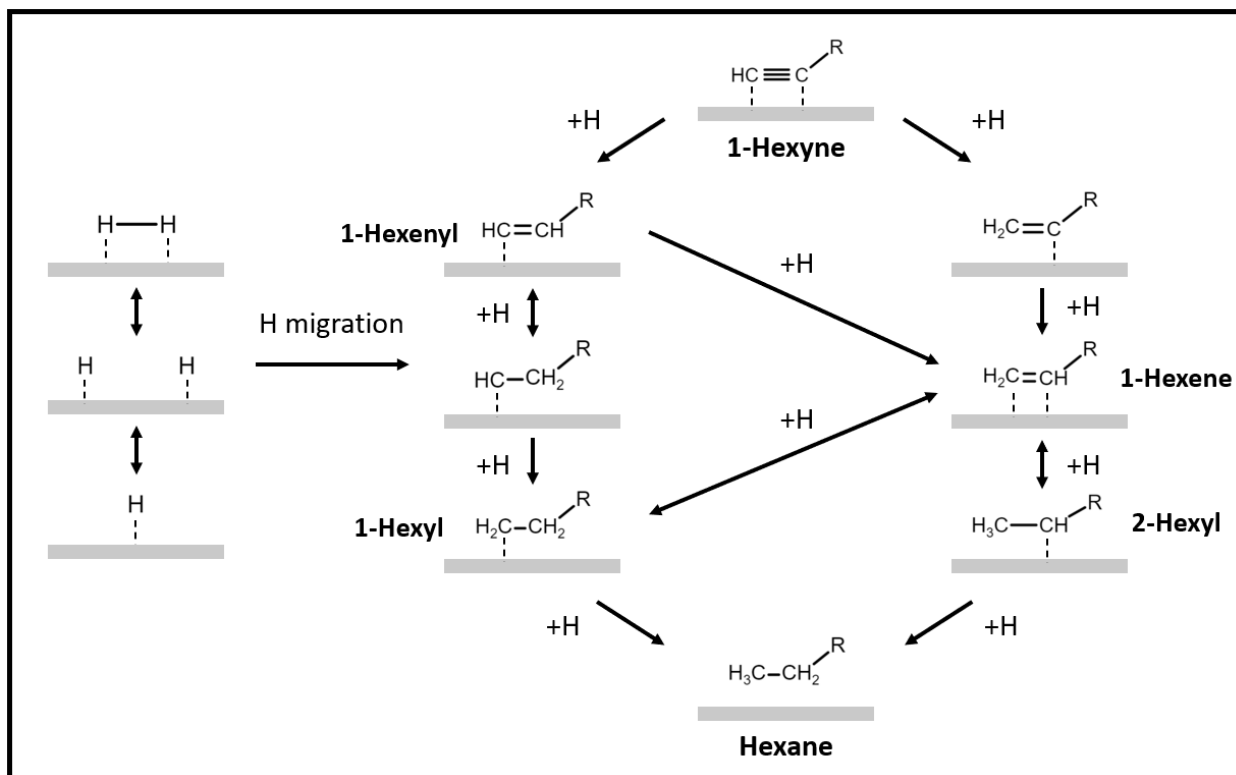


Figure 5.1 A schematic representation of the course of 1-hexyne hydrogenation. The leftmost pathway shows H_2 dissociation and subsequent migration to supply H atoms for 1-hexyne hydrogenation on another $\text{Pd}_1\text{Au}(111)$ site. 1-Hexyne can be hydrogenated either by fully hydrogenating one of the two unsaturated carbon atoms followed by the remaining one (left), or by alternately hydrogenating the two carbon atoms (right). The former is detrimental to selectivity as it skips 1-hexene formation and produces hexyls directly through 1-hexylidene. Double-headed and single-headed arrows indicate reversibility and irreversibility, respectively, based on experiments and theory in this paper.

Previously, dilute alloys of Pd in Cu, Ag or Au were used to improve the selectivity for partial hydrogenation of alkynes.^{22, 196-199} The work herein is motivated by investigations of dilute Pd-in-Au RCT- SiO_2 catalysts for which high selectivity for 1-hexene formation was retained even

at high conversions. In contrast, the selectivity substantially degraded at high conversion for pure Pd. Luneau et al. proposed that the high selectivity for the dilute Pd-in-Au alloys is a consequence of the relatively weak binding of half-hydrogenated 1-hexene (hexyl) to Pd single atoms on the dilute alloy, compared to that of the half hydrogenated 1-hexyne (1-hexenyl), resulting in the preferred β -C–H bond breaking to reform one of the hexene isomers.¹⁸⁶ The rate limiting step of the 1-hexyne hydrogenation was proposed to be the second hydrogenation step of 1-hexyne.

Herein, the origin of the high selectivity at high conversion of 1-hexyne hydrogenation catalyzed by a dilute Pd-in-Au catalyst was explored. Theoretical modeling using density functional theory (DFT) and microkinetic modeling were combined with results from isotopic exchange experiments to establish that the rate for alkyne hydrogenation on Pd single atoms embedded in Au is mainly controlled by H₂ dissociation, whereas C-H bond formation is widely thought to be the sole rate-determining step on pure Pd.²⁰⁰ The sizeable H₂ dissociation barrier and small barrier for the hydrogenation of 1-hexyne compared to that of 1-hexene control the selectivity in 1-hexene, enabling a high selectivity even at high conversion. Experiments and theory show that hydrogenation of 1-hexyne is irreversible. The DFT calculations further indicate that hydrocarbon adsorption (1-hexyne and 1-hexene) is considerably weaker on the dilute Pd-in-Au alloy compared to Pd(111), and that the undesired pathway to form 1-hexylidene is not favored, in agreement with previous work.^{186, 201} These results illustrate a powerful methodology to rationally design new catalysts for selective alkyne hydrogenation using the synergy of advanced theory and carefully-designed experiments.

5.2 Methods

5.2.1 DFT Calculations

All density functional theory (DFT) calculations were performed using the Vienna ab initio simulation package (VASP).⁷³⁻⁷⁵ The projector-augmented-wave (PAW) method was used to describe core electrons, while valence one-electron wavefunctions were developed using a set of plane waves with kinetic energy up to 400 eV.⁷⁸ The second-order Methfessel-Paxton smearing method with the width of smearing set to be 0.2 eV was used to calculate band occupancies.²⁰² Adsorption energies of a single H atom calculated using different exchange-correlation functionals were benchmarked against the low energy recoil scattering and nuclear micro-analysis experiments, and the optPBE-vdW functional was shown to be in closest agreement.²⁰³⁻²⁰⁹ In addition, various density functionals were also benchmarked by comparing their calculated adsorption energy of 1-hexyne to that obtained from TPD (**Section D.5**); the optPBE-vdW functional was also found to perform the best. Thus, only computations performed using this functional were reported.

A 6-layer slab and a (4x4) unit cell were employed to model the Pd₁Au(111) surface for 1-hexyne hydrogenation. It was constructed by replacing one surface Au atom of Au(111) with a single Pd atom. For this cell size, a Monkhorst-Pack generated 7x7x1 K-points grid was used.⁸⁴ During structural optimization, the bottom 4 atomic layers were fixed in the Au bulk position while the upper 2 layers and the adsorbates were allowed to relax until the convergence threshold of <0.03 eV/Å was reached. Transition states were fully optimized using the dimer method, and the quasi-Newton method.¹⁶⁸ All atomic structures reported in this study are visualized using VESTA.⁸⁹ For simplicity, only the translational and rotational entropies of the gaseous species

were considered in the free energy calculations. Zero-point energies and vibrational entropies were neglected for all species.

5.2.2 Microkinetic Simulations

Microkinetic simulations to quantitatively compare the theoretically proposed reaction pathway to the experimental measurements. The kinetic rate parameters were computed from DFT energetics. The forward and reverse rate constants of surface reactions were computed using transition state theory:

$$k_i = \frac{k_B T}{h} \exp\left(\frac{-\Delta G_{\text{act}}^\circ}{RT}\right) \quad (5.1)$$

The rate constants for the adsorption of gas molecules were computed with collision theory for adsorption and desorption steps²¹⁰:

$$k_{\text{ads},i} = \frac{\sigma A_{\text{site}} P^\circ}{\sqrt{2\pi m_i k_B T}} \quad (5.2)$$

where σ is the sticking coefficient, A_{site} is the area of the active site, P° is the standard state pressure, m_i is the mass of the adsorbate, and k_B is Boltzmann's constant. Here, the sticking coefficient was assumed to be 1. The surface area of an active site was calculated using the experimental bulk lattice constants of Pd and Au (3.88 and 4.06 Å, respectively).²¹¹ The atomic fraction of Pd in the alloy is set to 5%. Following Vegard's law, the area occupied by one atom on (111) facet is $7.10 \times 10^{-20} \text{ m}^2$. The corresponding rate constants of desorption were computed using the equilibrium constants of adsorption:

$$k_{\text{des},i} = \frac{k_{\text{ads},i}}{K_{\text{ads},i}} \quad (5.3)$$

$$K_{\text{ads},i} = \exp\left(-\frac{\Delta G_{\text{ads},i}^\circ}{k_B T}\right) \quad (5.4)$$

The rate of elementary step j was computed using the following equation:

$$r_j = k_j^{\text{fwd}} \prod_i \alpha_{i,\text{IS}}^{v_{ij}^{\text{fwd}}} \prod_i \alpha_{i,\text{gas}}^{v_{ij}^{\text{fwd}}} - k_j^{\text{rev}} \prod_i \alpha_{i,\text{IS}}^{v_{ij}^{\text{rev}}} \prod_i \alpha_{i,\text{gas}}^{v_{ij}^{\text{rev}}} \quad (5.5)$$

where k_j^{fwd} and k_j^{rev} are the forward and reverse rate constants, and v_{ij}^{fwd} and v_{ij}^{rev} are the stoichiometric coefficients of reactant i in the forward and reverse directions. The activity α_i was assumed to be the surface coverage fraction θ_i for surface intermediates (including bare sites) and as the ratio of the partial pressure to the standard pressure, P_i/P° , for gaseous species.¹⁷⁰

The time-dependent coverages of surface intermediates are obtained as the steady-state solution of the following system of ordinary differential equations:

$$\frac{d\theta_i}{dt} = -\sum_j v_{ij}^{\text{fwd}} r_j + \sum_j v_{ij}^{\text{rev}} r_j \quad (5.6)$$

Following Wang et al., the steady-state solution is achieved in two steps.⁶⁴ Starting from a bare surface, the equations are first integrated over 500 seconds until they have approximately reached a steady state. The resulting coverages are then used as an initial guess for numerical solution as follows:

$$0 = -\sum_j v_{ij}^{\text{fwd}} r_j + \sum_j v_{ij}^{\text{rev}} r_j \quad (5.7)$$

$$\theta_{\text{Pd}}(t = 0) = \sum_i \theta_{\text{Pd},i} \quad (5.8)$$

$$1 = \sum_i \theta_{\text{Pd},i} + \sum_i \theta_{\text{Au},i} \quad (5.9)$$

Here, $\theta_{\text{Pd},i}$ and $\theta_{\text{Au},i}$ are the surface coverages of species i on Pd and Au sites, respectively.

5.3 Results

5.3.1 H₂ Dissociation on Pd₁Au(111)

Dissociation of molecular hydrogen, a required step for alkyne hydrogenation, takes place on both single Pd atoms and small Pd ensembles on the surface, as described previously.²¹² The

calculations included here focus exclusively on Pd monomers embedded in the surface layer of Au(111), hereafter referred to as Pd₁Au(111), because they predominate on the Pd₄Au₉₆ catalyst investigated experimentally.²¹² The enthalpy barrier for H₂ dissociation on the isolated Pd atom is 0.30 eV. The Gibbs free energy (G) barrier is 0.86 eV under the reaction conditions T = 363 K and P(H₂) = 0.2 bar (**Figure D.1**). The resulting structure, with two hydrides bound to the Pd monomer, is metastable with respect to the gaseous H₂ molecules under these conditions.

The migration of one H atom across the Au surface is activated, but the Gibbs free energy of the transition state (TS-M, G=0.82 eV) is lower than that of the H-H dissociation step (**Figure D.1**); hence, the dissociation step is overall rate-limiting for dissociation and migration.²¹² For the purpose of analysis, the H₂ dissociation and H migration steps will be bundled into a single process with an effective enthalpy barrier of 0.30 eV (and effective Gibbs free energy barrier of 0.86 eV). This large barrier is markedly different from the extended Pd surface, on which there is no enthalpy barrier for dissociation and the dissociated H atoms are stable versus gas phase H₂.^{22, 213} The sizeable barrier for H₂ dissociation on Pd₁Au(111) contributes to the improved selectivity of the alloy catalyst for alkyne hydrogenation, as discussed below. Considering the metastable nature of H on the surface, it is assumed in the presentation of the reaction pathways that one of the two H atoms after dissociation will diffuse and react with 1-hexyne adsorbed at another Pd₁Au(111) site, while the second one will recombine with another surface H atom and desorb as molecular H₂. Hence, one H₂ molecule dissociation event is needed every time a H atom is required to form a C-H bond in the model underlying the free energy profiles. This constraint is lifted for the following microkinetic simulations as all elementary surface reactions are allowed to happen in parallel.

5.3.2 Hydrogenation Mechanism of 1-Hexyne to 1-Hexene over Pd₁Au(111)

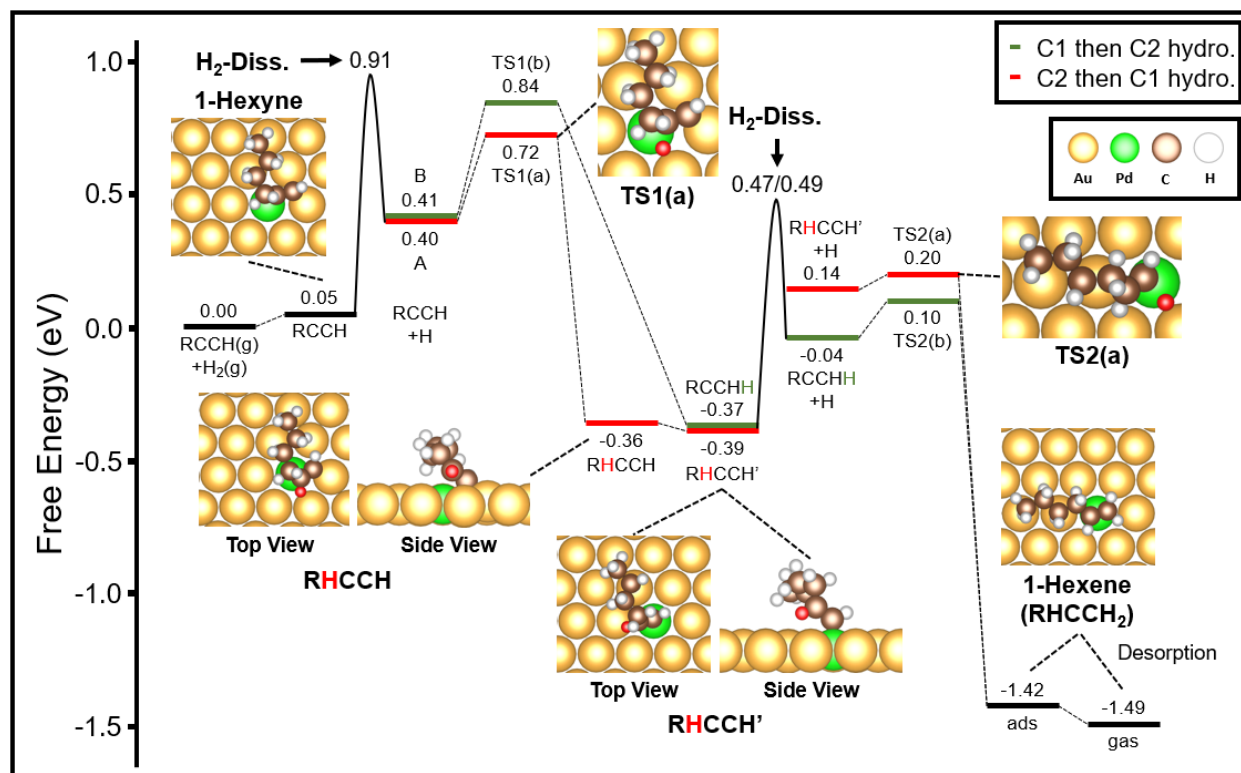


Figure 5.2 Free energy diagram for 1-hexyne hydrogenation to form 1-hexene on the Pd₁Au(111) surface. The butyl group attached to C≡C bond is abbreviated as R. All species are chemisorbed, unless indicated by (g) for gas phase species. The green and red pathways represent the hydrogenation of the terminal carbon atom (C1) and the carbon atom attached to the butyl group (C2), respectively, in the first reaction step, followed by the hydrogenation of the remaining carbon atom. The newly added H atoms are indicated in red or in green. Reaction conditions are: T = 363 K, P(H₂) = 0.2 bar, P(C₆H₁₀) = 0.01 bar, P(C₆H₁₂) = P(C₆H₁₄) = 0.001 bar.

Hydrogenation of 1-hexyne to form 1-hexene on Pd₁Au(111) is irreversible and is limited by H₂ dissociation (**Figure 5.2**). The first step, adsorption of 1-hexyne on the Pd₁Au(111) site is favorable with an adsorption enthalpy of -1.16 eV, yielding a slightly positive Gibbs free energy

of adsorption of +0.05 eV, due to the loss of gas phase entropy. As a result, Pd₁Au(111) active sites are partially covered by 1-hexyne, leaving some sites vacant for H₂ activation. Hydrogenation of adsorbed 1-hexyne can occur when a hydrogen atom is supplied to the adsorbed molecule after H₂ dissociation on another Pd₁Au(111) site followed by H migration. The Gibbs free energy barrier for H₂ dissociation and migration is 0.86 eV as described above, resulting in the co-adsorption of the single H atom and the 1-hexyne molecule (RCCH+H) on a single Pd₁Au(111) site. Notably, the adsorption of two separated H atoms on a Pd₁Au(111) site where a 1-hexyne molecule already resides is less energetically favored than on a bare Pd₁Au(111) site ($\Delta G_{\text{ads}} = 0.77$ eV for the former and $\Delta G_{\text{ads}} = 0.55$ eV for the latter), meaning that H₂ dissociation hardly takes place on Pd₁Au(111) sites occupied with one 1-hexyne molecule. Dissociation of H₂ and adsorption of 1-hexyne on two different Pd sites with spillover of one hydrogen through the Au surface towards the 1-hexyne is favored.

There are two pathways for the initial hydrogenation of 1-hexyne: addition of hydrogen to the terminal carbon (C₁) or to the second carbon atom (C₂) of the C≡C bond (**Figure 5.2**). The Gibbs free energy barriers for these first steps are low — 0.43 and 0.32 eV, for H addition to the C₁ and C₂ positions, respectively. The differences in the barriers are attributed to the greater degree of electron donation from the long carbon chain to C₂; hence, the transition state for C₂ hydrogenation (TS1(a)) has a free energy that is 0.12 eV lower than that of the transition state for C₁ hydrogenation (TS1(b)).

The stability of the resulting partially hydrogenated surface species is similar for hydrogenation at either the C₁ or C₂ position (**Figure 5.2**). There are two different adsorption structures of the intermediates formed from C₂ hydrogenation: RHCCH is in an η² binding mode where carbon C₁ is in a Pd-Au bridge site and C₂ is atop Pd, whereas RHCCH' is in an η¹ binding

mode where only the C₁ carbon interacts atop the Pd₁Au(111) site (see structures in **Figure 5.2**). The species formed from C₁ hydrogenation, RCCHH, is in an η^1 binding mode, with C₂ interacting atop the Pd₁Au(111) site (**Figure D.2**). An η^2 adsorption structure resulting from C₁ hydrogenation is not stable, which is attributed to steric hindrance.

Hydrogenation of the partially-hydrogenated intermediates, RHCCH' and RCCHH, is favored over the reverse reaction to re-form 1-hexyne on Pd₁Au(111) (**Figure 5.2**). Dehydrogenation has a Gibbs free energy barrier of 1.08-1.21 eV, which is higher than the 0.86 eV barrier for the dissociation of a second H₂ molecule. Once an H atom is co-adsorbed with the partially-hydrogenated intermediates (RHCCH'+H and RCCHH+H), C-H bond formation proceeds with very low activation barriers — 0.06 eV and 0.14 eV, respectively, for RHCCH'+H and RCCHH+H. Therefore, the H₂ dissociation and migration step is again rate limiting. Notably, 1-hexene irreversibly forms, based on the high reverse barrier of at least 1.52 eV. The adsorption of 1-hexene is moderate ($\Delta H = -1.22$ eV, $\Delta G = +0.07$ eV) so that in reaction conditions desorption of 1-hexene is slightly exergonic ($\Delta G_{\text{des}} = -0.07$ eV) and 1-hexene coverage on the catalyst should be low. It should be noted however that the adsorption energies of 1-hexyne and 1-hexene are very similar, so that hydrogenation selectivity is not controlled by adsorption competition between these two species, as it is the case on bulk Pd catalysts. Our further kinetic simulations are hence essential to explain the observed selectivity.

From the DFT free energy profile, the hydrogenation of 1-hexyne to 1-hexene on Pd₁Au(111) is therefore predicted to be irreversible and limited by H₂ dissociation with easy C-H bond formation steps. This behavior of single Pd atoms in Au(111) markedly contrasts with the case of pure Pd catalysts where hydrogen dissociation does not show an enthalpy barrier and the reaction is limited by the C-H bond formation.^{22,200,213}

Another distinctive feature is the rather weak 1-hexyne adsorption on Pd₁Au(111), with an adsorption enthalpy of -1.16 eV and a slightly endergonic nature in the considered temperature and pressure conditions. The adsorption on pure Pd catalysts, on the other hand, is much stronger, with ΔH being -2.33 eV on Pd(111). The selective hydrogenation product 1-hexene shows a similar adsorption enthalpy (-1.22 eV) as 1-hexyne on Pd₁Au(111), while its adsorption on Pd(111) (-1.46 eV) is much weaker than that of 1-hexyne. This suggests that the process controlling selectivity is different on the dilute Pd alloy, compared to bulk Pd catalysts.

5.3.3 Microkinetic Simulations of Catalytic Activity

Microkinetic simulations were used to determine the factors that control the activity and selectivity of the reaction as a function of temperature. The details of the model are summarized in the supplementary information (**Table D.2**). Briefly, the microkinetic simulations were parameterized using kinetic rate constants derived from the DFT energetics presented above. The adsorption rate constants of molecular H₂, 1-hexyne, 1-hexene, and n-hexane were computed using the kinetic theory of gases, while the desorption rate constants were computed as the ratio between the adsorption rate constant and the equilibrium constant of adsorption.

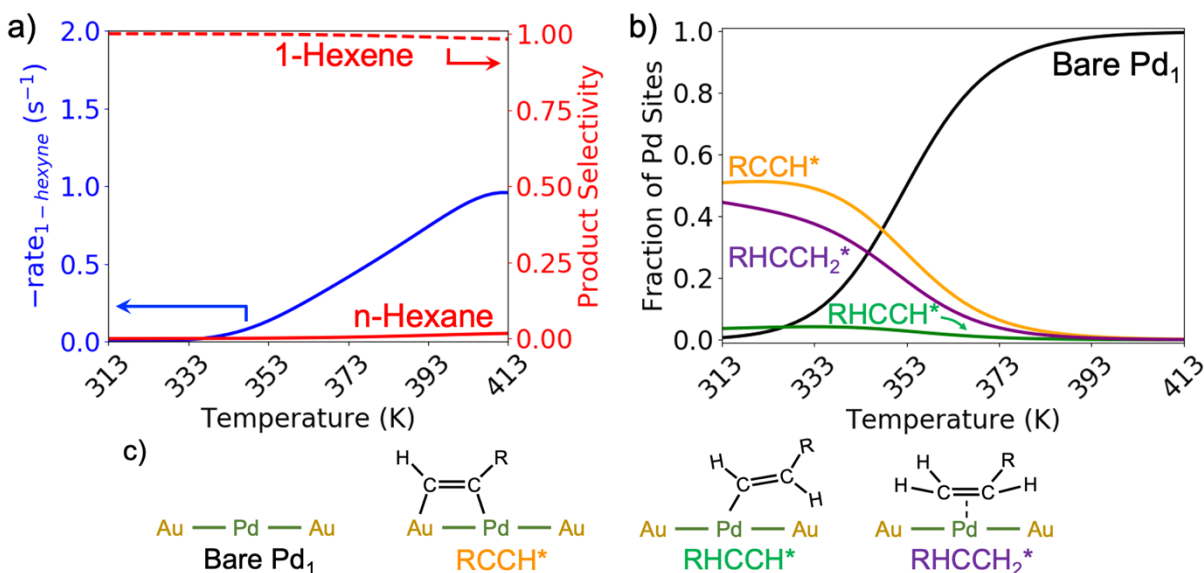


Figure 5.3 Microkinetic simulations of 1-hexyne hydrogenation to 1-hexene and n-hexane under a typical experimental reaction environment corresponding to low (<20%) conversion: $P(\text{H}_2) = 0.2$ bar, $P(1\text{-Hexyne}) = 0.01$ bar, $P(1\text{-Hexene}) = P(\text{n-Hexane}) = 0.001$ bar. (a) rate (s^{-1}) for the conversion of 1-hexyne (blue line) and selectivity for the formation of 1-hexene and n-hexane (red lines) as a function of temperature. The selectivity for 1-hexene was found to be above 98% through the temperature range $T = 313 - 413$ K. (b) Steady state fraction of reactive intermediates on Pd₁Au(111) as a function of temperature: adsorbed 1-hexyne (orange line) and 1-hexene (purple line) were found to be the most abundant reactive intermediates until 353 K. (c) Schematics of structures in panel (b).

In the reaction mechanism, the hydrogenation of carbonaceous intermediates was assumed to only take place on Pd₁Au(111) after H exchange between Pd₁Au(111) sites across the Au substrate. Microkinetic simulations demonstrate that Pd₁Au(111) is selective for 1-hexene formation at both low and high conversions. The rate-limiting step of the hydrogenation is found to be the dissociation of H_2 , which is consistent with the free-energy-based analysis and contrasts

with nanoparticle Pd catalysts. The kinetic orders of the reactants (1 for hydrogen and ~ 0 for hexyne) and the apparent activation energy are also in close agreement with the experimental results.^{186, 201}

The rate of 1-hexyne hydrogenation was evaluated under a typical experimental reaction environment at low conversion [$T = 313\sim 413$ K, $P(\text{H}_2) = 0.2$ bar, $P(1\text{-Hexyne}) = 0.01$ bar, $P(1\text{-Hexene}) = P(\text{n-Hexane}) = 0.001$ bar]. 1-Hexyne starts to react at 333 K. At 373 K, the rate of selective hydrogenation to 1-hexene is 0.42 s^{-1} , while the rate of complete hydrogenation to n-hexane is 0.0021 s^{-1} (**Figure 5.3**). Overall, in the temperature range of $T = 313 - 413$ K and low 1-hexyne conversion, the selectivity for the formation of 1-hexene was found to be consistently above 98%. The $\text{Pd}_1\text{Au}(111)$ active sites were found to be largely covered by adsorbed 1-hexyne and 1-hexene below 353 K, but become mostly bare above this temperature (**Figure 5.3b**). At up to 90% 1-hexyne conversion, the selectivity of 1-hexene remains high ($>70\%$), in agreement with experimental findings (**Figure D.4**).¹⁸⁶

For the formation of 1-hexene from 1-hexyne, the C_2 atom was found to be hydrogenated first, in agreement with the Gibbs free energy-based analysis (**Figure D.5**). The formation of 1-hexenyl and 1-hexene was exothermic and irreversible: the reversibility factor, defined as the ratio between the reverse and forward rates of an elementary step with a positive rate ($r_{\text{rev}}/r_{\text{fwd}}$), is below 10^{-4} in the whole considered temperature range.²¹⁴ On the other hand, the formation of 1-hexyl was found to be partially reversible in the temperature range, with a reversibility factor ranging from ~ 1 at 313 K to 0.46 at 413 K. Moreover, the formation of the 1-hexylidene intermediate, and then hexyl and hexane were found to be unfavorable at all temperatures (**Figure D.5b**).

Experimentally, the irreversibility of the hydrogenation of 1-hexyne to 1-hexene was checked by the reacting 1-hexyne with D₂ over a raspberry colloid-templated (RCT) SiO₂ supported dilute Pd-in-Au catalyst. The bimetallic Pd/Au nanoparticles consist of 4 at% Pd and 96% Au (Pd₄Au₉₆), with a total metal loading of 4.2 wt%. The absence of significant HD and deuterated 1-hexyne confirmed the hydrogenation of 1-hexyne to be irreversible. Further the decrease of steady state 1-hexyne conversion from 10.6% to 4.6% upon switch from H₂ to D₂ agree with the DFT result in that H₂/D₂ is the rate-limiting process in the hydrogenation of 1-hexyne.

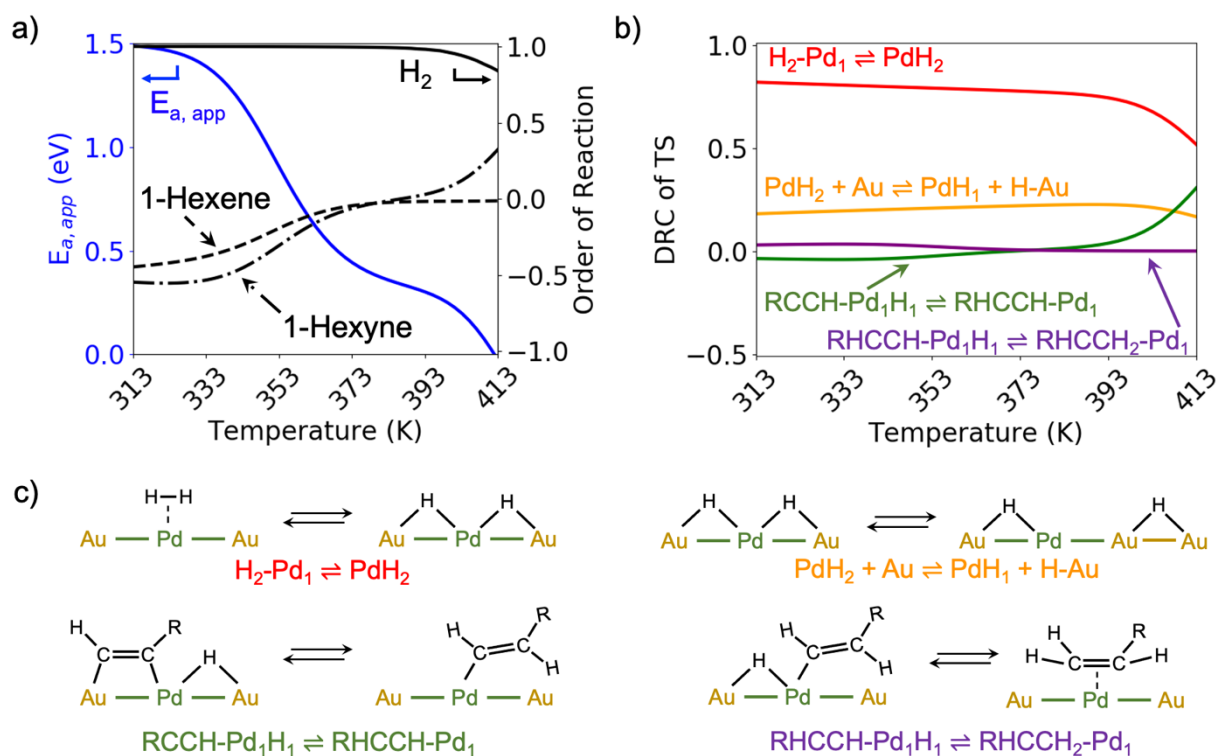


Figure 5.4 Analysis of the kinetics for hydrogenation of 1-hexyne shows H₂ dissociation to be the rate-controlling step. (a) Apparent activation enthalpy (blue line) and kinetic orders of H₂ (black solid line), 1-hexyne (dot-dashed line) and 1-hexene (dashed line) for the hydrogenation of 1-hexyne as a function of temperature. The apparent activation enthalpy of the reaction progressively

decreases in the temperature range $T = 313 - 413$ K, while the orders of 1-hexyne and 1-hexene increase. (b) Degree of rate control (DRC) of various transition states as a function of temperature. The transition state for H_2 dissociation is the main rate-controlling transition state (red line), while the migration of H from the Pd single atom to the Au substrate (orange line) is second in importance. Importantly, C-H bond formation steps (green and purple lines) do not appear to be rate-controlling. (c) Schematics of the four elementary steps shown in panel (b).

The apparent activation enthalpy and kinetic orders of H_2 , 1-hexyne, and 1-hexene for the consumption of 1-hexyne were next computed. Here, under an H_2 rich reaction environment and low 1-hexyne conversion [$P(H_2) = 0.2$ bar, $P(1\text{-Hexyne}) = 0.01$ bar, $P(1\text{-Hexene}) = 0.001$ bar] along the rise of temperature from 313 K to 373 K, the apparent activation enthalpy for the hydrogenation of 1-hexyne was found to decrease from 1.49 eV to 0.44 eV, the orders of 1-hexyne and 1-hexene were found to increase from ~ -0.5 to ~ 0 , and the order of H_2 was found to be roughly constant at 1 (**Figure 5.4a**). The lowering of apparent activation enthalpy and increase in the kinetic orders of 1-hexyne and 1-hexene accompany a sharp increase in the rate of 1-hexyne hydrogenation without compromising the selectivity (**Figure 5.3**). At a reaction temperature of 373 K, the apparent activation enthalpy, order of H_2 , and order of 1-hexyne were found to be 0.44 eV, 1, and -0.04, respectively.

The kinetics of the semi-hydrogenation of 1-hexyne catalyzed by dilute Pd-in-Au alloys have been studied by two groups of authors. For the gas phase hydrogenation of 1-hexyne to 1-hexene at 313 K, Luneau et al. found the rate of 1-hexyne hydrogenation over Pd_4Au_{96} nanoparticles supported on RCT-SiO₂ to depend largely on the partial pressure of H_2 (order of 0.94) but to weakly depend on the partial pressure of 1-hexyne (order of -0.08).¹⁸⁶ The authors

found the apparent activation enthalpy to be 0.39 eV between 303 – 343 K. Based on the similarity of the orders of H₂ and 1-hexyne over Pd₄Au₉₆ (0.94 for H₂ and -0.08 for 1-hexyne) to those over pure Pd (0.99 for H₂ and -0.20 for 1-hexyne), the authors suggested that the rate-controlling step over Pd₄Au₉₆ should be the hydrogenation of 1-hexenyl to 1-hexene.

For the liquid phase hydrogenation of 1-hexyne to 1-hexene, Liu et al. observed similar orders of reaction as Luneau et al. At 298 K, the authors found the rate of reaction to have linear dependence on the pressure of H₂ but no dependence on the concentration of 1-hexyne, corresponding to an order of ~1 for H₂ but ~0 for 1-hexyne.²⁰¹ In the temperature range of 273 ~ 318 K, the authors found the apparent activation enthalpy of the reaction to be 0.43 eV, and due to the similarity of this apparent activation enthalpy to that of the H/D exchange reaction [H₂ + D₂ → 2HD, E_{a,app} = 0.43 eV] over the same catalyst, they suggested that H₂ activation should be the rate-controlling step.

At face value, the calculated apparent activation enthalpy and orders of reaction in this work agree with those measured by Luneau et al., but they are appearing at a higher temperature, shifted by ~60 K. The origin of this shift will be discussed further later.

To determine the rate-limiting process and quantify the relative importance of surface intermediates and transition states, a Degree of Rate Control (DRC) analysis was performed on the rate of 1-hexyne hydrogenation (**Figure 5.4b and D.6**).¹⁷¹ In the temperature range T = 313 K – 353 K, the most abundant surface intermediates are adsorbed 1-hexyne and 1-hexene, but more than half the Pd sites become bare above 353 K (**Figure 5.3b**). This depletion of the surface C₆ intermediates is mirrored in the calculated DRCs of reactive intermediates, where the DRCs of surface intermediates gradually moves to 0 in this temperature range, while the bare surface becomes the rate controlling intermediate (**Figure D.6**). The loss of surface C₆ intermediates

accompany both the decrease of apparent activation enthalpy and increase of C_6 reaction orders in this temperature range. On the other hand, the dissociation of H_2 remains the main rate-controlling transition state for the reaction on the whole temperature range. The calculated apparent activation enthalpy and reaction orders can be rationalized through the DRCs. Following Mao and Campbell, the apparent activation enthalpy can be interpreted as approximately the difference between the enthalpic barrier for H_2 dissociation relative to H_2 gas and the enthalpies of adsorption of 1-hexyne and 1-hexene weighed by the DRCs of their adsorbed states.²¹⁵ Through these analyses, the transition state for the dissociation of H_2 was shown to be the main rate-controlling step for the hydrogenation of 1-hexyne to 1-hexene, in agreement with the qualitative analysis from reaction pathways.

$$r = \frac{K_1 k_{2f} P_{H_2} \theta_{Pd,0}}{1 + K_5 P_{1-HY} + K_{10} P_{1-HE}} \quad (5.10)$$

Rate laws derived by assuming the existence of a single rate-controlling transition state show that there are two cases that yield a rate law that is first-order in H_2 and zero-order in 1-Hexyne: H_2 dissociation or hydrogenation of 1-hexenyl to 1-hexene (**Table D.3**). In these derivations, the transition states of H_2 dissociation, hydrogenation of adsorbed 1-hexyne to 1-hexenyl, or hydrogenation of 1-hexenyl to 1-hexene could be the rate-controlling steps. Comparing the formulated rate laws to the measured orders of reaction, the hydrogenation of 1-hexyne to 1-hexenyl can be immediately ruled out as the possible rate-limiting step because its rate law will always be one half-order in H_2 . On the other hand, the H_2 dissociation-limited rate law (equation 5.10) best fits the results of the microkinetic simulations and the reported kinetic studies.^{186, 201} Under a reaction environment where the coverage of surface C_6 intermediates is low, the rate law indicates that the rate of 1-hexene formation is solely dependent on the partial pressure (or activity) of H_2 . At this limit, the apparent activation energy is simply equal to the enthalpy

barrier for dissociating H_2 over the Pd_1 site. The microkinetic model agrees well with the derived rate law. At $T = 393 \text{ K}$ and low 1-hexyne conversion [$P(\text{H}_2) = 0.2 \text{ bar}$, $P(1\text{-Hexyne}) = 0.01 \text{ bar}$, $P(1\text{-Hexene}) = P(\text{n-Hexane}) = 0.001 \text{ bar}$], the apparent activation energy was found to be 0.30 eV (**Figure 5.4**), very close to the 0.29 eV enthalpy barrier to dissociate H_2 gas over Pd_1 at this temperature.

From the derived rate laws, it also seems possible that the transition state of 1-hexenyl hydrogenation to 1-hexene is the rate-controlling step, if adsorbed 1-hexyne was the most abundant surface intermediate. However, this is unlikely due to two reasons. First, based on the temperature programmed desorption (TPD) experiments of Liu et al. and on gas phase chemical potential calculations, the adsorption of 1-hexyne on Pd sites must be endergonic (**Figure D.7**), resulting in a very low coverage of 1-hexyne under typical reaction temperatures.²⁰¹ Second, the requirement for 1-hexenyl hydrogenation to be the rate-controlling step and for 1-hexyne to be the most abundant surface intermediate imposes a thermodynamically inconsistent constraint on the reaction network. The Gibbs free energy barrier of H_2 dissociation over $\text{Pd}_1\text{Au}(111)$ was found to be 0.86 eV at 363 K and $P(\text{H}_2) = 0.2 \text{ bar}$ (**Figure D.1**). Following the Brønsted-Evans-Polanyi (BEP) relation for the C-H bond formation reactions studied in this work (**Figure D.8**), the hydrogenation of 1-hexenyl by co-adsorbed H must be highly endothermic ($\Delta E \gg 0 \text{ eV}$) to overtake the H_2 dissociation barrier and become the rate-controlling step. Assuming 1-hexyne and 1-hexene have similar adsorption energy, the hydrogenation of adsorbed 1-hexyne by co-adsorbed H to 1-hexenyl then must be extremely exothermic ($\Delta E \ll -2 \text{ eV}$) to ensure thermodynamic consistency of the gas phase reaction. The consequentially exothermic hydrogenation of 1-hexyne to 1-hexenyl must have a very small forward activation energy. In total, the thermodynamic constraint would make 1-hexenyl the most abundant surface intermediate, contradicting the

previous assumption, where 1-hexyne is the most abundant surface intermediate. Based on these reasons, the hydrogenation of 1-hexenyl can be ruled out as the rate-controlling step, further strengthening the proposal that the dissociation of H_2 is the rate-controlling step for the reaction.

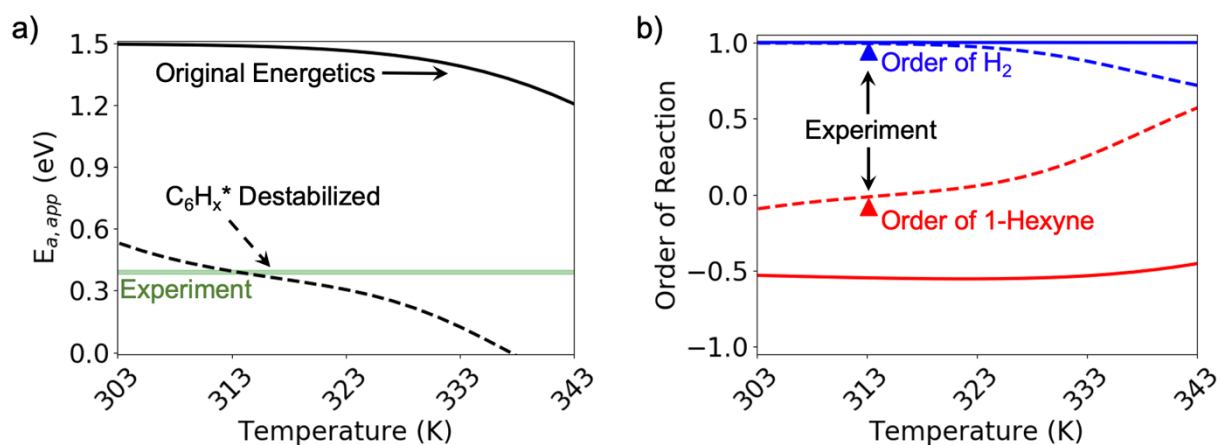


Figure 5.5 A destabilization of hydrocarbon intermediates and transition states energy by 0.2 eV enables an improved agreement with experiment for the kinetic order of 1-hexyne and the apparent activation enthalpy. (a) Apparent activation enthalpy (eV) of 1-hexyne hydrogenation as a function of temperature without (full line) and with (dashed line) destabilization of surface C_6H_x intermediates and transition states. Experimental is shown as a green horizontal bar.¹⁸⁶ (b) Orders of reaction of H_2 (blue) and 1-hexyne (red) as a function of temperature without (full line) and with (dashed line) destabilization of surface C_6H_x intermediates and transition states.¹⁸⁶

One possible origin of the difference between the microkinetic simulations and the kinetic experiments of Luneau et al. could be the calculated adsorption enthalpies of 1-hexyne and 1-hexene. In our calculations, the desorption enthalpies of 1-hexyne and 1-hexene were calculated to be 1.16 eV and 1.22 eV, respectively at 363 K. The values appear overestimated compared to the TPD experiments of Liu et al.²⁰¹ Comparing to the gas phase chemical potentials of 1-hexyne

and 1-hexene (**Figure D.7**), the overestimation of the desorption enthalpies would result in a higher calculated coverage of C_6 intermediates at typical reaction temperatures, 298 – 343 K.

To qualitatively reconcile the differences, a modified microkinetic model was created, where surface intermediate states and transition states containing adsorbed carbonaceous species were destabilized by 0.20 eV (**Figure 5.5**). At 313 K, the apparent activation enthalpy was found to be 0.39 eV, and the order of 1-hexyne -0.01. The calculated apparent activation enthalpy and orders of reaction from this modified model compare much more favorably with the experimental measurements by Luneau et al. (apparent activation enthalpy: +0.39 eV, order of 1-hexyne: -0.08) and Liu et al. (apparent activation enthalpy: +0.43 eV, order of 1-hexyne: ~ 0), while the dissociation of H_2 remains as the main rate-controlling transition state.

5.3.4 Origin of Improved 1-Hexene Selectivity

The Degree of Selectivity Controls (DSC)¹⁷¹ of all surface intermediates and transition states were computed at a typical low-conversion experimental reaction environment [$T = 373$. K, $P(H_2) = 0.2$ bar, $P(1\text{-Hexyne}) = 0.01$ bar, $P(1\text{-Hexene}) = 0.001$ bar] to quantitatively compare the influence of the elementary steps in the reaction network on 1-hexene selectivity. The DSCs of the transition states for H_2 dissociation on Pd_1 and for 1-hexyl hydrogenation to form n-hexane are negative (**Figure 5.6**), meaning that the selectivity for 1-hexene formation is decreased if the free energy of the TS for H_2 dissociation or for 1-hexyl hydrogenation is lowered. The former is justified by the fact that atomic H would become more readily available for 1-hexene hydrogenation when the H_2 dissociation barrier shrinks. The latter is even more natural as it directly controls the formation of the undesired n-hexane product. The calculated DSCs agree well with the Gibbs free energy-based analysis. On the other hand, the transition state with the largest

positive DSC goes to the hydrogenation of 1-hexyne to form 1-hexenyl (**Figure 5.6**). Since the first hydrogenation step of 1-hexyne has a larger activation barrier than the second step, lowering this TS free energy could more significantly increase the yield of 1-hexene and hence the selectivity. It is noted that the DSC analysis is carried out at a condition under which only 11% of all surface Pd sites are occupied by carbonaceous intermediates; thus, the influence of site-competition is negligible (**Figure 5.3b**).

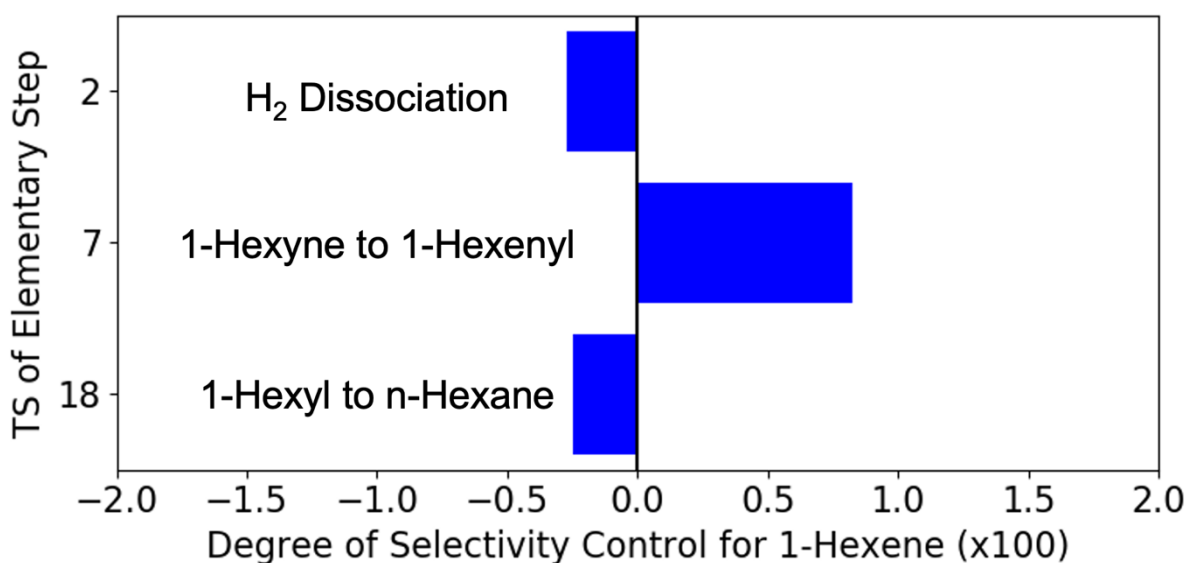


Figure 5.6 The degree of selectivity control (DSC), evaluated at $T = 373\text{ K}$, $P(\text{H}_2) = 0.2\text{ bar}$, $P(1\text{-Hexyne}) = 0.01\text{ bar}$, $P(1\text{-Hexene}) = 0.001\text{ bar}$, of the TS for H₂ dissociation over Pd₁ (**DSC** = -2.75×10^{-3}), 1-Hexyne hydrogenation to 1-Hexenyl (**DSC** = 8.24×10^{-3}), and 1-Hexyl hydrogenation to n-Hexane (**DSC** = -2.46×10^{-3}). The values were multiplied by 100 in the figure. Decreasing the free energy barrier for 1-hexyne hydrogenation to 1-hexenyl increases the selectivity for 1-hexene, while decreasing the free energy barrier of H₂ dissociation and 1-hexyl hydrogenation to n-hexane decreases the selectivity for 1-hexene.

At low conversion, Pd catalysts achieve high selectivity via competitive binding: strong binding of 1-hexyne expels the relatively weakly bound 1-hexene from the catalyst surface. This competitive binding, however, would be lost when conversion becomes higher. The high selectivity of the dilute Pd-in-Au catalyst at high conversion, on the other hand, does not rely on competitive binding, as can be seen from the similar magnitude of adsorption energies of 1-hexyne and 1-hexene. Instead, the selectivity is mainly controlled by the difference in the hydrogenation rates constants between 1-hexyne and 1-hexyl as shown by the DSC analysis. One important factor to slow down 1-hexyl hydrogenations is the high H₂ dissociation barrier which encourages hexyls to proceed in the reverse direction to form hexenes as also demonstrated by van der Hoeven et al. in the case of hexene hydrogenation on the same catalyst. [29] Notably, this sizable barrier is absent on the Pd catalysts. Since the H₂ dissociation barrier is independent of reaction conversion, the selectivity for hexene formation can be preserved even at high conversion. The production of hexyls via hexylidene, which is detrimental to the selectivity as it skips the formation of 1-hexene, is also energetically unfavorable on the alloy catalyst (**Figure D.5**). All these features together contribute to the much improved selectivity of the Pd₁Au(111) catalyst.

One can discuss in more details the differences between the Pd₁Au(111) and bulk Pd(111) catalysts for 1-hexyne hydrogenation. The hydrogenation energy profiles differ in that the surface intermediates and transition states are much more weakly adsorbed on Pd₁Au(111). Compared to Pd(111), adsorbed 1-hexyne is destabilized in free energy by 1.37 eV on Pd₁Au(111), and the first C-H bond formation TS1(a) by a similar amount of 1.33 eV. Hydrogen adsorption is weaker as well, destabilized by 0.49 eV/H atom.²¹⁶ The co-adsorbed state, where both 1-hexyne and H are interacting with Pd₁ is destabilized by 1.87 eV, and hence roughly cumulate the two effects. As a

result, for the elementary C-H bond formation process, the reactant state is more destabilized than the TS, leading to the activation energy being reduced from 0.86 eV on Pd(111) to 0.32 eV on Pd₁Au(111). The observed destabilizations on the single atom alloy^{186, 217-219} mainly stem from reduced active ensemble effects: for example on Pd(111) 1-hexyne binds to 3 Pd atoms, while it binds to 1 Pd and two Au atoms on Pd₁Au(111). The d states of Au are lower in energy, completely occupied, and cannot interact strongly with the adsorbate.²²⁰ Electronic effects are also present since the electronic states on Pd for the single atom alloy are less dispersed in energy than for a surface atom of Pd(111).²²¹ Note however that the d band center for the surface Pd atom have very similar value [-1.69 eV for Pd(111) and -1.65 eV for Pd₁Au(111), **Figure D.9**] so that electronic effects likely originate from the difference in the d band shape. The marked destabilization along the energy profile results in the H₂ dissociation activation energy to be large, and the C-H bond formation activation energy to be small on Pd₁Au(111), with strong positive consequences on the 1-hexyne hydrogenation selectivity, as shown from our kinetic analysis. Since ensemble effects dominate, one can expect that the phenomenon shown here would reasonably pertain for a wide range of single atom alloys.

The concepts obtained in this study can be used to design selective catalysts. One important parameter is the energy barrier for H₂ dissociation, for which we face a compromise between activity and selectivity. Increasing further the H₂ dissociation barrier would decrease the activity (it is the main rate controlling process) while decreasing it significantly could damage the selectivity. We can play however in an interval of favorable barrier values, to find an optimal situation. This can be done by keeping Pd as active metal but changing the host to Ag or Cu.²¹⁸ One other possibility is to change the active metal to Ni. Changing the active metal to Pt does not appear as a good idea, since the H₂ dissociation barrier is much smaller on Pt SAAs in Au, Ag and

Cu.²¹⁸ Larger ensembles of Pd or Ni as dimers or trimers would also markedly decrease the H₂ dissociation barrier, at the expense of selectivity, and should not be an efficient direction of design.

5.4 Conclusion

In this work, our combined theoretical and experimental study shows that, over dilute Pd-in-Au alloy catalysts, the H₂ dissociation elementary step, with a sizeable free energy barrier of 0.86 eV at 363 K and 0.2 bar of H₂, plays a major role to control the activity and selectivity of 1-hexyne hydrogenation. Specifically, our Gibbs free energy based analysis and first-principles microkinetic simulations show that H₂ dissociation is the rate-limiting process for 1-hexyne hydrogenation on Pd₁Au(111) while the C-H bond formation steps proceed with lower barriers. Somewhat more surprisingly, the sizeable H₂ dissociation barrier also favorably impacts the selectivity for partial hydrogenation to 1-hexene, because it slows down the undesired over-hydrogenation to hexane. This is shown by our DSC analysis, which indicates that decreasing the free energy barrier of H₂ dissociation decreases the selectivity for 1-hexene. Other elementary steps are also important for the selectivity: decreasing the barrier for 1-hexyl hydrogenation to n-hexane also decreases the selectivity for 1-Hexene, while decreasing the barrier for 1-hexyne hydrogenation to 1-hexenyl increases it.

This major role of H₂ dissociation in the kinetic control of 1-Hexyne hydrogenation on dilute Pd-in-Au catalysts markedly contrasts with previously studied extended Pd catalysts for which addition of atomic H to the adsorbed alkyne or alkenyl is accepted to be the rate-determining step, and the selectivity is controlled by competitive adsorption of alkyne and alkene. On dilute Pd-in-Au, the selectivity is controlled instead by competition of hydrogenation rates of alkyne and alkene, which maintains a high selectivity even at high conversion. Hence, the energetics and

kinetics of the 1-hexyne hydrogenation mechanism over dilute Pd-in-Au alloy is distinct with respect to bulk Pd catalysts. Our reaction profiles from first-principle calculations and microkinetic modelling also reveal that 1-hexyne hydrogenation to 1-hexene is an irreversible process due to the strongly exothermic nature of the reaction. This claim is validated through the isotopic exchange hydrogenation experiment conducted on Pd_{0.04}Au_{0.96} embedded in RCT-SiO₂.

Another key property of dilute Pd-in-Au alloys is that the adsorption energy of hydrocarbon species is moderate so that the coverage of Pd sites by these hydrocarbon intermediates is low, enabling access and activation of H₂, and preventing poisoning and coking of the catalysts. This is again different from extended Pd catalysts where hydrocarbon species bind strongly and can form coke at high coverage, deactivating the catalyst. Apparent activation enthalpies and reaction orders for dilute Pd-in-Au from our microkinetic modeling are in good agreement with previous experiments, despite a shift of ~60 K in temperature. The temperature shift is attributed to the slight over-estimation of the adsorption energies of the surface species when the xc-functional optPBE-vdW is used. Altogether, this work unprecedentedly demonstrates that the improved selectivity of the dilute Pd-in-Au alloy catalyst is attributed to the sizable H₂ dissociation barrier, and to the small barrier for C-H bond formation from 1-hexyne to 1-hexenyl (smaller than that for C-H bond formation from 1-Hexene to 1-Hexyl). The formation of dilute active species in a less active host metal can therefore be seen as a way to tune the binding energy of reactants, alter reaction profiles and induce distinct kinetic behaviors for an optimal catalytic activity and selectivity. This concept of dilute alloy catalyst is hence a versatile approach to design highly selective heterogeneous catalysts.

Chapter 6 1-Hexene Hydrogenation and Isomerization over Dilute Pd-in-Au

Catalysts

6.1 Introduction

The partial hydrogenation of alkynes and dienes are key processes in the petrochemical and polymer industries.¹⁷⁹ For the production of polymers, trace amounts of alkyne and diene impurities in an alkene-rich feed stream will poison the polymerization catalyst. Typically, Pd catalysts are used to remove the impurities, but suffer from selectivity issues at high alkyne conversion, where the desired mono-alkene product is instead fully hydrogenated to alkane.^{181, 222} Alloying Pd with a second non-reactive metal such as Cu, Ag, or Au has been demonstrated in improving the selectivity for alkenes.^{22, 197-199, 201, 223-225} An important step in further improvement in selective catalysts in alkyne and alkene hydrogenation, lies in understanding how dilute alloys prevent hydrogenation of the mono-alkenes and why they favor alkene isomerization over alkene hydrogenation.

In this study, isotope labeling experiments, DFT calculations, and microkinetic simulations were combined to unravel the reaction mechanism, rate-limiting and selectivity controlling steps of 1-hexene hydrogenation/isomerization over a dilute Au-in-Pd alloy nanoparticle catalyst. This study continues the investigation of the hydrogenation of 1-hexyne to 1-hexene in the previous chapter. Here, the main objective is to understand the favorable selectivity of the alloy for 1-hexene isomerization and its ability to prevent the hydrogenation to hexane. The combined approach provided insight in the reaction mechanism, associated energy barriers, rate-limiting and selectivity controlling processes, and established the key differences between dilute Pd-in-Au alloy and mono-metallic Pd nanoparticle catalysts.

6.2 Methods

6.2.1 DFT Calculations

All density functional theory (DFT) calculations were performed using the Vienna ab initio simulation package (VASP).⁷³⁻⁷⁵ The projector-augmented-wave (PAW) method was used to describe core electrons, while valence one-electron wavefunctions were developed using a set of plane waves with kinetic energy up to 400 eV.⁷⁸ The second-order Methfessel-Paxton smearing method with the width of smearing set to be 0.2 eV was used to calculate band occupancies.²⁰² The exchange and correlation energies were calculated using the optPBE-vdW functional, based on the benchmarking calculations in the previous chapter.²⁰³⁻²⁰⁹ A 6-layer slab and a (4x4) unit cell were employed to model the Pd₁Au(111) surface for 1-hexyne hydrogenation. For this cell size, a Monkhorst-Pack generated 7x7x1 K-points grid was used.⁸⁴ During structural optimization, the bottom 4 atomic layers were fixed in the Au bulk position while the upper 2 layers and the adsorbates were allowed to relax until the convergence threshold of <0.03 eV/Å was reached. Transition states were fully optimized using the dimer and the quasi-Newton method.¹⁶⁸ All atomic structures reported in this study are visualized using VESTA.⁸⁹ For simplicity, only the translational and rotational entropies of the gaseous species were considered in the free energy calculations. Zero-point energies and vibrational entropies were neglected for all species.

6.2.2 Microkinetic Simulations

Microkinetic simulations to quantitatively compare the theoretically proposed reaction pathway to the experimental measurements. The kinetic rate parameters were computed from DFT energetics. The forward and reverse rate constants of surface reactions were computed using transition state theory:

$$k_i = \frac{k_B T}{h} \exp\left(\frac{-\Delta G_{act}^\circ}{RT}\right) \quad (6.1)$$

The rate constants for the adsorption of gas molecules were computed with collision theory for adsorption and desorption steps²¹⁰:

$$k_{ads,i} = \frac{\sigma A_{site} P^\circ}{\sqrt{2\pi m_i k_B T}} \quad (6.2)$$

where σ is the sticking coefficient, A_{site} is the area of the active site, P° is the standard state pressure, m_i is the mass of the adsorbate, and k_B is Boltzmann's constant. Here, the sticking coefficient was assumed to be 1. The surface area of an active site was calculated using the experimental bulk lattice constants of Pd and Au (3.88 and 4.06 Å, respectively).²¹¹ The atomic fraction of Pd in the alloy is set to 5%. Following Vegard's law, the area occupied by one atom on (111) facet is $7.10 \times 10^{-20} \text{ m}^2$. The corresponding rate constants of desorption were computed using the equilibrium constants of adsorption:

$$k_{des,i} = \frac{k_{ads,i}}{K_{ads,i}} \quad (6.3)$$

$$K_{ads,i} = \exp\left(-\frac{\Delta G_{ads,i}^\circ}{k_B T}\right) \quad (6.4)$$

The rate of elementary step j was computed using the following equation:

$$r_j = k_j^{fwd} \prod_i \alpha_{i,IS}^{v_{ij}^{fwd}} \prod_i \alpha_{i,gas}^{v_{ij}^{fwd}} - k_j^{rev} \prod_i \alpha_{i,IS}^{v_{ij}^{rev}} \prod_i \alpha_{i,gas}^{v_{ij}^{rev}} \quad (6.5)$$

where k_j^{fwd} and k_j^{rev} are the forward and reverse rate constants, and v_{ij}^{fwd} and v_{ij}^{rev} are the stoichiometric coefficients of reactant i in the forward and reverse directions. The activity α_i was assumed to be the surface coverage fraction θ_i for surface intermediates (including bare sites) and as the ratio of the partial pressure to the standard pressure, P_i/P° , for gaseous species.¹⁷⁰

The time-dependent coverages of surface intermediates are obtained as the steady-state solution of the following system of ordinary differential equations:

$$\frac{d\theta_i}{dt} = -\sum_j v_{ij}^{\text{fwd}} r_j + \sum_j v_{ij}^{\text{rev}} r_j \quad (6.6)$$

Following Wang et al., the steady-state solution is achieved in two steps.⁶⁴ Starting from a bare surface, the equations are first integrated over 500 seconds until they have approximately reached a steady state. The resulting coverages are then used as an initial guess for numerical solution as follows:

$$0 = -\sum_j v_{ij}^{\text{fwd}} r_j + \sum_j v_{ij}^{\text{rev}} r_j \quad (6.7)$$

$$\theta_{\text{Pd}}(t = 0) = \sum_i \theta_{\text{Pd},i} \quad (6.8)$$

$$1 = \sum_i \theta_{\text{Pd},i} + \sum_i \theta_{\text{Au},i} \quad (6.9)$$

Here, $\theta_{\text{Pd},i}$ and $\theta_{\text{Au},i}$ are the surface coverages of species i on Pd and Au sites, respectively.

To evaluate the degree of H/D exchange in 1-hexene, 2-hexene, and n-hexane as a function of 1-hexene conversion, the above microkinetic model was embedded in an isothermal and isobaric plug-flow reactor (PFR). The metal content of the catalyst was assumed to be 4.2 wt%. Each Pd-in-Au nanoparticle in the catalyst was assumed to be a sphere 4.9 nm in diameter, with 5% of all atoms in each particle being Pd.

6.3 Results

6.3.1 Mechanism of 1-Hexene Hydrogenation and Isomerization over Pd₁Au(111)

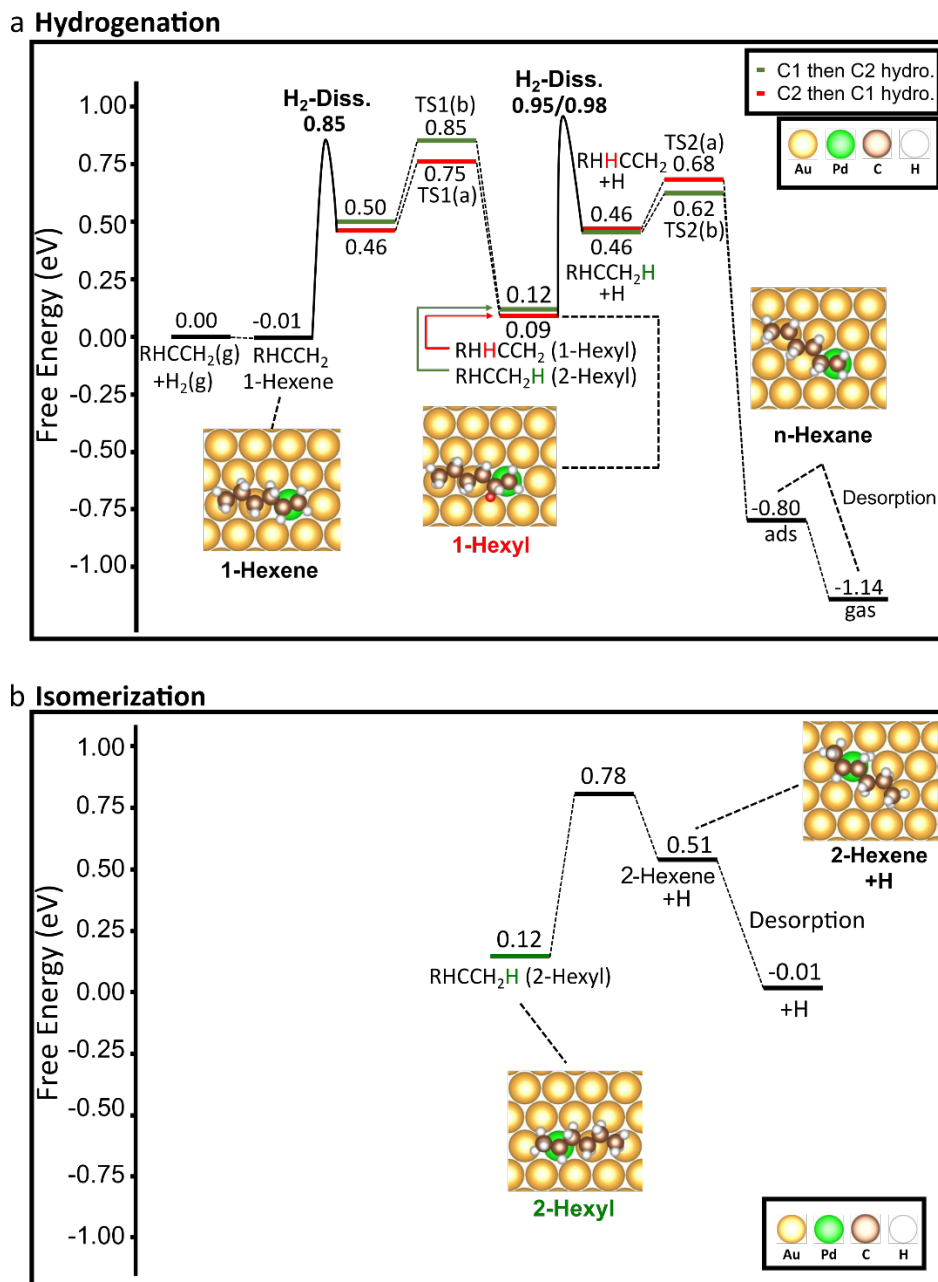


Figure 6.1 Free energy profiles for 1-hexene hydrogenation (a) and isomerization to 2-hexene (b) calculated using DFT. The abbreviation R represents the butyl group attached to the C=C bond. Two different hydrogenation pathways are shown in (a): the green pathway hydrogenates first the

terminal carbon atom of 1-hexene to form 2-hexyl while the red pathway hydrogenates first the carbon atom which is attached to the butyl group R, to form 1-hexyl. Both pathways finish by hydrogenating the remaining unsaturated carbon atom in the hexyl intermediates. The newly-added H atoms to the unsaturated hydrocarbons are denoted in red or in green. (b) shows the isomerization pathway of the 2-hexyl intermediate to 2-hexene. Reaction conditions are: $T = 363$ K, $P(\text{H}_2) = 0.2$ bar, $P(1\text{-hexene}) = 0.01$ bar, $P(2\text{-hexene}) = 0.001$ bar, and $P(\text{n-hexane}) = 0.001$ bar.

Kinetic tests were performed to examine the reactivity and selectivity of 1-hexene hydrogenation/isomerization over the RCT SiO_2 -supported $\text{Pd}_4\text{Au}_{96}$ catalyst, and the findings are summarized here. At 373 K, $\text{Pd}_4\text{Au}_{96}$ nanoparticles were found to preferentially isomerize 1-hexene to 2-hexene and 3-hexene, with only a 11% selectivity for n-hexane at 92% total 1-hexene conversion. When the H_2 reactant is switched to D_2 , the majority product remained 2-hexene and 3-hexene. At lower conversions, the fraction of deuterated products did not exceed the non-deuterated products. Only at very high conversions do they overtake the d_0 products. Catalytic tests with a pure Pd catalyst showed both higher selectivity (33%) for n-hexane and higher degrees of H/D exchange.

The free energy profiles for 1-hexene hydrogenation to n-hexane (**Figure 6.1a**), and for isomerization to 2-hexene (**Figure 6.1b**) reveal that on the Pd_1Au surface the isomerization pathway is favored over hydrogenation to n-hexane. The full set of adsorption configurations of the reactants, intermediates and products corresponding to the states in the energy profiles are provided in **Figure E.1**. Both the hydrogenation and isomerization pathway start with the adsorption of 1-hexene on the Pd_1 site, which is thermo-neutral in the considered conditions. This is followed by hydrogen dissociation on a different Pd site and migration of a H atom to the Pd site where the 1-hexene is bound, a process with an overall barrier of 0.86 eV. (**Figure D.1**)

Subsequent addition of the dissociated hydrogen atom on either the first or second carbon atom leads to the formation of the 2-hexyl (green) and 1-hexyl (red) intermediate, respectively. Next, the hexyl intermediates can be hydrogenated by spillover of another H atom to the Pd site and adding a H atom to the remaining carbon radical/remaining unsaturated carbon of the hexyl intermediate to form n-hexane. The effective free energy barrier for this process is 0.86 eV (H_2 -dissociation). Alternatively, the reverse process from the hexyl intermediates to 1-hexene via reductive H-elimination can occur. The effective barrier for this reverse process is 0.67-0.73 eV (for 1-hexyl to TS1(a) and 2-hexyl to TS(b), respectively) and hence is lower than the effective barrier for hydrogenation to n-hexane. The barrier for isomerization to 2-hexene is even a bit lower, 0.66 eV, indicating that the formation of both 1- and 2-hexene is favored over the formation of n-hexane. Hence, the DFT calculations indicate that on the Pd_1Au surface backward dehydrogenation to form a hexene isomer is favored over hydrogenation to n-hexane, and that isomerization to 2-hexene is favored over the re-formation of 1-hexene.

6.3.2 Microkinetic Simulations of 1-Hexene Hydrogenation and Isomerization over $Pd_1Au(111)$

The reactivity and product selectivity of the calculated reaction mechanism for $Pd_1Au(111)$ was evaluated under operating temperature and pressure using microkinetic models, which were parameterized using DFT-calculated reaction energies and barriers from **Figure 6.1**. In brief, the microkinetic model of 1-hexene hydrogenation/isomerization consists of four groups of reactions: i) the dissociation of H_2 on a vacant Pd site and the exchange of atomic H between Pd sites, eventually also occupied by the hydrocarbon intermediate via spillover on Au, ii) the hydrogenation of 1-hexene to n-hexane through either the 1-hexyl or iii) 2-hexyl intermediate, and

iv) the isomerization of 1-hexene to 2-hexene through the 2-hexyl intermediate. The hydrogenation of hydrocarbon intermediates was assumed to take place only after hydrogen exchange. **Table E.1** summarizes all elementary steps, their kinetic rate constants, Gibbs free energies of reaction and activation energies. At low 1-hexene conversion (fixed partial pressures of $p(\text{H}_2) = 0.2$ bar, $p(1\text{-hexene}) = 0.01$ bar, and $p(2\text{-hexene}) = p(\text{n-hexane}) = 0.001$ bar) the conversion of 1-hexene started at 333 K reaching a 1-hexene consumption rate of 0.331 s^{-1} at 373 K (**Figure 6.2a**), with 3% of the 1-hexene being isomerized to 2-hexene, and the rest hydrogenated to n-hexane (**Figure 6.2a**). 93% of the produced n-hexane formed through the 1-hexyl intermediate, while the rest proceeded through the 2-hexyl intermediate. The discrepancy between the calculated product selectivity to preferential n-hexane formation, and the experimental product selectivity to 2-hexene will be discussed later.

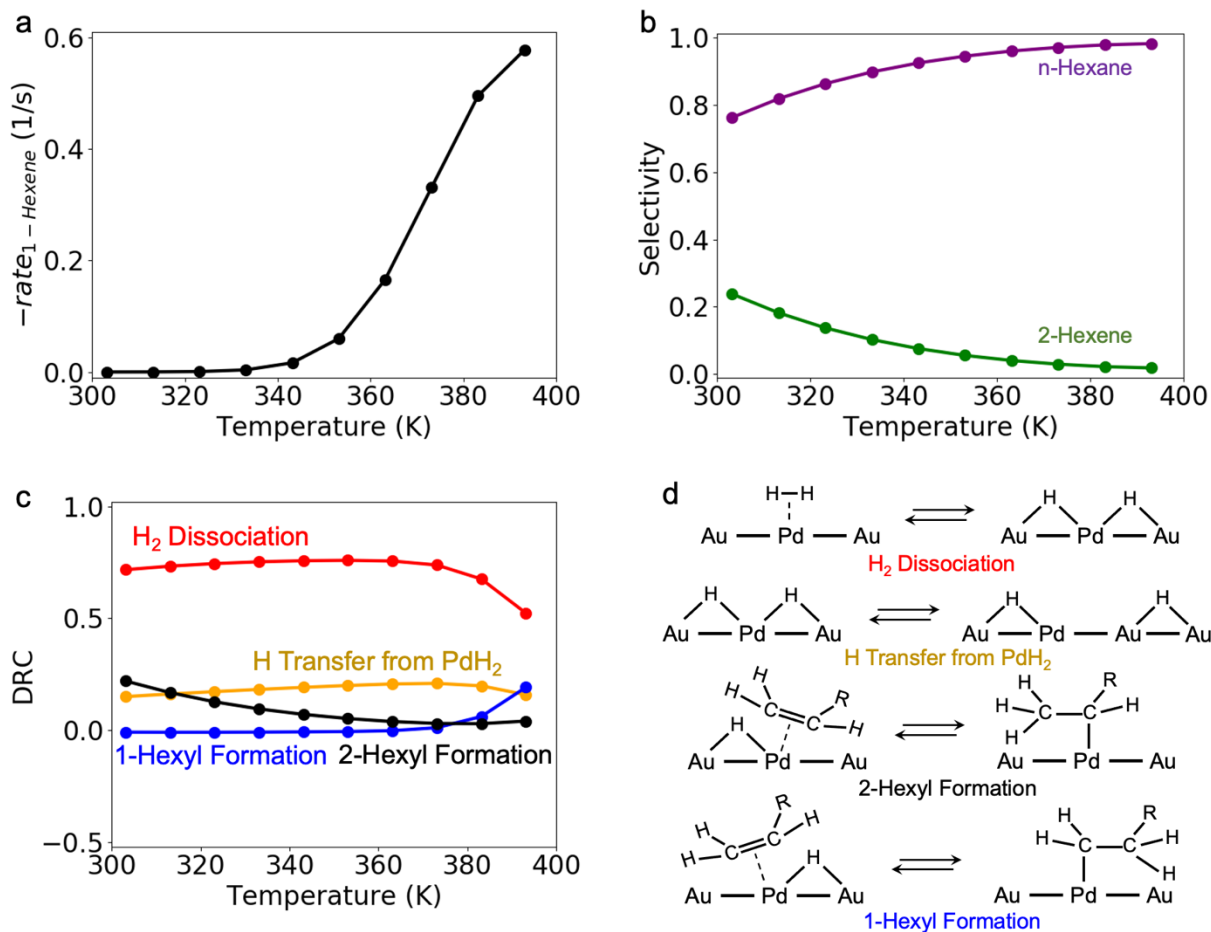


Figure 6.2 1-Hexene consumption rate, product selectivity and degrees of rate control (DRC) of transition states for 1-hexene consumption evaluated for the Pd₁Au(111) model catalyst at fixed partial pressures. Microkinetic model of 1-hexene reaction with H₂ evaluated at $p(\text{H}_2) = 0.2$ bar, $p(1\text{-hexene}) = 0.01$ bar, and $p(2\text{-hexene}) = p(\text{n-hexane}) = 0.001$ bar. (a) Rate of 1-hexene consumption, (b) selectivity of 2-hexene and n-hexane formation, and (c) main rate-controlling transition states (TS) and their DRC for 1-hexene consumption as functions of temperature. (d) Schematic representations of the elementary steps corresponding to the transition states in panel (c). The reaction was found to light off at ~350 K with 2-hexene as the minority product and H₂ dissociation as the main rate-controlling TS.

To identify the factors influencing the 1-hexene consumption rates and the 2-hexene selectivity, the degree of rate control (DRC) and degree of selectivity control (DSC) of transition states were computed. The DRC and DSC quantify the relative importance of surface intermediate and transition states to the overall reaction rate and product selectivity.¹⁷¹

The calculated DRC of transition states (**Figure 6.2**) for 1-hexene consumption at 373 K and partial pressures corresponding to low 1-hexene conversion indicate that H₂ dissociation (DRC = 0.74) is the main rate-controlling TS, similar to that of 1-hexyne hydrogenation. The TS of H transfer from the PdH₂ species onto the Au support is partially rate-controlling (DRC = 0.21), whereas the TS of C-H bond formation has only a very minor influence on the overall rate: DRC = 0.01 and 0.03 for the formation of 1-hexyl and 2-hexyl, respectively. The DSC showed that under the same conditions [T = 373 K, (H₂) = 0.2 bar, P(1-hexene) = 0.01 bar, and P(2-hexene) = P(n-hexane) = 0.001 bar], the TS of H₂ dissociation and that of H transfer to 2-hexyl to eventually form hexane (TS2(b)) impact the selectivity of 2-hexene most negatively (**Figure E.2**, DSC = -0.57 for both), meaning that if the energy of these TS is lowered the selectivity for 2-hexene decreases. On the other hand, the TS of 1-hexene hydrogenation to 2-hexyl (DSC = +0.93) and that of 2-hexyl dehydrogenation to 2-hexene (DSC = +0.69) positively influence the selectivity for 2-hexene (decreasing the energy favors the selectivity to 2-hexene).

The calculated DSCs and DRCs unambiguously show that the free energy barriers of H₂ dissociation and H-spillover are critical in controlling the overall reactivity and selectivity of the catalyst. This is in line with the rate controlling step in the partial hydrogenation of 1-hexyne over Pd₁/Au, where high H₂ dissociation and H-spillover free energy barriers result in the reversible formation of hexyls on Pd₁ sites, boosting the catalyst's selectivity for 1-hexene by hindering further hydrogenation of hexyls. Here, the large H₂ dissociation and H transfer barriers impact the

selectivity in a similar way: 1-hexene isomerization becomes favored when further hydrogenation of hexyl intermediates is hindered by large H₂ dissociation barriers. To test the importance of the barriers beyond a local derivative in the DRCs and DSCs, the rate of 1-hexene conversion and product selectivity were recalculated after increasing the barrier of the H₂ dissociation and H-spillover steps by 0.1 eV (**Figure E.3**). The recalculated 2-hexene selectivity is in much better agreement with experimental observations, where 2-hexene was found to be the majority product, and this will be further discussed below.

6.3.3 Theoretical Assessment of H/D Exchange in 1-Hexene Hydrogenation and Isomerization over Pd₁Au(111)

To further strengthen the argument that large H₂ dissociation and H-spillover barriers are responsible for the high selectivity to 2-hexene, the microkinetic models were extended to include D₂/HD adsorption, D exchange between Pd/Au sites and deuteration of hydrocarbon intermediates (**Table E.1**). For 1-hexene and 2-hexene, 1 H atom was allowed to be exchanged for D, while for n-hexane, up to 2 H atoms were allowed to be exchanged for D. To assess the degree of H/D exchange in the hexenes and n-hexane as a function of temperature and 1-hexene conversion, the microkinetic model was embedded in an isothermal and isobaric plug flow reactor (PFR) with 200 mg of catalyst loading. The inlet flow rate to the reactor was assumed to be 50 standard mL/min (corresponding to the standard condition of T = 273.15 K and P = 1 atm), consisting of 1 vol% 1-hexene and 20 vol% D₂ with balance inert. The reactor simulations were first performed without any shift to the barriers of H₂ dissociation and H-spillover (**Figure E.4**). Following the 1-hexene consumption rates and 2-hexene selectivity evaluated at fixed partial pressures (**Figure 6.2**), n-

hexane was found to be the major product. Marked H/D exchange was observed in the hydrocarbon species, with n-hexane d_1 as the most prevalent product at 10% 1-hexene conversion.

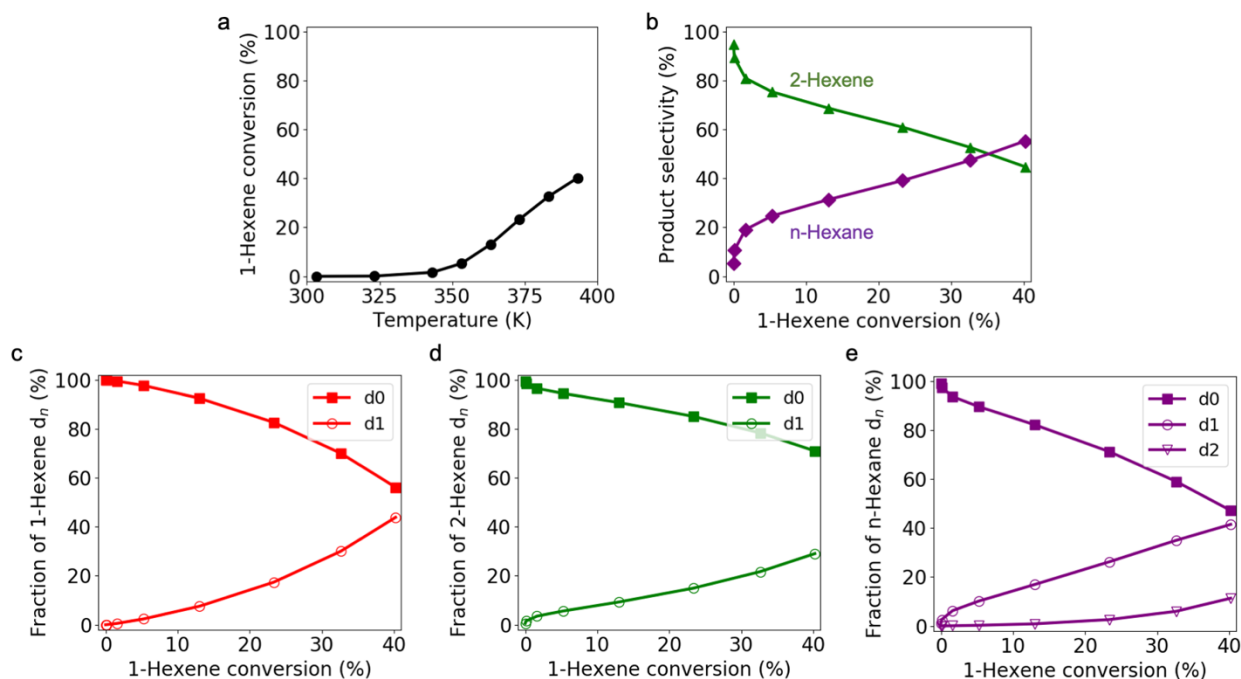


Figure 6.3 Product and isotope selectivity of 1-hexene deuteration and isomerization, with the barriers of H_2 dissociation and H-spillover increased by 0.1 eV. (a) 1-hexene conversion and (b) selectivity of 2-hexene and n-hexane as functions of reactor temperature. (c) 1-hexene isotope distribution, (d) 2-hexene isotope distribution, and (e) n-hexane isotope distribution as functions of 1-hexene conversion. The PFR, with 200 mg catalyst loading, was assumed to operate at constant temperature and pressure (1 bar). The 1-hexene conversion and product/isotope selectivity were evaluated under an inlet flow of 50 standard mL/min (corresponding to the standard condition of $T = 273.15$ K and $P = 1$ atm), consisting of 1 vol% 1-hexene and 20 vol% D_2 with balance inert.

With the barriers of H₂/D₂/HD dissociation and H/D spillover increased by 0.1 eV, the simulated product selectivity qualitatively agrees with experimental observations (**Figure 6.3**). 1-Hexene conversion started at 343 K, with its overall conversion rising to 40.2% at 393 K (**Figure 6.3a**). In the temperature range of 303 K to 383 K, 2-hexene was found to be the major product at most temperatures (**Figure 6.3b**), which is in agreement with experimental observation. At 373 K, the conversion of 1-hexene was 23.3%, with a 60.9% selectivity for 2-hexene. The calculated degree of H/D exchange (**Figure 6.3c-e**) also followed the trend observed in experiment. The amount of deuterated hexenes and n-hexane increased from 303 K to 393 K, but never overtakes the amount of non-deuterated carbonaceous species. Similar to the experimental findings, the microkinetic modeling results at 373 K indicate that the majority of all carbonaceous species in the reactor outlet remain d₀: 82.6% 1-hexene d₀, 85.1% 2-hexene d₀ and 71.2% n-hexane d₀.

Overall, DFT calculations and microkinetic modeling reveal that the preferential hexene isomerization of the Pd₄Au₉₆ catalysts is likely caused by H₂ dissociation and H-spillover being rate limiting on the Pd₁Au(111) alloy surface. The high selectivity towards the hexene isomers arising from a high H₂ dissociation barrier can be rationalized by the fact that hexane formation is hampered due to a limited availability of dissociated hydrogen on the alloy surface. The impact of the H-spillover can be explained by the fact that H₂ dissociation must occur on an empty Pd site, and H-spillover across the surface onto Au must occur to hydrogenate the C₆ intermediates on another Pd site. A higher barrier for H-spillover limits the amount of H transfer from one Pd site to an adsorbed 2-hexyl intermediate on a different Pd site. The latter process has a negative DSC. Hence, increasing the barrier H/D spillover improves the selectivity to 2-hexene.

6.4 Conclusion

In this study, we presented new mechanistic insight to unravel the enhanced alkene selectivity of dilute alloys catalyst and their ability to prevent 1-hexene hydrogenation under hydrogen. By combining isotope exchange experiments, DFT calculations and microkinetic modeling we show that hexene isomerization and hydrogenation on a dilute Pd-in-Au alloy catalyst occurs via a the same Horiuti–Polanyi mechanism as on a mono-metallic Pd surface, and that the rate limiting- and selectivity controlling elementary steps are H₂ dissociation and H-spillover onto the Au host. Importantly, hexene adsorption and H₂ dissociation cannot occur on the same Pd site; thus, H-migration is a key step for hexene conversion on the dilute alloys. Hydrogenation is prevented by the relatively high barrier for H₂ dissociation and H-spillover, which is different from the common assumption that the enhanced alkene selectivity of Pd alloys finds its origin in the weakening of the alkene adsorption energies. Our results have direct implications for the future design of more efficient alloy catalysts for alkyne and alkene hydrogenation, where optimized selectivity and activity can be achieved via careful tuning of the Pd ensemble size and choice of host metal to control hydrogen dissociation and spillover.

Chapter 7 Conclusion

Through this dissertation, we performed DFT calculations, thermodynamic modeling, and microkinetic simulations to study the structure, stability, and catalytic reactivity of various HDCs and SACs in detail. Our results show that the structure and stability of HDCs and SACs and their supports can be heavily affected by their surrounding gas environment, while catalytic reactions on such catalysts can follow nontraditional pathways with kinetic behavior differing from that over bulk metals.

In our study of the Rh/CeO₂ catalyst in the steam reforming of methane, we demonstrated that the structure of the Rh nanoclusters supported on CeO₂ evolves depending on the partial pressure of product CO in the gas environment to which the catalyst is subjected. In our system, the singly dispersed Rh cations in the as-prepared catalyst transformed to Rh NPs after reduction by H₂, but CO, a product formed from steam reforming of methane, was found to re-disperse Rh atoms of the Rh NPs into catalytically active CO liganded Rh₃ clusters during catalysis. As evidenced by our first principles atomistic thermodynamic calculations and in situ/operando spectroscopy, the CO product gas produced by the SRM was found to play a crucial role in inducing and maintaining the highly dispersed active sites, Rh₃(CO)_n of this Rh/CeO₂ catalyst. Overall, this work demonstrates the necessity of considering the composition of the reaction gas environment, especially product molecules, as a factor in identifying the active sites under catalytic conditions.

In our study of the surface structure of Co₃O₄(111), we investigated the surface structure of three terminations of Co₃O₄(111) in equilibrium with a wide range of gas environments and mapped out detailed surface stability diagrams with respect to vacancy formation and hydroxylation of the surface either from hydrogen or water adsorption. We found that all three

terminations are accessible, but the Co-poor $((\text{Co}^{\text{Td}})_x, 3.56 \text{ Co/nm}^2)$ and Co-rich $((\text{Co}^{\text{Oh}}\text{Co}^{\text{Td}})_x, 7.11 \text{ Co/nm}^2)$ terminations are the most prevalent.

We found that if the surface is in equilibrium with oxygen, the Co-poor/O-rich surface $(\text{Co}^{\text{Td}})_x$ is predominantly exposed. When equilibrated with oxygen and water, we found that this termination exhibits three stages of hydroxylation – formation of isolated OH at low $\Delta\mu_{\text{H}_2\text{O}}$, transition to isolated OH/H₂O clusters when $\Delta\mu_{\text{H}_2\text{O}} > -1.3 \text{ eV}$, and finally to a fully hydrated state when $\Delta\mu_{\text{H}_2\text{O}} > -1.0 \text{ eV}$. As such, we predict that hydroxyls will appear during oxidative reactions that produce water or even when water is present as an impurity at low partial pressure. We compared the calculations results regarding hydroxylation of $(\text{Co}^{\text{Td}})_x$ to those obtained from vibrational spectroscopy on Co₃O₄ single crystals and Co₃O₄(111) films and conclude that at low and medium temperature triqua surface complexes surrounded by OH/H₂O groups are observed, while only isolated OH are present at higher temperature.

On the other hand, we found that stabilization of the stoichiometric termination $(\text{Co}^{\text{Oh}_{0.5}}\text{Co}^{\text{Td}})_x$ and Co-rich termination $(\text{Co}^{\text{Oh}}\text{Co}^{\text{Td}})_x$ is only possible under vacuum at high temperature and in hydrogen and water at low temperatures. Unless the environment contains very little water, the O-poor termination $(\text{Co}^{\text{Oh}}\text{Co}^{\text{Td}})_x$ is predicted also be hydroxylated. We found that reduction of this Co-rich termination through H adsorption and O_{vac} formation is easy due to the large relaxation observed at 7.11 OH/nm^2 or $3.56 \text{ O}_{\text{vac}}/\text{nm}^2$. At 423 K and below and under realistic H₂/H₂O pressure, the $(\text{Co}^{\text{Oh}}\text{Co}^{\text{Td}})_x$ termination with 7.11 OH/nm^2 is highly stable. The OH groups on that termination exhibit vibrational frequencies that fall under the range observed in ex situ IR experiments. We believe that this termination should be considered when modeling reactions over Co₃O₄ in low temperature reducing environments. Overall, as many terminations of Co₃O₄ should be hydroxylated under a large range of conditions, it is therefore of high importance to include a

correct coverage in hydroxyl groups for a realistic modelling of the Co_3O_4 surface in calculations; the bare surface model usually used in reaction pathway calculations might not be adequate outside of conditions corresponding to model catalysts.

Continuing from our investigation of the $\text{Co}_3\text{O}_4(111)$ surface, we uncovered the reaction pathways of HDO of anisole on dual site $\text{Mo}_1+\text{Pd}_1/\text{Co}_3\text{O}_4$, and single site $\text{Pd}_1/\text{Co}_3\text{O}_4$ and $\text{Mo}_1/\text{Co}_3\text{O}_4$ catalysts. We simulated Pd_1 and Mo_1 active sites were simulated on the reduced $(\text{Co}^{\text{Oh}}\text{Co}^{\text{Td}})_x$ termination containing 7.11 OH/nm^2 . For the teamed single-atom site catalyst, we found that the Pd_1 site activates H_2 with a barrier of only 0.37 eV while Mo_1 cleaves the C-O bond of anisole. The hydroxylated Co_3O_4 support plays the crucial role of conducting H atoms from the Pd_1 to the Mo_1 site, where the hydrogenation of OCH_3 could be performed with only a net free energy barrier of 0.79 eV instead of 1.28 eV over Pd_1 . The analysis of microkinetic models built from proposed reaction mechanisms found that the $\text{Mo}_1+\text{Pd}_1/\text{Co}_3\text{O}_4$ catalyst has both a higher reactivity and lower apparent activation energy than the $\text{Pd}_1/\text{Co}_3\text{O}_4$ catalyst. The difference in reactivity also reflects the $\text{Mo}_1+\text{Pd}_1/\text{Co}_3\text{O}_4$ catalyst's insensitivity to the Pd_1 mass fraction, where a small amount of Pd_1 sites is enough to provide a source of atomic hydrogen for the HDO of anisole. Overall, we have demonstrated through DFT free energy calculations and microkinetic simulations that the HDO of anisole predominantly occurs through a H-spillover-mediated cooperative mechanism over the $\text{Mo}_1+\text{Pd}_1/\text{Co}_3\text{O}_4$ catalyst.

Next, in our study of the hydrogenation of 1-hexyne over $\text{Pd}_1\text{Au}(111)$, we showed that the H_2 dissociation elementary step, with a sizeable free energy barrier of 0.86 eV at 363 K and 0.2 bar of H_2 , plays a major role to control the activity and selectivity. Specifically, our Gibbs free energy based analysis and first-principles microkinetic simulations show that H_2 dissociation is the rate-limiting process for 1-hexyne hydrogenation on $\text{Pd}_1\text{Au}(111)$ while the C-H bond formation

steps proceed with lower barriers. Somewhat more surprisingly, the sizeable H₂ dissociation barrier also favorably impacts the selectivity for partial hydrogenation to 1-hexene, because it slows down the undesired over-hydrogenation to hexane. This is shown by our DSC analysis, which indicates that decreasing the free energy barrier of H₂ dissociation decreases the selectivity for 1-hexene. Other elementary steps are also important for the selectivity: decreasing the barrier for 1-hexyl hydrogenation to n-hexane also decreases the selectivity for 1-Hexene, while decreasing the barrier for 1-hexyne hydrogenation to 1-hexenyl increases it.

Our findings markedly contrast with extended Pd catalysts for which addition of atomic H to the adsorbed alkyne or alkenyl is accepted to be the rate-determining step, and the selectivity is controlled by competitive adsorption of alkyne and alkene. On dilute Pd-in-Au, the selectivity is controlled instead by competition of hydrogenation rates of alkyne and alkene, which maintains a high selectivity even at high conversion. Our reaction profiles from first-principle calculations and microkinetic modelling also reveal that 1-hexyne hydrogenation to 1-hexene is an irreversible process due to the strongly exothermic nature of the reaction. This claim is validated through the isotopic exchange hydrogenation experiment conducted on Pd_{0.04}Au_{0.96} embedded in RCT-SiO₂.

Another key property of dilute Pd-in-Au alloys is that the adsorption energy of hydrocarbon species is moderate so that the coverage of Pd sites by these hydrocarbon intermediates is low, enabling access and activation of H₂, and preventing poisoning and coking of the catalysts. This is again different from extended Pd catalysts where hydrocarbon species bind strongly and can form coke at high coverage, deactivating the catalyst. Apparent activation enthalpies and reaction orders for dilute Pd-in-Au from our microkinetic modeling are in good agreement with previous experiments, despite a shift of ~60 K in temperature. The temperature shift is attributed to the slight over-estimation of the adsorption energies of the surface species when the xc-functional

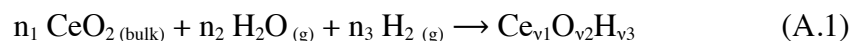
optPBE-vdW is used. Altogether, this work unprecedentedly demonstrates that the improved selectivity of the dilute Pd-in-Au alloy catalyst is attributed to the sizable H₂ dissociation barrier, and to the small barrier for C-H bond formation from 1-hexyne to 1-hexenyl (smaller than that for C-H bond formation from 1-Hexene to 1-Hexyl). The formation of dilute active species in a less active host metal can therefore be seen as a way to tune the binding energy of reactants, alter reaction profiles and induce distinct kinetic behaviors for an optimal catalytic activity and selectivity. This concept of dilute alloy catalyst is hence a versatile approach to design highly selective heterogeneous catalysts.

Finally, continuing from our investigation of 1-hexyne hydrogenation, we also studied in detail the kinetics of hydrogenation/isomerization of 1-hexene over Pd₁/Au(111), to provide mechanistic insight to the ability of dilute Pd-in-Au catalysts to prevent 1-hexene hydrogenation under hydrogen. By combining isotope exchange experiments, DFT calculations and microkinetic modeling we show that hexene isomerization and hydrogenation on a dilute Pd-in-Au alloy catalyst occurs via the same Horiuti–Polanyi mechanism as on a mono-metallic Pd surface, but the rate limiting- and selectivity controlling elementary steps are H₂ dissociation and H-spillover onto the Au host. Importantly, hexene adsorption and H₂ dissociation cannot occur on the same Pd site; thus, H-migration is a key step for hexene conversion on the dilute alloys. Hydrogenation is prevented by the relatively high barrier for H₂ dissociation and H-spillover, which is different from the common assumption that the enhanced alkene selectivity of Pd alloys finds its origin in the weakening of the alkene adsorption energies. Our results have direct implications for the future design of more efficient alloy catalysts for alkyne and alkene hydrogenation, where optimized selectivity and activity can be achieved via careful tuning of the Pd ensemble size and choice of host metal to control hydrogen dissociation and spillover.

Appendix A Supplementary Information for Chapter 2

A.1 Formulas for computing the stability of reduced CeO₂(111) surfaces and Rh active sites

The stability of CeO₂ surface structures was assessed by comparing their Gibbs free energy of formation, normalized by surface area.^{90, 91} As described, OH groups, surface O vacancies (O_{vac}), and subsurface O_{vac}s were considered as the possible surface motifs under the reactive gas environment. The surface structures on the slab were assumed to be thermodynamically controlled based on the studies referenced in the methods section. The formation of a reduced CeO₂(111) slab with formula Ce_{v1}O_{v2}H_{v3} was written with respect to bulk CeO₂, H₂ and H₂O gas as:



The stoichiometric coefficients n_i were found by solving the following equation:

$$\mathbf{M}_{\text{surf}} \mathbf{n}_{\text{surf}} = \mathbf{v}_{\text{slab}} \quad (\text{A.2})$$

where \mathbf{M}_{surf} is the (3×3) stoichiometric matrix composed of the three reference compounds. The surface energy of a reduced slab can then be computed by finding the Gibbs free energy of reaction and normalizing by its surface area:

$$\gamma_{\text{slab}} = \Delta G_{\text{rxn}} / 2A_{\text{surface}} \quad (\text{A.3})$$

Chemically, since only one side of the slab was modified in our calculations, this computed surface energy is the average surface energy between the bulk-truncated stoichiometric CeO₂(111) surface and the OH/O_{vac}-decorated CeO₂(111) surface. If we keep the same chemical potential references for all calculations, the surface energy of the constrained surface will be a constant; thus, it is only necessary to compare the surface-area-normalized Gibbs free energy of reaction for the relative stability of surfaces:

$$\gamma = \Delta G_{\text{rxn}} / A_{\text{surface}} \quad (\text{A.4})$$

A (3 × 3) supercell was used to simulate the Rh/CeO₂ active sites. When 2/3 of all Ce ions on the surface of many-nm-thick CeO₂(111) films were reduced to the +3 oxidation state, (3 × 3) and (3 × √7) periodicities of O vacancies form on the surface, as observed by LEED and AFM.^{82, 226, 227} The fully hydroxylated CeO₂(111) surface, H₂O, H₂, CO, and hypothetical supported Rh₁₃ clusters were used as chemical potential references to compute the stability of Rh active sites. The formation reaction of a Rh site with formula Ce_{v1}O_{v2}H_{v3}Rh_{v4}C_{v5} was written as:



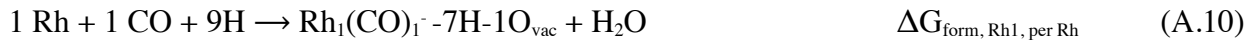
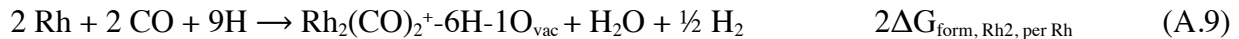
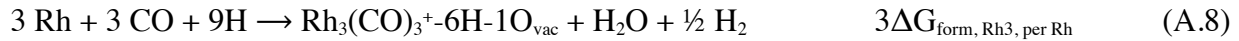
The stoichiometric coefficients were found using the following equation:

$$M_{\text{site}} n_{\text{site}} = v_{\text{site}} \cdot \quad (\text{A.6})$$

Since the same supercell size was used for all Rh site calculations, the surface area is not needed when comparing the Rh site's Gibbs free energy of formation. It is only necessary to normalize the Gibbs free energy of reaction by the number of Rh atoms in each simulated Rh/CeO₂ active site for stability comparisons:

$$\Delta G_{\text{form}} = \Delta G_{\text{rxn}} / \nu_{\text{Rh}} \quad (\text{A.7})$$

where ν_{Rh} is the nuclearity of the Rh active site. Chemically, normalizing ΔG_{rxn} by the number of Rh atoms in the formed site is the same as considering the Gibbs free energy of combining many Rh₁ units. For example, consider the sites: Rh₃(CO)₃⁺, Rh₂(CO)₂⁺ and Rh₁(CO)₁⁻ with the following formation reactions and normalized Gibbs free energies of reaction:



where “xH-yO_{vac}” represents the (3 × 3) CeO₂(111) surface, containing x adsorbed H and y O_{vac}. For the formation of Rh₂(CO)₂⁺ and Rh₁(CO)₁⁻, we can rearrange these reactions into one where two Rh₁(CO)₁⁻ units transform into one Rh₂(CO)₂⁺ unit:

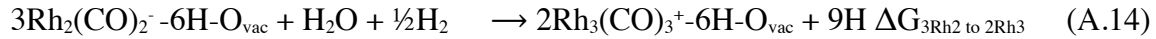


The dimerization restores one unit of the hydroxylated surface (9H). We see that the direct formation of $\text{Rh}_2(\text{CO})_2^+$ from the reference compounds is the same as forming two $\text{Rh}_1(\text{CO})^-$ units first, combining them, and restoring one unit of the Rh-free surface:

$$\Delta G_{2\text{Rh1 to 1Rh2}} = 2\Delta G_{\text{form, Rh1, per Rh}} - 2\Delta G_{\text{form, Rh2, per Rh}} \quad (\text{A.12})$$

$$\Delta G_{\text{form, Rh2, per Rh}} = 0.5 \Delta G_{2\text{Rh1 to 1Rh2, per Rh}} + \Delta G_{\text{form, Rh1, per Rh}} \quad (\text{A.13})$$

A reaction where three $\text{Rh}_2(\text{CO})_2^+$ units gather to form two $\text{Rh}_3(\text{CO})_3^+$ units and one empty surface unit can be written in the same way:



$$\Delta G_{3\text{Rh2 to 2Rh3}} = 6\Delta G_{\text{form, Rh3, per Rh}} - 6\Delta G_{\text{form, Rh2, per Rh}} \quad (\text{A.15})$$

$$\Delta G_{\text{form, Rh3, per Rh}} = 1/6 \Delta G_{3\text{Rh2 to 2Rh3}} + \Delta G_{\text{form, Rh2, per Rh}} \quad (\text{A.16})$$

A.2 Vibrational corrections for Gibbs free energy calculations

Bulk CeO_2 , H_2 gas, and H_2O gas were used as the chemical potential reference structures to compute the Gibbs free energy of formation of the reduced $\text{CeO}_2(111)$ surface, while the hydroxylated $\text{CeO}_2(111)$ surface, H_2 gas, H_2O gas, CO gas, and hypothetical supported Rh_{13} clusters were used as the chemical potential reference structures for Rh/CeO_2 sites. The translational and rotational contributions to Gibbs free energy of the H_2 , H_2O , and CO gases were computed using standard equations for ideal gases.¹⁶⁹ Since vibrational calculations are computationally expensive, the vibrational contributions to the Gibbs free energy of formation were approximated during screening calculations and the construction of **Figures 2.1 and 2.3** using the procedures described below.

In the screening for stable Rh active sites, the vibrational contributions to the sites' Gibbs free energy of formation (ΔG_{vib}) were approximated using 4th order polynomials of temperature fitted to the results of representative vibrational frequency calculations. These screening calculations were performed at a reduced accuracy, where the one electron wavefunctions were expanded in a set of plane waves up to 450 eV, and Brillouin zone integrations were performed only at the Gamma point. The vibrational modes of the outermost O-Ce-O trilayer and adsorbates were considered. Any soft modes with wavenumbers below 150 cm⁻¹ including any imaginary modes due to numerical inaccuracies were rounded up to 150 cm⁻¹.

To select the best structures to build the T/P_{CO} stability diagram, a sample stability diagram was constructed by applying the vibrational entropy correlations to the large group of sampled stable Rh sites, then the structures appearing on the diagram were selected for further structural optimization and vibrational calculations. The calculations in **Figure 2.2** were performed at a higher accuracy (ENCUT = 600 eV, PREC = 'A', EDIFF = 10⁻⁸ eV, EDIFFG = -0.02 eV/Å, Rh valence shell: 4s²4p⁶5s²4d⁷). The two lowest vibrational modes for surface calculations were discarded, following ref ²²⁸. Any soft modes with wavenumbers below 150 cm⁻¹ were rounded up to 150 cm⁻¹.

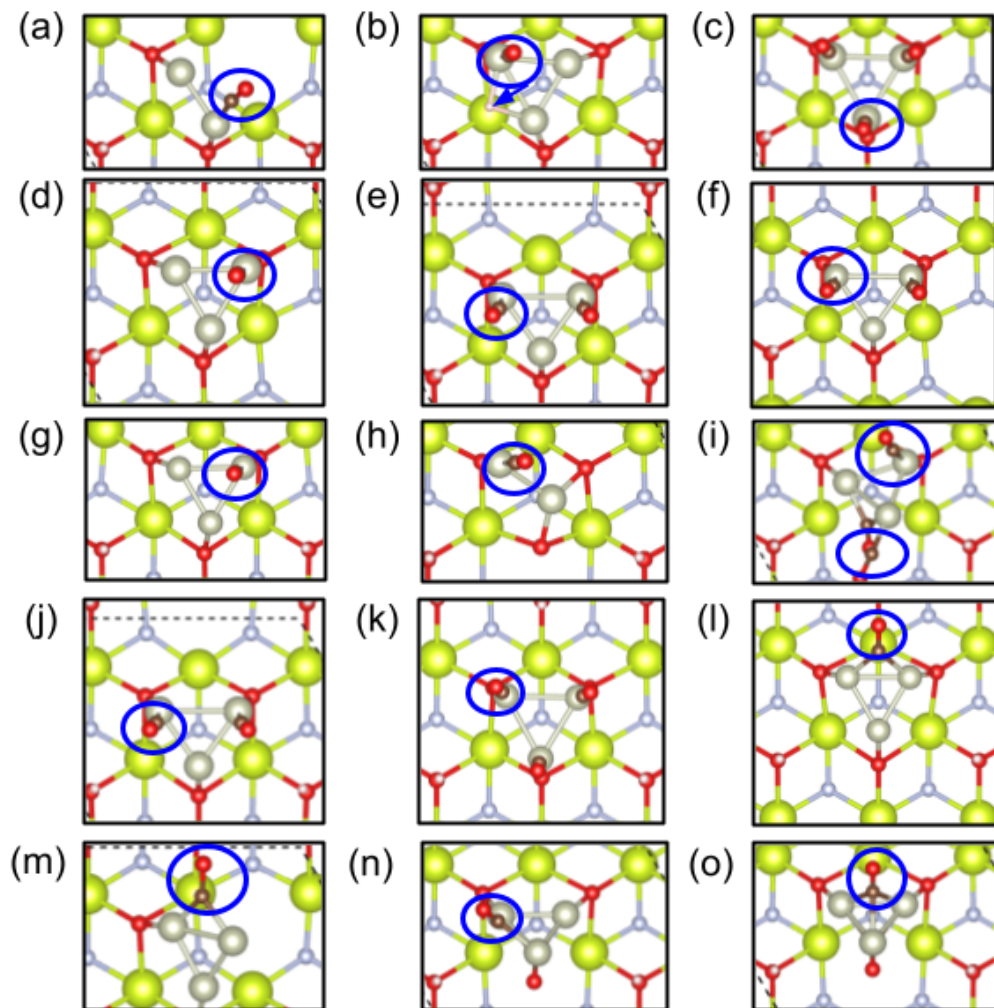


Figure A.1 Structures used in the fitting of the ΔG_{vib} of ordinary CO adsorption, where the O end of the CO molecule points away from the surface. The CO molecule accounted in each structure is circled in blue. The arrow in (b) indicates the shift of the H atom's binding site in response to CO adsorption.

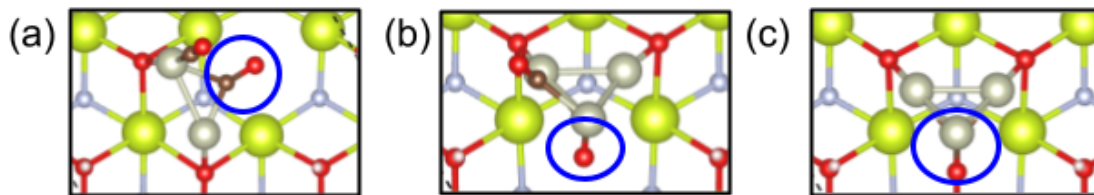


Figure A.2 Structures used in the fitting of the ΔG_{vib} of tilted CO adsorption, where the O of the CO molecule points towards the surface. The CO molecule accounted in each structure is circled in blue.

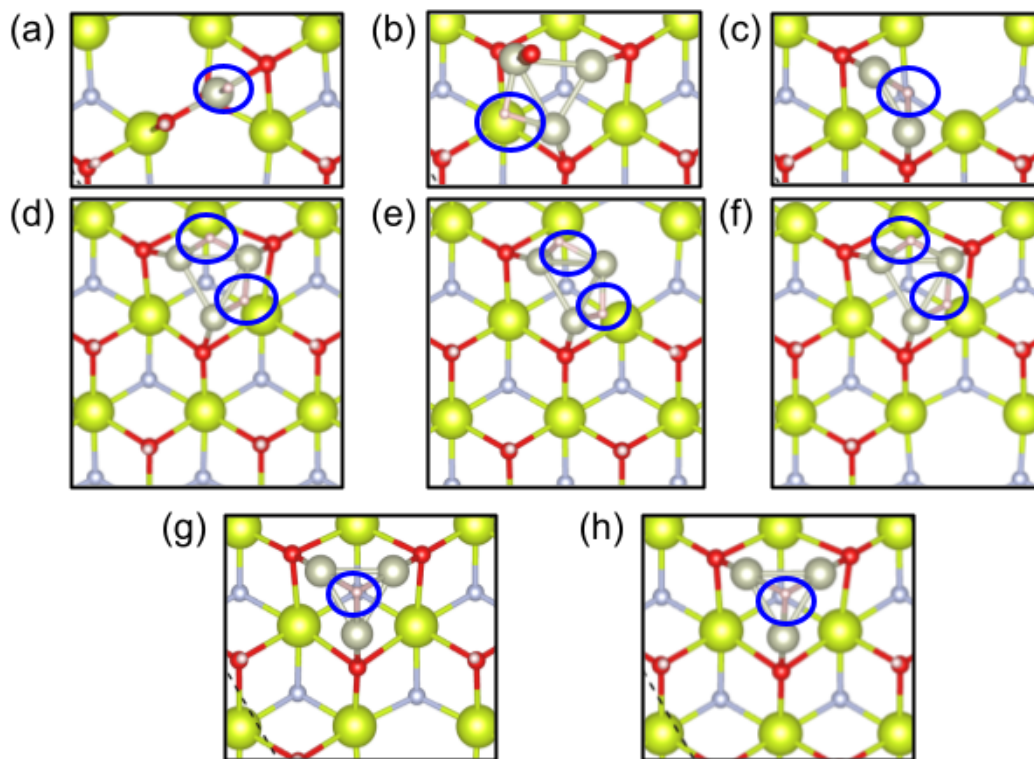


Figure A.3 Structures used in the fitting of the ΔG_{vib} of H adsorption on Rh. The adsorbed H is circled in blue.

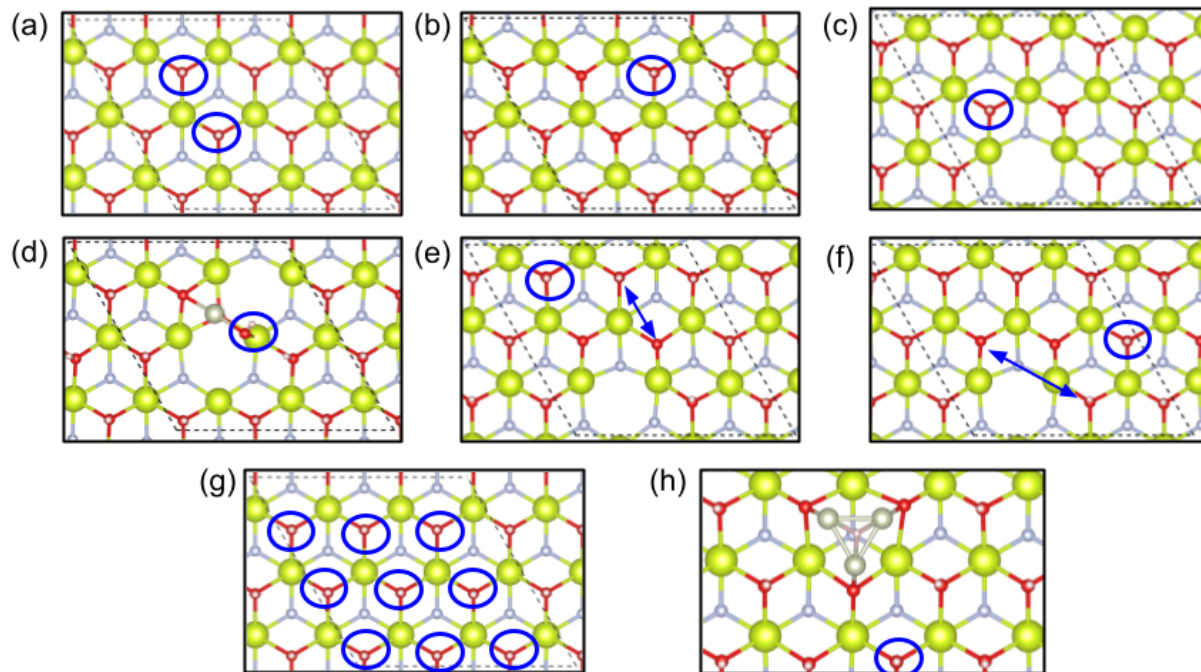


Figure A.4 Structures used in the fitting of the ΔG_{vib} of H adsorption on O. The adsorbed H is circled in blue. Arrows indicate H that was moved after the adsorption of the circled H.

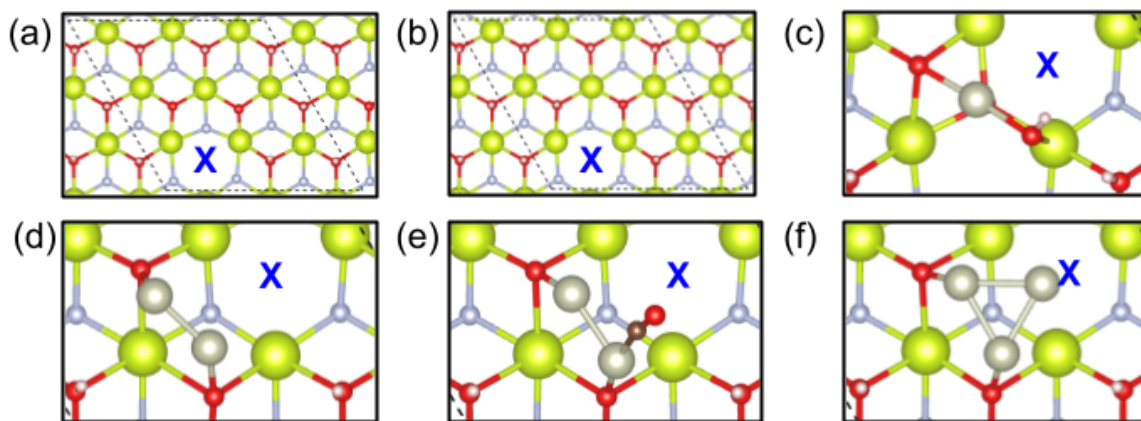


Figure A.5 Structures used in the fitting of the ΔG_{vib} of surface O vacancy formation. The formed surface O_{vac} is marked with a blue X.

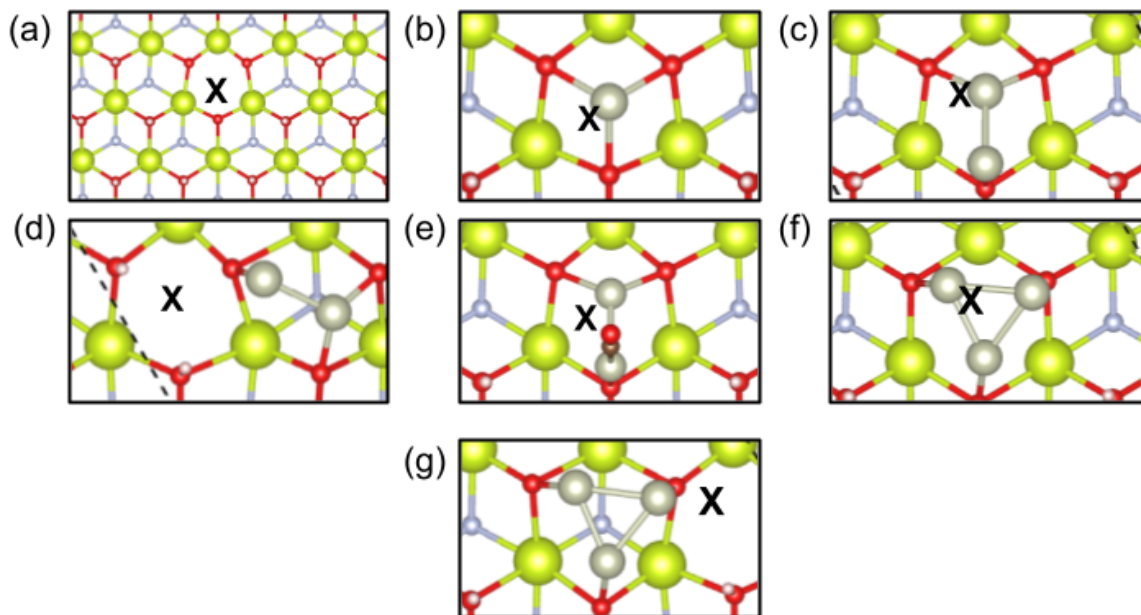
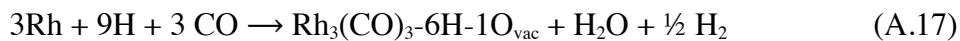


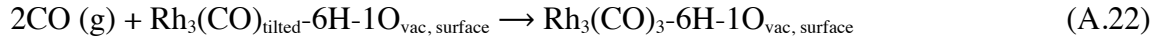
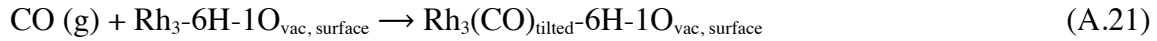
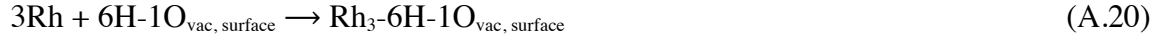
Figure A.6 Structures used in the fitting of the ΔG_{vib} of subsurface O vacancy formation. The formed subsurface O_{vac} is marked with a black X.

Since the stoichiometric matrix and the chemical potential references can be linearly recombined into independent reactions, the vibrational contributions to the formation of the following surface/active site motifs were fitted (**Supplementary Figures A.1~A.6**): surface O_{vac} formation, subsurface O_{vac} formation, H adsorption on O, H adsorption on Rh, upright CO adsorption on Rh, where the CO molecule is bound to Rh, and its O points away from the surface, and tilted CO adsorption on Rh, where the CO molecule is bound to more than 1 Rh, and its O tilts toward a surface O_{vac} .

For example, the formation reaction for the site $\text{Rh}_3(\text{CO})_3\text{-6H-O}_{\text{vac}}$ (**Figure 2.2e**) is:



Based on the structure of the $\text{Rh}_3(\text{CO})_3^+$ site, the above reaction can be rewritten as the sum of the following reactions:



where 1 instance of $\text{O}_{\text{vac, surface}}$ formation, 3 instances of H desorption, 1 instance of tilted CO adsorption, 1 instance of the adsorption of the Rh_3 cluster and 2 instances of upright CO adsorption have occurred in the formation of the $\text{Rh}_3(\text{CO})_3-6\text{H}-1\text{O}_{\text{vac-surface}}$.

Table A.1 Coefficients used in the ΔG_{vib} correlations ($\Delta G_{\text{vib}} = \text{AT}^4 + \text{BT}^3 + \text{CT}^2 + \text{DT} + \text{E}$).

Reaction	A (eV-K ⁻⁴)	B (eV-K ⁻³)	C (eV-K ⁻²)	D (eV-K ⁻¹)	E (eV)
Upright CO adsorption	-6.84E-14	3.13E-10	-7.46E-7	1.28E-4	1.11E-1
Tilted CO adsorption	-1.10E-13	4.46E-10	-9.20E-7	1.16E-4	5.64E-2
H adsorption on O	-8.24E-14	2.88E-10	-4.84E-7	4.19E-5	1.24E-1
H adsorption on Rh	4.02E-14	-8.72E-11	-6.75E-8	4.89E-5	5.09E-2
Surface O_{vac} formation	6.08E-14	-2.58E-10	5.05E-7	-1.04E-4	2.32E-1
Subsurface O_{vac} formation	1.12E-13	-4.10E-10	6.79E-7	-6.10E-5	2.54E-1

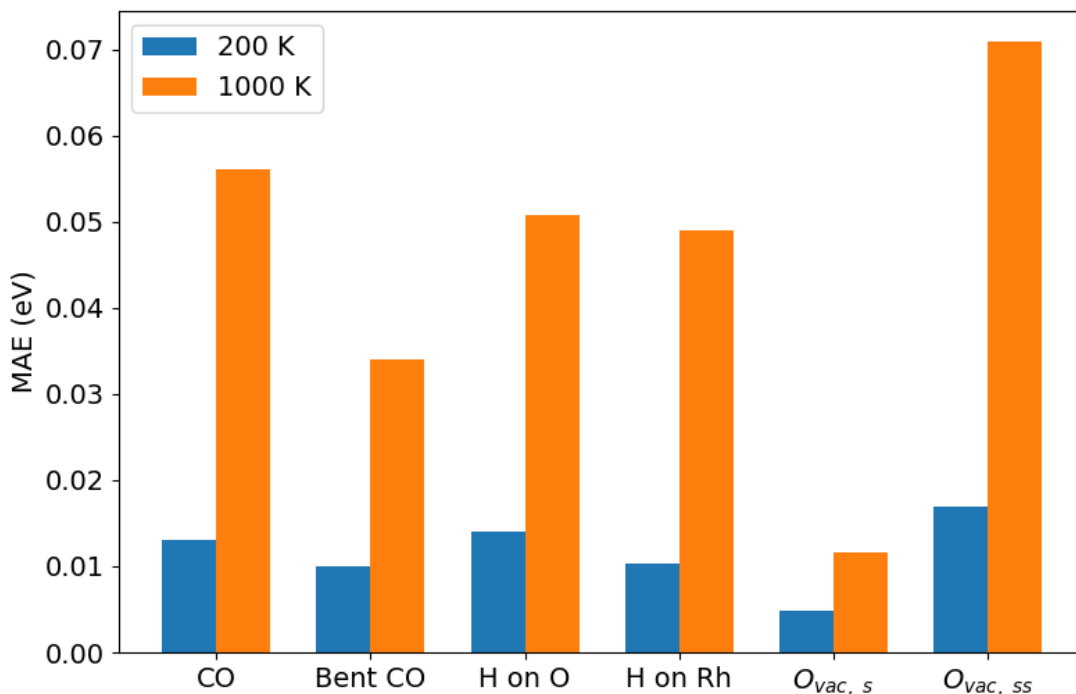


Figure A.7 Mean absolute errors (MAE) of the six ΔG_{vib} correlations at 200 K and 1000 K.

The ΔG_{vib} correlations were obtained by fitting the average ΔG_{vib} of each set of structures (Table A.1). The error of the fits is approximately $k_{\text{B}}T$ or lower at 200 K and 1000 K for each motif (Figure A.7).

A.3 Configurational entropy of Rh sites

For a binary system of n adsorbates and N sites, the configurational entropy of the system is maximized when $x = n/N = 0.5$. Since we are interested in the Gibbs free energy of formation per Rh atom, we divided the configurational entropy of the whole system by the number of Rh.

We begin with the equation of configurational entropy of the whole system:

$$S_{\text{config}}/N = k_B[-\ln(1 - x) + x \ln(1/x - 1)] \quad (\text{A.23})$$

Here, x is the fraction of the total surface sites occupied by Rh structures of nuclearity m . Let $x_0 = xm = mn/N$, where x_0 is the atomic fraction of Rh on the catalyst surface, taken as the Rh atomic fraction on the surface, 0.5%. The configurational entropy per Rh atom is written as:

$$S_{\text{config}}/mn = S_{\text{config}}/N/x_0 \quad (\text{A.24})$$

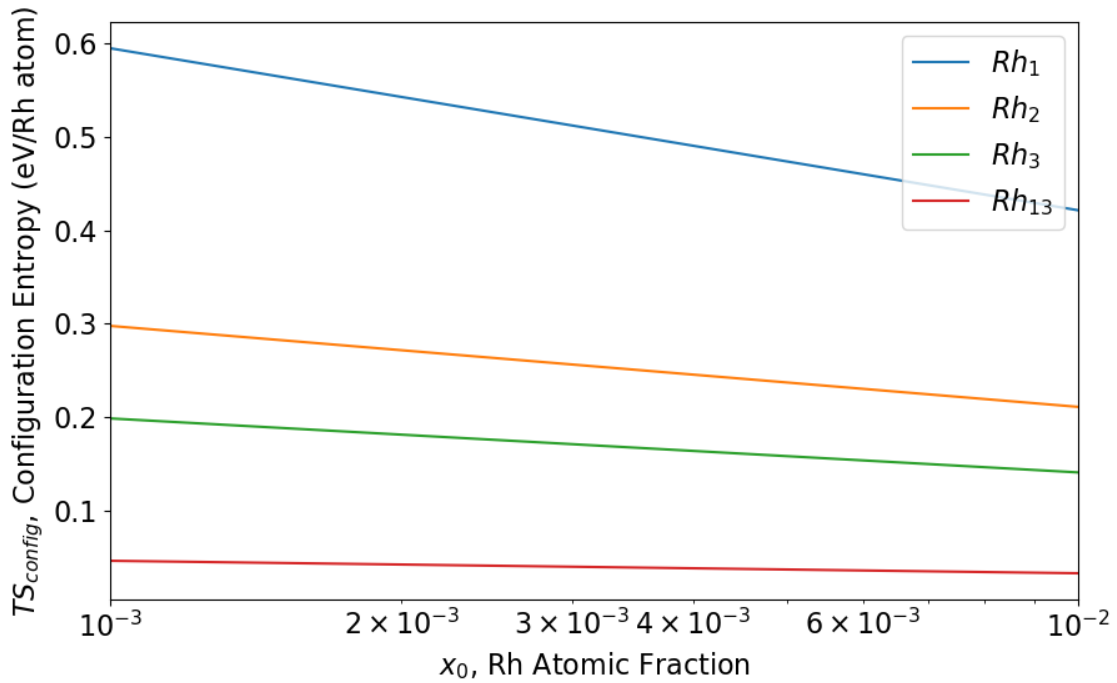


Figure A.8 Configurational entropy per Rh at 873 K, plotted for Rh_1 , Rh_2 , Rh_3 , and Rh_{13} sites as a function of the surface Rh atomic fraction.

For a nuclearity of 1, the configurational entropy per Rh varies by roughly 0.15 eV between $x_0 = 0.001$ and $x_0 = 0.01$ at 873 K (**Figure A.8**).

A.4 Chemical potential of Rh atoms

Under a given gas environment, the lower bound of the Rh chemical potential is that of the most stable bulk Rh phase. To quantify the stability of Rh sites, the Rh chemical potential reference was chosen as a hypothetical supported Rh_{13} particle. We imagine that the largest possible Rh particle in the Rh_1/CeO_2 catalysts studied here will be formed in the H_2 -rich pretreatment, as the gas environment most heavily favors the formation of metallic Rh. Based on the structure of bulk Rh, a cubooctahedral Rh_{13} particle would have an average coordination number of 6, like that measured by EXAFS.

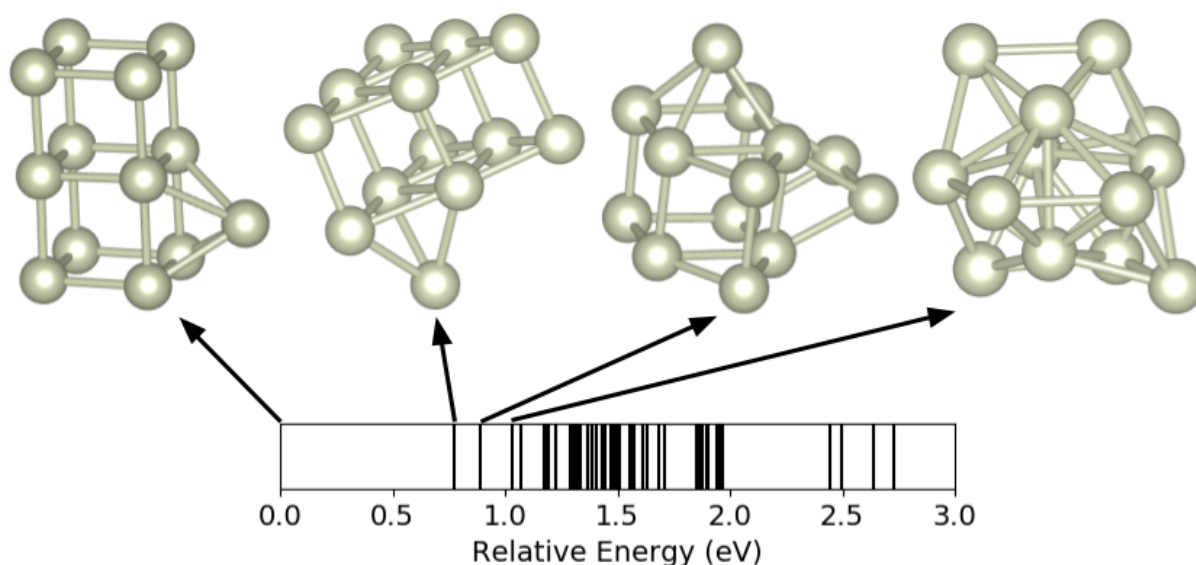


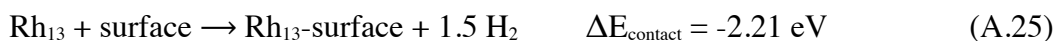
Figure A.9 The sampled Rh_{13} clusters ranked by their relative total energy. High symmetry structures from Piotrowski et al. and the Pt_{13} LEME from Sun and Sautet were used as the starting points.^{58, 102}

To sample the Rh_{13} structures, we compared the energies of the five high-symmetry structures studied by Piotrowski et al. with geometries found in the Pt_{13} low-energy metastable ensemble (LEME).⁵⁸ The structural optimization of the Rh_{13} structures were done starting from the

reported geometries with neither spin state restrictions nor initial guesses to magnetization. Rh₁₃ clusters appear to prefer open structures as the three most stable Rh₁₃ isomers found this group have a Rh-Rh coordination number of around 4. The most stable cluster was found to be the double-simple-cubic (DSC) Rh₁₃ cluster. The fourth most stable Rh₁₃ has an average coordination number of 5.85 and a Rh-Rh bond length of 2.58 Å (**Figure A.9**). The difference in the cohesive energy between the two structures is 0.08 eV/atom.

Since the reactive gas environment contains a mixture of CO and H₂, we also tested the adsorption energy of H and CO on the most stable DSC Rh₁₃ cluster. We adopted the NO adsorption geometries found by Piotrowski et al. for CO adsorption.²²⁹ The CO adsorption energy correction (**Section A.5**) was applied to these structures. The lowest corrected CO adsorption energy on the cluster was found to be -2.02 eV. In this configuration, CO is coordinated to the single Rh at the apex of DSC-Rh₁₃. Factoring in the chemical potential of CO during catalysis, the adsorption of CO is only slightly exergonic. On the other hand, the adsorption energy of ½ H₂ was found to be -0.55 eV at a 3-fold site on the Rh₁₃ particle; thus, H adsorption is unfavorable during catalysis. For these reasons, we did not consider any ligands on the Rh₁₃ cluster, as they will not significantly impact the Rh chemical potential.

The most important modification to the Rh chemical potential is the adsorption of the cluster to the surface. The adsorption energy of the DSC Rh₁₃ cluster on three lattice O in a (4x4) cell was found to be -5.53 eV. To adsorb the cluster, three surface H must be also removed. 3.32 eV is needed to desorb 1.5 H₂ molecules from a hydroxylated (3x3) surface, resulting in the following reaction:



The ΔG_{vib} of this reaction is approximately equal to the change of vibrational Gibbs free energy associated with the loss the three surface H. Setting the chemical potential of H_2 from rotation and translation to those during catalysis and using the fitted ΔG_{vib} correlation in Table A.1, the chemical potential of Rh would be:

$$\mu_{\text{Rh}} = (E_{\text{Rh13}} + G_{\text{vib, Rh13}} + \Delta E_{\text{contact}} - 3\Delta G_{\text{vib, H on O}} + 1.5\Delta\mu_{\text{H}_2, \text{Trans+Rot}})/13 - TS_{\text{config, Rh13}}, \quad (\text{A.26})$$

$$\mu_{\text{Rh}} = E_{\text{Rh, bulk}} + \Delta\mu_{\text{Rh}}. \quad (\text{A.27})$$

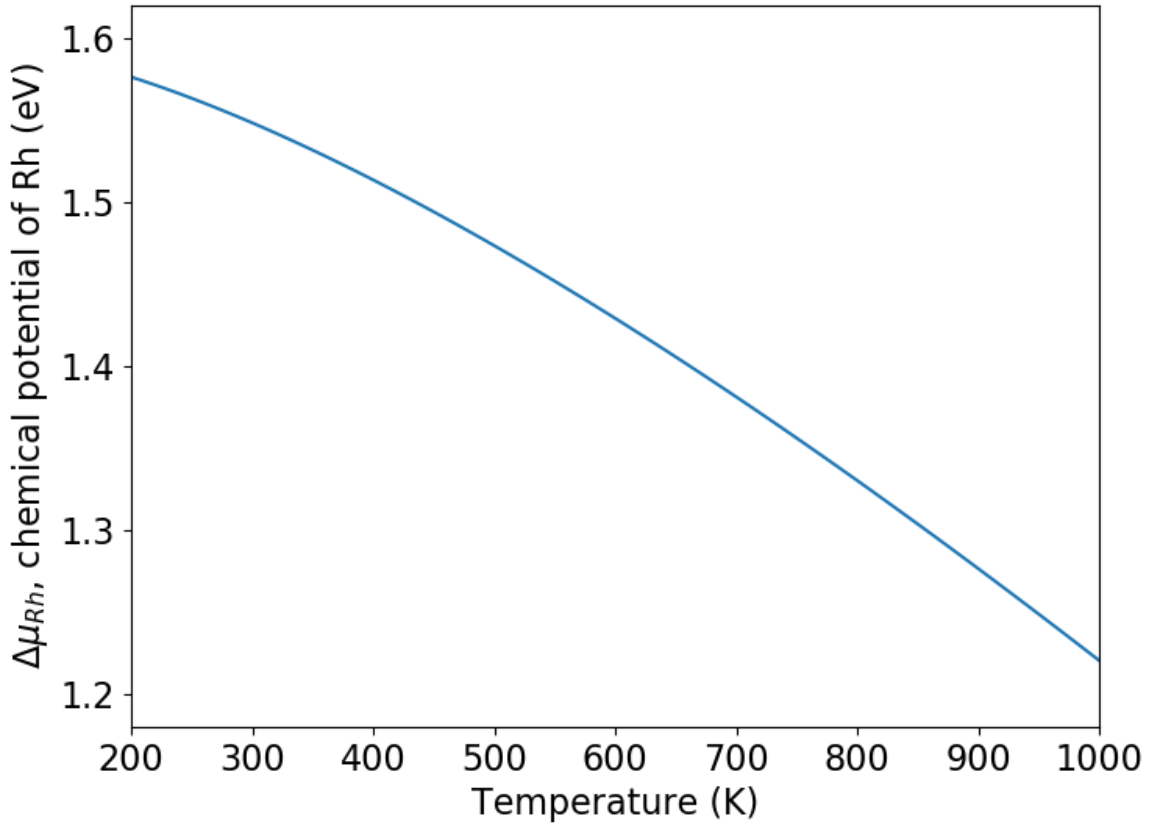


Figure A.10 The $\Delta\mu_{\text{Rh}}$ plotted against temperature. $\Delta\mu_{\text{Rh}}$ ranges from 1.58 eV to 1.22 eV in the range of 200-1000 K.

Between 200 K and 1000 K, $\Delta\mu_{\text{RH}}$ ranges from 1.58 eV to 1.22 eV (Figure A.10).

A.5 CO adsorption energy correction

The CO adsorption energy correction is developed based on the on the extrapolative scheme described by Mason et al. and Sumaria et al.^{105, 107} The authors found that the increasing singlet-triplet transition energy (ΔE_{ST}), a result of decreasing the C and O pseudopotential core radii, correlates positively with the CO adsorption energy (ΔE_{ads}) on Pt(111) (i.e. higher ΔE_{ST} means higher ΔE_{ads} and weaker Pt-CO bonding). Extrapolation to the ΔE_{ST} value determined by configuration interaction (CI) calculations reproduces a CO stability trend in agreement with experimental results:

$$\Delta E_{\text{ads,ext}} = \Delta E_{\text{ads,N}} + \frac{d\Delta E_{\text{ads}}}{d\Delta E_{\text{ST}}} (\Delta E_{\text{ST,CI}} - \Delta E_{\text{ST,N}}) \quad (\text{A.28})$$

where $\Delta E_{\text{ads, ext}}$ is the extrapolated CO adsorption energy, $\Delta E_{\text{ads, N}}$ is the CO adsorption energy calculated using 1.5 Bohr and 1.52 Bohr as C and O core radii, respectively, $\Delta E_{\text{ST, N}}$ is the singlet-triplet transition energy using the same pseudopotentials, $\Delta E_{\text{ST, CI}}$ is the CI singlet-triplet transition energy, and $\frac{d\Delta E_{\text{ads}}}{d\Delta E_{\text{ST}}}$ is the slope of the $\Delta E_{\text{ads}} - \Delta E_{\text{ST}}$ trendline calculated from changing the C/O pseudopotential pairs.

The resulting CO adsorption energy correction, $\Delta E_{\text{ads, ext}} - \Delta E_{\text{ads, N}}$, can be fitted as a linear function of average CO bond length:

$$\Delta E_{\text{ads,ext}} - \Delta E_{\text{ads,N}} = \frac{d\Delta E_{\text{ads}}}{d\Delta E_{\text{ST}}} (\Delta E_{\text{ST,CI}} - \Delta E_{\text{ST,N}}) \quad (\text{A.29})$$

$$\Delta E_{\text{corr}} = \frac{d\Delta E_{\text{ads}}}{d\Delta E_{\text{ST}}} (\Delta E_{\text{ST,CI}} - \Delta E_{\text{ST,N}}) \quad (\text{A.30})$$

$$\Delta E_{\text{corr}} = ar_{\text{CO}} + b \quad (\text{A.31})$$

Table A.2 Settings used in developing the extrapolative CO adsorption energy correction at the PBE level.

C-O PP pair (names in VASP)	Plane wave kinetic energy cutoff (eV)	C core radius [a_0]	O core radius (a_0)	ΔE_{ST} , singlet triplet transition energy (eV)	R_{CO} , bond length of the CO molecule (\AA)
s-s	500	1.850	1.850	5.253	1.179
(Default)	600	1.500	1.520	5.566	1.143
h-h	800	1.100	1.100	5.655	1.136
GW-GW	500	1.500	1.520	5.595	1.139
GW_new-GW_new	750	1.600	1.600	5.642	1.138
h_GW-h_GW	850	1.100	1.10	5.651	1.135

Table A.3 The Rh₁, Rh₂, Rh₄, and Rh₆ carbonyls used in developing the CO adsorption energy correction for Rh carbonyl molecules.

Rh(CO)	Rh(CO) ₂ A	Rh(CO) ₂ B	Rh(CO) ₂ C
Rh(CO) ₃	Rh(CO) ₄ A	Rh(CO) ₄ B	Rh ₂ (CO)
Rh ₂ (CO) ₂	Rh ₂ (CO) ₃ 1	Rh ₂ (CO) ₃ 2	Rh ₂ (CO) ₃ 3
Rh ₂ (CO) ₃ 4	Rh ₂ (CO) ₃ 23	Rh ₂ (CO) ₃ 28	Rh ₂ (CO) ₈ C _{2v}
Rh ₂ (CO) ₈ D _{2d}	Rh ₂ (CO) ₈ D _{3d}	Rh ₂ (CO) ₈ D _{4d}	Rh ₄ (CO) ₁₂ C _{3v}
Rh ₄ (CO) ₁₂ T _d	Rh ₆ (CO) ₁₆ D _{2d}	Rh ₆ (CO) ₁₆ T _d	

Table A.4 Extrapolated average CO adsorption energies for the Rh carbonyl molecules.

Molecule	Extrapolated ΔE_{ads} (eV)	Molecule	Extrapolated ΔE_{ads} (eV)
Rh(CO)	-2.650	Rh ₂ (CO) ₃ 4	-2.189
Rh(CO) ₂ A	-2.281	Rh ₂ (CO) ₃ 23	-1.980
Rh(CO) ₂ B	-2.230	Rh ₂ (CO) ₃ 28	-1.978
Rh(CO) ₂ C	-2.244	Rh ₂ (CO) ₈ - C _{2v}	-1.578
Rh(CO) ₃	-2.047	Rh ₂ (CO) ₈ - D _{2d}	-1.573
Rh(CO) ₄ A	-1.753	Rh ₂ (CO) ₈ - D _{3d}	-1.556
Rh(CO) ₄ B	-1.814	Rh ₂ (CO) ₈ - D _{4d}	-1.476
Rh ₂ (CO)	-2.357	Rh ₄ (CO) ₁₂ - C _{3v}	-1.668
Rh ₂ (CO) ₂	-2.418	Rh ₄ (CO) ₁₂ - T _d	-1.595
Rh ₂ (CO) ₃ 1	-2.068	Rh ₆ (CO) ₁₆ - D _{2d}	-1.586
Rh ₂ (CO) ₃ 2	-2.215	Rh ₆ (CO) ₁₆ - T _d	-1.649
Rh ₂ (CO) ₃ 3	-1.984		

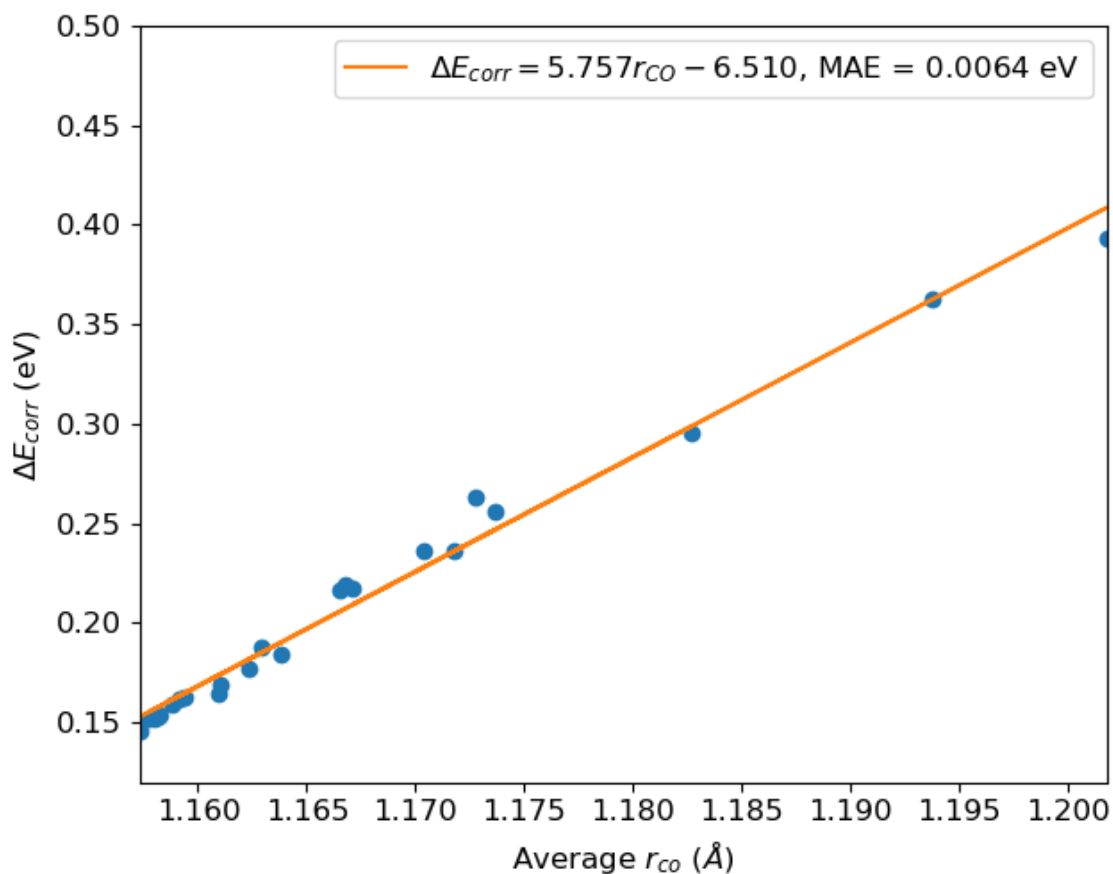
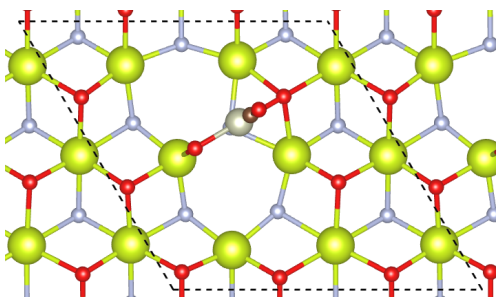
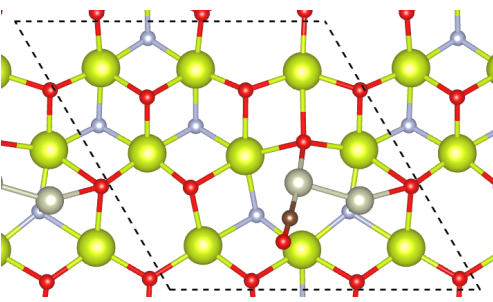
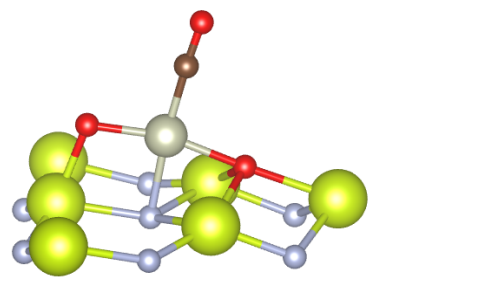
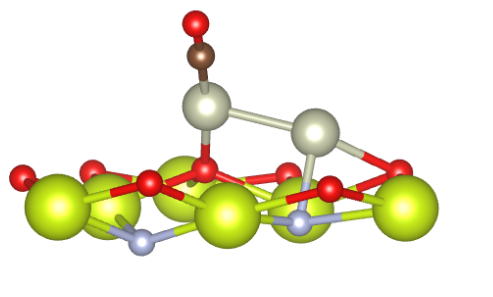
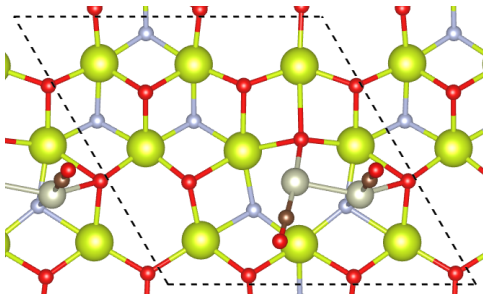
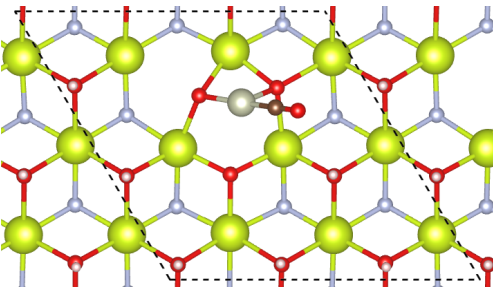
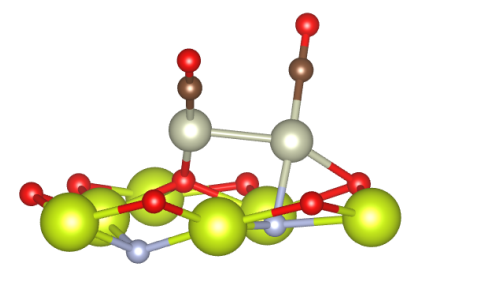
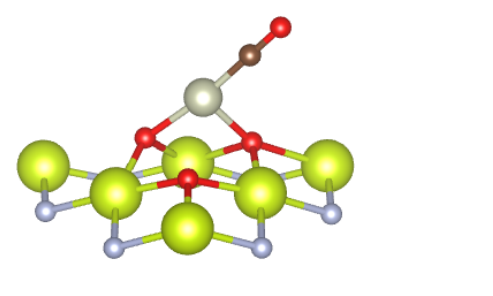


Figure A.11 The CO adsorption energy correction developed from Rh carbonyl molecules. The average CO bond length correlates linearly with the computed correction.

Table A.5 Top (2nd row) and side (3rd row) views of supported Rh carbonyl sites used to develop the CO adsorption energy correction.

Formula	$\text{Ce}_{27}\text{O}_{53}\text{-Rh}(\text{CO})$	$\text{Ce}_{27}\text{O}_{50}\text{-Rh}_2(\text{CO})$
Top view		
Side view		
Formula	$\text{Ce}_{27}\text{O}_{50}\text{-Rh}_2(\text{CO})_2$	$\text{Ce}_{27}\text{O}_{53}\text{H}_6\text{-Rh}(\text{CO})$
Top view		
Side view		

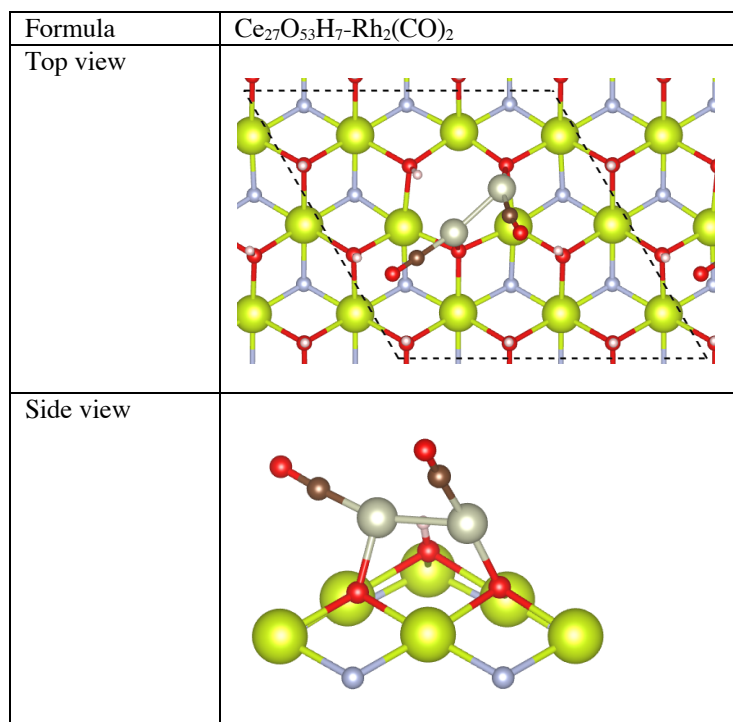
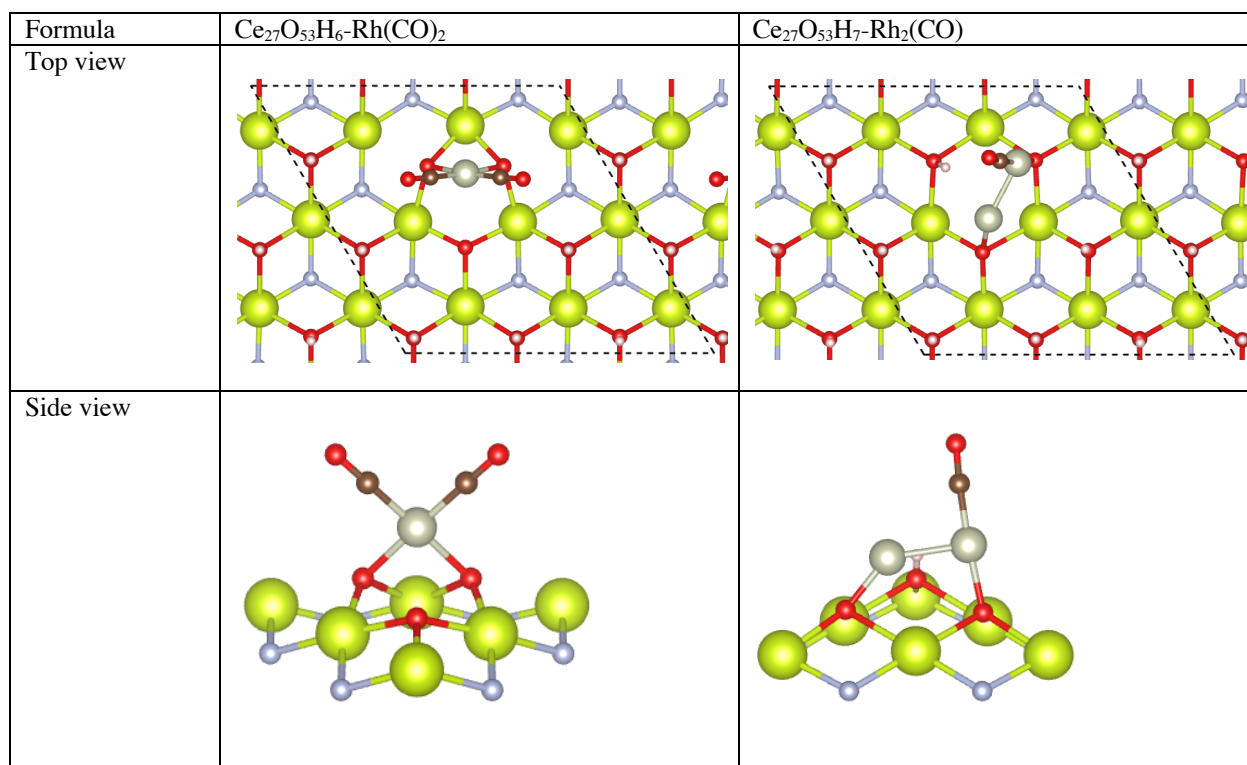


Table A.6 Extrapolated average CO adsorption energies of ceria-supported Rh carbonyls.

Supported Site	Extrapolated ΔE_{ads} (eV)	Supported Site	Extrapolated ΔE_{ads} (eV)
$\text{Ce}_{27}\text{O}_{53}\text{-Rh}(\text{CO})$	-2.069	$\text{Ce}_{27}\text{O}_{53}\text{H}_6\text{-Rh}(\text{CO})_2$	-2.082
$\text{Ce}_{27}\text{O}_{50}\text{-Rh}_2(\text{CO})$	-3.076	$\text{Ce}_{27}\text{O}_{53}\text{H}_7\text{-Rh}_2(\text{CO})$	-2.933
$\text{Ce}_{27}\text{O}_{50}\text{-Rh}_2(\text{CO})_2$	-2.720	$\text{Ce}_{27}\text{O}_{53}\text{H}_7\text{-Rh}_2(\text{CO})_2$	-2.403
$\text{Ce}_{27}\text{O}_{53}\text{H}_6\text{-Rh}(\text{CO})$	-1.925		

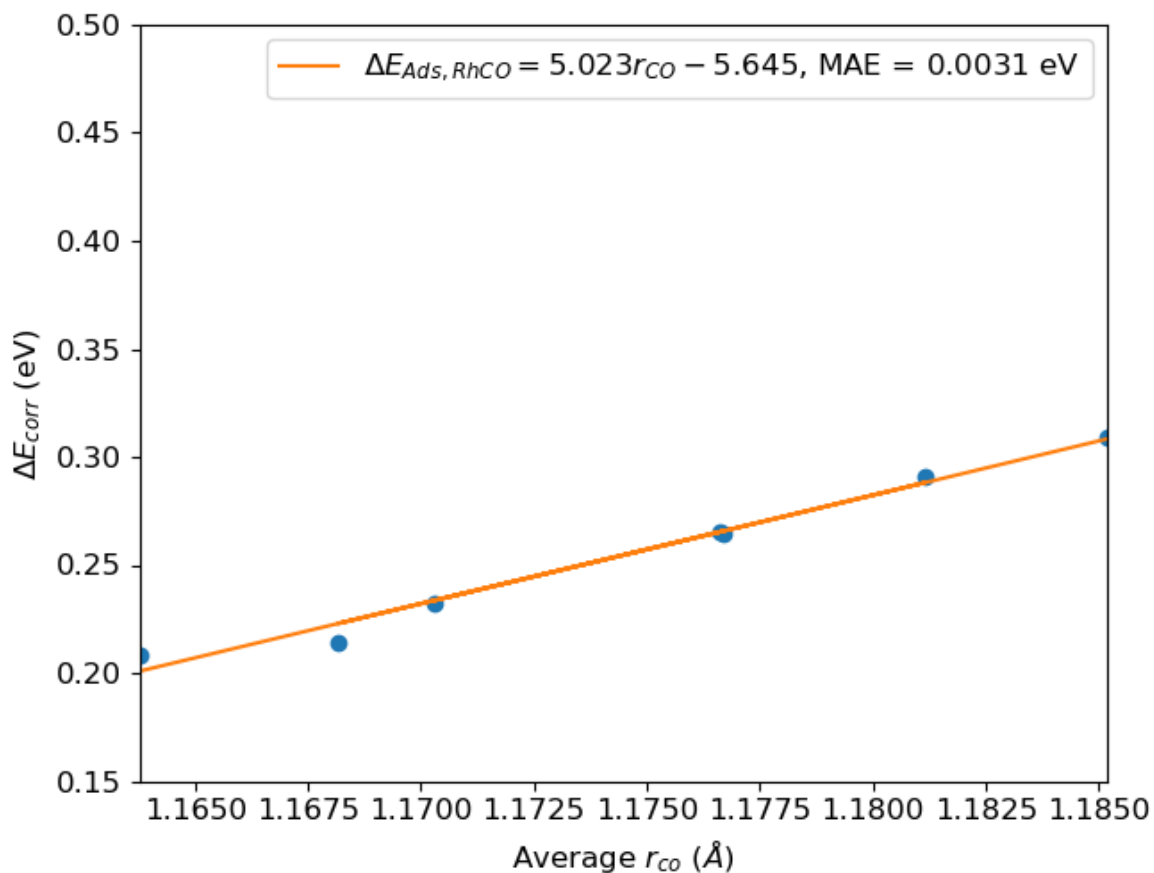


Figure A.12 The CO adsorption energy correction developed for supported Rh carbonyls. CO bond lengths again correlate linearly with the computed correction.

The PAW pseudopotentials and plane wave cutoff energies used for the construction of the correlations are summarized in **Table A.2**, and the Rh molecules used are shown in **Table A.3**. The computed corrections for the strength of CO adsorption correlate well with the average C-O

bond length (**Table A.4 and Figure A.11**). We then performed the same analysis for ceria-supported Rh carbonyls (**Table A.5**). The Brillouin zone of these surface structures was sampled using a $(3 \times 3 \times 1)$ mesh centered at the Gamma point. A similar linear correlation between the CO adsorption energy correction and the average C-O bond length (**Table A.6 and Figure A.12**) was found; this trendline was used as the CO adsorption energy correction for the supported Rh carbonyls.

Table A.7 Performance of the CO adsorption energy correction in predicting CO adsorption energies in molecular Rh carbonyls compared to those obtained by Fang et al. with CCSD(T).⁴³

Reaction	$\Delta H_{\text{rxn}}(0 \text{ K})$, CCSD(T) (eV)	$\Delta H_{\text{rxn}}(0 \text{ K})$, PBE, without correction (eV)	$\Delta H_{\text{rxn}}(0 \text{ K})$, PBE, with correction (eV)
$\text{Rh}(\text{CO})_2 + 2 \text{CO} \rightarrow \text{Rh}(\text{CO})_4$	-2.051	-2.748	-2.545
$\text{Rh}(\text{CO})_4 + \text{CO} \rightarrow \text{Rh}(\text{CO})_5$	0.173	0.024	0.100

Although DFT's descriptions of the gas phase single Rh atom and Rh₂ dimer lack static correlation, the addition of strong-field CO ligands can lower the degeneracy of the ground state wavefunction.^{230, 231} Through MRCI calculations, Dai and Balasubramanian found that the electronic wavefunction in the Σ^2 state makes up 92% of Rh(CO)'s electronic wavefunction.²³¹ It is thus likely that accurate post-Hartree-Fock methods, such as CCSD(T), can make good predictions of Rh-CO bond energies in Rh bound to more than one CO. For confirmation, we performed the T₁ diagnostic on the Rh(CO)₂-A molecule. This calculation was performed using Gaussian09.²³² The aug-cc-pVTZ basis set were used for the C, O, and Rh atoms, and a 17-electron RECP was used to describe Rh's core electrons.²³³⁻²³⁵ We found both the T₁ value and the maximum t₁ amplitude to be acceptable (T₁ = 0.029, max(t₁) = 0.0545).²³⁶ For the reactions, Rh(CO)₂ + 2 CO → Rh(CO)₄ and Rh(CO)₄ + CO → Rh(CO)₅, Fang et al. calculated the reaction enthalpies at the

CCSD(T)/aug-cc-pVDZ//SVWN5/aug-cc-pVDZ level.⁴³ Through the correction scheme developed, the $\Delta H_{\text{rxn}}(0 \text{ K})$ calculated at the PBE level becomes closer to the reported CCSD(T) values. The zero-point energies were computed using VASP at the PBE level (**Table A.7**).

In contrast to the PBE-only calculations, our calculation of the CO adsorption energies on $\text{Rh}(\text{CO})_2$ has improved; however, the corrected CO adsorption energies are still overestimated by 0.25 eV/CO compared to these values in the referenced post-HF calculations. We note that, however, the compared calculations are for unsupported $\text{Rh}_1(\text{CO})_x$ molecules but not for Rh_3 clusters anchored on a surface. For surface calculations such as our groups' recent collaborative work on the CO/Pt system, our correction scheme gives slightly smaller errors (i.e. 0.15-0.2 eV for CO on Pt(111)).¹⁰⁷ In addition, based on computational results in **Figures 2.2 and 2.3**, we note that varying the CO pressure by 1-2 orders of magnitude, or by varying the CO chemical potential by 0.15 eV does not change our conclusions in terms of the structure of catalytic site. Even a change of 0.25 eV would still result in $\text{Rh}_3(\text{CO})_x$ as the most stable configuration under reaction conditions. Therefore, we do not think that the remaining error has a large impact on the identification of $\text{Rh}_3(\text{CO})_3$ as the active site.

Table A.8 Performance of the CO adsorption energy correction in predicting the $\text{Rh}(\text{CO})_4$ dimerization energy and relative energy of $\text{Rh}_2(\text{CO})_8$ isomers compared to those obtained by Fang et al. with CCSD(T).⁴³

Reaction	$\Delta H_{\text{rxn}}(0 \text{ K})$, CCSD(T) (eV)	$\Delta H_{\text{rxn}}(0 \text{ K})$, PBE, without correction (eV)	$\Delta H_{\text{rxn}}(0 \text{ K})$, PBE, with correction (eV)
$2\text{Rh}(\text{CO})_4 \rightarrow \text{Rh}_2(\text{CO})_8 - \text{C}_{2v}$	-2.155	-1.500	-1.467
$\text{Rh}_2(\text{CO})_8 - \text{D}_{3d} \rightarrow \text{Rh}_2(\text{CO})_8 - \text{C}_{2v}$	-0.121	-0.319	-0.171

Table A.9 Performance of the CO adsorption energy correction in predicting the relative stability of $\text{Rh}_4(\text{CO})_{12}$ isomers. The result is comparable to those predicted by averaging the energies calculated by MP2 and the ωB97xD functional.⁴³

Reaction	Relative Stability (eV)	ΔE_{rxn} , PBE, without correction (eV)	ΔE_{rxn} , PBE, with correction (eV)
$\text{Rh}_4(\text{CO})_{12} - \text{C}_{3v} \rightarrow \text{Rh}_4(\text{CO})_{12} - \text{T}_d$	0.222	1.068	0.876

For the Rh dimers, although the CO bond correction does not change the Rh-Rh bond energy, the description of the relative stability of $\text{Rh}_2(\text{CO})_8$ isomers was improved (**Table A.8**). By tracking the fraction of the two $\text{Rh}_4(\text{CO})_{12}$ isomers using IR spectroscopy, Allian and Garland found the C_{3v} isomer to be 5.11 kcal/mol (0.222 eV) more stable.²³⁷ Through extensive benchmarking, Ding et al. found the B97-D functional to be the best in the description of relative stability of the two isomers.²³⁸ Upon application of the C-O bond correction, the T_d - C_{3v} energy difference is 0.876 eV, a large improvement from the uncorrected values (**Table A.9**).

A.6 The structure of the CeO₂(111) surface during catalysis

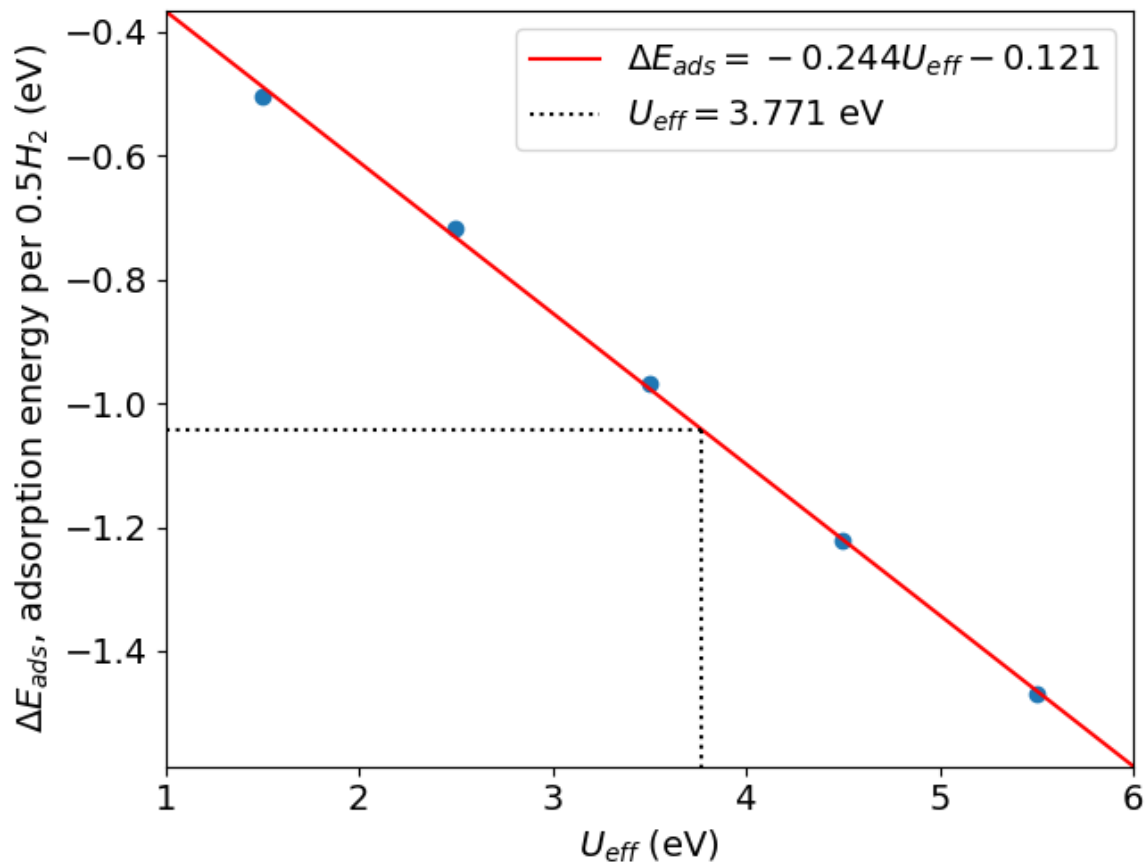


Figure A.13 Fitted U_{eff} value for H₂ adsorption energy at a full monolayer. A U_{eff} value of 3.771 eV reproduces the H₂ adsorption energy determined through HSE06.

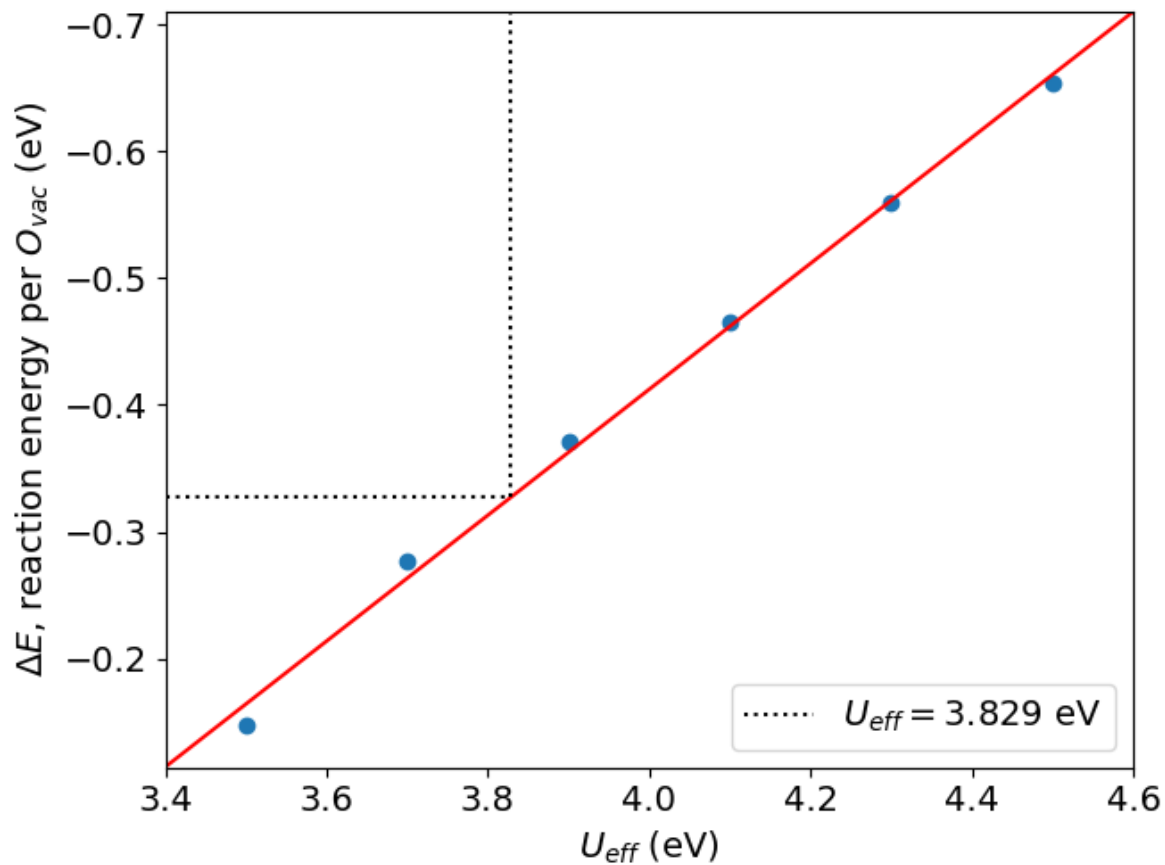


Figure A.14 Fitted U_{eff} value for average O_{vac} formation energy by H_2 reduction at 1/3 monolayer.

A U_{eff} value of 3.829 eV reproduces the vacancy formation energy determined through HSE06.

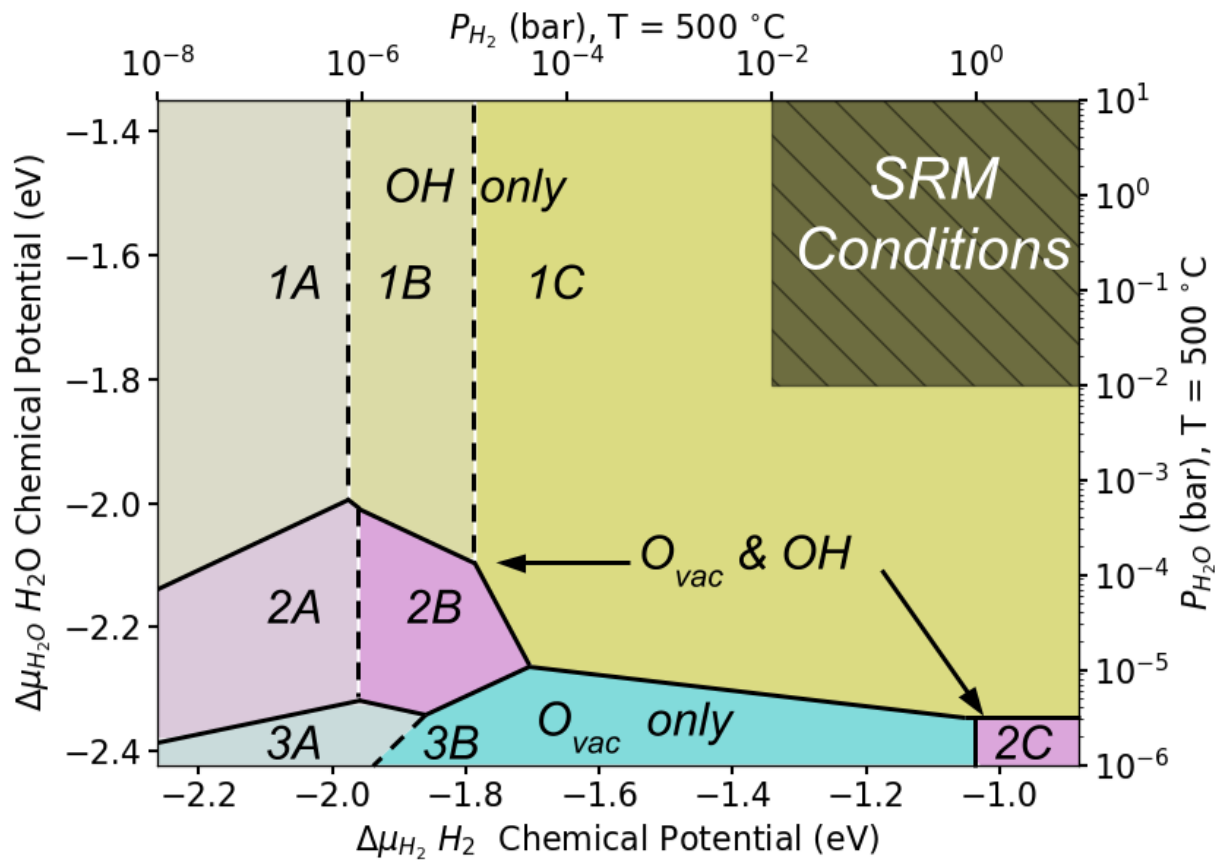


Figure A.15 H₂O/H₂ 2D stability diagram computed using the major structures appearing on **Figure 2.1** and $U_{\text{eff}} = 3.67$ eV. The olive-colored hatched region represents the possible H₂O/H₂ chemical potentials encountered by the catalyst under the SRM catalytic conditions.

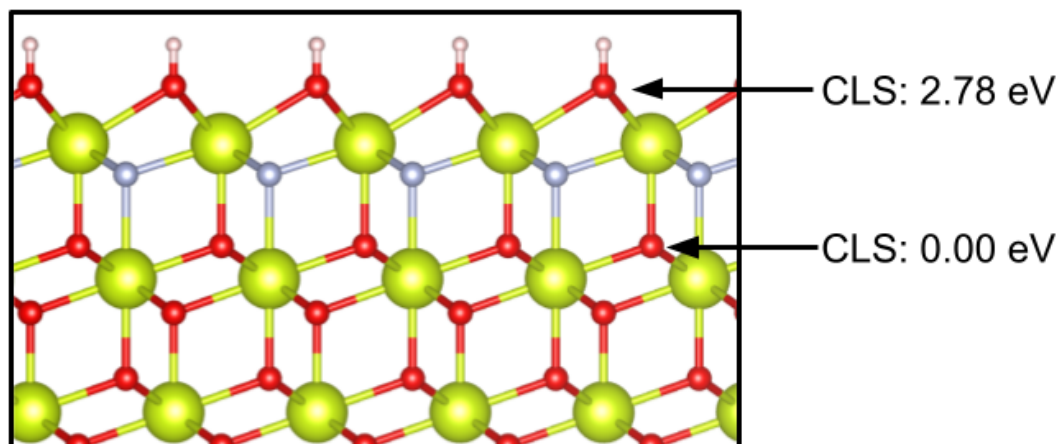
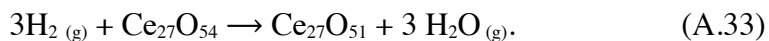


Figure A.16 Calculated O 1s core level shift of surface OH groups on CeO₂(111). The final state approximation is used here with an O ion in the 4th layer beneath the layer of OH groups as the reference. An additional O-Ce-O trilayer was added in these calculations.

Using the screening procedures specified previously and a constant 0.4 eV vibrational penalty per O vacancy, we obtained the following surface stability diagram for CeO₂(111) under an environment of H₂ and H₂O (**Figure 2.1**). The presence of guest H'O' groups on the catalyst surface under SRM condition is evidenced by the observed blue peaks at 531.3 eV in the AP-XPS spectra assigned to O atoms of guest H'O' bonded to the reduced Ce³⁺ based on the reference²³⁹ and the green peak at 532.0 eV attributed to native O_{surf}* atom bonding to both a guest H' atom and a Ce³⁺ underneath (H'-O_{surf}*-Ce³⁺-O) based on reference²⁴⁰. Notably, our DFT calculations suggest that the O 1s core level binding energy of guest H'O' groups on CeO₂(111) is higher than the subsurface O atoms fully bonding with Ce⁴⁺ ions in CeO₂ lattice by 2.78 eV (**Figure A.16**). The predicted difference is consistent with the experimentally observed upshift by 1.6-2.3 eV resulting from the difference between 531.3 eV of H'-O_{surf}*-Ce³⁺-O or 532.0 eV of H'O'-Ce³⁺-O and 529.7 eV of regular lattice oxide uncovered by AP-XPS. In addition, the OH vibrational

frequency (3706 cm⁻¹) we calculated is close to the bridging OH band at 3690 cm⁻¹ observed on CeO₂ nanorods to grow in intensity after treatment in H₂ from 533 K up to 673 K.⁹³ Obviously, these experimental observations of H'O'- or H'-covered surfaces are consistent with the proposed phase diagrams of the CeO₂(111) surface in H₂O or H₂.

Since there are many choice of U_{eff} in the modeling of materials with strongly correlated electrons, we also examined the effect of using a U_{eff} value fitted to energetics determined by the HSE06 hybrid functional.¹⁵⁰ The following surface reduction reactions were used to empirically calibrate U_{eff} (Figures A.13 and A.14):



The same plane wave cutoff and k-mesh specified in the supplementary methods were used in these calculations. Forces on atoms were converged to below 0.03 eV/Å. Applying a value of U_{eff} = 3.67 eV to the major structures present on **Figure 2.1** and using the same 0.4 eV penalty per O_{vac}, we obtained a similar 2D stability diagram (**Figure A.15**). The same hydroxylated surface structure was obtained under steam reforming conditions.

A.7 Distribution of Rh active sites during catalysis

With the methods for calculating Gibbs free energy and CO adsorption energy corrections in hand, we can estimate the Gibbs free energies of formation of the Rh sites and rank them by stability (**Figure 2.3**). The correlations were applied to the selected stable Rh structures computed at the accuracy level specified in the method section (146 structures out of 500+ screened structures). We see that the most stable Rh_m(CO)_n structure under reaction at 500 °C is the

$\text{Rh}_3(\text{CO})_3$ site, with a slightly different $\text{Rh}_3(\text{CO})_3$ configuration as the runner-up. Overall, the $\text{Rh}_3(\text{CO})_n$ species should make up the majority of surface Rh.

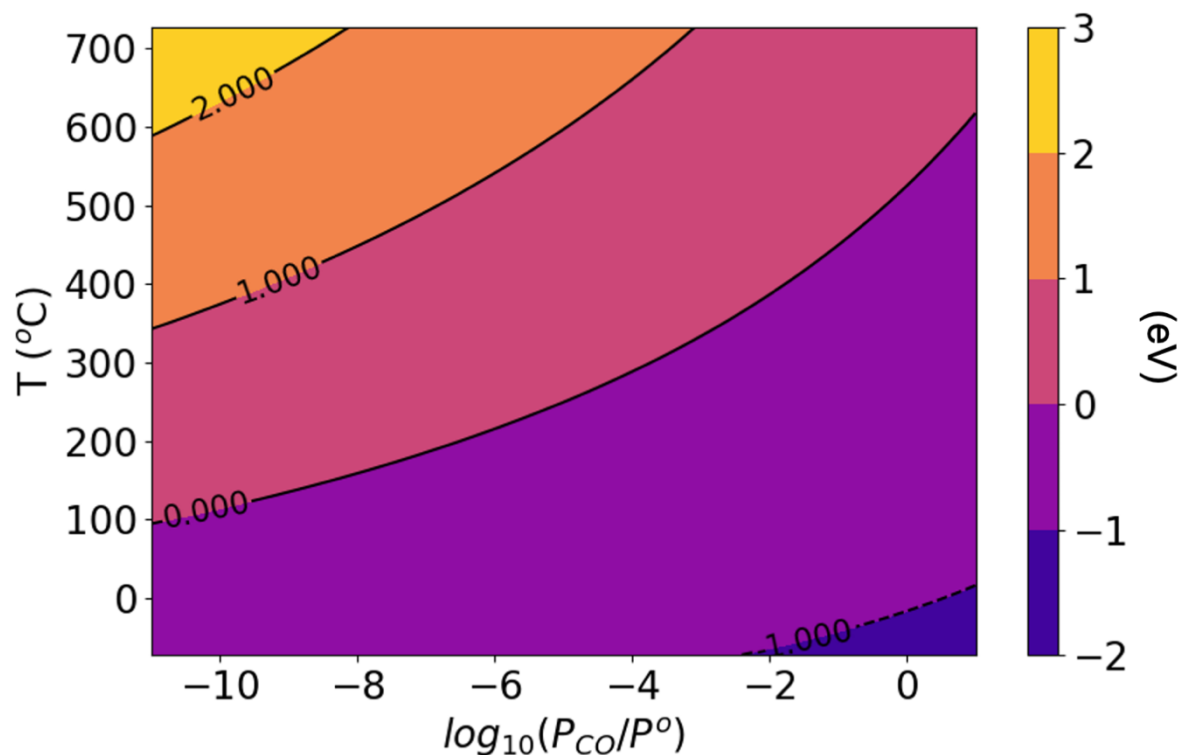


Figure A.17 The Gibbs free energy of formation of the $\text{Rh}_3(\text{CO})_3$ site as a function of temperature and CO pressure. The solid line between the Salmon and Purple regions demarcates the phase boundary between Rh nanoparticles and $\text{Rh}_3(\text{CO})_3$ sites, above which the Rh NP is the more stable species.

By varying the temperature and CO pressure while holding constant the chemical potentials of H_2 and H_2O , we can examine the evolution of supported Rh clusters in response to changes in the gas environment. The most stable Rh structures (excluding Rh_{13}) are shown in **Figure 2.2a**, and the minimum Gibbs free energy of formation of the Rh structures are plotted in **Figure 2.2b**. For reference, the Gibbs free energy of formation of $\text{Rh}_3(\text{CO})_3$ is shown in **Figure A.17**.

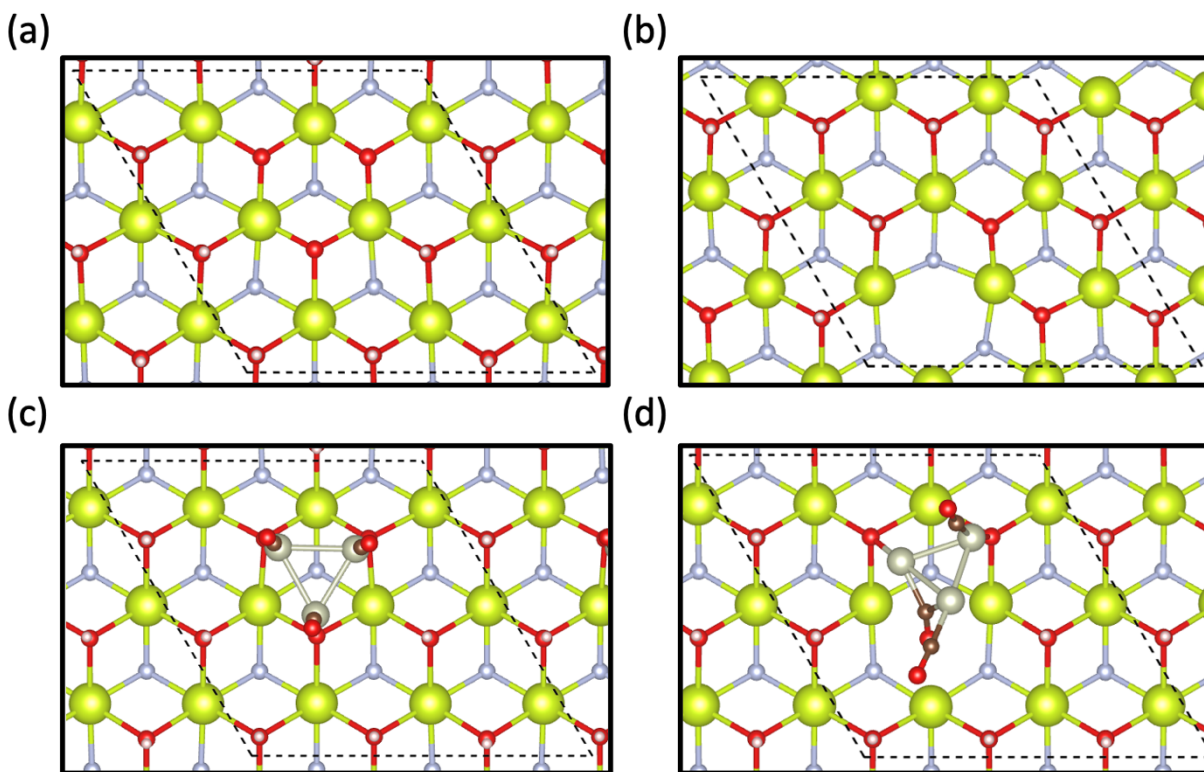


Figure A.18 (a) The hydroxylated CeO_2 surface with $5.09 \text{ OH}/\text{nm}^2$ (Region 1B in **Figure 2.1**) and (b) one with $5.09 \text{ OH}/\text{nm}^2$ and $0.85 \text{ O}_{\text{vac}}/\text{nm}^2$. (c) The geometry a $\text{Rh}_3(\text{CO})_3$ cluster adsorbed on the hydroxylated CeO_2 surface without and (d) with a surface O vacancy.

Geometries used to analyze the interaction strength between Rh clusters and the CeO_2 surface are shown in **Figure A.18**.

A.8 DFT-based spectroscopic calculations of simulated Rh active sites

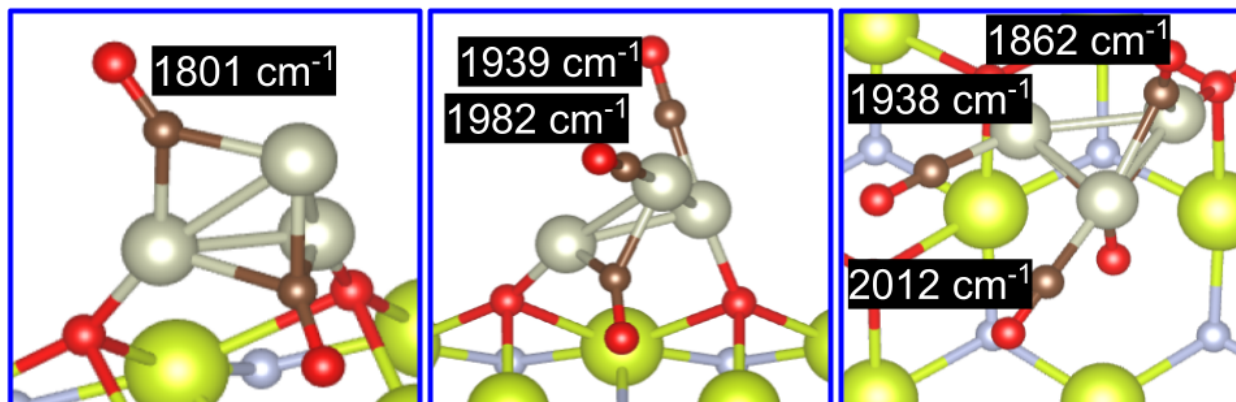


Figure A.19 Principal $\nu(\text{CO})$ vibrational modes of $\text{Rh}_3(\text{CO})_2^+$, $\text{Rh}_3(\text{CO})_3^+$, and $\text{Rh}_3(\text{CO})_4^+$. The vibrational frequency of the principal C-O stretching mode increases with coverage.

To track the vibrational signatures of $\text{Rh}_m(\text{CO})_n$ sites, we computed the principal $\nu(\text{CO})$ vibrational mode of the most stable $\text{Rh}_3(\text{CO})_{2-4}$ clusters (**Figure A.19**). The vibrational modes of $\text{Rh}_3(\text{CO})_3$ are in qualitative agreement with the $\nu(\text{CO})$ modes detected by in-situ DRIFTS. We see that the stretching mode of CO in the “atop” binding configuration increases with coverage.

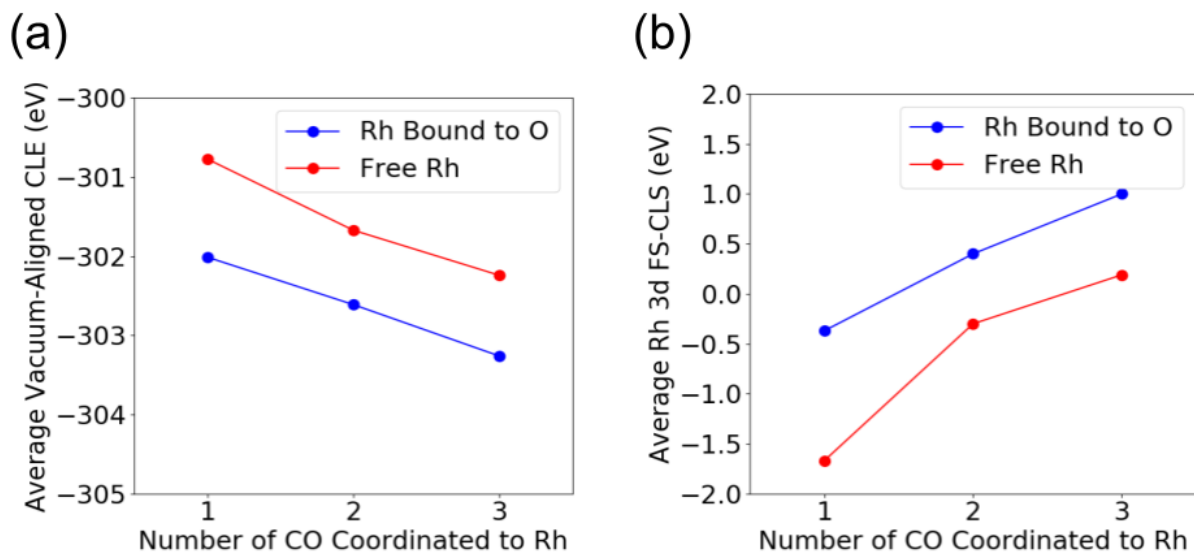


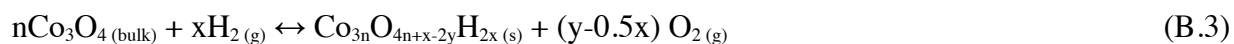
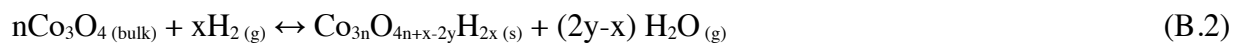
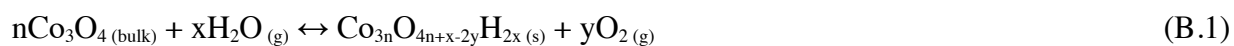
Figure A.20 (a) Initial state approximation and (b) final state approximation core level shift calculations performed to assess the role of CO on the Rh 3d binding energy. Both approximations show that the adsorption of CO increases the Rh 3d binding energy of the supported $\text{Rh}_3(\text{CO})_x$ cluster.

To further assess the effect of CO on the spectroscopic signatures of Rh, Rh 3d core level shift (CLS) calculations of 27 $\text{Rh}_3(\text{CO})_{2.4}$ clusters were performed. By comparing the average initial state and final state Rh 3d CLS against the number of CO coordinated to the Rh atom (**Figure A.20**), we see that the adsorption of CO results in a positive CLS. Each adsorbed CO raises the binding energy by roughly 0.4 eV. Further, binding to lattice O also results in a positive CLS.

Appendix B Supplementary Information for Chapter 3

B.1 Procedure for Surface Energy Calculations

For a given gas phase condition, the most stable surface is that with the lowest surface free energy (γ). Since only one side of the slab was modified, the directly determined γ is the average between those of the unmodified and the modified sides.^{90, 91} To compare only the modifications, contributions from the unmodified slab must be subtracted from the total. The formation reaction of a surface with some degree of vacancies and hydroxylation, defined as $\text{Co}_{3n}\text{O}_{4n+x-2y}\text{H}_{2x}$, is given as one of the following, depending on which gases the surface was in equilibrium with:



In reaction (B.1), n moles of bulk Co_3O_4 react with x moles of gas phase H_2O (H reservoir) to form the target surface and y moles of O_2 (O reservoir). In reaction (B.2) the H reservoir is replaced with H_2 and the O reservoir with H_2O . Finally, in reaction (B.3), the O reservoir is replaced back with O_2 . The free energy (ΔG) of each formation reaction was estimated by assuming that vibrational effect differences for solid systems are negligible.⁹⁰ For the case of reaction (B.1), equation (B.4) was used, for reaction (B.2), equation (B.5), and for reaction (B.3), equation (B.6):

$$\Delta G \approx E + 2y\mu_{\text{O}} - nE_{\text{Co}_3\text{O}_4} - x\mu_{\text{H}_2\text{O}} \quad (\text{B.4})$$

$$\Delta G \approx E + (2y - x)\mu_{\text{H}_2\text{O}} - nE_{\text{Co}_3\text{O}_4} - x\mu_{\text{H}_2} \quad (\text{B.5})$$

$$\Delta G \approx E + (2y - x)\mu_{\text{O}} - nE_{\text{Co}_3\text{O}_4} - x\mu_{\text{H}_2} \quad (\text{B.6})$$

The chemical potentials for each gas species were estimated using equations (B.7) and (B.8):

$$\mu_i \approx E_i + \Delta\mu_i^0(T, P^0) + k_{\text{B}}T \ln\left(\frac{P}{P^0}\right) \quad (\text{B.7})$$

$$\Delta\mu_i \approx H(T, P^0) - H(0 \text{ K}, P^0) - TS(T, P^0) + TS(0 \text{ K}, P^0) \quad (\text{B.8})$$

Where E is the energy of the slab calculated by DFT, μ_i is the approximate chemical potential of compound i , $E_{\text{Co}_3\text{O}_4}$ is the energy of a bulk unit of Co_3O_4 , $\Delta\mu_i^0$ is the chemical potential correction, calculated from H and S values taken from the NIST JANAF tables, P is the pressure of the system, P^0 is the reference pressure (1 bar), T is the temperature of the system, and k_{B} is the Boltzmann constant.²⁴¹ We considered the chemical potential of oxygen as half that of the triplet oxygen.

Finally, the surface energy of the full $\text{Co}_{3n}\text{O}_{4n+x-2y}\text{H}_{2x}$ or $\text{Co}_{3n}\text{O}_{4n-y}\text{H}_{2x-2y}$ structure was computed and corrected for the presence of two different surfaces in the slab (B.9, B.10):

$$\gamma_{\text{s}} = \frac{\Delta G}{2A} \quad (\text{B.9})$$

$$\gamma = 2\gamma_{\text{s}} - \gamma_0 \quad (\text{B.10})$$

Where A is the surface area of the slab model, γ_s is the surface energy of the structure without correcting for the blank surface, γ_0 is the surface energy of the blank surface, and γ is corrected surface energy.

B.2 Surface energy as functions of $\text{H}_2\text{O}/\text{H}_2/\text{O}_{\text{vac}}$ coverage as functions of $\text{H}_2\text{O}/\text{H}_2/\text{O}$ chemical potential and temperature

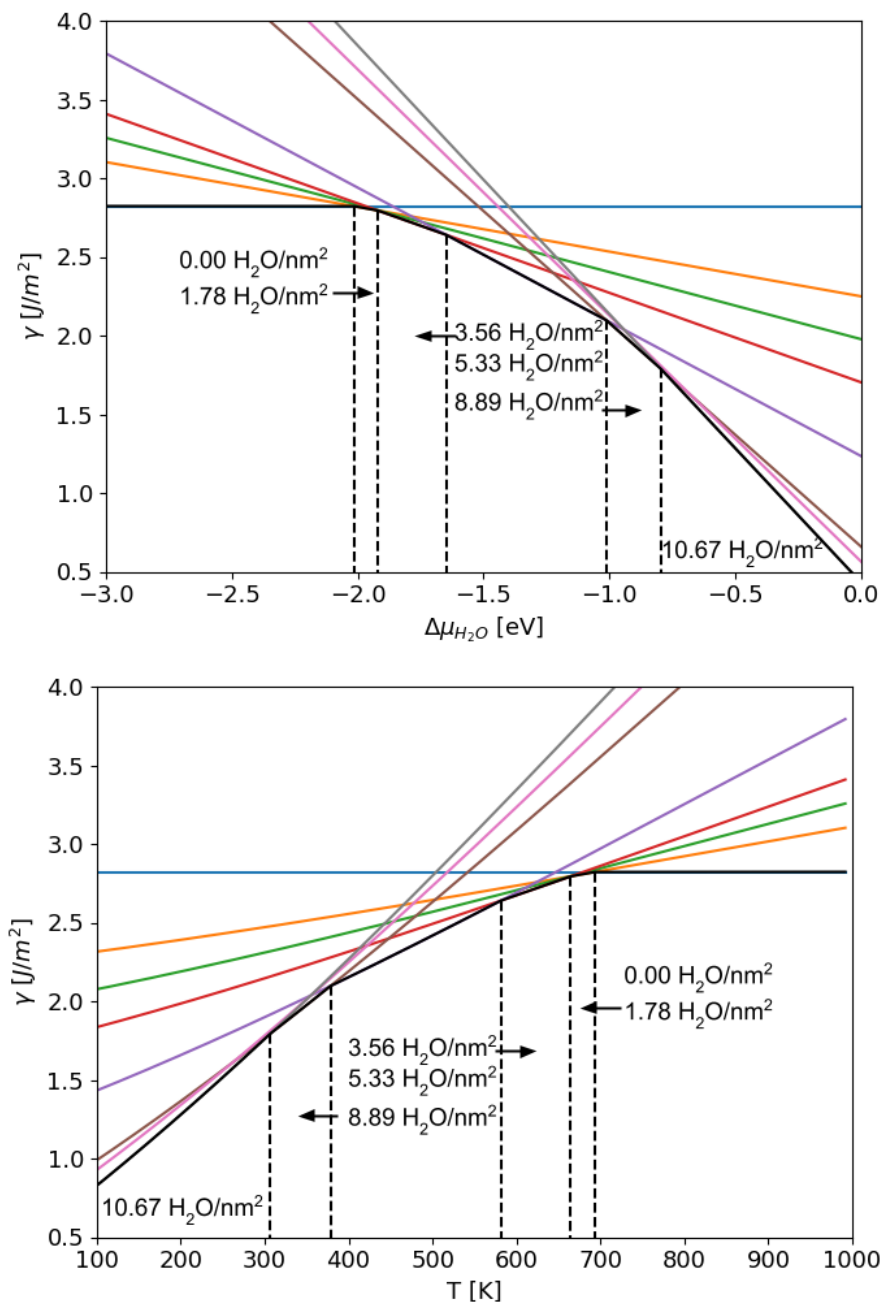


Figure B.1 Hydroxylation of $(\text{Co}^{\text{Td}}\text{Co}^{\text{Oh}})_x$ through H_2O adsorption on the bare surface at oxygen rich conditions ($\Delta\mu_{\text{O}} = 0$ eV). Surface energy of is plotted as (top) $\gamma(\Delta\mu_{\text{H}_2\text{O}})$ and (bottom) $\gamma(T, P_{\text{H}_2\text{O}}=10^{-5}$ bar). Vertical lines represent surface structure transition points.

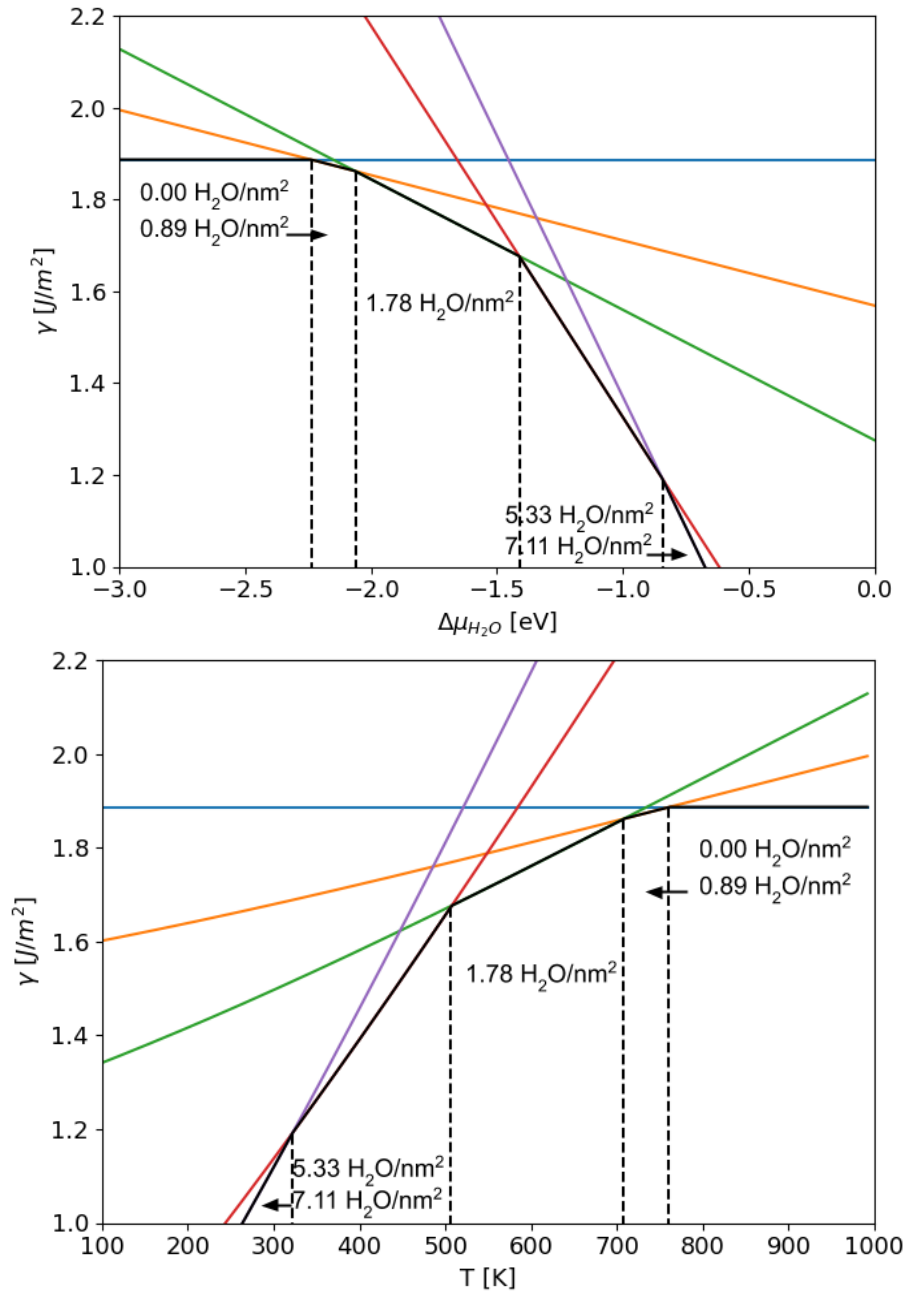


Figure B.2 Hydroxylation of $(\text{Co}^{\text{Td}}\text{Co}^{\text{Oh}}_{0.5})_x$ through H_2O adsorption on the bare surface under oxygen rich conditions ($\Delta\mu_{\text{O}} = 0 \text{ eV}$). Surface energy of is plotted as (top) $\gamma(\Delta\mu_{\text{H}_2\text{O}})$ and (bottom) $\gamma(T, P_{\text{H}_2\text{O}}=10^{-5} \text{ bar})$.

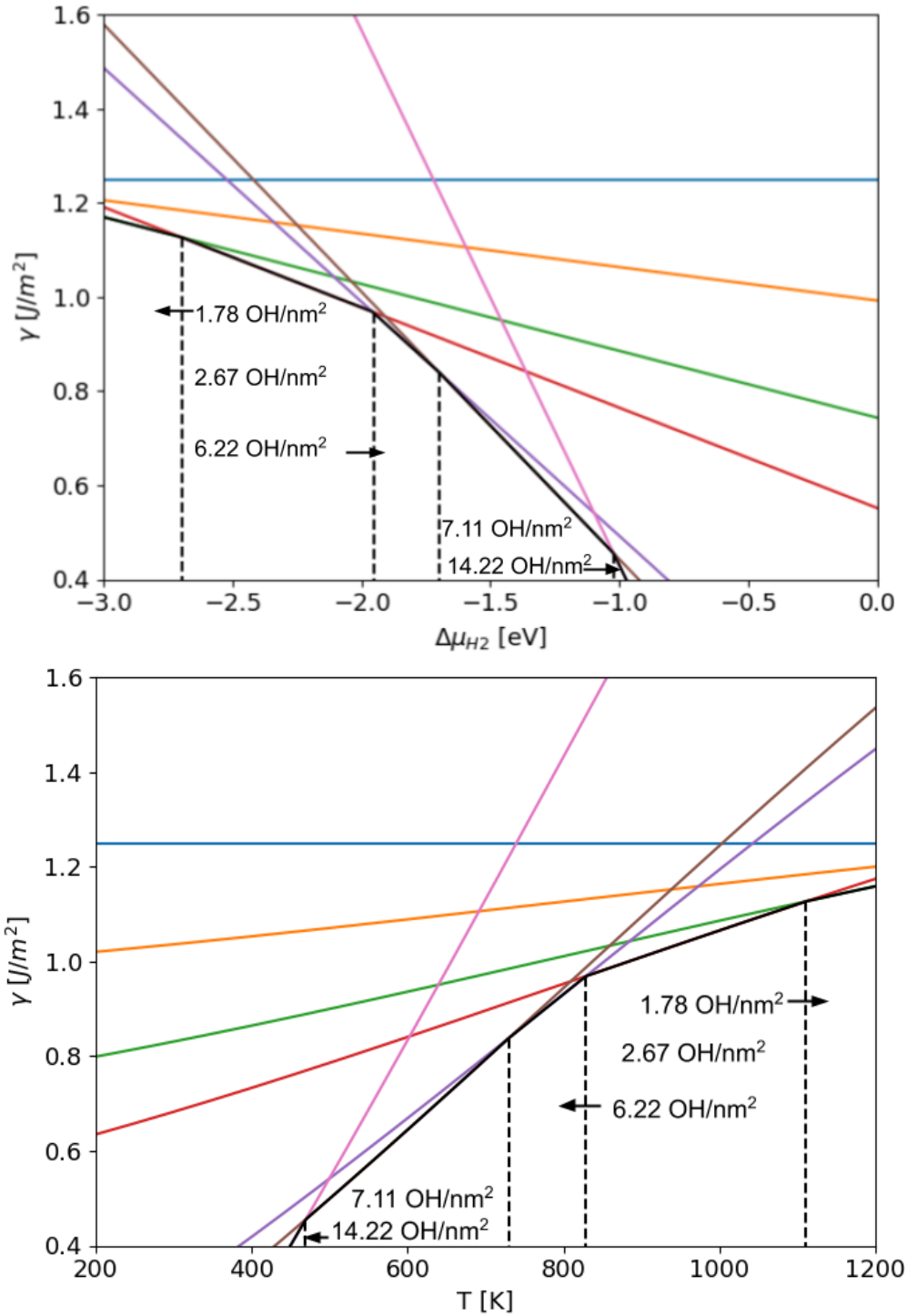


Figure B.3 Reduction of $(Co^{Td})_x$ through H_2 chemisorption at oxygen rich conditions, $\Delta\mu_O = 0$ eV. Surface energy of is plotted as (top) $\gamma(\Delta\mu_{H_2})$ and (bottom) $\gamma(T, P_{H_2}=10^{-5}$ bar).

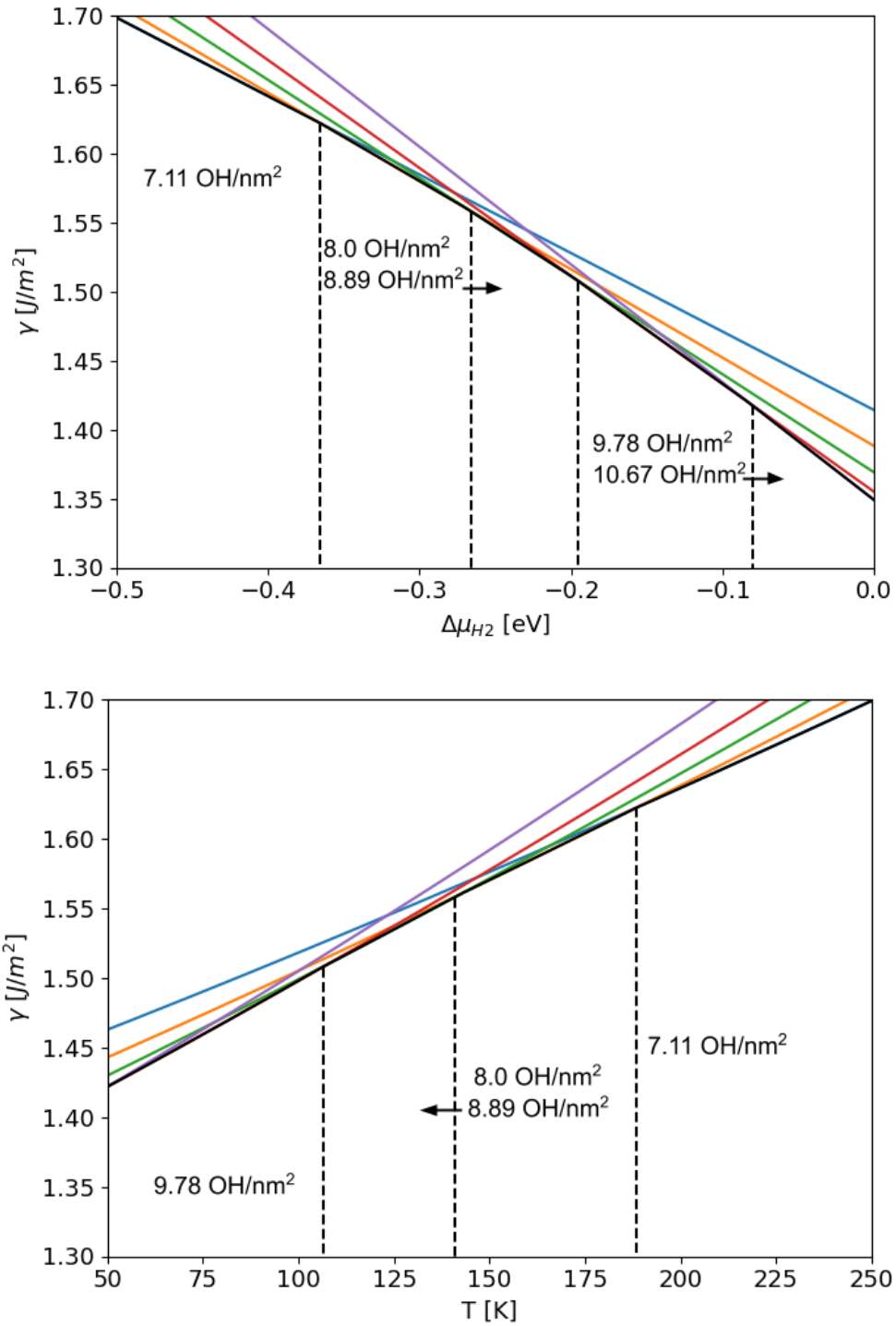


Figure B.4 Reduction of $(Co^{Td}Co^{Oh})_x$ through H_2 chemisorption at oxygen rich conditions, $\Delta\mu_o = 0$ eV. Surface energy of is plotted as (top) $\gamma(\Delta\mu_{H_2})$ and (bottom) $\gamma(T, P_{H_2}=10^{-5}$ bar).

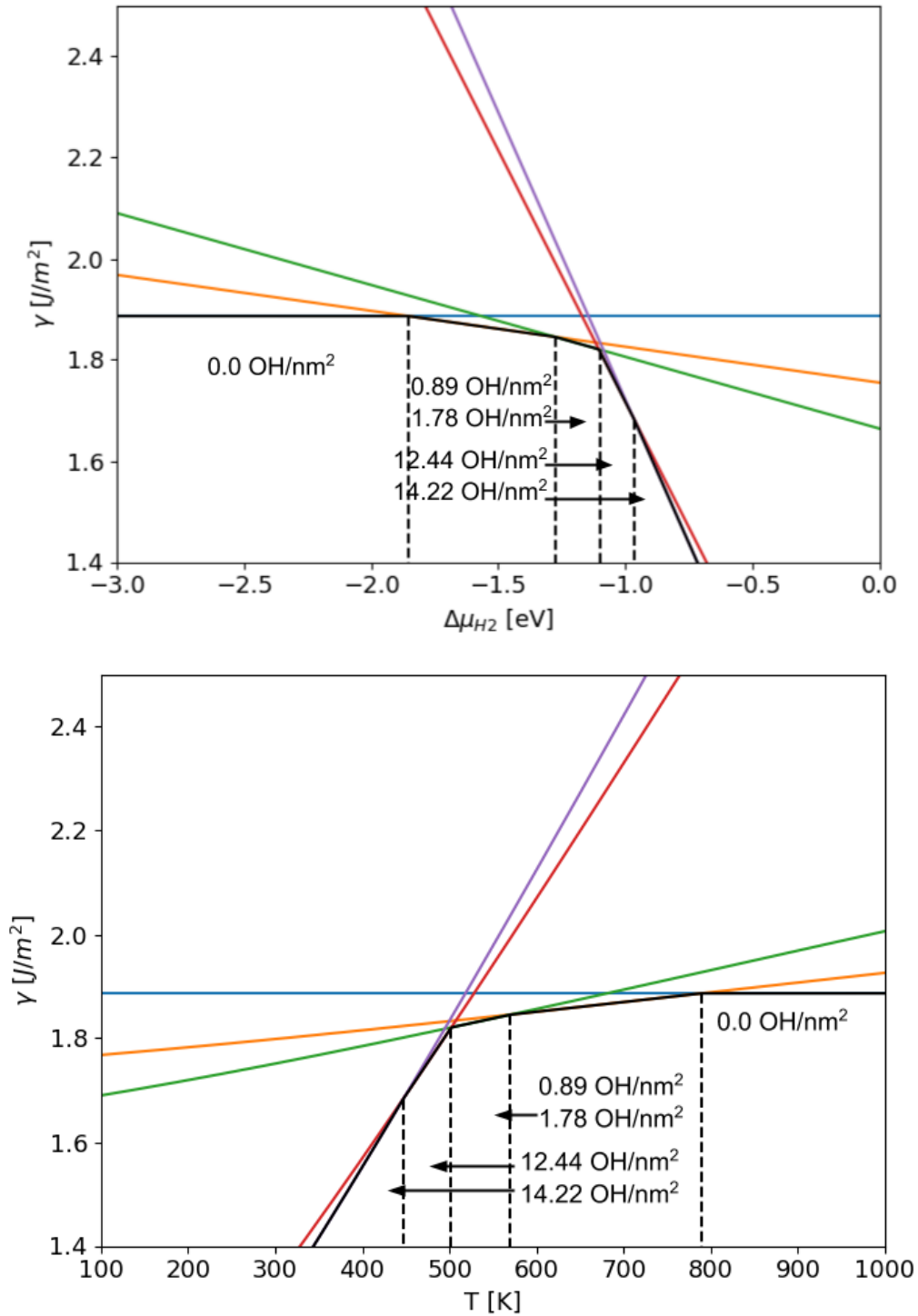


Figure B.5 Reduction of $(\text{Co}^{\text{Td}}\text{Co}^{\text{Oh}}_{0.5})_x$ through H_2 chemisorption at oxygen rich conditions, $\Delta\mu_{\text{O}} = 0$ eV. Surface energy of is plotted as (top) $\gamma(\Delta\mu_{\text{H}_2})$ and (bottom) $\gamma(T, P_{\text{H}_2}=10^{-5}$ bar).

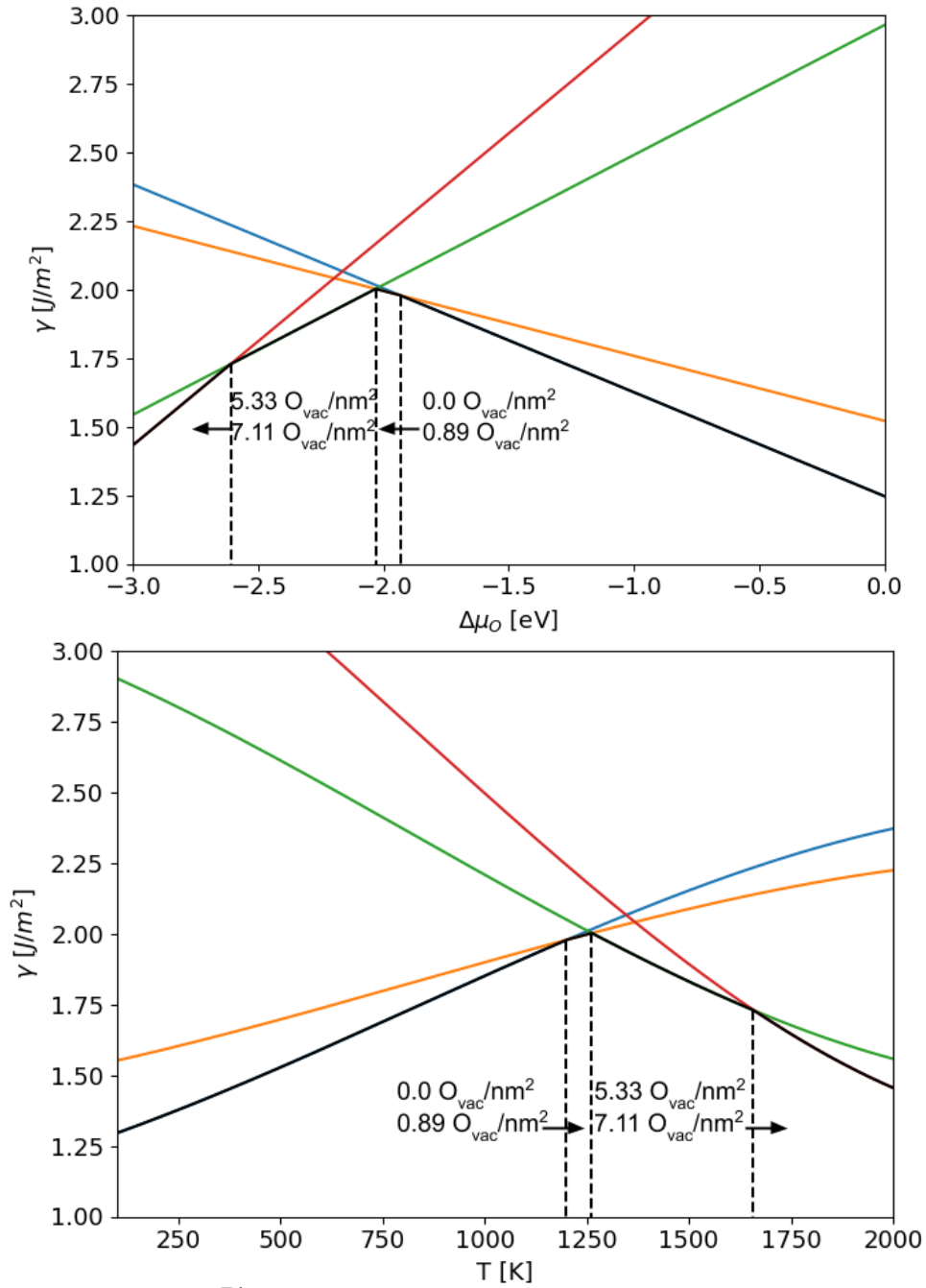


Figure B.6 Reduction of $(\text{Co}^{\text{Td}})_x$ through O_{vac} formation without consideration of H_2 or H_2O , (top) as $\gamma(\Delta\mu_{\text{O}})$ and (bottom) as $\gamma(T, P_{\text{O}_2}=10^{-5} \text{ bar})$.

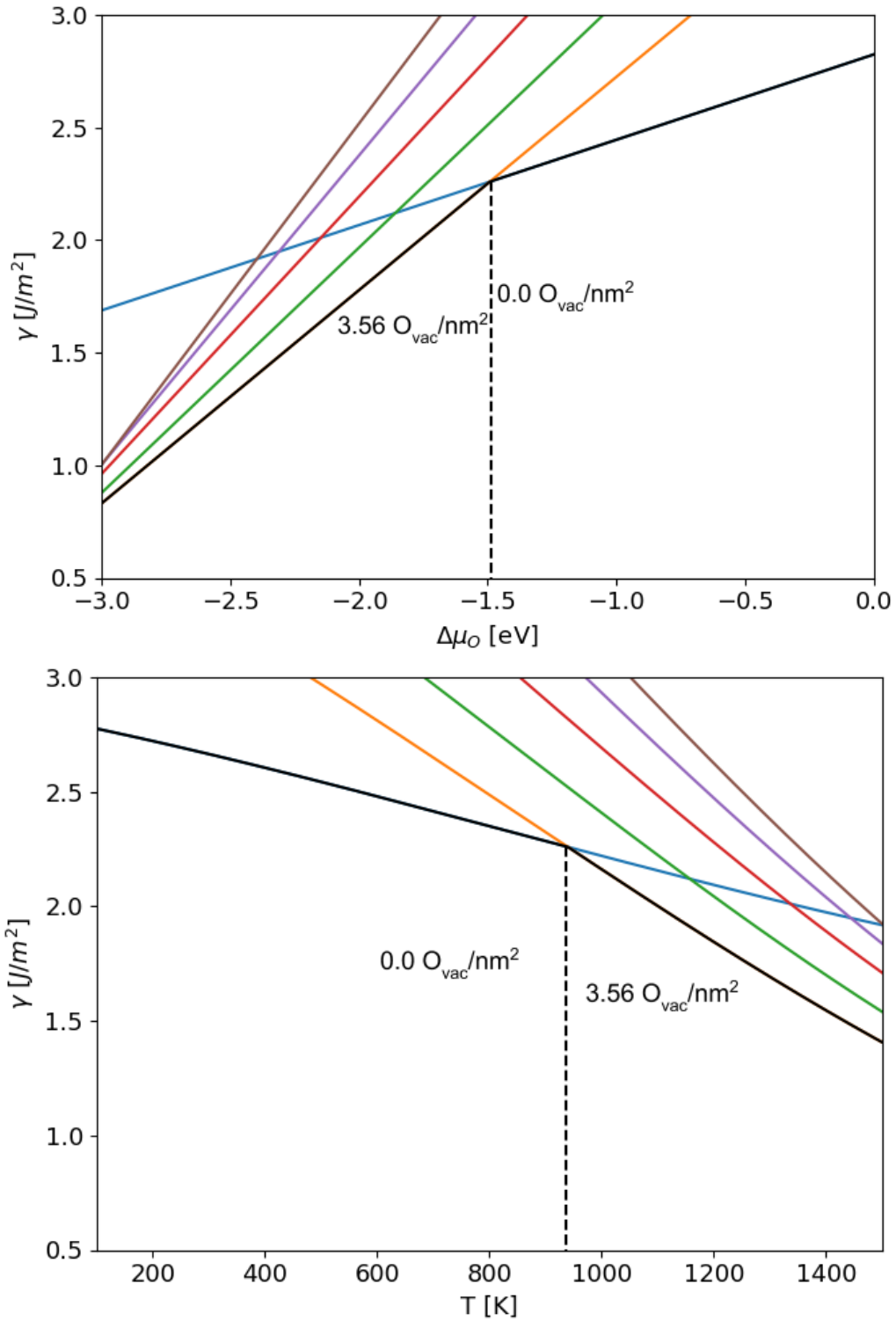


Figure B.7 Reduction of $(\text{Co}^{\text{Td}}\text{Co}^{\text{Oh}})_x$ through O_{vac} formation without consideration of H_2 or H_2O , (top) as $\gamma(\Delta\mu_{\text{O}})$ and (bottom) as $\gamma(T, P_{\text{O}_2}=10^{-5} \text{ bar})$.

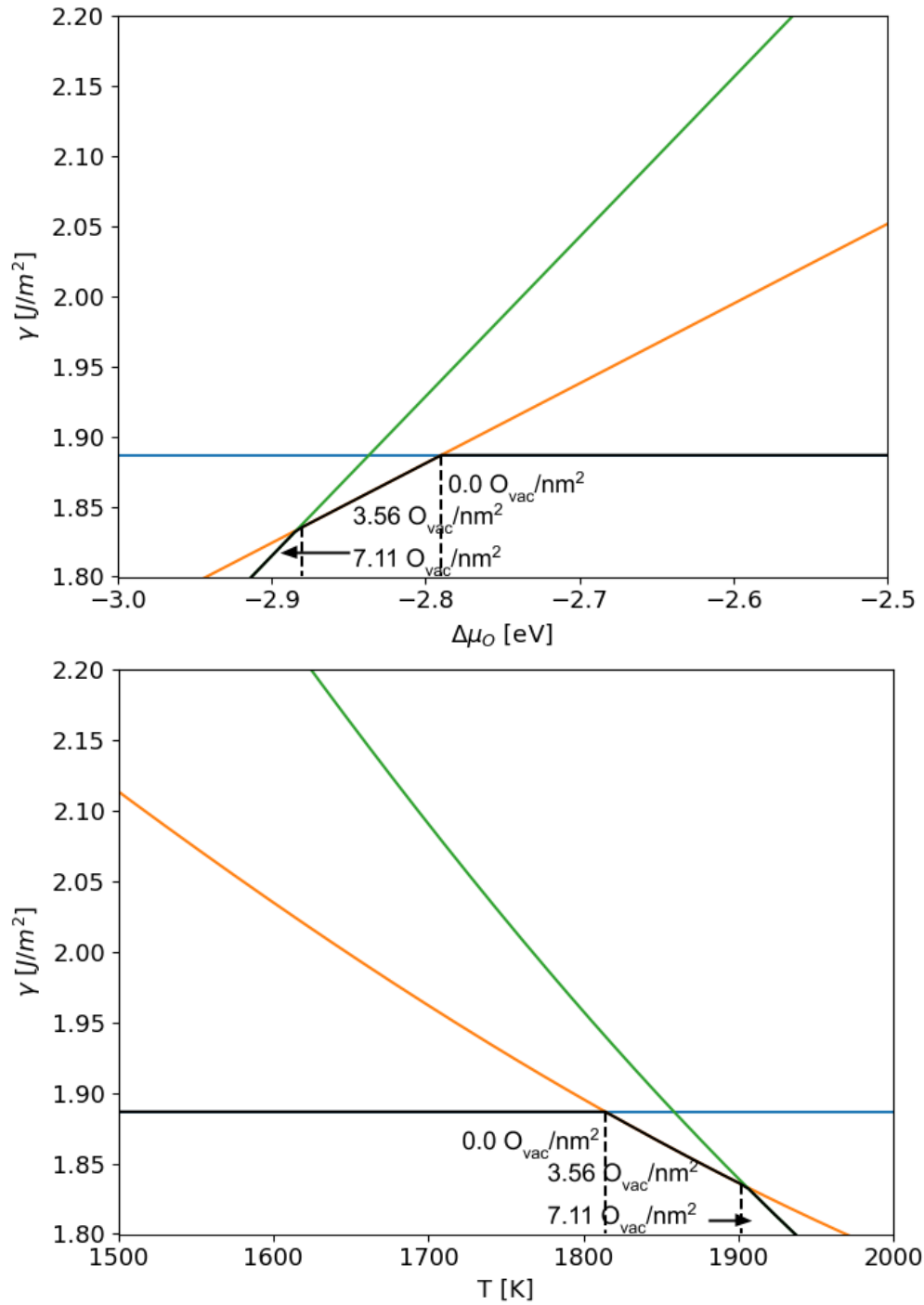


Figure B.8 Reduction of $(\text{Co}^{\text{Td}}\text{Co}^{\text{Oh}}_{0.5})_x$ through O_{vac} formation without consideration of H_2 or H_2O , (top) as $\gamma(\Delta\mu_O)$ and (bottom) as $\gamma(T, P_{\text{O}_2}=10^{-5} \text{ bar})$.

Table B.1 Energies of H₂ adsorption on the Co Poor (Co^{Td})_x termination

OH Coverage [nm ⁻²]	$\Delta E_{\text{ads, per } 1/2\text{H}_2}$ [eV]
0.89	-1.80
1.78	-1.78
2.67	-1.63
3.56	-1.40
4.44	-1.34
5.33	-1.29
6.22	-1.26
7.11	-1.21
8.89	-0.94
10.67	-0.69
12.44	-0.74
14.22	-0.86

Table B.2 Energies of H₂ adsorption on the stoichiometric (Co^{Td}Co^{Oh}_{0.5})_x termination

OH Coverage [nm ⁻²]	$\Delta E_{\text{ads, per } 1/2\text{H}_2}$ [eV]
0.89	-0.93
1.78	-0.78
2.67	-0.65
3.56	-0.65
4.44	-0.63
5.33	-0.58
6.22	-0.47
7.11	-0.41
8.89	-0.44
10.67	-0.55
12.44	-0.59
14.22	-0.57

Table B.3 Energies of H₂ adsorption on the Co-rich (Co^{Td}Co^{Oh})_x termination

OH Coverage [nm ⁻²]	$\Delta E_{\text{ads, per } 1/2\text{H}_2}$ [eV]
1.78	-1.10
3.56	-1.05
5.33	-1.04
7.11	-1.24
8.00	-1.12
8.89	-1.02
9.78	-0.94
10.67	-0.86

Table B.4 Energies of oxygen vacancy (O_{vac}) formation on the Co Poor $(\text{Co}^{\text{Td}})_x$ termination

O_{vac} Coverage [nm^{-2}]	$\Delta E_{\text{form, per } O_{\text{vac}}}$ [eV]
0.89	1.93
1.78	2.03
2.67	2.11
3.56	2.07
4.44	2.17
5.33	2.01
6.22	2.13
7.11	2.16

Table B.5 Energies of oxygen vacancy (O_{vac}) formation on the stoichiometric $(\text{Co}^{\text{Td}}\text{Co}^{\text{Oh}}_{0.5})_x$ termination

O_{vac} Coverage [nm^{-2}]	$\Delta E_{\text{form, per } O_{\text{vac}}}$ [eV]
0.89	3.20
1.78	2.85
2.67	3.01
3.56	2.79
4.44	3.03
5.33	2.94
6.22	2.88
7.11	2.84

Table B.6 Energies of oxygen vacancy (O_{vac}) formation on the Co-rich $(\text{Co}^{\text{Td}}\text{Co}^{\text{Oh}})_x$ termination

O_{vac} Coverage [nm^{-2}]	$\Delta E_{\text{form, per } O_{\text{vac}}}$ [eV]
0.89	2.12
1.78	1.86
2.67	1.71
3.56	1.49
4.44	1.88
5.33	2.15
6.22	2.31
7.11	2.40

Table B.7 Energies of H₂O adsorption on the Co Poor (Co^{Td})_x termination, retrieved from ref¹⁴⁵

Amount adsorbed [nm ⁻²]	Surface Species Generated	$\Delta E_{\text{ads, per H}_2\text{O}}$ [eV]
0.89	1.78 OH/nm ²	-1.25
1.78	3.56 OH/nm ²	-1.12
2.67	2.67 H ₂ O/nm ²	-1.15
3.56	2.67 H ₂ O/nm ² , 1.78 OH/nm ²	-1.09
4.44	2.67 H ₂ O/nm ² , 3.56 OH/nm ²	-1.09
5.33	3.56 H ₂ O/nm ² , 3.56 OH/nm ²	-1.10
6.22	3.56 H ₂ O/nm ² , 5.33 OH/nm ²	-1.06
7.11	4.44 H ₂ O/nm ² , 5.33 OH/nm ²	-1.04

Table B.8 Energies of H₂O adsorption on the stoichiometric (Co^{Td}Co^{Oh}_{0.5})_x termination

Amount adsorbed [nm ⁻²]	Surface Species Generated	$\Delta E_{\text{ads, per H}_2\text{O}}$ [eV]
0.89	1.78 OH/nm ²	-2.09
1.78	3.56 OH/nm ²	-2.00
2.67	5.33 OH/nm ²	-1.72
3.56	7.11 OH/nm ²	-1.63
4.44	8.89 OH/nm ²	-1.54
5.33	8.89 OH/nm ² , 0.89 H ₂ O/nm ²	-1.51
6.22	10.67 OH/nm ² , 0.89 H ₂ O/nm ²	-1.32
7.11	10.67 OH/nm ² , 1.78 H ₂ O/nm ²	-1.25

Table B.9 Energies of H₂O adsorption on the Co-rich (Co^{Td}Co^{Oh})_x termination

Amount adsorbed [nm ⁻²]	Surface Species Generated	$\Delta E_{\text{ads, per H}_2\text{O}}$ [eV]
0.89	1.78 OH/nm ²	-1.83
1.78	3.56 OH/nm ²	-1.87
2.67	5.33 OH/nm ²	-1.83
3.56	7.11 OH/nm ²	-1.82
4.44	7.11 OH/nm ² and 0.89 H ₂ O/nm ²	-1.63
5.33	8.89 OH/nm ² and 0.89 H ₂ O/nm ²	-1.71
6.22	7.11 OH/nm ² and 2.67 H ₂ O/nm ²	-1.49
7.11	7.11 OH/nm ² and 3.56 H ₂ O/nm ²	-1.40
8.00	7.11 OH/nm ² and 4.44 H ₂ O/nm ²	-1.38
8.89	7.11 OH/nm ² and 5.33 H ₂ O/nm ²	-1.37
9.78	7.11 OH/nm ² and 6.22 H ₂ O/nm ²	-1.29
10.67	7.11 OH/nm ² and 7.11 H ₂ O/nm ²	-1.25

B.3 Fully labeled surface stability diagrams and tabulated top/side/bird's eye view of structures appearing on the diagram

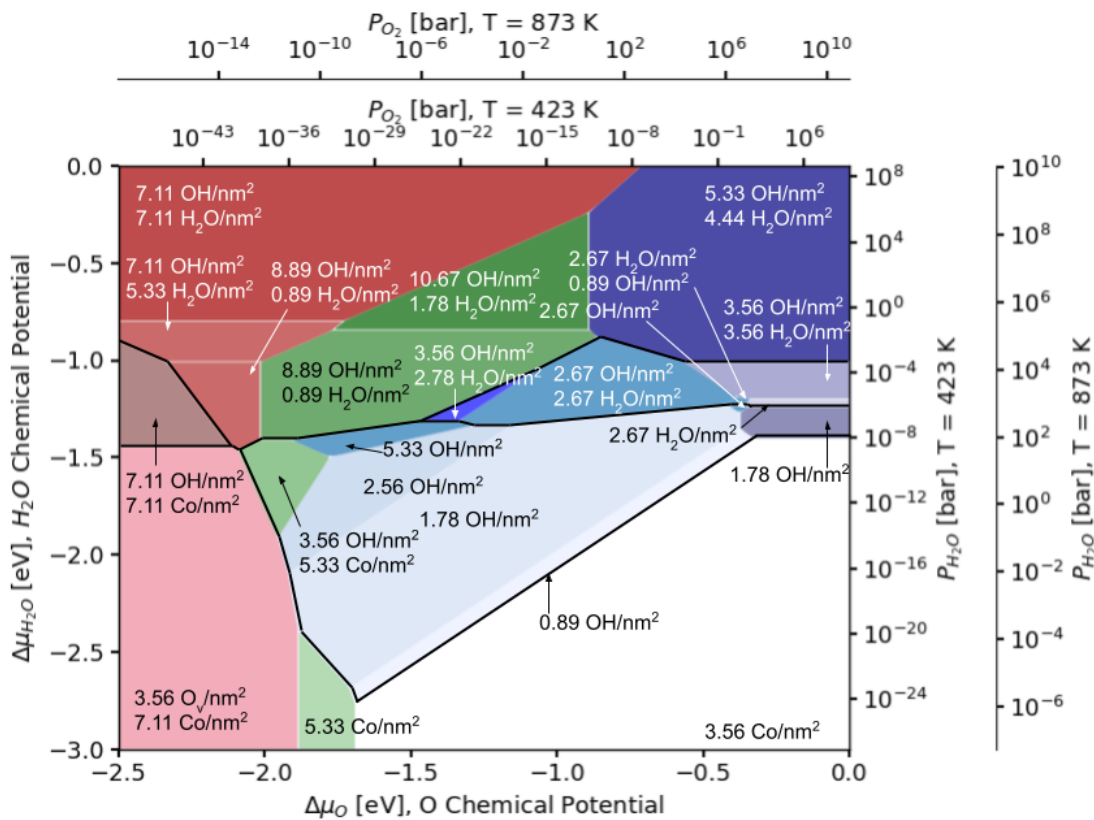
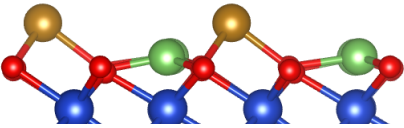
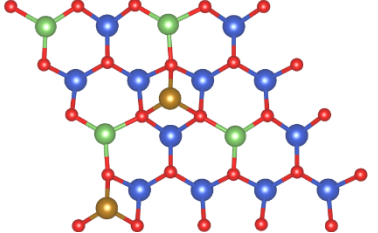
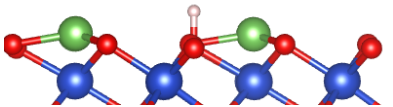
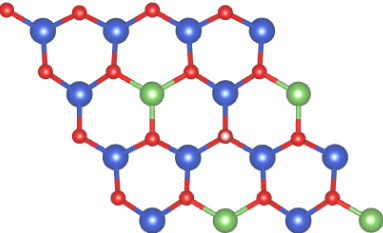
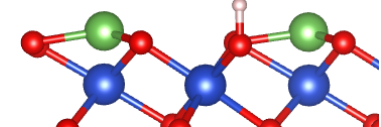
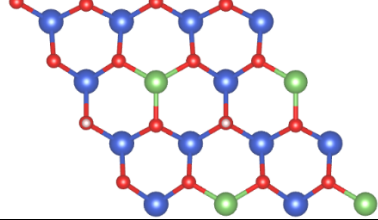
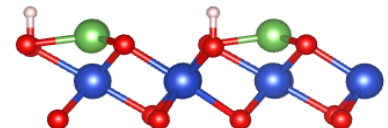
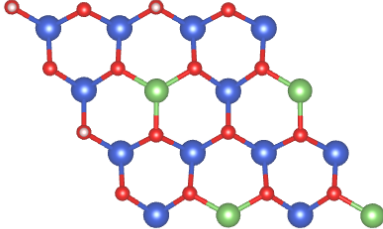
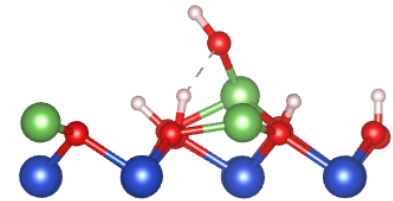
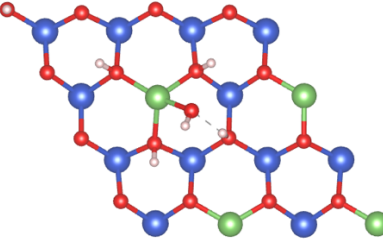
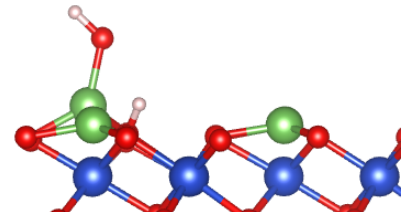
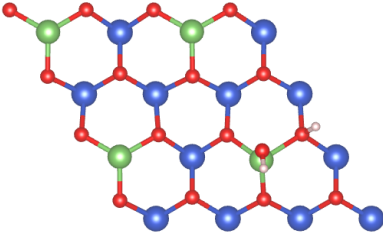
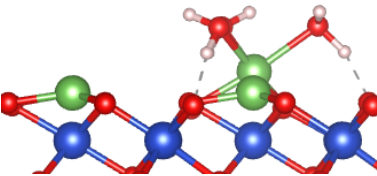
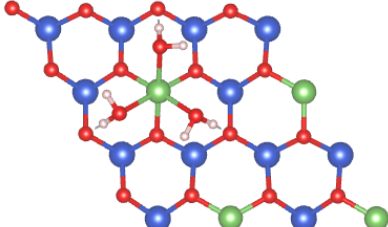
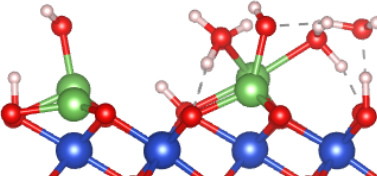
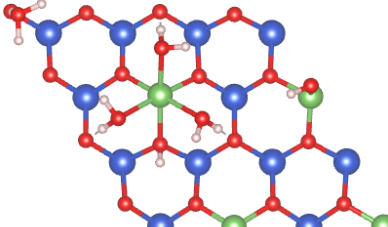
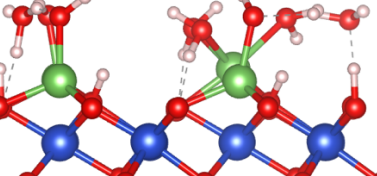
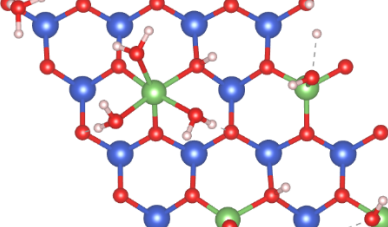
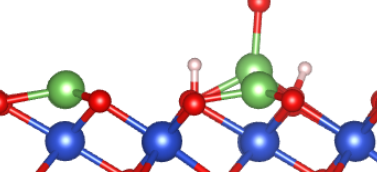
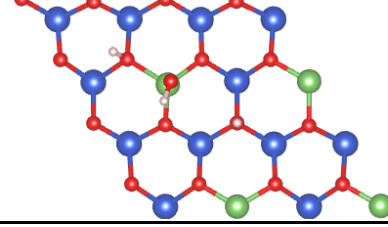
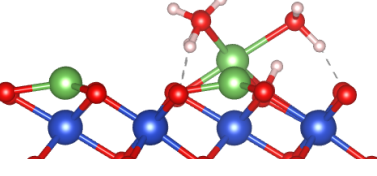
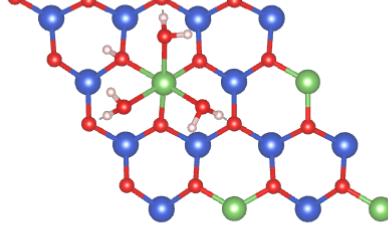
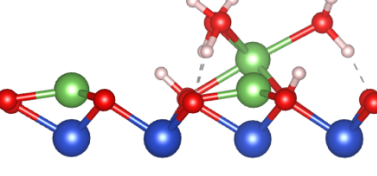
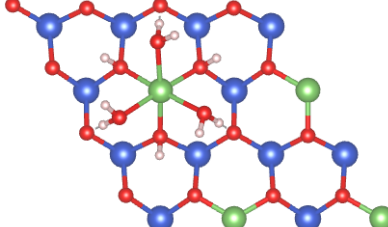


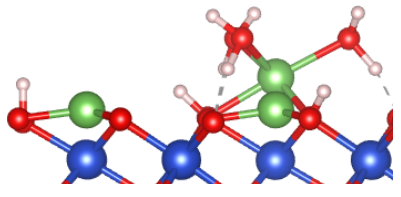
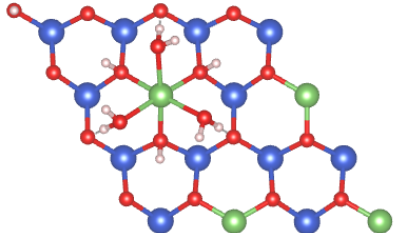
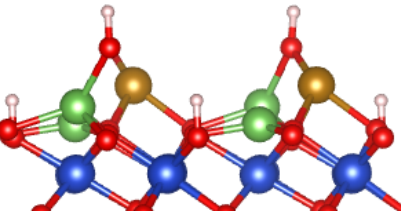
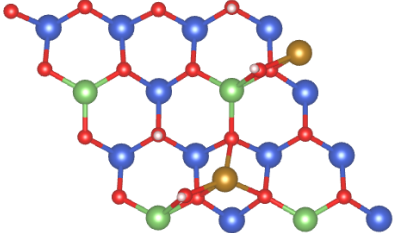
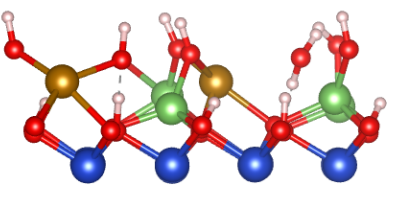
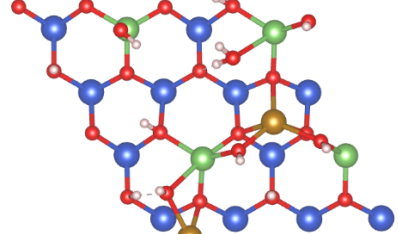
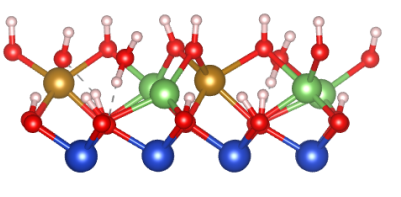
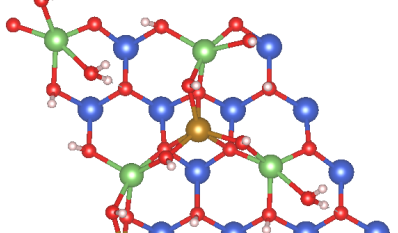
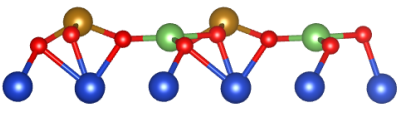
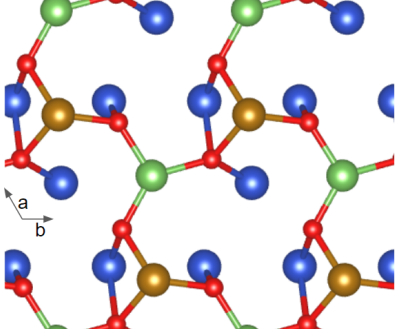
Figure B.9 O₂/H₂O surface stability diagram with all regions labeled.

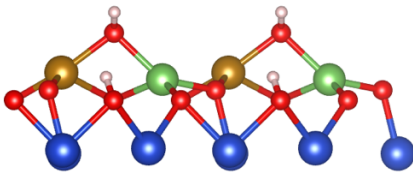
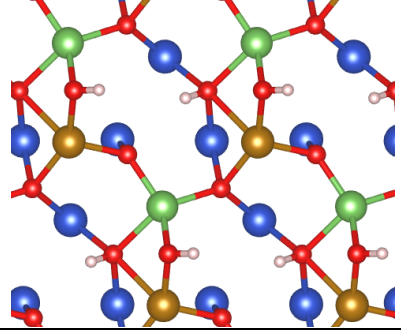
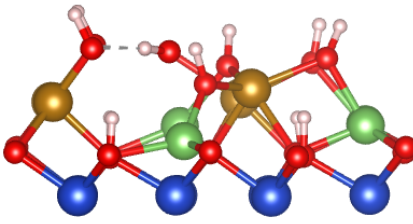
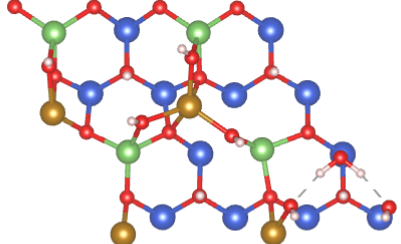
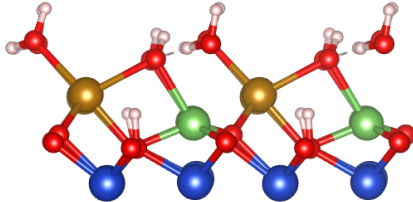
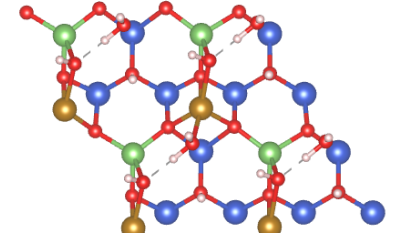
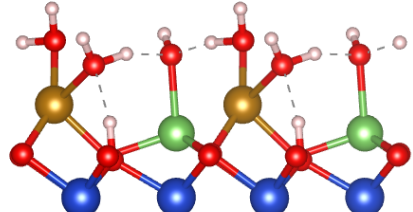
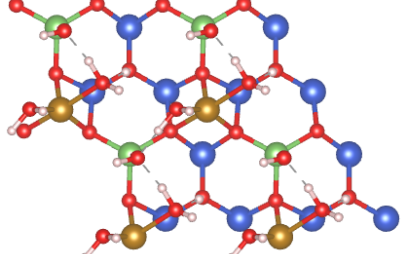
Table B.10 Surface structures present on the H₂O/O₂ surface stability diagram. Key: Co³⁺: blue, Co²⁺ on the surface: green, Co²⁺ added to the surface: gold, O²⁻: yellow, H: white.

Termination/Surface Species	Side view	Bird's eye view
3.56 Co/nm ² (Co poor)		

5.33 Co/nm ² (Stoichiometric)		
Co-poor, 0.89 OH/nm ² , from H ₂ dissociation		
Co-poor, 1.78 OH/nm ² , from H ₂ dissociation		
Co-poor, 2.56 OH/nm ² , from H ₂ dissociation		
Co-poor, 5.33 OH/nm ² , from H ₂ and H ₂ O dissociation		
Co-poor, 1.78 OH/nm ² , from H ₂ O adsorption, adapted from ref ⁵		

<p>Co-poor, 2.67 H₂O/nm², from H₂O adsorption, adapted from ref⁵</p>		
<p>Co-poor, 3.56 H₂O/nm² and 3.56 OH/nm² from H₂O adsorption, adapted from ref⁵</p>		
<p>Co-poor, 7.11 OH/nm² and 3.56 H₂O/nm², from H₂O adsorption, adapted from ref⁵</p>		
<p>Co-poor, 2.67 OH/nm², from H₂O and H₂ simultaneous adsorption 0.89 H₂O/nm² is dissociated</p>		
<p>Co-poor, 0.89 OH/nm² and 2.67 H₂O/nm², from H₂O and H₂ simultaneous adsorption</p>		
<p>Co-poor, 2.67 OH/nm² and 2.67 H₂O/nm², from H₂O and H₂ simultaneous adsorption</p>		

<p>Co-poor, 3.56 OH/nm² and 2.67 H₂O/nm², from H₂O and H₂ simultaneous adsorption</p>		
<p>Stoichiometric, 3.56 OH/nm² from H₂O adsorption</p>		
<p>Stoichiometric, 8.89 OH/nm² and 0.89 H₂O/nm² from H₂O adsorption</p>		
<p>Stoichiometric, 10.67 OH/nm² and 1.78 H₂O/nm² from H₂O adsorption</p>		
<p>Co-rich, 3.56 O_{vac}/nm²</p>		

<p>Co-rich, 7.11 OH/nm²</p>		
<p>Co-rich, 8.89 OH/nm² and 0.89 H₂O/nm² from H₂O adsorption</p>		
<p>Co-rich, 7.11 OH/nm² and 3.56 H₂O/nm² from H₂O adsorption</p>		
<p>Co-rich, 7.11 OH/nm² and 7.11 H₂O/nm² from H₂O adsorption</p>		

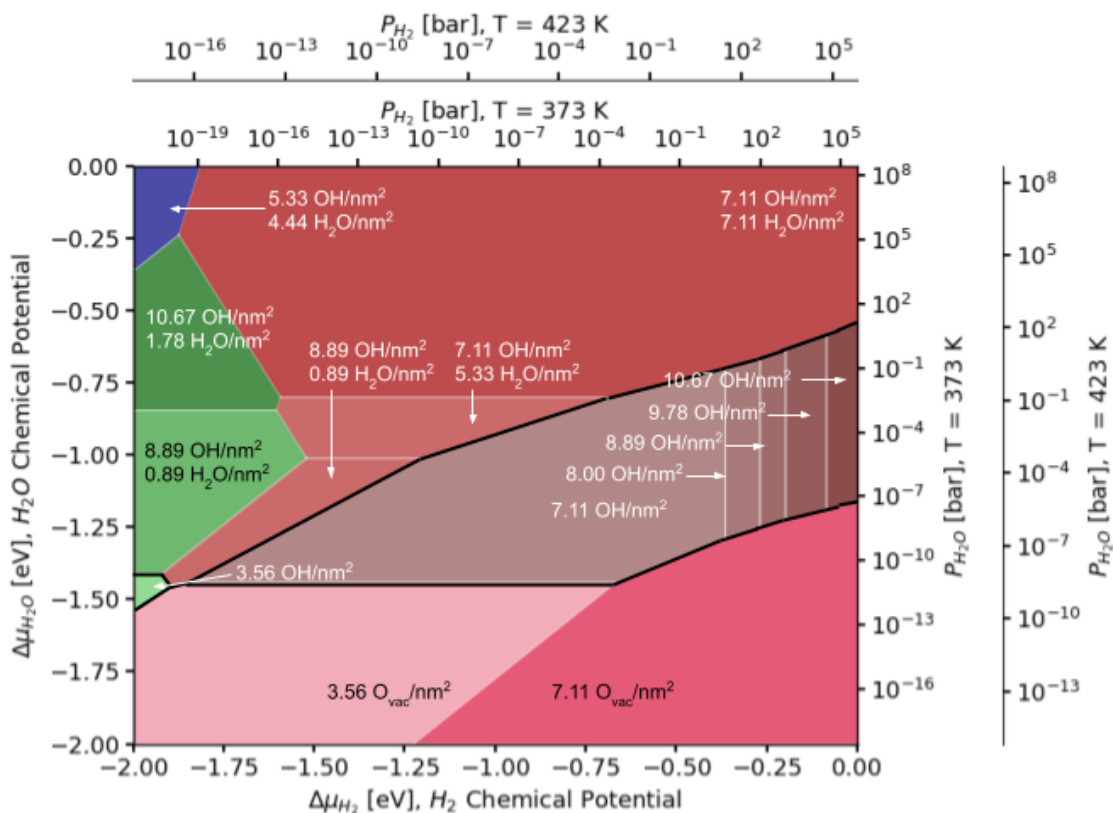
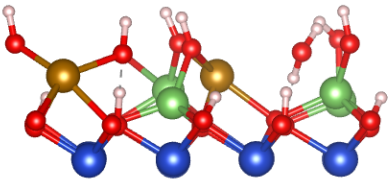
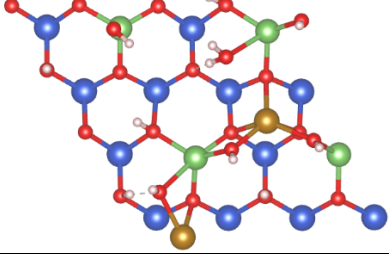
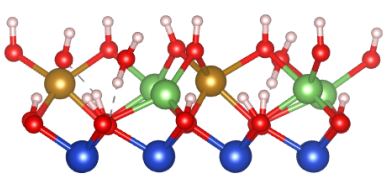
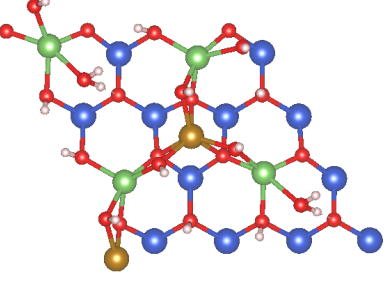
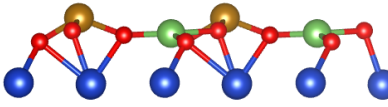
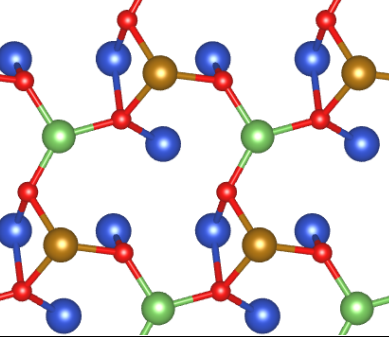
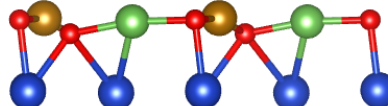
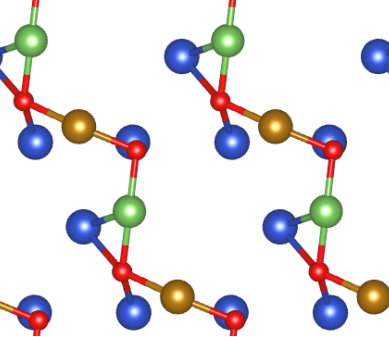
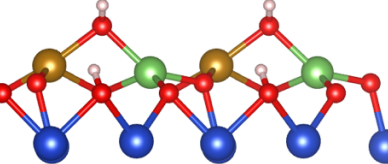
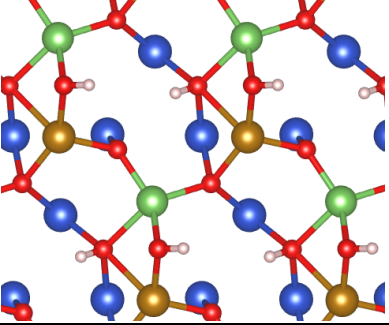
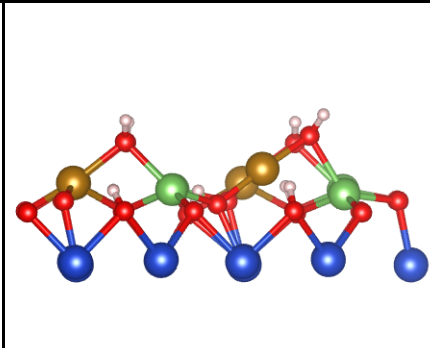
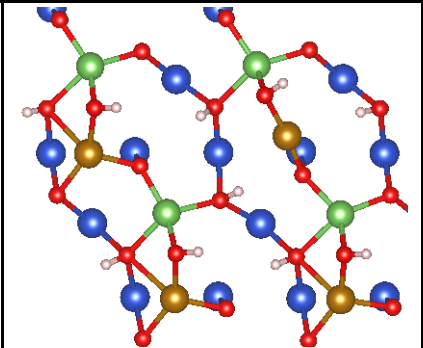
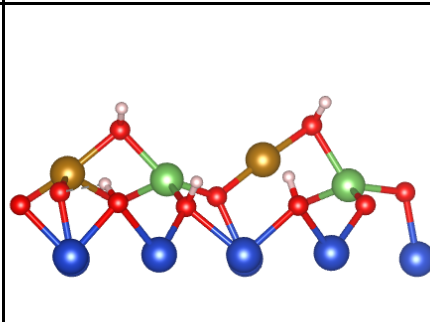
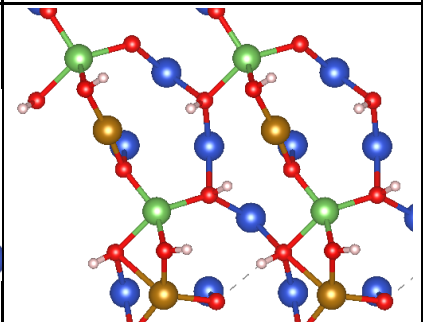
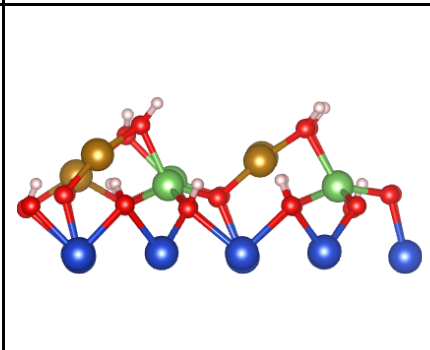
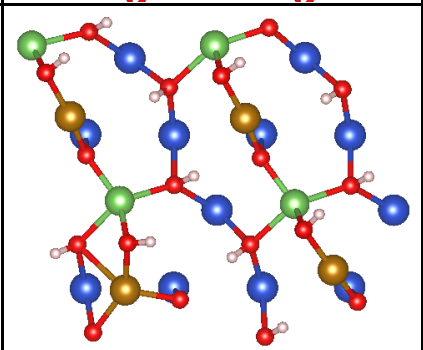
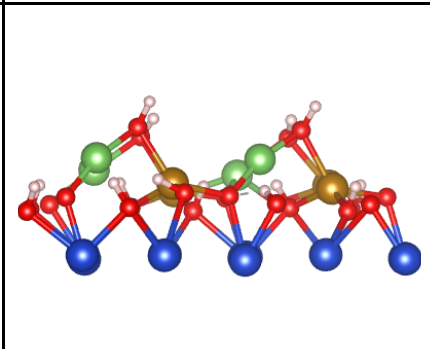
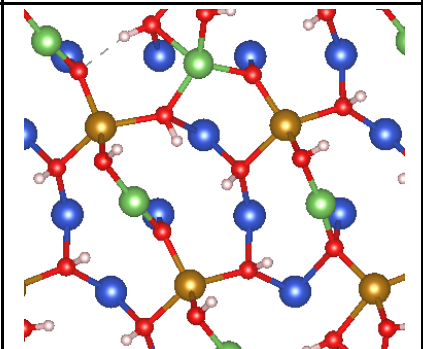
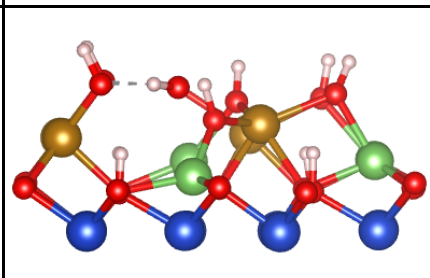
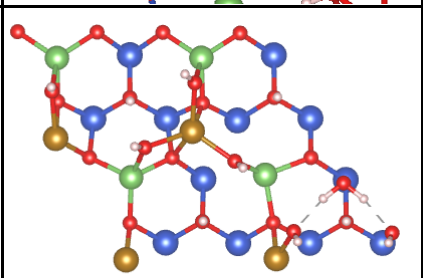


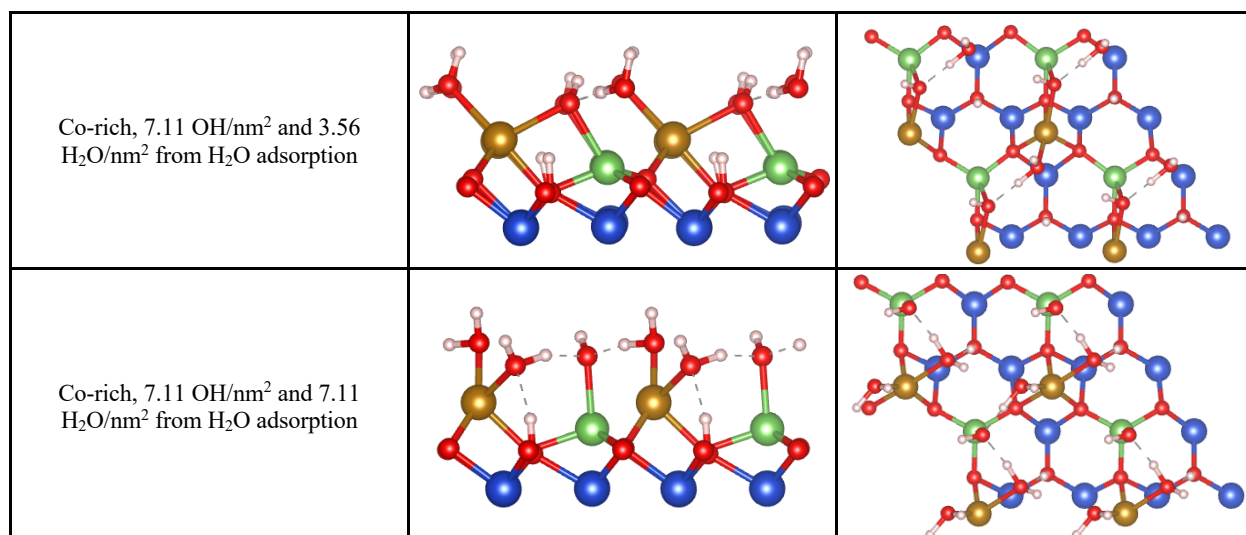
Figure B.10 Fully labeled H₂/H₂O surface stability diagram

Table B.11 Surface structures present on the H₂O/H₂ surface stability diagram

Termination/Surface Species	Side view	Bird's eye view
Co-poor, 5.33 OH/nm ² and 4.44 H ₂ O/nm ² , from H ₂ O adsorption, adapted from ref ⁵		
Stoichiometric, 3.56 OH/nm ² from H ₂ O adsorption		

<p>Stoichiometric, 8.89 OH/nm² and 0.89 H₂O/nm² from H₂O adsorption</p>		
<p>Stoichiometric, 10.67 OH/nm² and 1.78 H₂O/nm² from H₂O adsorption</p>		
<p>Co-rich, 3.56 O_{vac}/nm²</p>		
<p>Co-rich, 7.11 O_{vac}/nm²</p>		
<p>Co-rich, 7.11 OH/nm²</p>		

<p>Co-rich, 8.00 OH/nm²</p>		
<p>Co-rich, 8.89 OH/nm²</p>		
<p>Co-rich, 9.78 OH/nm²</p>		
<p>Co-rich, 10.67 OH/nm²</p>		
<p>Co-rich, 8.89 OH/nm² and 0.89 H₂O/nm² from H₂O adsorption</p>		

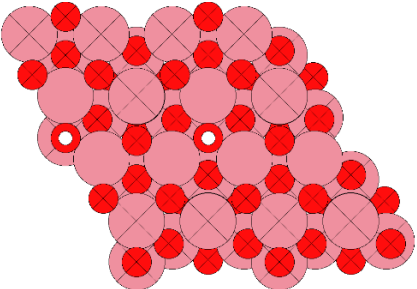
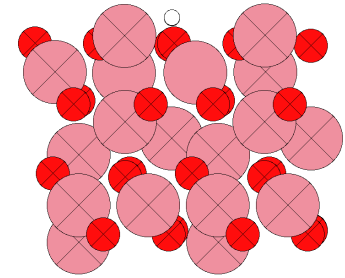
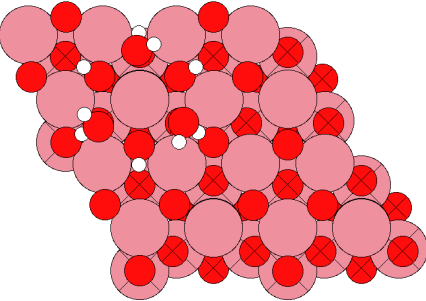
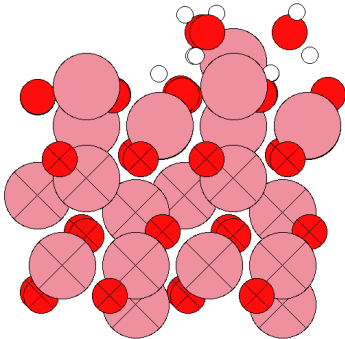
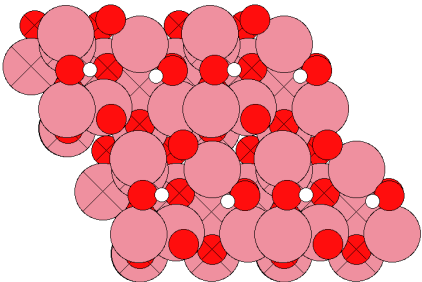
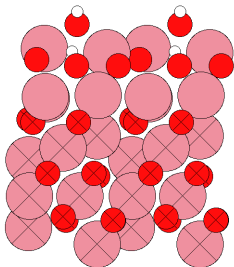


B.4 More Details on Frequency Calculations

Table B.12 $\nu(\text{O-D})$ and $\nu(\text{O-H})$ vibrational mode calibration for PBE+dDsC, where the ratio between the experimental and calculated average wavenumbers is taken as calibration factor

Description	Calculated mode [cm ⁻¹]	Experimental mode ¹⁴⁷ [cm ⁻¹]	Calibration Factor
$\nu(\text{O-D})_s$ of D ₂ O	2687	2668	-
$\nu(\text{O-D})_a$ s of D ₂ O	2814	2788	-
Average $\nu(\text{O-D})$	2750	2728	0.9918
$\nu(\text{O-H})_s$ of H ₂ O	3730	3657	-
$\nu(\text{O-H})_a$ s of H ₂ O	3843	3756	-
Average $\nu(\text{O-H})$	3786.5	3706.5	0.9788

Table B.13 Side and top views of geometries used in frequency calculations, where the constrained atoms are crossed out. Co: pink, O: red, H: white

Description	Geometry, top view	Geometry, side view
Co-poor, 1.78 OH/nm ²		
Co-poor, 2.67 OH/nm ² , 2.67 H ₂ O/nm ²		
Co-rich, 7.11 OH/nm ²		

B.5 Surface relaxation experienced by the $(\text{Co}^{\text{Oh}}\text{Co}^{\text{Td}})_x$ termination upon reduction, the magnetic structure of the $(\text{Co}^{\text{Oh}}_{0.5}\text{Co}^{\text{Td}})_x$ termination, and isomers of the fully hydroxylated $(\text{Co}^{\text{Td}})_x$ termination

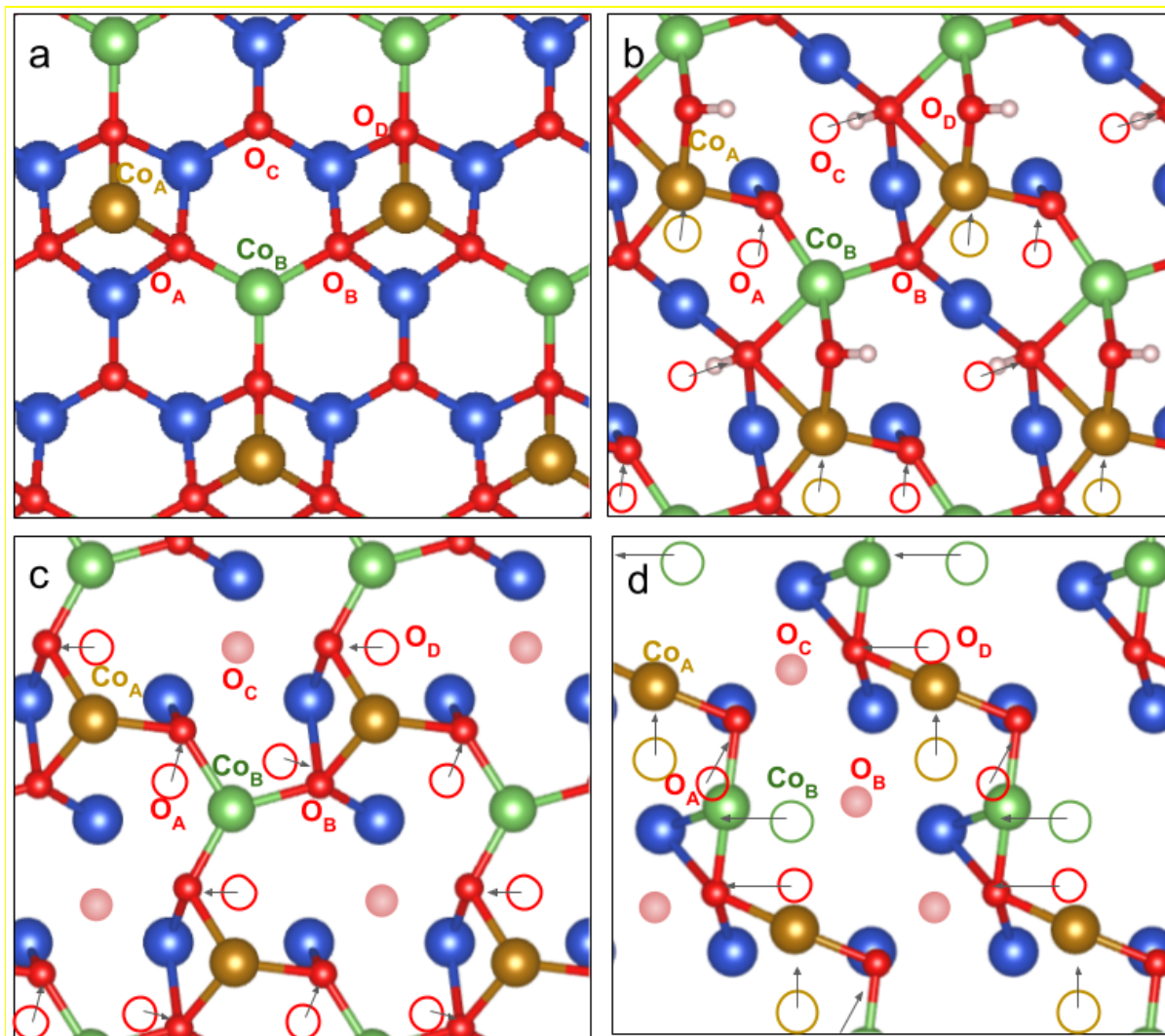


Figure B.11 Surface distortion experienced by the Co-rich termination (a) after reduction by (b) adsorption of 7.11 H/nm^2 , (c) formation of $3.56 \text{ O}_{\text{vac}}/\text{nm}^2$, and (d) formation of $7.11 \text{ O}_{\text{vac}}/\text{nm}^2$. After relaxation, Co-O_h, Co-T_d, and surface O, following the arrows, move from their initial positions, denoted by open gold, green, and red circles, to their final positions. Pink circles represent O_{vac}. Two types of surface Co and four types of surface O are indicated as Co_A, Co_B, O_A, O_B, O_C, and O_D.

Table B.14 Displacements of surface Co and O ions upon H adsorption and generation of the structure in **Figure B.11b**

Species	Δx [Å]	Δy [Å]	Δz [Å]
Co_A	-0.067	0.729	0.080
Co_B	-0.092	0.431	0.628
O_A	0.422	1.129	0.776
O_B	0.123	0.083	0.480
O_C	1.298	0.647	0.613
O_D	0.114	0.797	2.476

Table B.15 Displacements of surface Co and O ions upon H adsorption and generation of the structure in **Figure B.11c**

Species	Δx [Å]	Δy [Å]	Δz [Å]
Co_A	-0.117	0.401	-0.036
Co_B	-0.165	0.233	0.198
O_A	0.399	0.952	0.755
O_B	0.067	-0.170	0.380
O_D	-1.027	0.430	0.610

Table B.16 Displacements of surface Co and O ions upon H adsorption and generation of the structure in **Figure B.11d**

Species	Δx [Å]	Δy [Å]	Δz [Å]
Co_A	-0.139	1.241	-0.188
Co_B	-1.522	0.446	0.474
O_A	0.258	1.342	0.981
O_D	-1.708	0.485	0.597

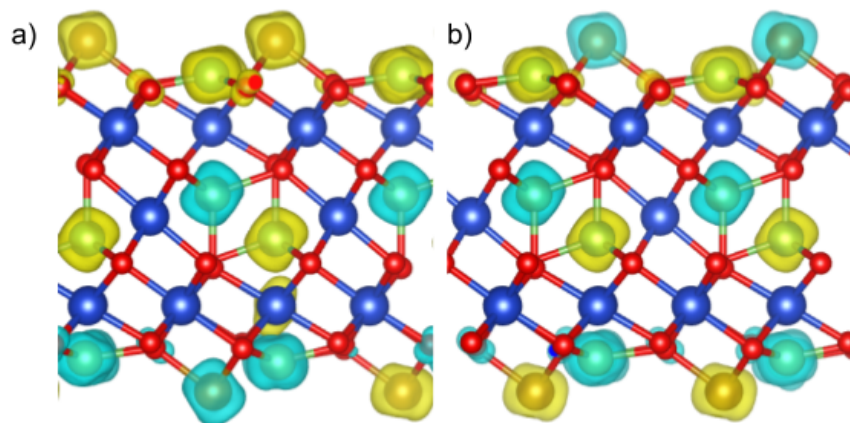


Figure B.12 Magnetic alignment for the stoichiometric termination in calculations used for this work a) and the ground state b). The energies differ by -0.76 eV/cell in favor of structure (b) and the correction was applied to all structures of this termination in constructing the stability diagrams. The difference at $U_{\text{eff}} = 2$ eV was -1.01 eV/cell.

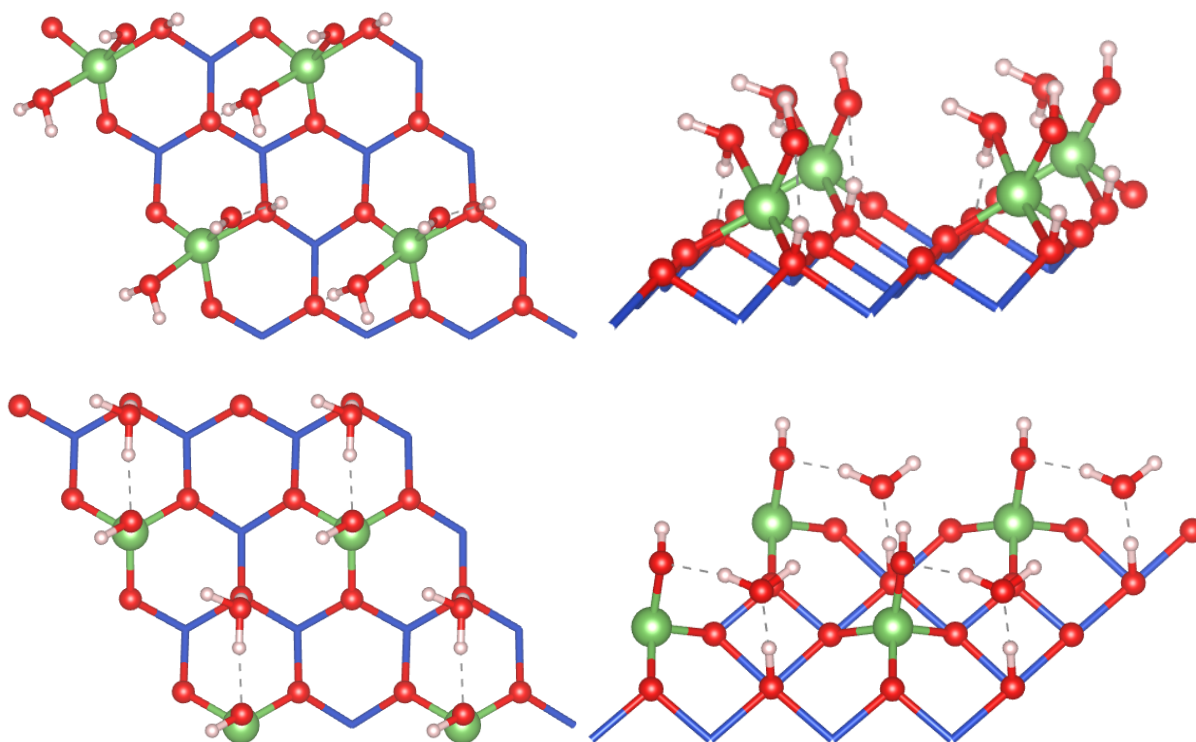


Figure B.13 The (top two, left: top view, right: side view) pairs (one H_2O molecule-OH pair per surface Co^{2+}) and (bottom two, left: top view, right: side view) hexagonal (OH and H_2O connect

to form a hexagonal hydroxyl overlayer) configurations of hydroxyl overlayers on the $(\text{Co}^{\text{Td}})_x$ termination, adapted from ref¹⁴⁵

Appendix C Supplementary Information for Chapter 4

C.1 Structure of the $\text{Co}_3\text{O}_4(111)$ surface, Mo_1 , and Pd_1 active sites

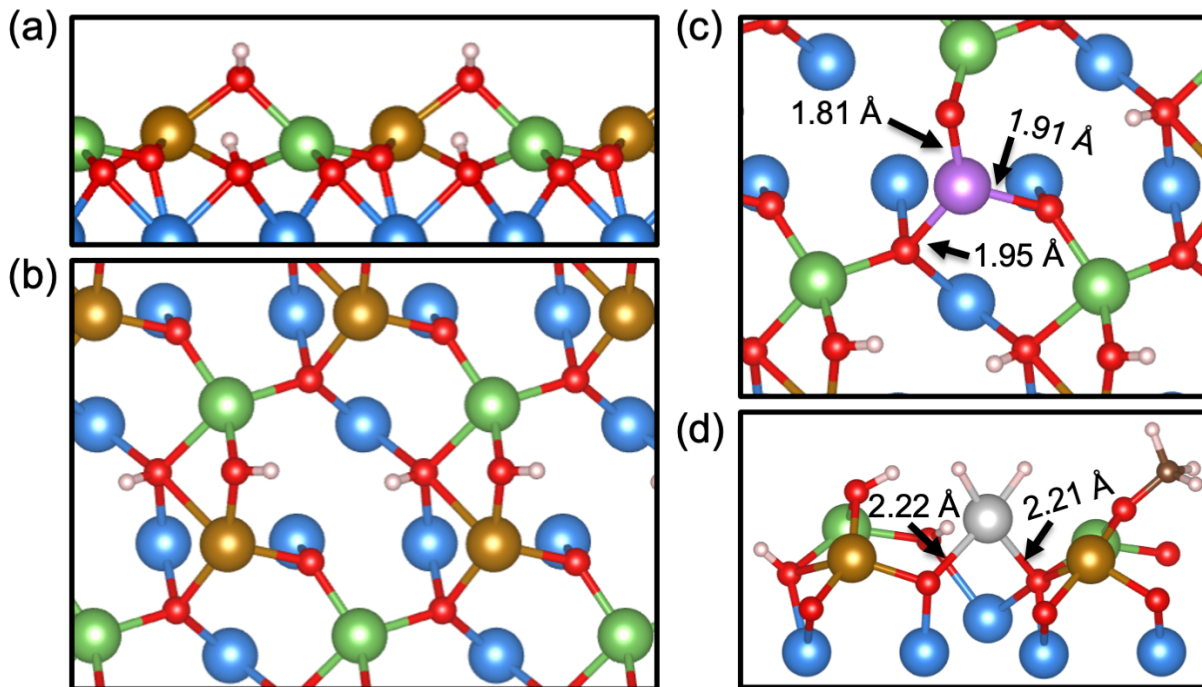


Figure C.1 Structure of the $\text{Co}_3\text{O}_4(111)$ surface in equilibrium with the gas environment during steady state reaction (adapted from ¹⁷²) and Mo_1 and Pd_1 active sites. The surface (a: top view, b: side view) is Co-enriched and hydroxylated, terminated with 7.11 Co/nm^2 and 7.11 OH/nm^2 . Oxidized $\text{Co}_3\text{O}_4(111)$ films are terminated by O (red) and Co (green). Co (gold) atoms are added to simulate surface reduction without phase-change in the near-surface layers. 2 types of OH exist on the surface: bidentate OH which bridge over surface (gold and green) Co, and tetradentate OH which are bound to 2 subsurface (blue) Co as well as surface (gold and green) Co. (c) The Mo_1 site is constructed by substituting one of the gold Co cations on the surface with Mo and removing one unit of H_2O . (d) The Pd_1 site is constructed by adsorbing one unit of PdH_2 and substituting a nearby OH group by OCH_3 .

As observed in TEM of spent catalyst particles, the (111) surface is exposed in the largest fraction; thus, we used this surface as the catalyst support to graft Pd and Mo single sites. The surface can have many different terminations, depending on the reaction conditions. Under steady state anisole HDO conditions (150 °C, 1 bar, $P_{H_2} = 0.995 \sim 0.985$ bar, $P_{H_2O} = 3.88 \times 10^{-5} \sim 3.83 \times 10^{-3}$ bar, i.e. corresponding to 1~99% anisole conversion, 83% selectivity to benzene over methoxycyclohexane, and 99% selectivity to CH_4 over CH_3OH ; hereby referred to as “steady state conditions”), the equilibrated surface is enriched in Co (7.11 Co/nm²) and heavily hydroxylated (one OH per exposed Co, 7.11 OH/nm², **Figure C.1**).¹⁷²

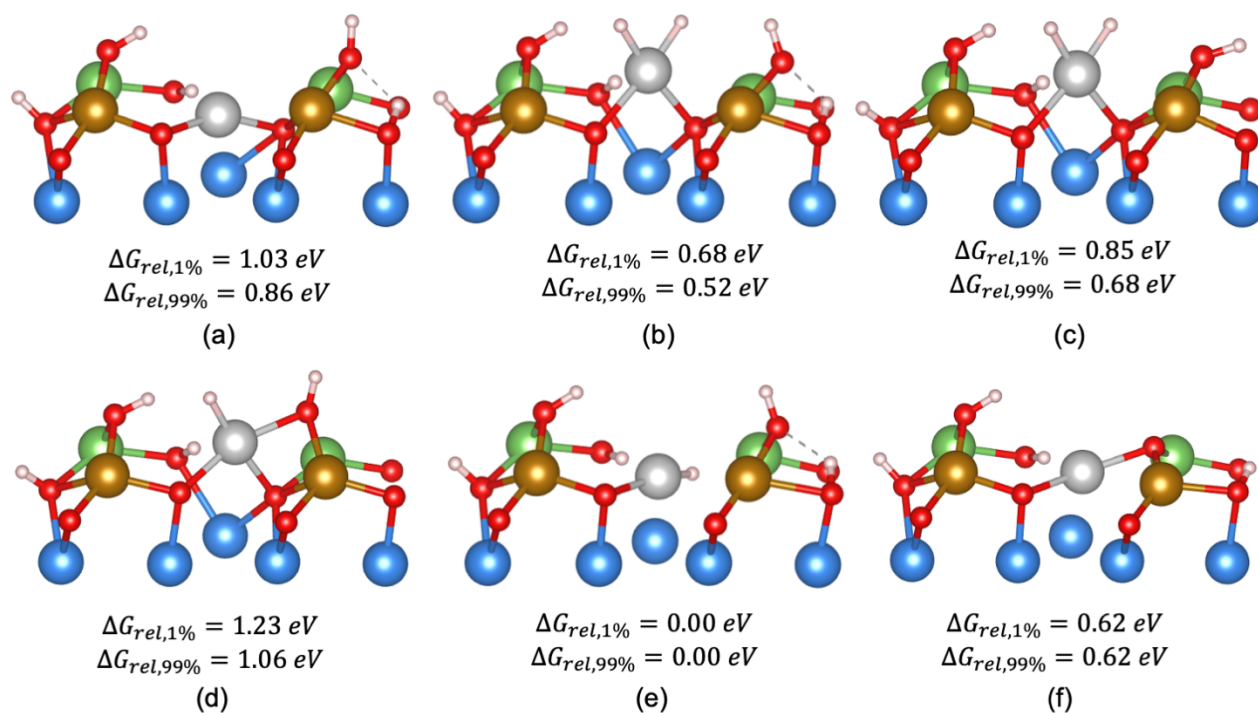


Figure C.2 Selected geometries of the Pd₁ site considered in this work. The relative Gibbs free energy under steady state conditions compared to the most stable configuration is provided for each geometry.

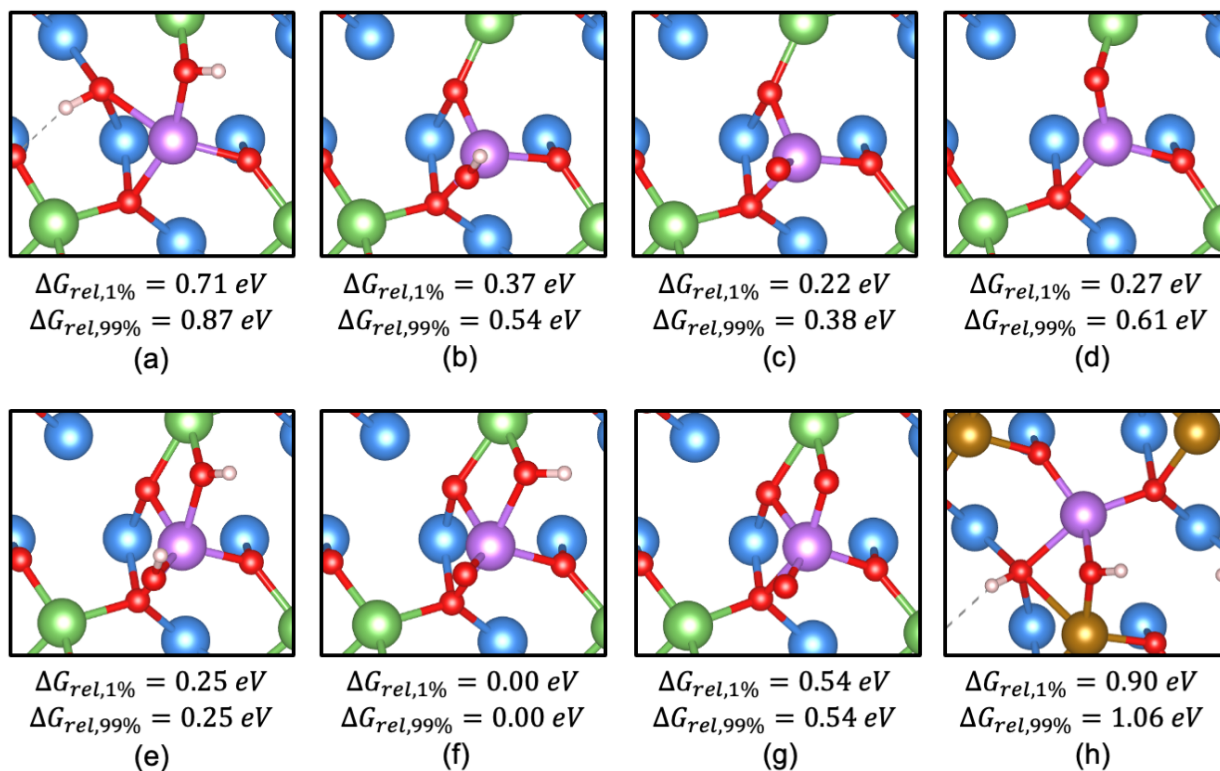


Figure C.3 Selected geometries of the Mo₁ site considered in this work. The relative Gibbs free energy under steady state conditions compared to the most stable configuration is provided for each geometry.

We have explored several adsorption sites for Pd and Mo atoms; their relative free energies in reaction conditions are given in **Figure C.2 and C.3**. Besides bare Pd single atoms, we considered also structures with 1 or 2 H added on the Pd (**Figure C.2**). Structure shown in **Figure C.2b**, with Pd bridging two O atoms on the support, bearing two H atoms and another H atom adsorbed on O in a neighboring cell provides a good stability. Compared to that structure, the formation of one extra subsurface O vacancy appears exergonic (by 0.68-0.52 eV), but this requires to first access a PdH₁ intermediate (**Figure C.2b**, 0.54 eV higher than b) and was hence considered as kinetically unfavorable.

On the other hand, we also considered several substituted Mo sites. We found that Mo prefers to replace surface Co added to simulate surface reduction (**Figure C.3**). Although the mono-oxo-molybdenum is the most stable configuration (**Figure C.3f**), studies on the reactivity of such Mo₁ sites revealed them to be rather inactive.¹⁷³ Here, the 3-coordinated O vacancy-containing configuration of this Mo₁ species is slightly metastable (by 0.27-0.61 eV); thus, we considered it as the candidate to dissociate anisole. The in-situ EXAFS study also found that the Mo₁ sites only have a few O neighbors during reaction, suggesting that such O-deficient Mo₁ sites could be dynamically stabilized by the reaction.

C.2 Geometry and formal oxidation of all states in the reaction mechanisms

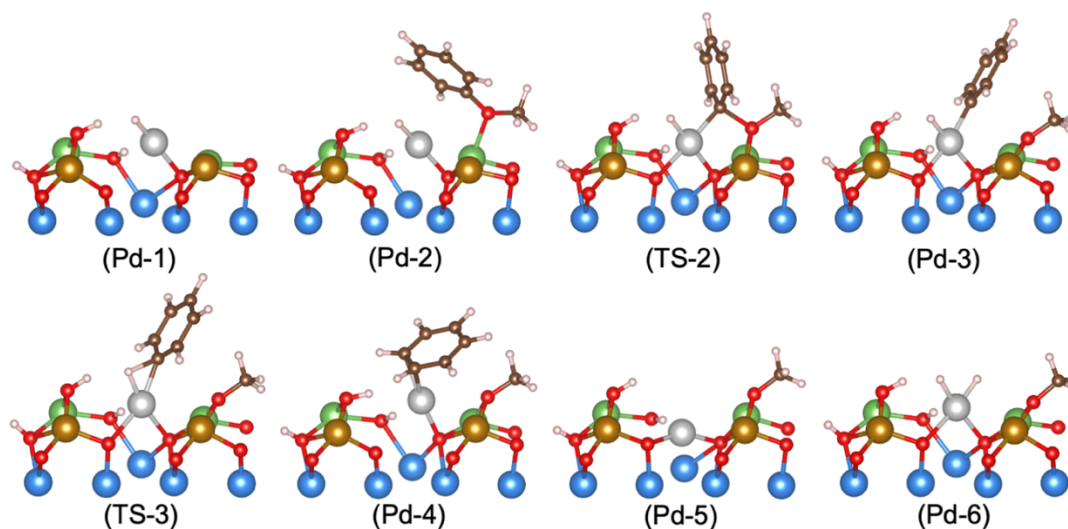


Figure C.4 All intermediate and transition state geometries in the HDO reaction mechanism over Pd₁ only. Only atoms near the Pd₁ site and its adjacent Co are shown.

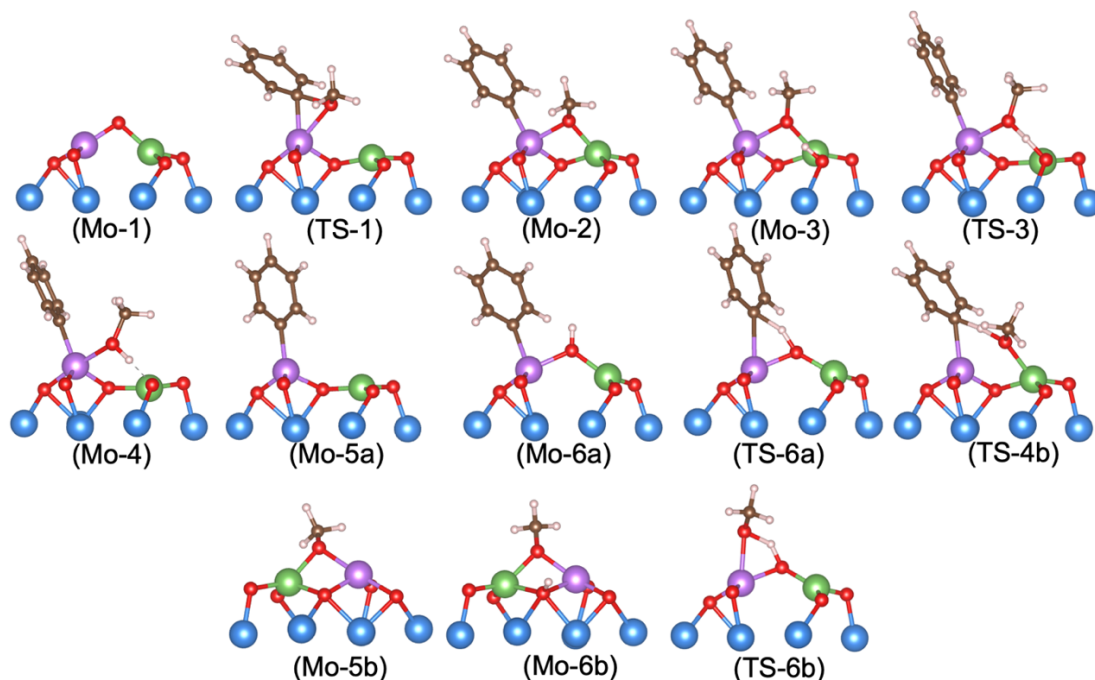


Figure C.5 All intermediate and transition state geometries in the HDO reaction mechanism over Mo_1 assisted by H spillover. Only atoms near the Mo_1 site and its adjacent Co are shown.

The formal oxidation states of the Pd and Mo centres in the reaction mechanism were assigned by Bader charge analysis. As the chemical environments of the anchored Pd and Mo single atoms greatly differ from their respective bulk oxides, molecular complexes were used as references for assignment. The following complexes (**Table C.1**) were used as references for the Pd-associated states.

Table C.1 Bader charges of Pd complexes for assignment of Pd oxidation states.

Chemical Formula	Formal Oxidation State of Pd	Bader Charge of Pd
$\text{Pd}_1(\text{H}_2\text{O})_2$	0	-0.121
$\text{Pd}_1(\text{H})_1(\text{H}_2\text{O})_1$	+I	+0.089
cis- $\text{Pd}_1(\text{H})_2(\text{H}_2\text{O})_2$	+II	+0.044
$\text{Pd}_1(\text{H})_1(\text{C}_{12}\text{H}_{19}\text{P}_2)$ (ref ²⁴²)	+II	-0.024
$\text{Pd}_1(\text{H})_1(\text{OH})$	+II	+0.518
$\text{Pd}_1(\text{OH})_2$	+II	+0.773

The following complexes (**Table C.2**) were used as references for the Mo-associated states.

Table C.2 Bader charges of Mo complexes for assignment of Mo oxidation states.

Chemical Formula	Formal Oxidation State of Mo	Bader Charge of Mo
Mo(OH) ₂ (H ₂ O) ₂	+II	+1.358
Mo(OH) ₃	+III	+1.752
Mo(O) ₁ (OH) ₂	+IV	+1.969
Mo(OH) ₄	+IV	+2.190
Mo(OH) ₄ (H ₂ O) ₂	+IV	+2.249
Mo(O) ₂ (OH) ₁	+IV	+2.194
Mo(O) ₃	+VI	+2.389
Mo(O) ₂ (OH) ₂	+VI	+2.562
Mo(O) ₁ (OH) ₄	+VI	+2.739
Mo(OH) ₆	+VI	+2.887

Using the tabulated references, the following formal oxidation states were assigned to intermediate and transition states along the anisole HDO pathways over Pd₁ and Mo₁ (**Tables C.3 and C.4**).

Table C.3 Bader charges of intermediate and transition states along the anisole HDO pathway over Pd₁.

Name of State	Formal Oxidation State of Pd	Bader Charge of Pd
Pd-1	0	-0.240
Pd-2	0	-0.215
TS-2	+II	+0.262
Pd-3	+II	+0.216
TS-3	+II	+0.126
Pd-4	0	+0.064
Pd-5	0	-0.013
Pd-6	+II	+0.095

Table C.4 Bader charges of intermediate and transition states along the anisole HDO pathway over Mo₁.

Name of State	Formal Oxidation State of Mo	Bader Charge of Mo
Mo-1	+III	+1.581
TS-1	+IV	+1.836
Mo-2	+IV	+2.017
Mo-3	+IV	+2.010
TS-3	+IV	+2.017
Mo-4	+IV	+2.014
Mo-5a	+IV	+1.914
Mo-6a	+III	+1.732
TS-6a	+III	+1.685
TS-4b	+IV	+1.967
Mo-5b	+III	+1.703
Mo-6b	+III	+1.641
TS-6b	+III	+1.747

C.3 Hydrogen activation and spillover mechanism over the hydroxylated Co₃O₄(111) surface

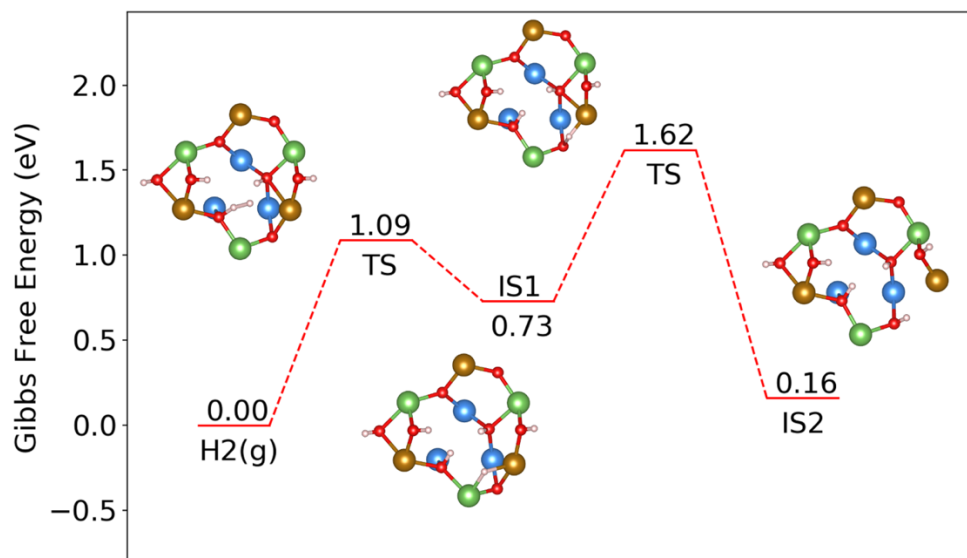


Figure C.6 Hydrogen dissociation over the Co₃O₄ substrate. H₂ dissociation on the Co₃O₄(111) substrate requires a rather large free energy barrier of 1.62 eV.

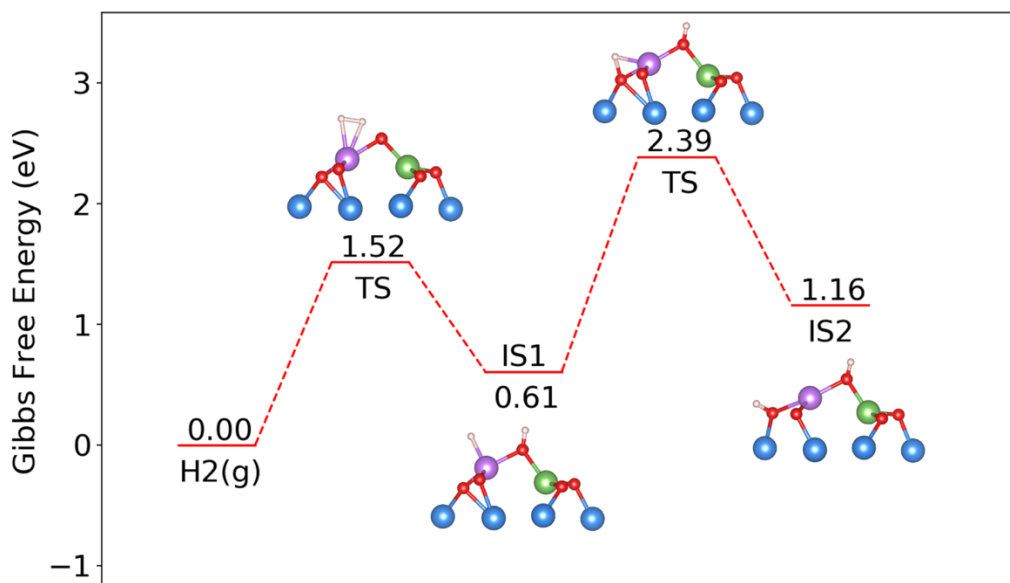


Figure C.7 Hydrogen dissociation over the Mo₁ site. H₂ dissociates on the Mo₁ site requires a rather large free energy barrier of 2.39 eV.

Beyond dissociation H₂ over the Pd₁ site, we also assessed the possibility of activating H₂ directly over the hydroxylated Co₃O₄ support and over the Mo₁ site (**Figure C.6 and C.7**). Under reaction conditions, the dissociation of H₂ were found to proceed heterolytically with a rather high free energy barrier of 1.62 eV over the Co₃O₄ surface and of 2.39 eV over the Mo₁ site. As both free energy barriers are much higher than the free energy span of anisole HDO over Pd₁+Mo₁, it is straightforward that the Mo₁ site alone will not be active for the HDO of anisole.

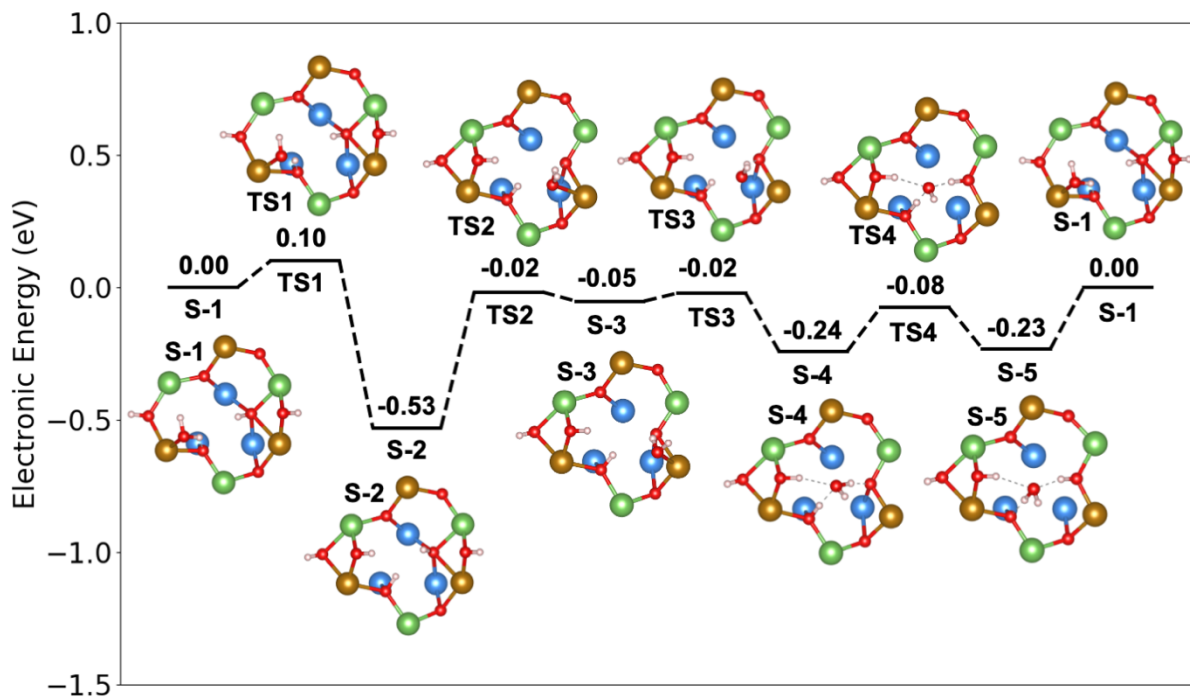


Figure C.8 Hydrogen spillover pathway across the Co_3O_4 substrate. One additional H on the hydroxylated $\text{Co}_3\text{O}_4(111)$ support can migrate across it through a Grotthuss-type mechanism. A metastable H-bonded water intermediate (seen all states beside S-2) facilitates the diffusion of H. The spillover process has an electronic energy barrier of 0.63 eV.

The simulated hydrogen spillover pathway is shown in **Figure C.8**. Since the Co_3O_4 support is covered with OH under steady state HDO, we expect the Pd_1 -generated H to spillover quickly across the substrate. H diffuses over the hydroxylated surface in an H_2O -mediated pathway. Starting from the surface with an additional H (S-2), two surface OH can recombine into an adsorbed water molecule (TS2). This metastable water intermediate can easily reposition itself atop two OH groups (TS3 and S-4), where it can shuttle one H to the next cell (TS4). Finally, the water intermediate can restore the surface OH (TS1). Overall, the spillover of H across the Co_3O_4 substrate is rapid, costing only 0.63 eV in electronic energy (barrier between S-2 and TS1).

C.4 Alternative anisole HDO pathway over a grafted Mo_1 site

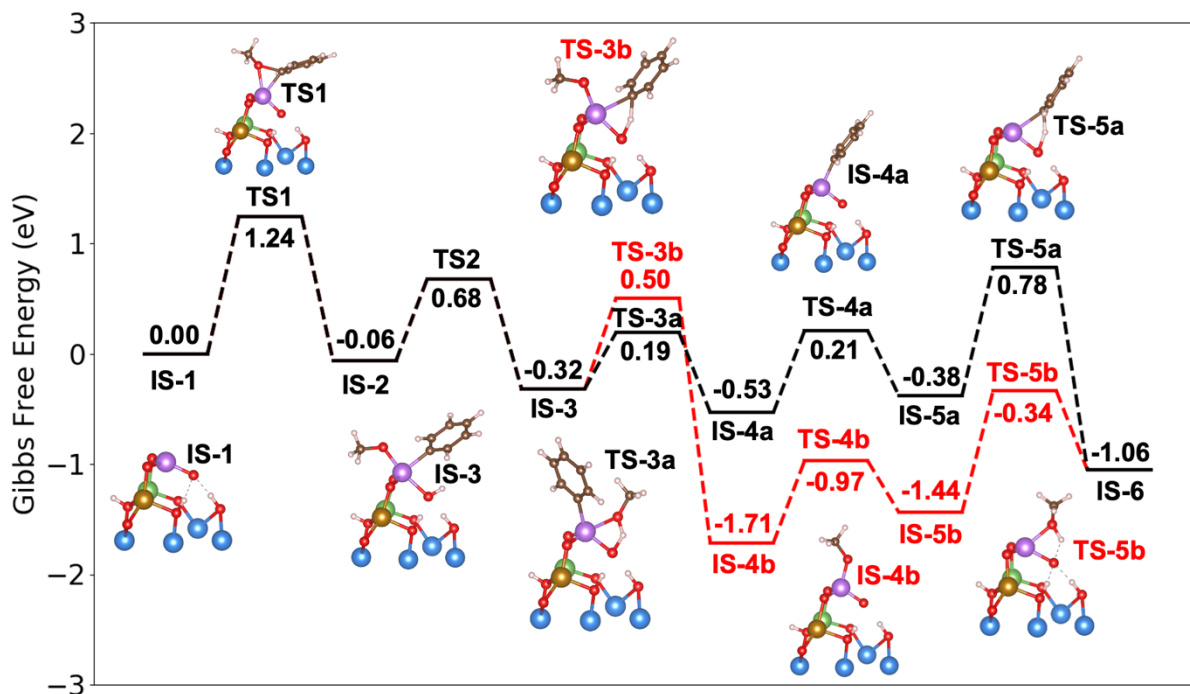


Figure C.9 The HDO of anisole over a grafted Mo_1 site assisted by H spillover from Pd_1 . The reaction can proceed through hydrogenation of the methoxy fragment first (black pathway) or the phenyl fragment first (red pathway). The overall reaction has a rather high Gibbs free energy span of 1.90 eV and thus is unlikely to be responsible for the reactivity of $\text{Mo}_1+\text{Pd}_1/\text{Co}_3\text{O}_4$.

Aside from the reaction pathway shown in **Figure 4.2** over a substituted Mo_1 site, we also examined the HDO of anisole was also over a grafted Mo_1 site (**Figure C.9**). Here, SCF cycles were considered converged when the energy between consecutive electronic steps fall below 10^{-6} eV. Forces on the atoms were converged to below 0.05 eV/Å. The reaction proceeds in a similar fashion. First, the anisole molecule directly dissociates over the Mo_1 site, forming a $-\text{C}_6\text{H}_5$ and an $-\text{OCH}_3$ ligand. The ligands are then hydrogenated one at a time with H atoms generated by spillover across the $\text{Co}_3\text{O}_4(111)$ surface (**Figure C.9**). The reaction could proceed through either the $-\text{OCH}_3$ ligand or the $-\text{C}_6\text{H}_5$ ligand first. Compared to the reaction network shown in **Figure 4.2**, we see

that it is difficult to eliminate the residual OCH₃ group (state IS-4b) in this network. As a result, the Gibbs free energy span of the catalytic cycle is 1.90 eV, rendering the grafted Mo₁ site rather unreactive under reaction conditions.

C.5 Estimation of the Gibbs free energy barrier for adsorption

A Gibbs free energy barrier for molecular adsorption steps can be estimated based on the collision theory rate constant of adsorption. Assuming that there is no potential energy barrier in the adsorption process, we have the following rate constant for adsorption:²¹⁰

$$k_{\text{ads},i} = \frac{\sigma A_{\text{site}} P^\circ}{\sqrt{2\pi m_i k_B T}} \quad (\text{C.1})$$

where σ is the sticking coefficient, A_{site} is the area of the active site, P° is the standard state pressure, m_i is the mass of the adsorbate, and k_B is Boltzmann's constant.

Recasting the rate constant into transition state theory, we can extract the following Gibbs free energy of activation for adsorption. We note that a similar derivation was carried out by Cohen and Vlachos to include adsorption/desorption rate constants in the energetic span model.⁶² For simplicity, we assumed the sticking coefficient to be 1:

$$\frac{k_B T}{h} \exp\left(\frac{-\Delta G_{\text{act}}^\circ}{RT}\right) = \frac{A_{\text{site}} P^\circ}{\sqrt{2\pi m_i k_B T}} \quad (\text{C.2})$$

$$\Delta G_{\text{act}}^\circ = -RT \ln\left(\frac{h}{\sqrt{2\pi m_i k_B T}} A_{\text{site}} \frac{P^\circ}{k_B T}\right) \quad (\text{C.3})$$

The entropy and enthalpy of activation can be derived from the Gibbs free energy of activation:

$$\Delta S_{\text{act}}^\circ = R \ln\left(\frac{h}{\sqrt{2\pi m_i k_B T}} A_{\text{site}} \frac{P^\circ}{k_B T} e^{-3/2}\right) \quad (\text{C.4})$$

$$\Delta H_{\text{act}}^\circ = \frac{-3RT}{2} \quad (\text{C.5})$$

The standard Gibbs free energy of this state can be found as the following:

$$G_{\text{TS,ads}}^{\circ} = \Delta G_{\text{act}}^{\circ} + G_i^{\circ} + G_{*}^{\circ} \quad (\text{C.6})$$

where G_i° is the Gibbs free energy of adsorbate i at standard pressure and G_{*}° is the standard Gibbs free energy of the vacant active site. Starting from the BET surface area of the catalyst (111 m^2/g), the mass fraction of Pd (0.25 wt%), and the atomic fraction of Pd and on the surface (0.00504 Pd/Co, 0.0585 Mo/Co), we find the area per active site to be $3.72 \times 10^{-20} \text{ m}^2$. This site area was used to compute the free energy barriers of adsorption in **Figures 4.1 and 4.2**.

C.6 Energetic span assessment of the reaction kinetics

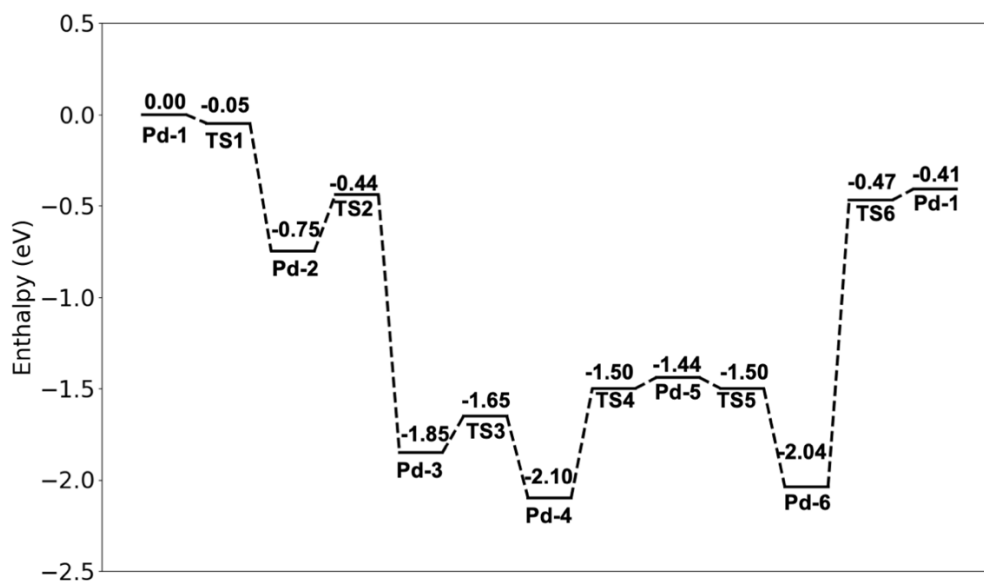


Figure C.10 The enthalpy pathway for the HDO of anisole over Pd₁. The structures of the respective intermediates and transition states are shown in **Figure C.4**.

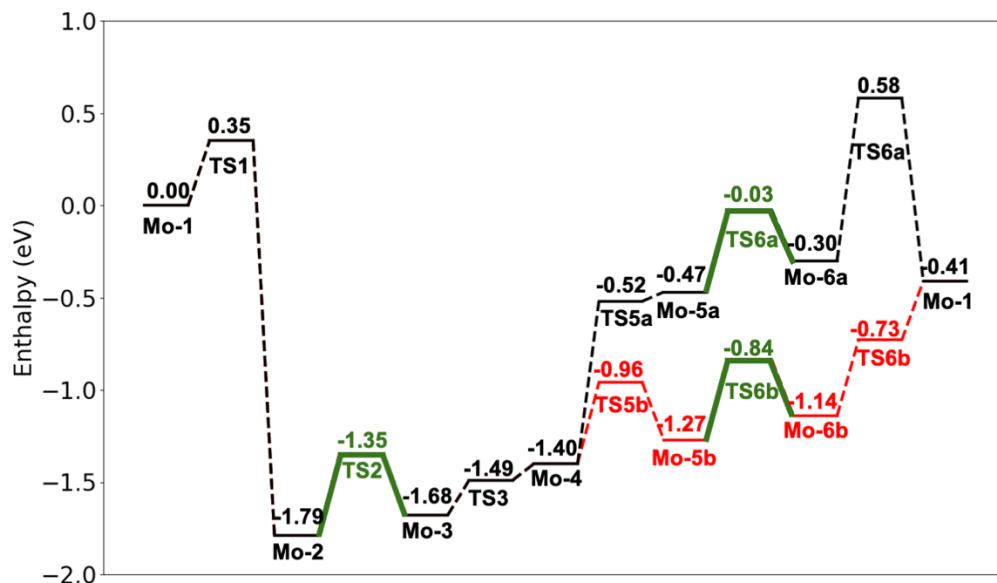


Figure C.11 The enthalpy pathway for the HDO of anisole over Mo_1 assisted by H spillover. The structures of the respective intermediates and transition states are shown in **Figure C.5**.

With the Gibbs free energy of all reactants, products, intermediates, and transition states in the reaction defined, we may assess the kinetics of anisole HDO using the energetic span model. Since the energetic span model is derived from the analytical solution for the steady state rate of single-site catalytic reactions, it can be applied to the single-site HDO mechanisms developed in this work (**Figure 4.1 and 4.2**).⁵⁹⁻⁶¹

For the HDO reaction over Mo_1 assisted by H spillover at 1% anisole conversion, we find that both Mo-1 and Mo-5b are possible candidates for the TOF-determining intermediate (TDI), while TS1 is the sole candidate for the TOF-determining transition state (TDTS). The Gibbs free energy span between Mo-1 and TS-1 is 1.30 eV, and that between Mo-5b and TS1 is 1.31 eV.

For the reaction over Pd_1 only, we find two possible TOF-determining intermediates (TDIs), the bare Pd (Pd-5) and PdH_2 (Pd-6), but one TOF-determining transition state (TDTS). In

this case, the Gibbs free energy spans are 1.23 eV and 1.28 eV for the Pd-5-to-TS6 and Pd-6-to-TS6 cycles, respectively, while the enthalpy spans are 0.98 eV and 1.57 eV for the two cycles.

From the general form of the analytical rate in ref ⁵⁹, we see that the rate of reaction should be:

$$r \approx \frac{k_B T}{h} \frac{\theta_{Pd,0}}{\exp\left(\frac{\Delta G_{span,Pd-5 \text{ to TS6}}}{RT}\right) + \exp\left(\frac{\Delta G_{span,Pd-6 \text{ to TS6}}}{RT}\right)} \quad (C.7)$$

The apparent activation energy of a rate law is in the above form is:

$$E_{a,app} = RT + \sum_{i,j} P_{i,j} H_{i,j} \quad (C.8)$$

$$P_{i,j} = \frac{\exp\left(\frac{\Delta G_{span,IS-i \text{ to TS-j}}}{RT}\right)}{\sum_{i,j} \exp\left(\frac{\Delta G_{span,IS-i \text{ to TS-j}}}{RT}\right)} \quad (C.9)$$

where *i* and *j* denote the *i*th intermediate and *j*th transition state, and $H_{i,j}$ is the corresponding enthalpy span between the *i*th intermediate and *j*th transition state, defined in the same way as the Gibbs free energy span but over the enthalpy landscape. We note that equation (13) is similar to the equation of Mao and Campbell which relates the degree of rate control to apparent activation energy.²¹⁵ Using the two equations, we find the rate of reaction over only the Pd₁ sites to be $1.08 \times 10^{-3} \text{ min}^{-1}$ and the apparent activation energy to be 1.49 eV at 150 °C.

For the HDO reaction mechanism over Mo₁ assisted by H spillover, we find the enthalpy spans to be 1.21 eV between Mo-5a and TS1 and 0.35 eV between Mo-1 and TS1. Using the two equations again, we find the rate of reaction over the Mo sites assisted by H spillover to be $3.97 \times 10^{-3} \text{ min}^{-1}$ and the apparent activation energy to be 0.93 eV at 150 °C.

C.7 Parameters and additional results of microkinetic simulations

Table C.5 Elementary steps of the HDO of anisole over Pd₁. The rate constants, Gibbs free energies of reaction, and Gibbs free energy are computed at 150 °C and 1 bar. The Gibbs free energy barriers for adsorption steps modelled with collision theory are marked as N/A.

#	Elementary step	ΔG° (eV)	$\Delta G_{\text{fwd}}^{0\ddagger}$ (eV)	k^{fwd} (s ⁻¹)	k^{rev} (s ⁻¹)
1	$\text{Pd} - 1 + \text{C}_6\text{H}_5\text{OCH}_3(\text{g}) \rightleftharpoons \text{Pd} - 2$	0.04	N/A	4.58×10^7	1.42×10^8
2	$\text{Pd} - 2 \rightleftharpoons \text{Pd} - 3$	-1.06	0.40	1.59×10^8	3.69×10^{-5}
3	$\text{Pd} - 3 \rightleftharpoons \text{Pd} - 4$	-0.30	0.22	2.21×10^{10}	5.55×10^6
4	$\text{Pd} - 5 + \text{C}_6\text{H}_6(\text{g}) \rightleftharpoons \text{Pd} - 4$	0.01	N/A	5.39×10^7	7.26×10^7
5	$\text{Pd} - 5 + \text{H}_2(\text{g}) \rightleftharpoons \text{Pd} - 6$	-0.05	N/A	3.35×10^8	7.89×10^7
6	$\text{Pd} - 1 + \text{CH}_3\text{OH}(\text{g}) \rightleftharpoons \text{Pd} - 6$	0.86	N/A	8.41×10^7	4.71×10^{-3}

Table C.6 Elementary steps of the HDO of anisole over Mo₁ assisted by H spillover. The rate constants, Gibbs free energies of reaction, and Gibbs free energy are computed at 150 °C and 1 bar. The Gibbs free energy barriers for adsorption steps modelled with collision theory are marked as N/A. Sites on the substrate are denoted as “s”.

#	Elementary step	ΔG° (eV)	$\Delta G_{\text{fwd}}^{0\ddagger}$ (eV)	k^{fwd} (s ⁻¹)	k^{rev} (s ⁻¹)
1	$\text{Mo} - 1 + \text{C}_6\text{H}_5\text{OCH}_3(\text{g}) \rightleftharpoons \text{Mo} - 2$	-1.07	1.10	6.92×10^{-1}	1.21×10^{-13}
2	$\text{Mo} - 2 + \text{H} - \text{s} \rightleftharpoons \text{Mo} - 3 + \text{s}$	0.14	0.49	1.31×10^7	5.63×10^8
3	$\text{Mo} - 3 \rightleftharpoons \text{Mo} - 4$	0.25	0.19	5.03×10^{10}	5.18×10^{13}
4	$\text{Mo} - 5\text{a} + \text{CH}_3\text{OH}(\text{g}) \rightleftharpoons \text{Mo} - 4$	-0.26	N/A	8.41×10^7	7.46×10^4
5	$\text{Mo} - 5\text{a} + \text{H} - \text{s} \rightleftharpoons \text{Mo} - 6\text{a} + \text{s}$	0.24	0.49	1.31×10^7	8.94×10^9
6	$\text{Mo} - 1 + \text{C}_6\text{H}_6(\text{g}) \rightleftharpoons \text{Mo} - 6\text{a}$	0.80	1.66	1.40×10^{-7}	4.25×10^2
7	$\text{Mo} - 5\text{b} + \text{C}_6\text{H}_6(\text{g}) \rightleftharpoons \text{Mo} - 4$	0.46	1.00	1.24×10^1	3.29×10^6
8	$\text{Mo} - 5\text{b} + \text{H} - \text{s} \rightleftharpoons \text{Mo} - 6\text{b} + \text{s}$	0.12	0.49	1.31×10^7	3.88×10^8
9	$\text{Mo} - 1 + \text{CH}_3\text{OH}(\text{g}) \rightleftharpoons \text{Mo} - 6\text{b}$	-0.03	0.41	1.12×10^8	4.93×10^7

Under the specified temperature range and gas environment, we find the Mo₁ sites, with assistance from Pd₁-enabled H spillover, are more active than the Pd₁ sites alone. As temperature

risers, the apparent activation energy of the HDO reaction over both Mo_1 assisted by H spillover and Pd_1 decrease as the coverage of reactive intermediates decrease. For further analysis, we computed the DRC of key intermediates and transition states in the reaction mechanisms.

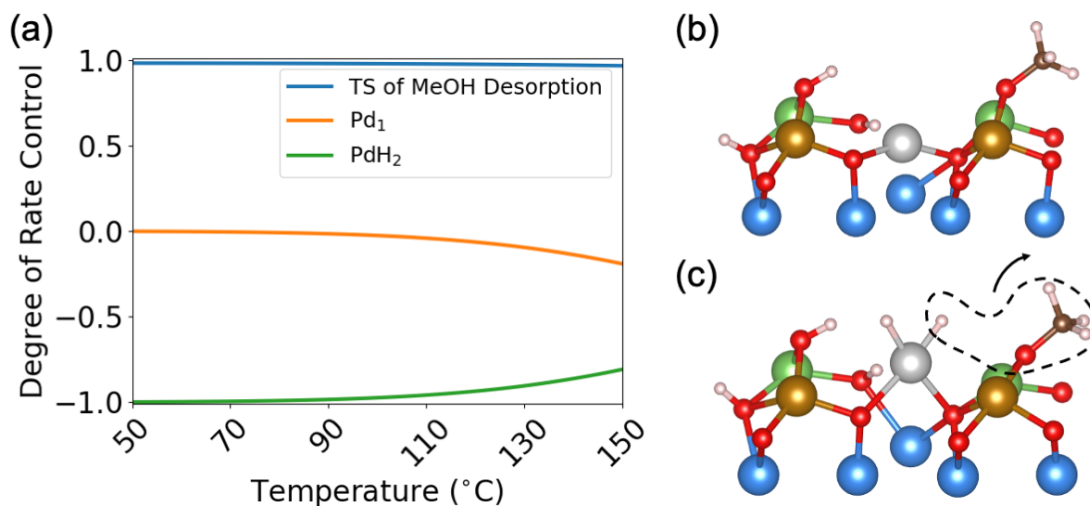


Figure C.12 (a) The DRC of key intermediates and transition states in the HDO of anisole over Pd_1 and (b, c) their geometries. The desorption of methanol is the sole rate-controlling transition state, while the PdH_2 is the main rate-controlling intermediate. The DRC of PdH_2 decreases with temperature.

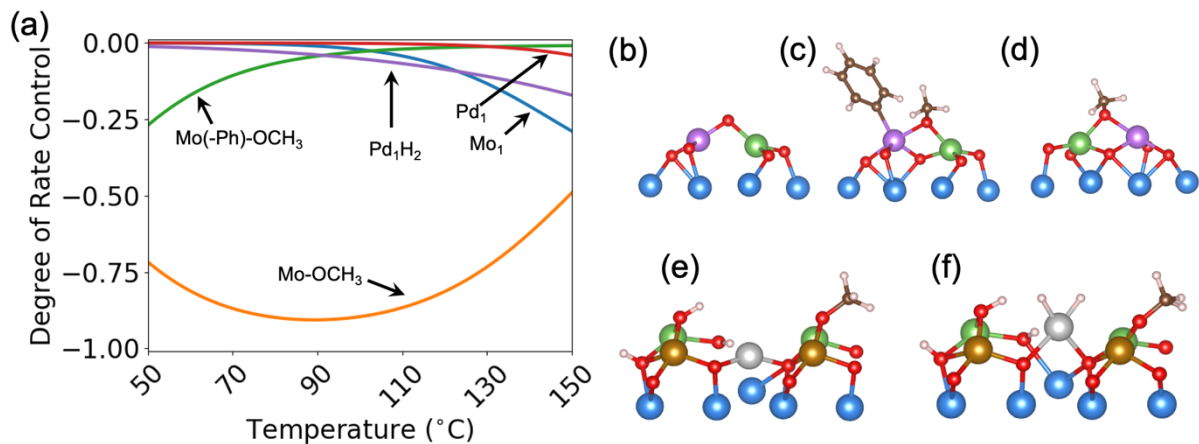


Figure C.13 (a) The DRC of key intermediates in the HDO of anisole over Mo₁+Pd₁ and (b-f) their geometries. The Mo-OCH₃ species has the lowest DRC in the temperature range studied, but gradually becomes less rate-controlling as temperature increases.

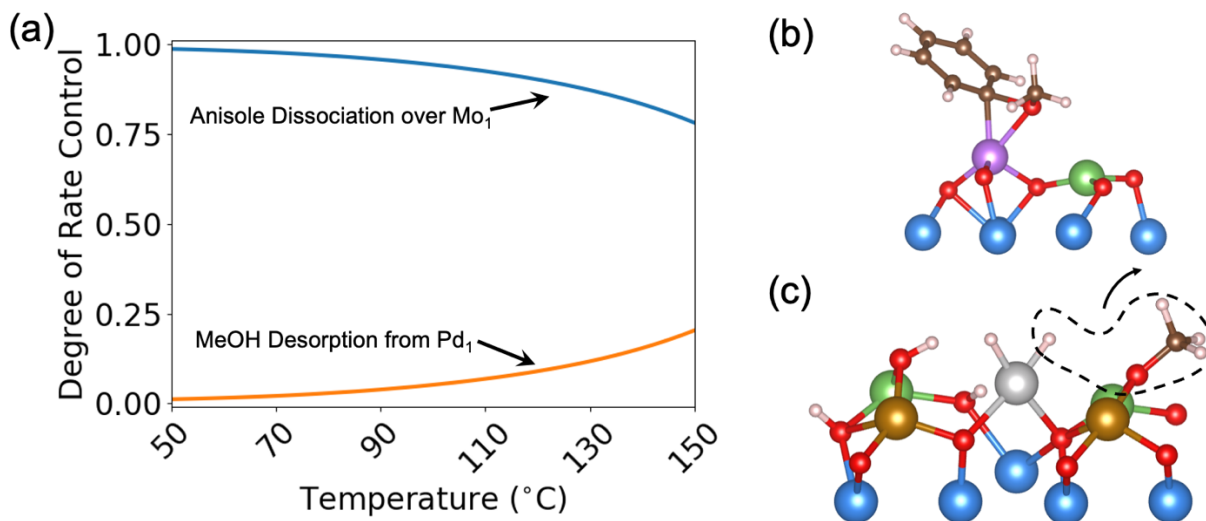


Figure C.14 (a) The DRC of key transition states in the HDO of anisole over Mo₁+Pd₁ and (b-c) their geometries. The dissociation of anisole has the highest DRC in the temperature range studied, but gradually becomes less rate-controlling as temperature increases.

As shown in **Figure C.12**, in the HDO of anisole over Pd₁, the desorption of methanol is the sole rate-controlling TS, while the bare Pd₁ species and the PdH₂ species are the rate-controlling

intermediates. The coverage of hydrides on Pd₁ gradually decreases with time, resulting in an increasing DRC of PdH₂ and a lowering apparent activation energy. These results agree with those from our energetic span analysis, where we found the TS of the desorption of methanol to be the sole TDTS and the bare Pd₁ site and PdH₂ to be the TDIs.

On the other hand, the dissociation of anisole is the main rate-controlling TS in the HDO of anisole over Mo₁+Pd₁ with an increasing contribution of the recombination of methanol with increasing temperature (**Figure C.13 and C.14**). The rate-controlling intermediate, on the other hand, changes more with temperature. Near 50 °C, the dissociated anisole (Mo-2) and the bridging methoxy (Mo-5b) are the two rate-controlling intermediates. The importance of these two states is reflected in the high apparent activation energy at this temperature. As temperature increases, the DRC of Mo-2 quickly increases to 0, while the DRC of Mo-5b gradually decreases. These changes also result in a decrease of the apparent activation energy with temperature. Like the case of anisole HDO over only Pd₁, these results also agree with those from our energetic span analysis, where we found the dissociation of anisole to be the sole TDTS and the bare Mo₁ site and the Mo₁ with a bridging methoxy to be the TDIs. With a further increase in temperature, the bare Mo₁ site gains rate controlling nature, accompanying another decrease in the apparent activation energy.

Appendix D Supplementary Information for Chapter 5

D.1 Supplementary energetics and adsorption configurations

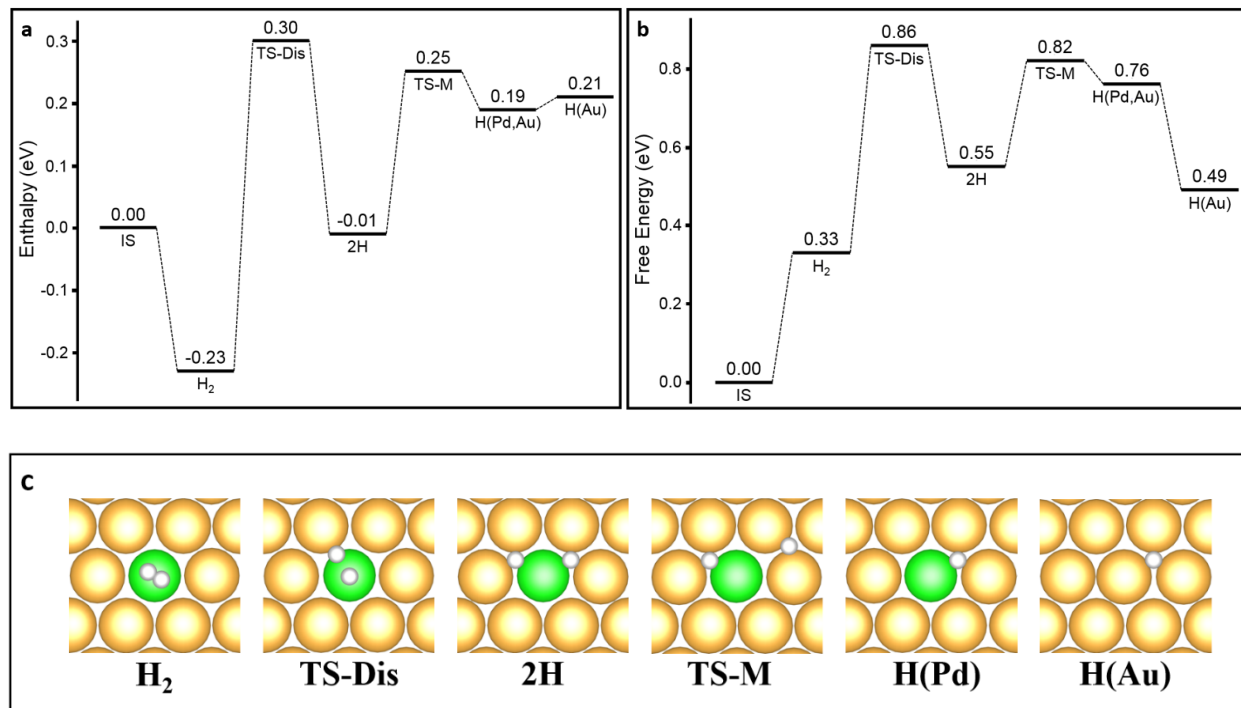


Figure D.1 (a) Enthalpy and (b) free energy profiles for hydrogen dissociation and migration on the Pd₁-in-Au(111) surface. The reaction starts with H₂ molecular adsorption [H₂], followed by the transition state of dissociation [TS-Dis] to form two separated hydrogen atoms [2H]. One of the hydrogen atoms would migrate to the Au surface by going through the transition state for migration [TS-M], reaching the [H(Pd,Au)] state. The H atom at the Pd site would eventually combine with another H atom and desorb while the one at the Au site remains on the surface [H(Au)]. Conditions used for the free energy profile are: T = 363 K and P(H₂) = 0.2 bar. (c) Configurations of each of the steps in the energy profiles.

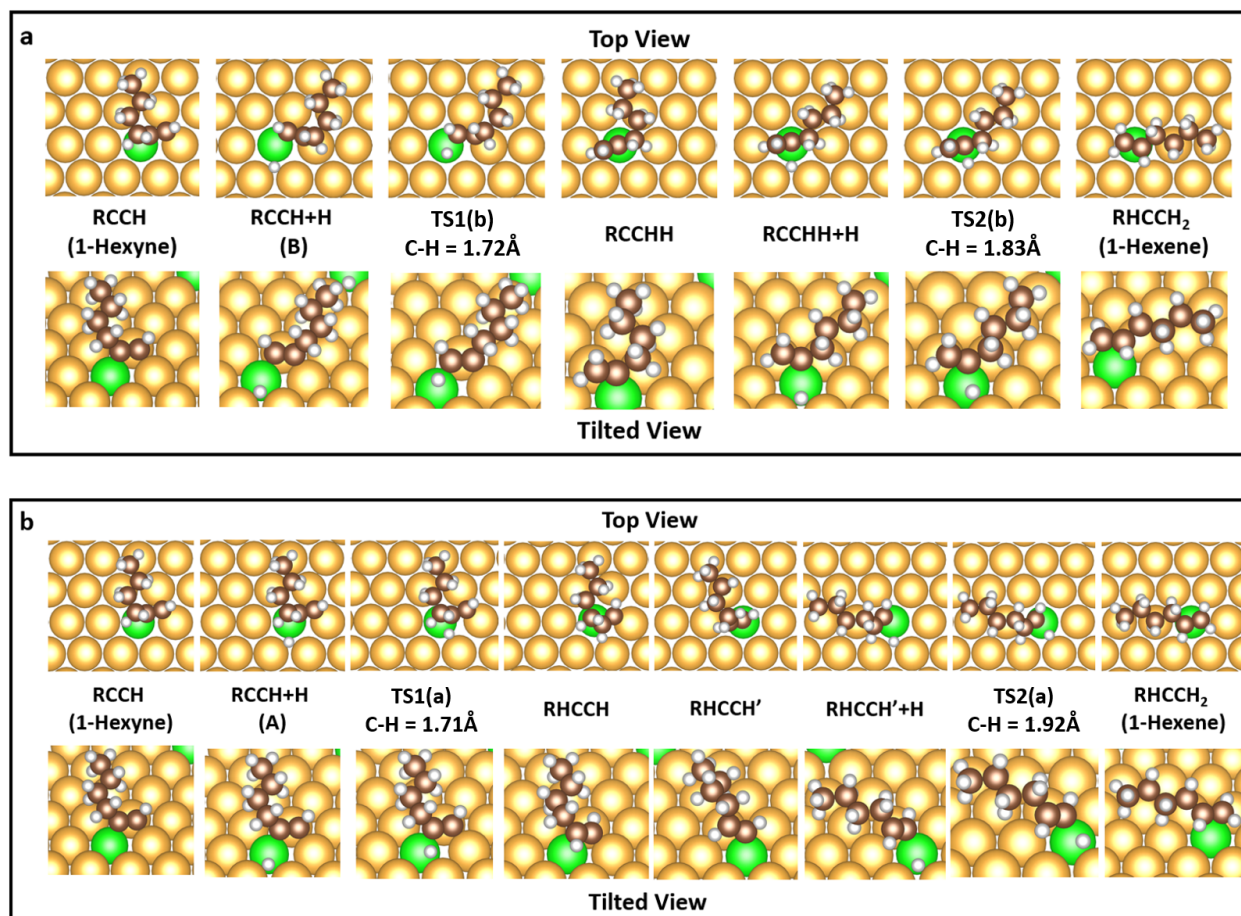


Figure D.2 Adsorption configuration of the carbonaceous intermediates on Pd₁Au(111) for (a) the hydrogenation of the terminal carbon atom (C₁) in the first reaction step, followed by the hydrogenation of the carbon atom attached to the butyl group (C₂) and for (b) the hydrogenation of C₂ in the first step, followed by the hydrogenation of C₁.

Table D.1 Free energy values for 1-hexene hydrogenation to form hexane. The same reference for 1-hexyne hydrogenation was used, i.e. 1-hexyne and H₂ in the gas phase. Conditions are: T = 363 K, P(H₂) = 0.2 bar, P(C₆H₁₀) = 0.01 bar, P(C₆H₁₂) = P(C₆H₁₄) = 0.001bar.

States	Free Energy (eV)
RHCCH ₂ (1-Hexene)	-1.42
TS (H atom to RHCCH ₂)	-0.56
RHCCH ₂ + H (To form 1-Hexyl)	-0.96
RHCCH ₂ + H (To form 2-Hexyl)	-0.91
TS (To form 1-Hexyl)	-0.65
TS (To form 2-Hexyl)	-0.56
RH ₂ CCH ₂ (1-Hexyl)	-1.33
RHCCH ₃ (2-Hexyl)	-1.29
TS (H atom to RH ₂ CCH ₂)	-0.47
TS (H atom to RHCCH ₃)	-0.43
RH ₂ CCH ₂ + H	-0.95
RHCCH ₃ + H	-0.95
TS (From RH ₂ CCH ₂ + H)	-0.74
TS (From RHCCH ₃ + H)	-0.79
Hexane	-2.22
Hexane (g)	-2.56

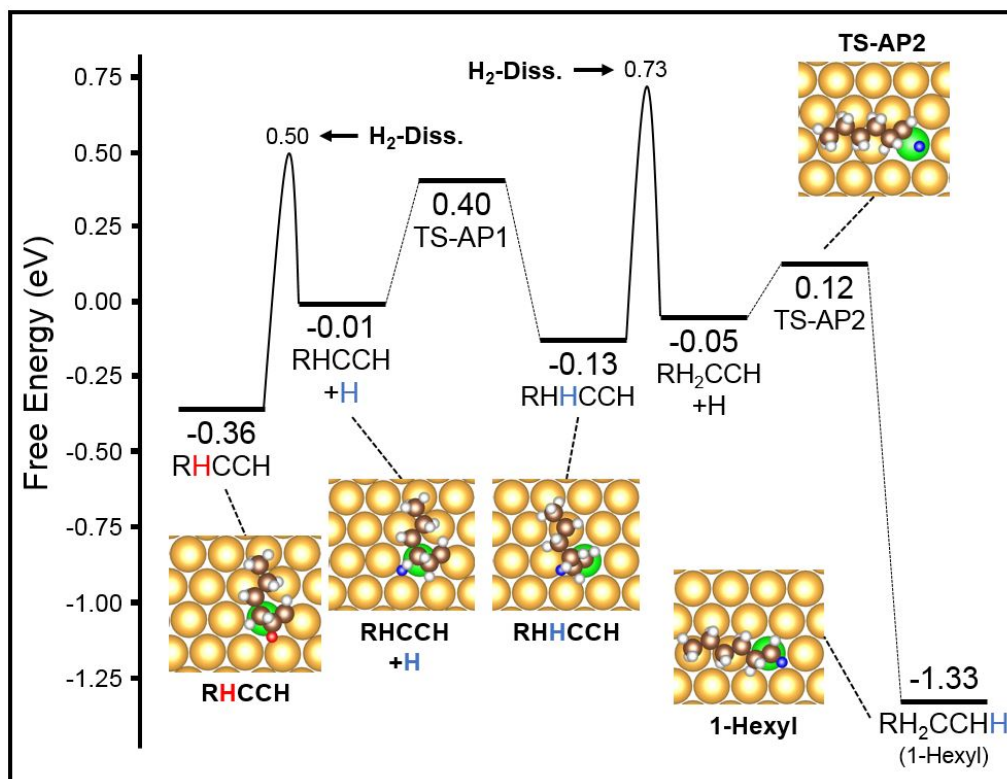


Figure D.3 Free energy diagram of 1-hexyl formation via 1-hexylidene on the Pd₁Au(111) surface.

The C2 atom was chosen in the first place for the over-hydrogenation as there is electron donation from the carbon chain to help stabilize the transition state. The barrier for the forward hydrogenation of 1-hexylidene (RHCCH) is 0.33 eV higher than the reverse barrier. In addition, this side-pathway has an overall free energy barrier (1.09 eV) that is at least 0.26 eV higher than that of the regular pathway to form 1-hexyl via 1-hexene (0.83 eV). Hence, this pathway is energetically unfavorable and is unlikely to deteriorate the selectivity for 1-hexene formation. Conditions are: T = 363 K, P(H₂) = 0.2 bar, P(C₆H₁₀) = 0.01 bar, P(C₆H₁₂) = P(C₆H₁₄) = 0.001 bar.

D.2 Detailed description of the microkinetic model

Table D.2 Kinetic parameters, Gibbs free energies of reaction and activation derived from DFT-computed electronic energies evaluated at 363 K and standard pressure (1 bar). The n-butyl tail of gaseous and adsorbed C₆ species is denoted as “R”. Hydrogen atoms co-adsorbed with carbonaceous intermediates are indicated as (H).

#	Elementary step	ΔG° (eV)	$\Delta G_{\text{fwd}}^{\ddagger}$ (eV)	k^{fwd} (s ⁻¹)	k^{rev} (s ⁻¹)
1	$\text{Pd}_1 + \text{H}_{2(\text{g})} \rightleftharpoons \text{H}_2 - \text{Pd}_1$	0.28	N/A	6.92×10^8	6.07×10^{12}
2	$\text{H}_2 - \text{Pd}_1 \rightleftharpoons \text{PdH}_2$	0.22	0.52	4.02×10^5	4.59×10^8
3	$\text{PdH}_2 + \text{Au} \rightleftharpoons \text{PdH}_1 + \text{H} - \text{Au}$	0.20	0.26	1.77×10^9	1.12×10^{12}
4	$\text{PdH}_1 + \text{Au} \rightleftharpoons \text{Pd} + \text{H} - \text{Au}$	0.23	0.28	8.71×10^8	1.18×10^{12}
5	$\text{Pd}_1 + \text{RCCH}_{(\text{g})} \rightleftharpoons \text{RCCH} - \text{Pd}_1$	-0.09	N/A	1.08×10^8	5.58×10^6
6	$\text{RCCH} - \text{Pd}_1 + \text{H} - \text{Au}$ $\rightleftharpoons (\text{H})\text{RCCH} - \text{Pd}_1 + \text{Au}$	-0.14	0.06	1.15×10^{12}	1.16×10^{10}
7	$(\text{H})\text{RCCH} - \text{Pd}_1 \rightleftharpoons \text{RHCCH} - \text{Pd}_1$	-0.79	0.32	2.80×10^8	3.30×10^{-3}
8	$\text{RHCCH} - \text{Pd}_1 + \text{H} - \text{Au}$ $\rightleftharpoons \text{RHCCH}(\text{H}) - \text{Pd}_1 + \text{Au}$	0.03	0.06	1.15×10^{12}	3.38×10^{12}
9	$\text{RHCCH}(\text{H}) - \text{Pd}_1 \rightleftharpoons \text{RHCCH}_2 - \text{Pd}_1$	-1.56	0.07	9.33×10^{11}	2.13×10^{-10}
10	$\text{Pd}_1 + \text{RHCCH}_{2(\text{g})} \rightleftharpoons \text{RHCCH}_2 - \text{Pd}_1$	-0.15	N/A	1.07×10^8	8.57×10^5
11	$\text{RCCH} - \text{Pd}_1 + \text{H} - \text{Au}$ $\rightleftharpoons \text{RCCH}(\text{H}) - \text{Pd}_1 + \text{Au}$	-0.13	0.06	1.15×10^{12}	1.67×10^{10}
12	$\text{RCCH}(\text{H}) - \text{Pd}_1 \rightleftharpoons \text{RCCH}_2 - \text{Pd}_1$	-0.78	0.43	7.36×10^6	9.75×10^{-5}
13	$\text{RCCH}_2 - \text{Pd}_1 + \text{H} - \text{Au}$ $\rightleftharpoons (\text{H})\text{RCCH}_2 - \text{Pd}_1 + \text{Au}$	-0.16	0.06	1.15×10^{12}	8.09×10^9
14	$(\text{H})\text{RCCH}_2 - \text{Pd}_1 \rightleftharpoons \text{RHCCH}_2 - \text{Pd}_1$	-1.39	0.13	1.08×10^{11}	6.38×10^{-9}
15	$\text{RHCCH}_2 - \text{Pd}_1 + \text{H} - \text{Au}$ $\rightleftharpoons (\text{H})\text{RHCCH}_2 - \text{Pd}_1 + \text{Au}$	-0.03	0.06	1.15×10^{12}	4.95×10^{11}
16	$(\text{H})\text{RHCCH}_2 - \text{Pd}_1 \rightleftharpoons \text{RH}_2\text{CCH}_2 - \text{Pd}_1$	-0.37	0.31	4.26×10^8	3.24×10^3
17	$\text{RH}_2\text{CCH}_2 - \text{Pd}_1 + \text{H} - \text{Au}$ $\rightleftharpoons \text{RH}_2\text{CCH}_2(\text{H}) - \text{Pd}_1 + \text{Au}$	-0.12	0.06	1.15×10^{12}	2.64×10^{10}
18	$\text{RH}_2\text{CCH}_3 - \text{Pd}_1 \rightleftharpoons \text{RH}_2\text{CCH}_3 - \text{Pd}_1$	-1.26	0.22	7.81×10^9	2.41×10^{-8}
19	$\text{Pd}_1 + \text{RH}_2\text{CCH}_{3(\text{g})} \rightleftharpoons \text{RH}_2\text{CCH}_3 - \text{Pd}_1$	0.12	N/A	1.06×10^8	5.53×10^9
20	$\text{RHCCH}_2 - \text{Pd}_1 + \text{H} - \text{Au}$ $\rightleftharpoons \text{RHCCH}_2(\text{H}) - \text{Pd}_1 + \text{Au}$	0.02	0.06	1.15×10^{12}	2.17×10^{12}
21	$\text{RHCCH}_2(\text{H}) - \text{Pd}_1 \rightleftharpoons \text{RHCCH}_3 - \text{Pd}_1$	-0.38	0.35	1.14×10^8	6.18×10^2
22	$\text{RHCCH}_3 - \text{Pd}_1 + \text{H} - \text{Au}$ $\rightleftharpoons (\text{H})\text{RHCCH}_3 - \text{Pd}_1 + \text{Au}$	-0.15	0.06	1.15×10^{12}	8.42×10^9
23	$(\text{H})\text{RHCCH}_3 - \text{Pd}_1 \rightleftharpoons \text{RH}_2\text{CCH}_3 - \text{Pd}_1$	-1.26	0.16	4.43×10^{10}	1.37×10^{-7}
24	$\text{RHCCH} - \text{Pd}_1 + \text{H} - \text{Au}$ $\rightleftharpoons (\text{H})\text{RHCCH} - \text{Pd}_1 + \text{Au}$	-0.11	0.06	1.15×10^{12}	3.69×10^{10}
25	$(\text{H})\text{RHCCH} - \text{Pd}_1 \rightleftharpoons \text{RH}_2\text{CCH} - \text{Pd}_1$	-0.13	0.40	2.09×10^7	3.59×10^5

26	$\text{RH}_2\text{CCH} - \text{Pd}_1 + \text{H} - \text{Au} \rightleftharpoons \text{RH}_2\text{CCH}(\text{H}) - \text{Pd}_1 + \text{Au}$	-0.40	0.06	1.15×10^{12}	2.87×10^6
27	$\text{RH}_2\text{CCH}(\text{H}) - \text{Pd}_1 \rightleftharpoons \text{RH}_2\text{CCH}_2 - \text{Pd}_1$	-1.28	0.16	4.04×10^{10}	6.47×10^{-8}

To quantitatively compare the reaction mechanism proposed from theory, microkinetic models were constructed using reaction kinetic parameters computed from the DFT energetics. In total, 27 reactions were included in the overall microkinetic model, which can be classified into 6 groups (**Table D.2**). In the 1st group of reactions (Reactions 1-4, **Table D.2**), a molecule of H₂ is adsorbed and dissociated at a vacant Pd₁ site. The two dissociated H atoms can then individually exchange across the Au substrate for further reaction or recombination. In the 2nd (Reactions 5-10, **Table D.2**) and 3rd group (Reactions 11-14, **Table D.2**) of reactions, a molecule of 1-hexyne is adsorbed at a vacant Pd₁ site and hydrogenated to 1-hexene with H atoms exchanged across the Au substrate. The C2 atom is hydrogenated first in the 2nd group of reactions, while the C1 atom is hydrogenated first in the 3rd group of reactions. The forward barrier for the exchange of H from the Au substrate to the C₆-containing Pd₁ sites was assumed to be the average of the barriers for the exchange of H from the Au substrate to the bare Pd₁ site and Pd₁H₁. In the 4th (Reactions 15-19, **Table D.2**) and the 5th group (Reactions 20-23, **Table D.2**) of reactions, an adsorbed 1-hexene molecule is hydrogenated to form n-hexane by exchanged H. These two groups are distinguished in the same way as in the hydrogenation of 1-hexyne to 1-hexene: the C2 atom is hydrogenated first in the 4th group, while the C1 atom is hydrogenated first in the 5th group. Finally, in the 6th group of reactions (Reactions 24-27, **Table D.2**), the 1-hexenyl intermediate is hydrogenated to the 1-hexylidene intermediate and then to the 1-hexyl intermediate by exchanged H.

D.3 Additional results from microkinetic modeling

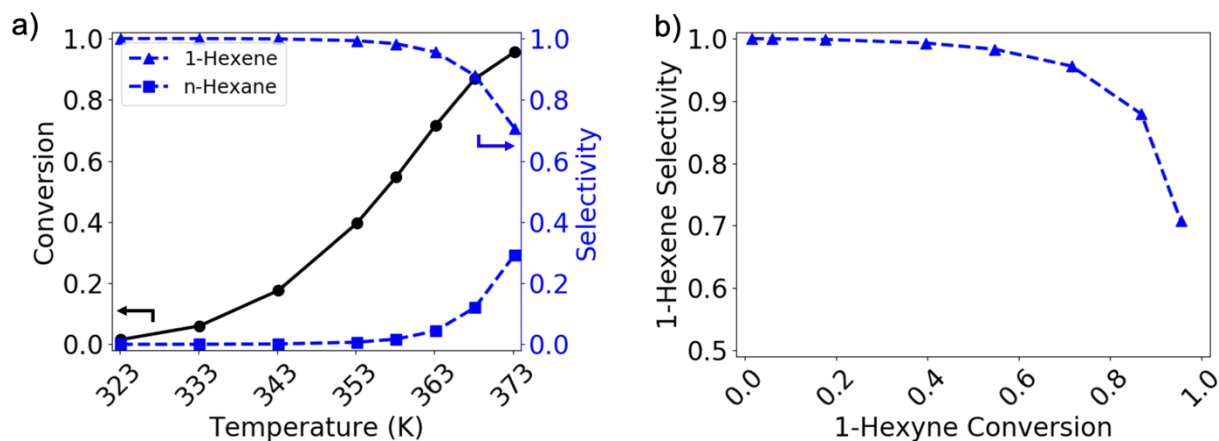


Figure D.4 Microkinetic simulations performed in the temperature range of 323~373 K at a constant inlet flow rate (50 SCCM, 20% H₂, 1% 1-Hexyne, balance inert) and catalyst loading (20 mg). (a) 1-Hexyne conversion (black circles, full line), 1-hexene selectivity (blue triangles, dashed line), and 1-hexyne selectivity (blue squares, dashed line) as a function of reactor temperature. (b) 1-Hexene selectivity plotted against 1-hexyne conversion.

As a qualitative comparison to the steady state experiments of Luneau et al. at varying conversion and temperature, the reaction model (**Table D.2**) was embedded in an isothermal and isobaric plug-flow reactor (PFR), assumed to be operated at 1 bar. The reactant flow rate was set to 50 standard cubic centimeter per minute (SCCM, corresponding to $T = 273.15$ K and $P = 1$ atm), containing 20% H₂, 1% 1-Hexyne, and balance inert. The catalyst loading was set to 20 mg. The metal content of the catalyst was assumed to be 4.2 wt%. Each Pd-in-Au nanoparticle in the catalyst was assumed to be a sphere 4.9 nm in diameter, with 5% of all atoms in each particle being Pd. In the temperature range of 323~373 K, the conversion of 1-hexyne was found to rise from 1.5% to 95.5% (**Figure D.4**). The selectivity of 1-hexene was found to be above 70% in this

temperature range (**Figure D.4b**). The calculated relationship between selectivity and conversion agrees with the reported findings of Luneau et al.¹⁸⁶

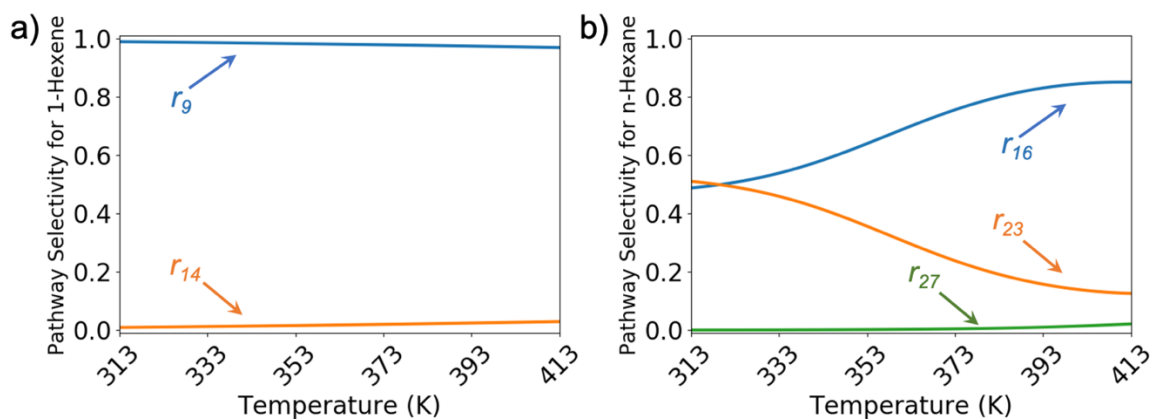


Figure D.5 Pathway selectivity for (a) the formation of 1-hexene through the hydrogenation of adsorbed 1-hexyne to 1-hexenyl (r_9 , blue) and through the hydrogenation of adsorbed 1-hexyne to 2-hexenyl (r_{14} , orange), and (b) the formation of n-hexane through the hydrogenation of adsorbed 1-hexene to 1-hexyl (r_{16} , blue), through the hydrogenation of adsorbed 1-hexene to 2-hexyl (r_{23} , orange), and through the hydrogenation of 1-hexenyl to 1-hexylidene and then 1-hexyl (r_{27} , green).

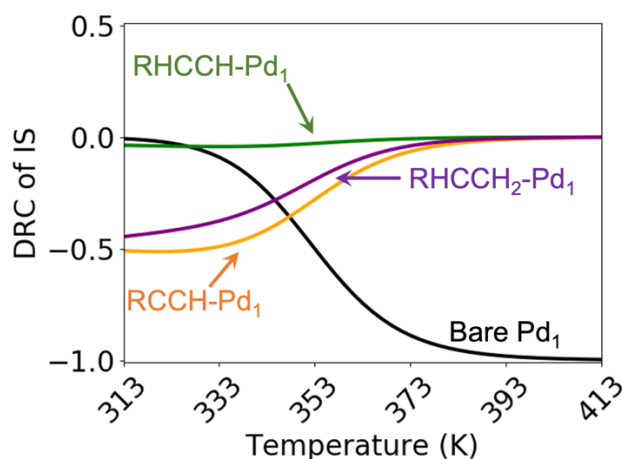


Figure D.6 The degrees of rate control of key intermediate states in the hydrogenation of 1-hexyne to 1-hexene. Adsorbed 1-hexyne (orange line) and 1-hexene (purple line) are the main rate-controlling intermediates until 353 K, largely mirroring the influence of temperature on coverages.

D.4 Derived rate laws for the hydrogenation of 1-hexyne

Table D.3 Three possible rate laws for the hydrogenation of 1-hexyne, derived by assuming H₂ dissociation, 1-hexyne hydrogenation to 1-hexenyl, or 1-hexenyl hydrogenation to 1-hexene is the rate-controlling transition state. K_i: equilibrium constant of elementary step i. k_{if}: forward rate constant of elementary step i. P_j: partial pressure of reactant (or product) j. θ_{Pd,0}: fraction of Pd sites on the catalyst surface.

Rate-Controlling Transition State	Derived Rate Law
H ₂ Dissociation	$r = \frac{K_1 k_{2f} P_{H_2} \theta_{Pd,0}}{1 + K_5 P_{1-HY} + K_{10} P_{1-HE}}$
1-Hexyne to 1-Hexenyl	$r = \frac{(K_1 K_2 K_3 K_4 P_{H_2})^{0.5} K_5 K_6 k_{7f} P_{1-HY} \theta_{Pd,0}}{1 + K_5 P_{1-HY} + K_{10} P_{1-HE}}$
1-Hexenyl to 1-Hexene	$r = \frac{(\prod_{i=1}^8 K_i) k_{9f} P_{1-HY} P_{H_2} \theta_{Pd,0}}{1 + K_5 P_{1-HY} + K_{10} P_{1-HE}}$

From the proposed reaction mechanism (**Table D.3**) and the results of the microkinetic simulations, analytical rate laws were derived to describe the rate of 1-hexyne hydrogenation (**Table D.3**). Based on the microkinetic simulations, the hydrogenation of 1-hexyne was assumed to occur through the 1-hexenyl intermediate, non-rate-controlling steps were assumed to be equilibrated, and the rate of n-hexane formation was assumed to be negligible. Additionally, adsorbed 1-hexene and 1-hexyne were assumed to be the most abundant surface intermediates based on the calculated coverages. One of three transition states (TS) were assumed to be the sole rate-controlling TS: 1) TS of H₂ dissociation, 2) TS of 1-hexyne hydrogenation to 1-hexenyl, or 3) TS of 1-hexenyl hydrogenation to 1-hexene. Based on the form of the derived rate laws, it is only possible for H₂ dissociation or 1-hexenyl hydrogenation to 1-hexene to be the rate-controlling TS to recover the experimentally measured orders of reaction.

D.5 Performance of density functionals for the adsorption energy of 1-hexyne

Table D.4 The desorption energy of 1-hexyne on Pd₁/Au(111) predicted by various density functionals. The desorption energy predicted by optPBE-vdW is the closest to the desorption enthalpy of 1-hexyne reported by Liu et al.²⁰¹

Exchange-Correlation Functional	1-Hexyne Desorption Energy (eV)
PBE ⁷⁶	0.49
PBE-dDsC ^{76, 142, 143}	1.16
optPBE-vdW ²⁰⁶⁻²⁰⁹	1.03
optB86b-vdW ²⁰⁶⁻²⁰⁹	1.43
BEEF-vdW ²⁴³	0.46

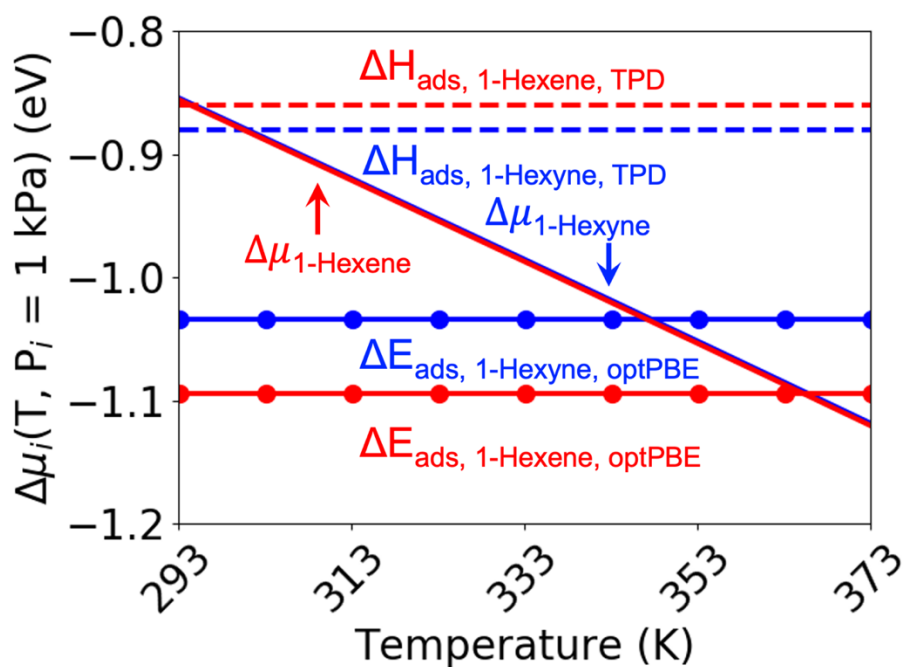


Figure D.7 The chemical potentials of 1-hexyne (blue) and 1-hexene (red) as functions of temperature at fixed pressures (1 kPa for both 1-hexyne and 1-hexene), compared to their adsorption enthalpies measured by TPD (dashed lines) and their adsorption energies calculated by the optPBE XC functional (dots).

Besides the adsorption energy of H₂, our choice of the optPBE-vdW exchange-correlation density functional was also motivated by its performance in predicting the desorption energy of 1-hexyne (**Table D.4**). Out of the five density functionals tested, PBE and BEEF-vdW were found to underpredict the desorption energy, while optPBE-vdW, PBE-dDsC, and optB86b-vdW were found to overpredict the desorption energy. optPBE-vdW performed the best, as its predicted desorption energy (1.03 eV) is the closest to the desorption enthalpy found by TPD.²⁰¹ Under reaction conditions of 1-hexyne hydrogenation studied in this work and the literature (T = 293 ~ 373 K, P_{1-Hexyne} = 1 kPa), the 1-hexyne adsorption energy predicted by optPBE-vdW results in an exergonic adsorption of 1-hexyne, while the adsorption energy found by TPD would result in an endergonic adsorption of 1-hexyne (**Figure D.7**).

D.6 Brønsted-Evans-Polanyi relation of C-H bond formation steps

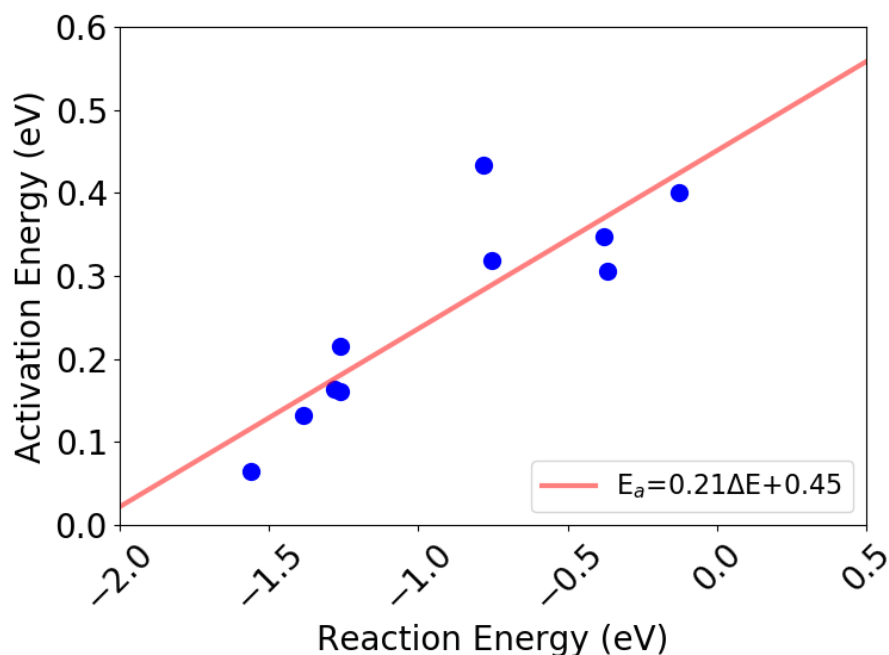


Figure D.8 Brønsted-Evans-Polanyi relation between the reaction energies and activation energies of C-H bond formation steps on Pd₁/Au(111).

D.7 Electronic structure of Pd(111) and Pd₁Au(111)

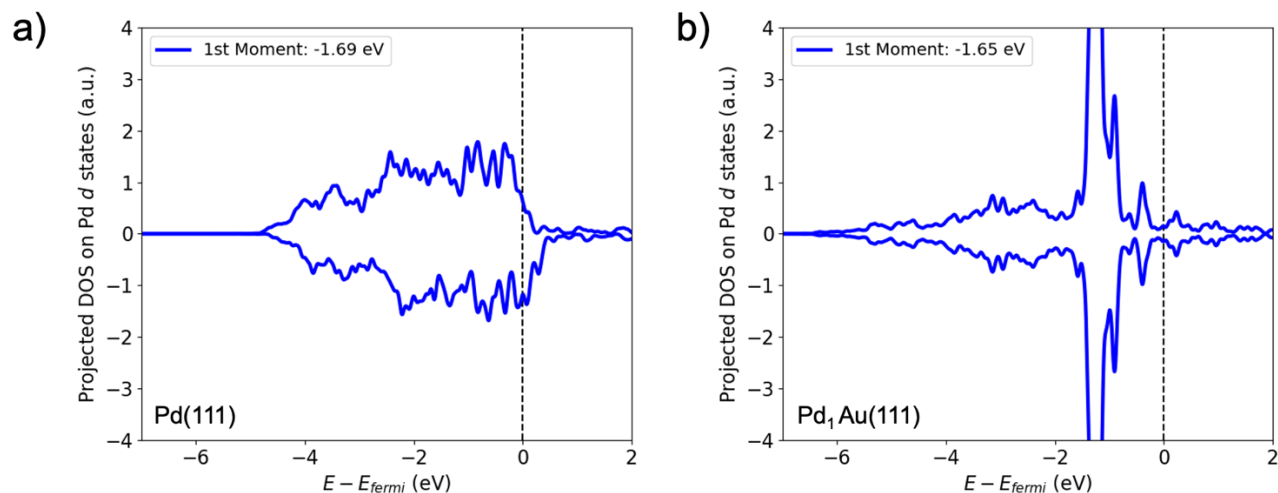


Figure D.9 Projected density of states (DOS) onto the Pd 4d orbitals of a single Pd atom on the surface of (a) Pd(111) and (b) Pd₁Au(111). The first moment of the Pd 4d states (d band center) in two situations is not very different, but the 4d band of the Pd single atom is much narrower.

To qualitatively compare the electronic structure of bulk Pd and Pd₁Au, we computed the projected DOS on both a single Pd atom on the surface of Pd(111) and one on the surface of Pd₁Au(111) (**Figure D.9**). These DOS calculations were performed in (3 × 3) cells, and the Brillouin zone integrations were performed over (9 × 9 × 1) Gamma point-centered k-point meshes. To obtain the first moment, the Pd 4d DOS was integrated from -7 eV to 2 eV relative to the Fermi level. We found that the Pd 4d band centers of the Pd atom in the two states to be very similar, at -1.69 eV for Pd(111) and -1.65 eV for Pd₁Au(111); though, the shape of the Pd 4d bands are very different.

Appendix E Supplementary Information for Chapter 6

E.1 Intermediate and transition state geometries in the isomerization/hydrogenation of 1-Hexene over Pd₁Au(111)

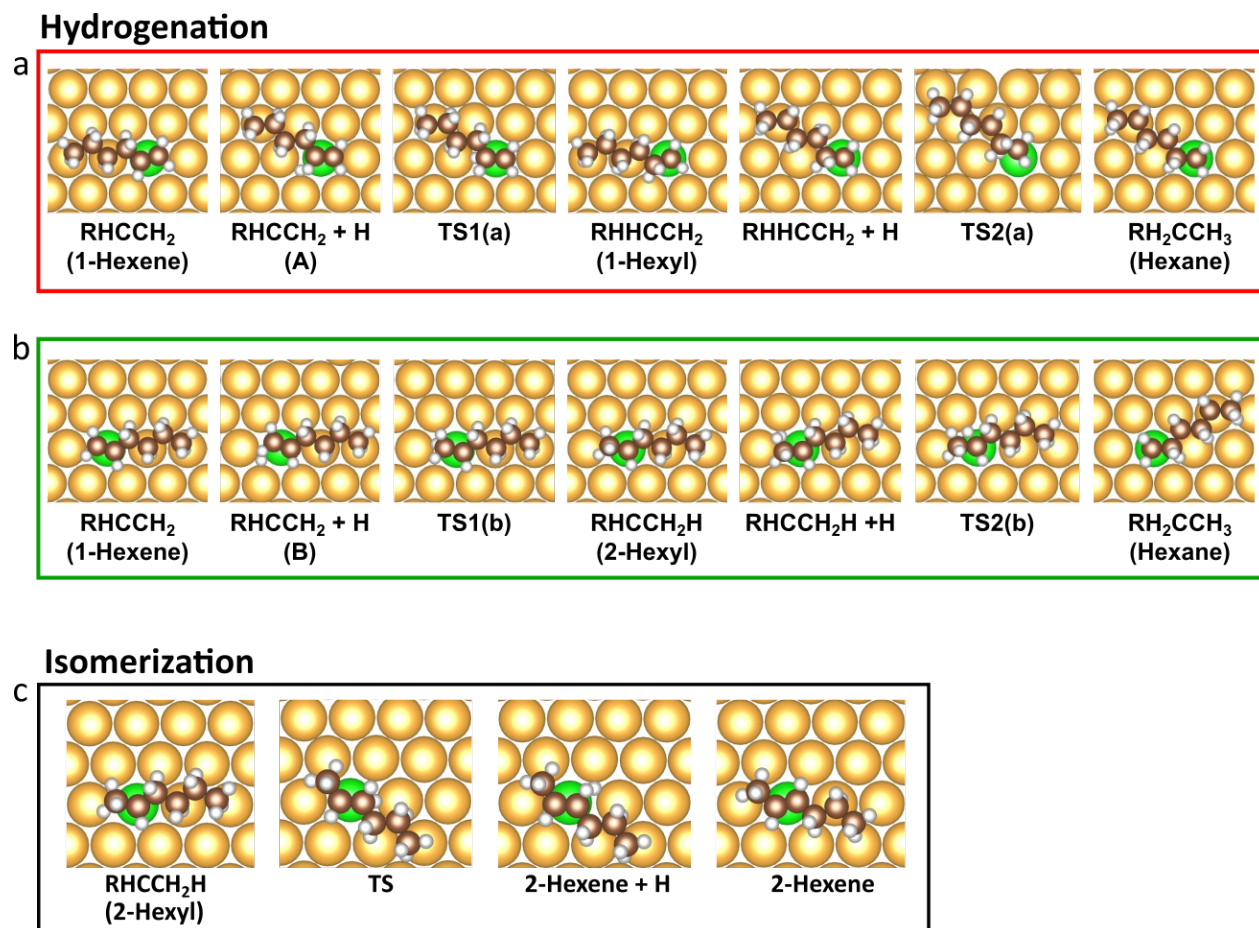


Figure E.1 Adsorption configurations of the reactant, the intermediates and the products on Pd₁Au(111) for hydrogenation of 1-hexene to n-hexane via the 1-hexyl (a) and 2-hexyl (b) intermediate, and (c) isomerization of the 2-hexyl intermediate to 2-hexene.

E.2 Additional details and results of microkinetic simulations

Table E.1 Kinetic rate constants, Gibbs free energies of reaction and of activation derived from DFT-computed electronic energies and evaluated at 373.15 K and standard pressure (1 bar). The n-propyl tail of gaseous and adsorbed C₆ species is denoted as “R”. Steps in bold indicate those not involving deuterium. No shift was applied to the barriers of H₂/D₂/HD dissociation or H/D spillover steps.

#	Elementary step	ΔG° (eV)	$\Delta G_{\text{fwd}}^{\text{of}}$ (eV)	k^{fwd} (s ⁻¹)	k^{rev} (s ⁻¹)
1	$\text{Pd}_1 + \text{H}_{2(\text{g})} \rightleftharpoons \text{H}_2 - \text{Pd}_1$	0.30	N/A	6.82E+08	7.29E+12
2	$\text{H}_2 - \text{Pd}_1 \rightleftharpoons \text{PdH}_2$	0.22	0.52	6.48E+05	6.12E+08
3	$\text{PdH}_2 + \text{Au} \rightleftharpoons \text{PdH}_1 + \text{H} - \text{Au}$	0.20	0.26	2.27E+09	1.21E+12
4	$\text{PdH}_1 + \text{Au} \rightleftharpoons \text{Pd} + \text{H} - \text{Au}$	0.23	0.28	1.14E+09	1.27E+12
5	$\text{Pd}_1 + \text{D}_{2(\text{g})} \rightleftharpoons \text{D}_2 - \text{Pd}_1$	0.35	N/A	4.83E+08	2.91E+13
6	$\text{D}_2 - \text{Pd}_1 \rightleftharpoons \text{PdD}_2$	0.22	0.52	6.48E+05	6.12E+08
7	$\text{PdD}_2 + \text{Au} \rightleftharpoons \text{PdD}_1 + \text{D} - \text{Au}$	0.20	0.26	2.27E+09	1.21E+12
8	$\text{PdD}_1 + \text{Au} \rightleftharpoons \text{Pd} + \text{D} - \text{Au}$	0.23	0.28	1.14E+09	1.27E+12
9	$\text{Pd}_1 + \text{HD}_{(\text{g})} \rightleftharpoons \text{HD} - \text{Pd}_1$	0.35	N/A	5.57E+08	2.91E+13
10	$\text{HD} - \text{Pd}_1 \rightleftharpoons \text{PdHD}$	0.22	0.52	6.48E+05	6.12E+08
11	$\text{PdHD} + \text{Au} \rightleftharpoons \text{PdH}_1 + \text{D} - \text{Au}$	0.20	0.26	2.27E+09	1.21E+12
12	$\text{PdHD} + \text{Au} \rightleftharpoons \text{PdD}_1 + \text{H} - \text{Au}$	0.20	0.26	2.27E+09	1.21E+12
13	$\text{Pd}_1 + \text{RCH}_3\text{CHCH}_{2(\text{g})} \rightleftharpoons \text{RCH}_3\text{CHCH}_2 - \text{Pd}_1$	-0.12	N/A	1.06E+08	2.40E+06
14	$\text{RCH}_3\text{CHCH}_2 - \text{Pd}_1 + \text{H} - \text{Au}$ $\rightleftharpoons \text{RCH}_3\text{CHCH}_2 - \text{Pd}_1 - \text{H} + \text{Au}$	-0.03	0.06	1.24E+12	5.47E+11
15	$\text{RCH}_3\text{CHCH}_2 - \text{Pd}_1 - \text{H} \rightleftharpoons \text{RCH}_3\text{CH}_2\text{CH}_2 - \text{Pd}_1$	-0.37	0.31	5.69E+08	5.94E+03
16	$\text{RCH}_3\text{CH}_2\text{CH}_2 - \text{Pd}_1 + \text{H} - \text{Au}$ $\rightleftharpoons \text{RCH}_3\text{CH}_2\text{CH}_2 - \text{Pd}_1 - \text{H} + \text{Au}$	-0.12	0.06	1.24E+12	3.16E+10
17	$\text{RCH}_3\text{CH}_2\text{CH}_2 - \text{Pd}_1 - \text{H} \rightleftharpoons \text{RCH}_3\text{CH}_2\text{CH}_3 - \text{Pd}_1$	-1.26	0.22	9.65E+09	8.76E-08
18	$\text{RCH}_3\text{CH}_2\text{CH}_2 - \text{Pd}_1 + \text{D} - \text{Au}$ $\rightleftharpoons \text{RCH}_3\text{CH}_2\text{CH}_2 - \text{Pd}_1 - \text{D} + \text{Au}$	-0.12	0.06	1.24E+12	3.16E+10

19	$\text{RCH}_3\text{CH}_2\text{CH}_2 - \text{Pd}_1 - \text{D} \rightleftharpoons \text{RCH}_3\text{CH}_2\text{CH}_2\text{D} - \text{Pd}_1$	-1.26	0.22	9.65E+09	8.76E-08
20	$\text{Pd}_1 + \text{RCH}_3\text{CH}_2\text{CH}_3(\text{g}) \rightleftharpoons \text{RCH}_3\text{CH}_2\text{CH}_3 - \text{Pd}_1$	0.15	N/A	1.04E+08	1.21E+10
21	$\text{Pd}_1 + \text{RCH}_3\text{CH}_2\text{CH}_2\text{D}(\text{g}) \rightleftharpoons \text{RCH}_3\text{CH}_2\text{CH}_2\text{D} - \text{Pd}_1$	0.18	N/A	1.04E+08	2.54E+10
22	$\text{RCH}_3\text{CHCH}_2 - \text{Pd}_1 + \text{H} - \text{Au}$ $\rightleftharpoons \text{RCH}_3\text{CHCH}_2 - \text{H} - \text{Pd}_1 + \text{Au}$	0.02	0.06	1.24E+12	2.31E+12
23	$\text{RCH}_3\text{CHCH}_2 - \text{H} - \text{Pd}_1 \rightleftharpoons \text{RCH}_3\text{CHCH}_3 - \text{Pd}_1$	-0.38	0.35	1.57E+08	1.18E+03
24	$\text{RCH}_3\text{CHCH}_3 - \text{Pd}_1 + \text{H} - \text{Au}$ $\rightleftharpoons \text{RCH}_3\text{CHCH}_3 - \text{Pd}_1 - \text{H} + \text{Au}$	-0.15	0.06	1.24E+12	1.04E+10
25	$\text{RCH}_3\text{CHCH}_3 - \text{Pd}_1 - \text{H} \rightleftharpoons \text{RCH}_3\text{CH}_2\text{CH}_3 - \text{Pd}_1$	-1.26	0.16	5.22E+10	4.73E-07
26	$\text{RCH}_3\text{CHCH}_3 - \text{Pd}_1 + \text{D} - \text{Au}$ $\rightleftharpoons \text{RCH}_3\text{CHCH}_3 - \text{Pd}_1 - \text{D} + \text{Au}$	-0.15	0.06	1.24E+12	1.04E+10
27	$\text{RCH}_3\text{CHCH}_3 - \text{Pd}_1 - \text{D} \rightleftharpoons \text{RCH}_3\text{CHDCH}_3 - \text{Pd}_1$	-1.26	0.16	5.22E+10	4.73E-07
28	$\text{RCH}_3\text{CHCH}_3 - \text{Pd}_1 \rightleftharpoons \text{RCH}_2\text{CHCH}_3 - \text{Pd}_1 - \text{H}$	0.38	0.65	1.12E+04	1.69E+09
29	$\text{RCH}_2\text{CHCH}_3 - \text{Pd}_1 - \text{H} + \text{Au}$ $\rightleftharpoons \text{RCH}_2\text{CHCH}_3 - \text{Pd}_1 + \text{H} - \text{Au}$	0.07	0.13	1.44E+11	1.24E+12
30	$\text{Pd}_1 + \text{RCH}_3\text{CHDCH}_3(\text{g}) \rightleftharpoons \text{RCH}_3\text{CHDCH}_3 - \text{Pd}_1$	0.18	N/A	1.04E+08	2.55E+10
31	$\text{Pd}_1 + \text{RCH}_2\text{CHCH}_3(\text{g}) \rightleftharpoons \text{RCH}_2\text{CHCH}_3 - \text{Pd}_1$	0.17	N/A	1.06E+08	2.28E+10
32	$\text{RCH}_3\text{CHCH}_2 - \text{Pd}_1 + \text{D} - \text{Au}$ $\rightleftharpoons \text{RCH}_3\text{CHCH}_2 - \text{Pd}_1 - \text{D} + \text{Au}$	-0.03	0.06	1.24E+12	5.47E+11
33	$\text{RCH}_3\text{CHCH}_2 - \text{Pd}_1 - \text{D} \rightleftharpoons \text{RCH}_3\text{CHDCH}_2 - \text{Pd}_1$	-0.37	0.31	5.69E+08	5.94E+03
34	$\text{RCH}_3\text{CHDCH}_2 - \text{Pd}_1 + \text{H} - \text{Au}$ $\rightleftharpoons \text{RCH}_3\text{CHDCH}_2 - \text{Pd}_1 - \text{H} + \text{Au}$	-0.12	0.06	1.24E+12	3.16E+10
35	$\text{RCH}_3\text{CHDCH}_2 - \text{Pd}_1 - \text{H} \rightleftharpoons \text{RCH}_3\text{CHDCH}_3 - \text{Pd}_1$	-1.26	0.22	9.65E+09	8.76E-08
36	$\text{RCH}_3\text{CHDCH}_2 - \text{Pd}_1 + \text{D} - \text{Au}$ $\rightleftharpoons \text{RCH}_3\text{CHDCH}_2 - \text{Pd}_1 - \text{D} + \text{Au}$	-0.12	0.06	1.24E+12	3.16E+10
37	$\text{RCH}_3\text{CHDCH}_2 - \text{Pd}_1 - \text{D} \rightleftharpoons \text{RCH}_3\text{CHDCH}_2\text{D} - \text{Pd}_1$	-1.26	0.22	9.65E+09	8.76E-08
38	$\text{RCH}_3\text{CHDCH}_2 - \text{Pd}_1 \rightleftharpoons \text{RCH}_3\text{CDCH}_2 - \text{Pd}_1 - \text{H}$	0.37	0.68	5.94E+03	5.69E+08
39	$\text{RCH}_3\text{CDCH}_2 - \text{Pd}_1 - \text{H} + \text{Au}$ $\rightleftharpoons \text{RCH}_3\text{CDCH}_2 - \text{Pd}_1 + \text{H} - \text{Au}$	0.03	0.09	5.47E+11	1.24E+12
40	$\text{RCH}_3\text{CHDCH}_2\text{D}(\text{g}) + \text{Pd}_1 \rightleftharpoons \text{RCH}_3\text{CHDCH}_2\text{D} - \text{Pd}_1$	0.18	N/A	1.03E+08	2.68E+10
41	$\text{RCH}_3\text{CDCH}_2(\text{g}) + \text{Pd}_1 \rightleftharpoons \text{RCH}_3\text{CHDCH}_2 - \text{Pd}_1$	-0.12	N/A	1.05E+08	2.52E+06

42	$\text{RCH}_3\text{CHCH}_2 - \text{Pd}_1 + \text{D} - \text{Au}$ $\rightleftharpoons \text{RCH}_3\text{CHCH}_2 - \text{D} - \text{Pd}_1 + \text{Au}$	0.02	0.06	1.24E+12	2.31E+12
43	$\text{RCH}_3\text{CHCH}_2 - \text{D} - \text{Pd}_1 \rightleftharpoons \text{RCH}_3\text{CHCH}_2\text{D} - \text{Pd}_1$	-0.38	0.35	1.57E+08	1.18E+03
44	$\text{RCH}_3\text{CHCH}_2\text{D} - \text{Pd}_1 + \text{H} - \text{Au}$ $\rightleftharpoons \text{RCH}_3\text{CHCH}_2\text{D} - \text{Pd}_1 - \text{H} + \text{Au}$	-0.15	0.06	1.24E+12	1.04E+10
45	$\text{RCH}_3\text{CHCH}_2\text{D} - \text{Pd}_1 - \text{H} \rightleftharpoons \text{RCH}_3\text{CH}_2\text{CH}_2\text{D} - \text{Pd}_1$	-1.26	0.16	5.22E+10	4.73E-07
46	$\text{RCH}_3\text{CHCH}_2\text{D} - \text{Pd}_1 + \text{D} - \text{Au}$ $\rightleftharpoons \text{RCH}_3\text{CHCH}_2\text{D} - \text{Pd}_1 - \text{D} + \text{Au}$	-0.15	0.06	1.24E+12	1.04E+10
47	$\text{RCH}_3\text{CHCH}_2\text{D} - \text{Pd}_1 - \text{D} \rightleftharpoons \text{RCH}_3\text{CHDCH}_2\text{D} - \text{Pd}_1$	-1.26	0.16	5.22E+10	4.73E-07
48	$\text{RCH}_3\text{CHCH}_2\text{D} - \text{Pd}_1 \rightleftharpoons \text{RCH}_2\text{CHCH}_2\text{D} - \text{Pd}_1 - \text{H}$	0.38	0.65	1.12E+04	1.69E+09
49	$\text{RCH}_2\text{CHCH}_2\text{D} - \text{Pd}_1 - \text{H} + \text{Au}$ $\rightleftharpoons \text{RCH}_2\text{CHCH}_2\text{D} - \text{Pd}_1 + \text{H} - \text{Au}$	0.07	0.13	1.44E+11	1.24E+12
50	$\text{RCH}_3\text{CHCH}_2\text{D} - \text{Pd}_1 \rightleftharpoons (\text{E}) \text{RCH}_2\text{CHCHD} - \text{H} - \text{Pd}_1$	0.38	0.73	1.18E+03	1.57E+08
51	$(\text{E}) \text{RCH}_2\text{CHCHD} - \text{H} - \text{Pd}_1 + \text{Au}$ $\rightleftharpoons (\text{E}) \text{RCH}_2\text{CHCHD} - \text{Pd}_1 + \text{H} - \text{Au}$	-0.02	0.04	2.31E+12	1.24E+12
52	$\text{RCH}_3\text{CHCH}_2\text{D} - \text{Pd}_1 \rightleftharpoons (\text{Z}) \text{RCH}_2\text{CHCHD} - \text{H} - \text{Pd}_1$	0.38	0.73	1.18E+03	1.57E+08
53	$(\text{Z}) \text{RCH}_2\text{CHCHD} - \text{H} - \text{Pd}_1 + \text{Au}$ $\rightleftharpoons (\text{Z}) \text{RCH}_2\text{CHCHD} - \text{Pd}_1 + \text{H} - \text{Au}$	-0.02	0.04	2.31E+12	1.24E+12
54	$\text{RCH}_3\text{CDCH}_2(\text{g}) + \text{Pd}_1 \rightleftharpoons \text{RCH}_3\text{CDCH}_2 - \text{Pd}_1$	0.17	N/A	1.05E+08	2.40E+10
55	$(\text{E}) \text{RCH}_2\text{CHCHD}(\text{g}) + \text{Pd}_1$ $\rightleftharpoons (\text{E}) \text{RCH}_2\text{CHCHD} - \text{Pd}_1$	-0.12	N/A	1.05E+08	2.54E+06
56	$(\text{Z}) \text{RCH}_2\text{CHCHD}(\text{g}) + \text{Pd}_1 \rightleftharpoons (\text{Z}) \text{RCH}_2\text{CHCHD} - \text{Pd}_1$	-0.12	N/A	1.05E+08	2.55E+06

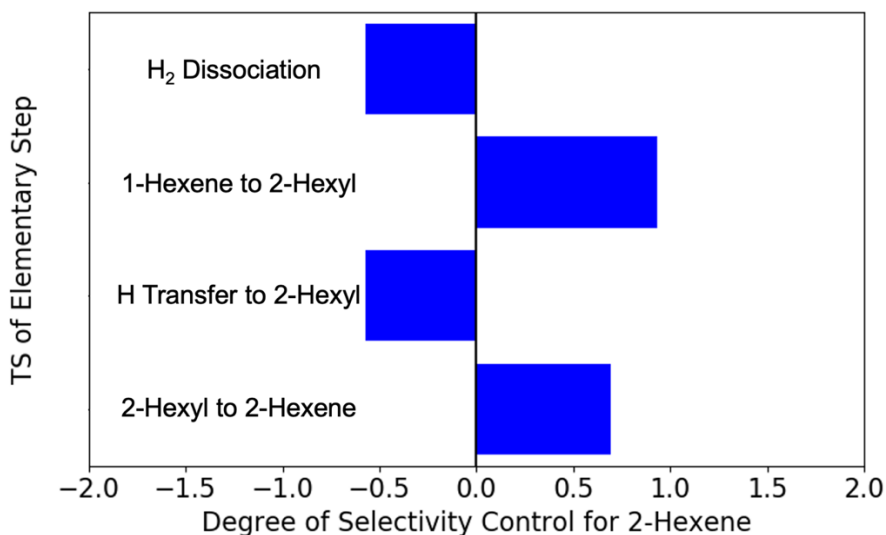


Figure E.2 Degree of selectivity control (DSC) for 2-hexene formation of selected TS evaluated at fixed partial pressures. DSC for 2-hexene formation evaluated at $T = 373$ K, $P(\text{H}_2) = 0.2$ bar, $P(1\text{-hexene}) = 0.01$ bar, and $P(2\text{-hexene}) = P(\text{n-hexane}) = 0.001$ bar. The TS of H₂ dissociation (DSC = -0.57) and H spillover to 2-Hexyl (DSC = -0.57) have the most negative impact on the selectivity of 2-hexene, while the TS of the hydrogenation of 1-hexene to 2-hexyl (DSC = 0.93) and the dehydrogenation of 2-hexyl to 2-hexene (DSC = 0.69) have the most positive impact on the selectivity of 2-hexene.

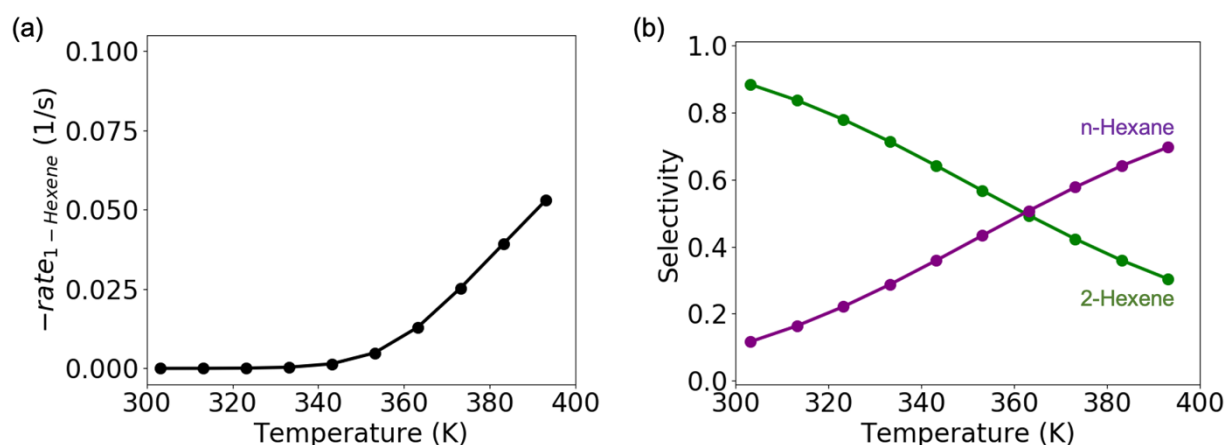


Figure E.3 1-hexene consumption rate and product selectivity evaluated at fixed partial pressures after increasing the barriers of H₂ dissociation and H spillover by 0.1 eV. Microkinetic model of 1-hexene reaction with H₂ evaluated at $P(\text{H}_2) = 0.2$ bar, $P(1\text{-hexene}) = 0.01$ bar, and $P(2\text{-hexene})$

= P(n-hexane) = 0.001 bar. (a) Rate of 1-hexene consumption, (b) selectivity of 2-hexene and n-hexane.

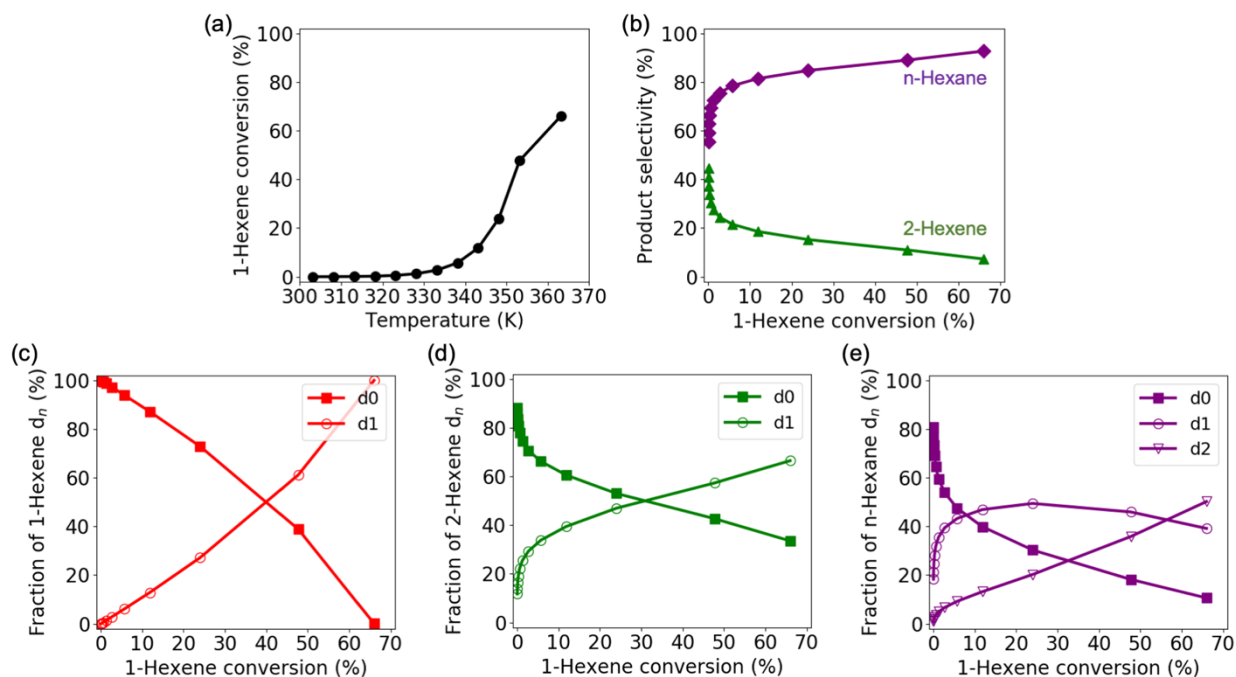


Figure E.4 Plug flow reactor (PFR) simulations of product and isotope selectivity of 1-Hexene deuteration and isomerization without shifts to the barrier of H_2 dissociation and spillover. (a) 1-Hexene conversion and (b) selectivity of 2-Hexene and n-Hexane as functions of reactor temperature. (c) 1-Hexene isotope distribution, (d) 2-Hexene isotope distribution, and (e) n-Hexane isotope distribution as functions of 1-Hexene conversion. The same catalyst loading and reaction conditions as (Figure 6.3) were used here.

Bibliography

1. Davis, M. E.; Davis, R. J., *Fundamentals of chemical reaction engineering*. Courier Corporation: 2012.
2. Calle-Vallejo, F.; Tymoczko, J.; Colic, V.; Vu, Q. H.; Pohl, M. D.; Morgenstern, K.; Loffreda, D.; Sautet, P.; Schuhmann, W.; Bandarenka, A. S., Finding optimal surface sites on heterogeneous catalysts by counting nearest neighbors. *Science* **2015**, *350* (6257), 185-189.
3. Van Santen, R. A., Complementary structure sensitive and insensitive catalytic relationships. *Acc. Chem. Res.* **2008**, *42*, 57-66.
4. Liu, L.; Corma, A., Metal catalysts for heterogeneous catalysis: from single atoms to nanoclusters and nanoparticles. *Chem. Rev.* **2018**, *118* (10), 4981-5079.
5. Bruix, A.; Rodriguez, J. A.; Ramírez, P. J.; Senanayake, S. D.; Evans, J.; Park, J. B.; Stacchiola, D.; Liu, P.; Hrbek, J.; Illas, F., A new type of strong metal–support interaction and the production of H₂ through the transformation of water on Pt/CeO₂(111) and Pt/CeO_x/TiO₂(110) catalysts. *J. Am. Chem. Soc.* **2012**, *134* (21), 8968-8974.
6. Lykhach, Y.; Kozlov, S. M.; Skála, T.; Tovt, A.; Stetsovych, V.; Tsud, N.; Dvořák, F.; Johánek, V.; Neitzel, A.; Myslivoček, J., Counting electrons on supported nanoparticles. *Nat. Mater.* **2016**, *15* (3), 284-288.
7. Kong, D.; Wang, G.; Pan, Y.; Hu, S.; Hou, J.; Pan, H.; Campbell, C. T.; Zhu, J., Growth, Structure, and Stability of Ag on CeO₂(111): Synchrotron Radiation Photoemission Studies. *J. Phys. Chem. C* **2011**, *115* (14), 6715-6725.
8. Li, G.; Hu, S.; Xu, Q.; Zhu, J., Interaction between Cu Nanoparticles and CeO₂ (111) Film Surfaces. *J. Phys. Chem. C* **2019**, *123* (38), 23563-23571.

9. James, T. E.; Hemmingson, S. L.; Ito, T.; Campbell, C. T., Energetics of Cu adsorption and adhesion onto reduced CeO₂ (111) surfaces by calorimetry. *J. Phys. Chem. C* **2015**, *119* (30), 17209-17217.
10. Hemmingson, S. L.; James, T. E.; Feeley, G. M.; Tilson, A. M.; Campbell, C. T., Adsorption and adhesion of Au on reduced CeO₂ (111) surfaces at 300 and 100 K. *J. Phys. Chem. C* **2016**, *120* (22), 12113-12124.
11. Lu, J.-L.; Gao, H.-J.; Shaikhutdinov, S.; Freund, H.-J., Gold supported on well-ordered ceria films: nucleation, growth and morphology in CO oxidation reaction. *Catal. Lett.* **2007**, *114* (1), 8-16.
12. Pan, Y.; Nilus, N.; Freund, H.-J.; Paier, J.; Penschke, C.; Sauer, J., Titration of Ce 3+ ions in the CeO₂ (111) surface by Au adatoms. *Phys. Rev. Lett.* **2013**, *111* (20), 206101.
13. Penschke, C.; Paier, J., Reduction and oxidation of Au adatoms on the CeO₂ (111) surface—DFT+ U versus hybrid functionals. *Phys. Chem. Chem. Phys.* **2017**, *19* (19), 12546-12558.
14. Mao, Z.; Lustemberg, P. G.; Rumpitz, J. R.; Ganduglia-Pirovano, M. V.; Campbell, C. T., Ni nanoparticles on CeO₂ (111): energetics, electron transfer, and structure by Ni adsorption calorimetry, spectroscopies, and density functional theory. *ACS Catal.* **2020**, *10* (9), 5101-5114.
15. Mullins, D. R., The surface chemistry of cerium oxide. *Surf. Sci. Rep.* **2015**, *70* (1), 42-85.
16. Paier, J.; Penschke, C.; Sauer, J., Oxygen defects and surface chemistry of ceria: quantum chemical studies compared to experiment. *Chem. Rev.* **2013**, *113* (6), 3949-3985.

17. Tang, Y.; Asokan, C.; Xu, M.; Graham, G. W.; Pan, X.; Christopher, P.; Li, J.; Sautet, P., Rh single atoms on TiO₂ dynamically respond to reaction conditions by adapting their site. *Nat. Commun.* **2019**, *10* (1), 1-10.
18. DeRita, L.; Resasco, J.; Dai, S.; Boubnov, A.; Thang, H. V.; Hoffman, A. S.; Ro, I.; Graham, G. W.; Bare, S. R.; Pacchioni, G.; Pan, X.; Christopher, P., Structural evolution of atomically dispersed Pt catalysts dictates reactivity. *Nat. Mater.* **2019**, *18* (7), 746-751.
19. Parkinson, G. S.; Novotny, Z.; Argentero, G.; Schmid, M.; Pavelec, J.; Kosak, R.; Blaha, P.; Diebold, U., Carbon monoxide-induced adatom sintering in a Pd-Fe₃O₄ model catalyst. *Nat. Mater.* **2013**, *12* (8), 724-728.
20. Fu, Q.; Saltsburg, H.; Flytzani-Stephanopoulos, M., Active nonmetallic Au and Pt species on ceria-based water-gas shift catalysts. *Science* **2003**, *301* (5635), 935-938.
21. Qiao, B.; Wang, A.; Yang, X.; Allard, L. F.; Jiang, Z.; Cui, Y.; Liu, J.; Li, J.; Zhang, T., Single-atom catalysis of CO oxidation using Pt₁/FeO_x. *Nat. Chem.* **2011**, *3* (8), 634-641.
22. Kyriakou, G.; Boucher, M. B.; Jewell, A. D.; Lewis, E. A.; Lawton, T. J.; Baber, A. E.; Tierney, H. L.; Flytzani-Stephanopoulos, M.; Sykes, E. C. H., Isolated Metal Atom Geometries as a Strategy for Selective Heterogeneous Hydrogenations. *Science* **2012**, *335* (6073), 1209-1212.
23. Wang, A.; Li, J.; Zhang, T., Heterogeneous single-atom catalysis. *Nat. Rev. Chem.* **2018**, *2* (6), 65-81.
24. Hannagan, R. T.; Giannakakis, G.; Flytzani-Stephanopoulos, M.; Sykes, E. C. H., Single-atom alloy catalysis. *Chem. Rev.* **2020**, *120* (21), 12044-12088.
25. Kaiser, S. K.; Chen, Z.; Faust Akl, D.; Mitchell, S.; Pérez-Ramírez, J., Single-atom catalysts across the periodic table. *Chem. Rev.* **2020**, *120* (21), 11703-11809.

26. Dvořák, F.; Farnesi Camellone, M.; Tovt, A.; Tran, N.-D.; Negreiros, F. R.; Vorokhta, M.; Skála, T.; Matolínová, I.; Mysliviček, J.; Matolín, V., Creating single-atom Pt-ceria catalysts by surface step decoration. *Nat. Commun.* **2016**, *7* (1), 1-8.
27. Deaven, D.; Tit, N.; Morris, J.; Ho, K., Structural optimization of Lennard-Jones clusters by a genetic algorithm. *Chem. Phys. Lett.* **1996**, *256* (1-2), 195-200.
28. Wales, D. J.; Doye, J. P., Global optimization by basin-hopping and the lowest energy structures of Lennard-Jones clusters containing up to 110 atoms. *J. Phys. Chem. A* **1997**, *101* (28), 5111-5116.
29. Zhang, Z.; Zandkarimi, B.; Alexandrova, A. N., Ensembles of metastable states govern heterogeneous catalysis on dynamic interfaces. *Acc. Chem. Res.* **2020**, *53* (2), 447-458.
30. Sun, G.; Sautet, P., Active Site Fluxional Restructuring as a New Paradigm in Triggering Reaction Activity for Nanocluster Catalysis. *Acc. Chem. Res.* **2021**, *54* (20), 3841-3849.
31. Venables, J. A., Atomic processes in crystal growth. *Surf. Sci.* **1994**, *299*, 798-817.
32. Su, Y.-Q.; Zhang, L.; Wang, Y.; Liu, J.-X.; Muravev, V.; Alexopoulos, K.; Filot, I. A.; Vlachos, D. G.; Hensen, E. J., Stability of heterogeneous single-atom catalysts: a scaling law mapping thermodynamics to kinetics. *npj Comput. Mater.* **2020**, *6* (1), 1-7.
33. Xu, L.; Henkelman, G.; Campbell, C. T.; Jonsson, H., Pd diffusion on MgO (1 0 0): The role of defects and small cluster mobility. *Surf. Sci.* **2006**, *600* (6), 1351-1362.
34. Wang, Y.; Kalscheur, J.; Su, Y.-Q.; Hensen, E. J.; Vlachos, D. G., Real-time dynamics and structures of supported subnanometer catalysts via multiscale simulations. *Nat. Commun.* **2021**, *12* (1), 1-9.
35. Farmer, J. A.; Campbell, C. T., Ceria maintains smaller metal catalyst particles by strong metal-support bonding. *Science* **2010**, *329* (5994), 933-936.

36. Hemmingson, S. L.; Campbell, C. T., Trends in adhesion energies of metal nanoparticles on oxide surfaces: understanding support effects in catalysis and nanotechnology. *ACS nano* **2017**, *11* (2), 1196-1203.
37. Parker, S. C.; Campbell, C. T., Kinetic model for sintering of supported metal particles with improved size-dependent energetics and applications to Au on TiO₂ (110). *Phys. Rev. B* **2007**, *75* (3), 035430.
38. Xu, L.; Campbell, C. T.; Jonsson, H.; Henkelman, G., Kinetic Monte Carlo simulations of Pd deposition and island growth on MgO (1 0 0). *Surf. Sci.* **2007**, *601* (14), 3133-3142.
39. O'Connor, N. J.; Jonayat, A.; Janik, M. J.; Senftle, T. P., Interaction trends between single metal atoms and oxide supports identified with density functional theory and statistical learning. *Nat. Catal.* **2018**, *1* (7), 531-539.
40. Figueroba, A.; Kovács, G.; Bruix, A.; Neyman, K. M., Towards stable single-atom catalysts: strong binding of atomically dispersed transition metals on the surface of nanostructured ceria. *Catal. Sci. & Technol.* **2016**, *6* (18), 6806-6813.
41. Daelman, N.; Capdevila-Cortada, M.; López, N., Dynamic charge and oxidation state of Pt/CeO₂ single-atom catalysts. *Nat. Mater.* **2019**, *18* (11), 1215-1221.
42. Yang, A. C.; Garland, C. W., Infrared studies of carbon monoxide chemisorbed on rhodium. *J. Phys. Chem.* **1957**, *61*, 1504-1512.
43. Fang, C.-Y.; Zhang, S.; Hu, Y.; Vasiliu, M.; Perez-Aguilar, J. E.; Conley, E. T.; Dixon, D. A.; Chen, C.-Y.; Gates, B. C., Reversible metal aggregation and redispersion driven by the catalytic water gas shift half-reactions: interconversion of single-site rhodium complexes and tetra-rhodium clusters in zeolite HY. *ACS Catal.* **2019**, *9* (4), 3311-3321.

44. Ouyang, R.; Liu, J.-X.; Li, W.-X., Atomistic theory of ostwald ripening and disintegration of supported metal particles under reaction conditions. *J. Am. Chem. Soc.* **2013**, *135* (5), 1760-1771.
45. Liu, J. C.; Wang, Y. G.; Li, J., Toward rational design of oxide-supported single-atom catalysts: atomic dispersion of gold on ceria. *J. Am. Chem. Soc.* **2017**, *139* (17), 6190-6199.
46. Su, Y.-Q.; Wang, Y.; Liu, J.-X.; Filot, I. A.; Alexopoulos, K.; Zhang, L.; Muravev, V.; Zijlstra, B.; Vlachos, D. G.; Hensen, E. J., Theoretical approach to predict the stability of supported single-atom catalysts. *ACS Catal.* **2019**, *9* (4), 3289-3297.
47. Wang, Y.-G.; Mei, D.; Glezakou, V.-A.; Li, J.; Rousseau, R., Dynamic formation of single-atom catalytic active sites on ceria-supported gold nanoparticles. *Nat. Commun.* **2015**, *6* (1), 1-8.
48. Campbell, C. T.; Mao, Z., Chemical potential of metal atoms in supported nanoparticles: dependence upon particle size and support. *ACS Catal.* **2017**, *7* (12), 8460-8466.
49. Krcha, M. D.; Mayernick, A. D.; Janik, M. J., Periodic trends of oxygen vacancy formation and C–H bond activation over transition metal-doped CeO₂ (1 1 1) surfaces. *J. Catal.* **2012**, *293*, 103-115.
50. Vayssilov, G. N.; Lykhach, Y.; Migani, A.; Staudt, T.; Petrova, G. P.; Tsud, N.; Skála, T.; Bruix, A.; Illas, F.; Prince, K. C., Support nanostructure boosts oxygen transfer to catalytically active platinum nanoparticles. *Nat. Mater.* **2011**, *10* (4), 310-315.
51. Su, Y.-Q.; Xia, G.-J.; Qin, Y.; Ding, S.; Wang, Y.-G., Lattice oxygen self-spillover on reducible oxide supported metal cluster: the water–gas shift reaction on Cu/CeO₂ catalyst. *Chem. Sci.* **2021**, *12* (23), 8260-8267.

52. Vayssilov, G. N.; Gates, B. C.; Rösch, N., Oxidation of supported rhodium clusters by support hydroxy groups. *Angew. Chem. Int. Ed.* **2003**, *42* (12), 1391-1394.
53. Hu, C. H.; Chizallet, C.; Mager-Maury, C.; Corral-Valero, M.; Sautet, P.; Toulhoat, H.; Raybaud, P., Modulation of catalyst particle structure upon support hydroxylation: Ab initio insights into Pd₁₃ and Pt₁₃/γ-Al₂O₃. *J. Catal.* **2010**, *274* (1), 99-110.
54. Mayernick, A. D.; Janik, M. J., Ab initio thermodynamic evaluation of Pd atom interaction with CeO₂ surfaces. *J. Chem. Phys.* **2009**, *131* (8), 084701.
55. Senftle, T. P.; van Duin, A. C. T.; Janik, M. J., Role of site stability in methane activation on Pd_xCe_{1-x}O₈ surfaces. *ACS Catal.* **2015**, *5* (10), 6187-6199.
56. Su, Y.-Q.; Filot, I. A.; Liu, J.-X.; Hensen, E. J. M., Stable Pd-Doped Ceria Structures for CH₄ Activation and CO Oxidation. *ACS Catal.* **2018**, *8* (1), 75-80.
57. Su, Y.-Q.; Liu, J.-X.; Filot, I. A.; Zhang, L.; Hensen, E. J., Highly active and stable CH₄ oxidation by substitution of Ce⁴⁺ by two Pd²⁺ ions in CeO₂ (111). *ACS Catal.* **2018**, *8* (7), 6552-6559.
58. Sun, G.; Sautet, P., Metastable structures in cluster catalysis from first-principles: Structural ensemble in reaction conditions and metastability triggered reactivity. *J. Am. Chem. Soc.* **2018**, *140* (8), 2812-2820.
59. Kozuch, S.; Shaik, S., How to conceptualize catalytic cycles? The energetic span model. *Acc. Chem. Res.* **2011**, *44* (2), 101-110.
60. Kozuch, S.; Shaik, S., A combined kinetic-quantum mechanical model for assessment of catalytic cycles: Application to cross-coupling and Heck reactions. *J. Am. Chem. Soc.* **2006**, *128* (10), 3355-3365.

61. Christiansen, J. A., The elucidation of reaction mechanisms by the method of intermediates in quasi-stationary concentrations. *Adv. Catal.* **1953**, *5*, 311-353.
62. Cohen, M.; Vlachos, D. G., Modified Energy Span Analysis Reveals Heterogeneous Catalytic Kinetics. *Ind. Eng. Chem. Res.* **2022**, *61* (15), 5117-5128.
63. Medford, A. J.; Shi, C.; Hoffmann, M. J.; Lausche, A. C.; Fitzgibbon, S. R.; Bligaard, T.; Nørskov, J. K., CatMAP: a software package for descriptor-based microkinetic mapping of catalytic trends. *Catal. Lett.* **2015**, *145* (3), 794-807.
64. Wang, T.; Ibañez, J.; Wang, K.; Fang, L.; Sabbe, M.; Michel, C.; Paul, S.; Pera-Titus, M.; Sautet, P., Rational design of selective metal catalysts for alcohol amination with ammonia. *Nat. Catal.* **2019**, *2* (9), 773-779.
65. Motagamwala, A. H.; Dumesic, J. A., Microkinetic modeling: a tool for rational catalyst design. *Chem. Rev.* **2020**, *121* (2), 1049-1076.
66. Alexopoulos, K.; Wang, Y.; Vlachos, D. G., First-principles kinetic and spectroscopic insights into single-atom catalysis. *ACS Catal.* **2019**, *9* (6), 5002-5010.
67. Tao, F.; Grass, M. E.; Zhang, Y.; Butcher, D. R.; Renzas, J. R.; Liu, Z.; Chung, J. Y.; Mun, B. S.; Salmeron, M.; Somorjai, G. A., Reaction-driven restructuring of Rh-Pd and Pt-Pd core-shell nanoparticles. *Science* **2008**, *322* (5903), 932-934.
68. Tao, F.; Dag, S.; Wang, L.-W.; Liu, Z.; Butcher, D. R.; Bluhm, H.; Salmeron, M.; Somorjai, G. A., Break-up of stepped platinum catalyst surfaces by high CO coverage. *Science* **2010**, *327*, 850-853.
69. Tao, F. F.; Salmeron, M., In situ studies of chemistry and structure of materials in reactive environments. *Science* **2011**, *331* (6014), 171-175.

70. Zhang, S.; Shan, J.; Zhu, Y.; Nguyen, L.; Huang, W.; Yoshida, H.; Takeda, S.; Tao, F., Restructuring transition metal oxide nanorods for 100% selectivity in reduction of nitric oxide with carbon monoxide. *Nano Lett.* **2013**, *13* (7), 3310-3314.
71. Resasco, J.; DeRita, L.; Dai, S.; Chada, J. P.; Xu, M.; Yan, X.; Finzel, J.; Hanukovich, S.; Hoffman, A. S.; Graham, G. W.; Bare, S. R.; Pan, X.; Christopher, P., Uniformity is key in defining structure-function relationships for atomically dispersed metal catalysts: the case of Pt/CeO₂. *J. Am. Chem. Soc.* **2020**, *142* (1), 169-184.
72. Liu, L.; Meira, D. M.; Arenal, R.; Concepcion, P.; Puga, A. V.; Corma, A., Determination of the evolution of heterogeneous single metal atoms and nanoclusters under reaction conditions: which are the working catalytic sites? *ACS Catal.* **2019**, *9* (12), 10626-10639.
73. Kresse, G.; Furthmüller, J., Efficient iterative schemes for ab initio total-energy calculations using a plane-wave basis set. *Phys. Rev. B* **1996**, *54* (16), 11169-11186.
74. Kresse, G.; Furthmüller, J., Efficiency of ab-initio total energy calculations for metals and semiconductors using a plane-wave basis set. *Comput. Mater. Sci.* **1996**, *6* (1), 15-50.
75. Kresse, G.; Hafner, J., Ab initio molecular dynamics for liquid metals. *Phys. Rev. B* **1993**, *47* (1), 558-561.
76. Perdew, J. P.; Burke, K.; Ernzerhof, M., Generalized gradient approximation made simple. *Phys. Rev. Lett.* **1996**, *77* (18), 3865-3868.
77. Blöchl, P. E., Projector augmented-wave method. *Phys. Rev. B* **1994**, *50* (24), 17953-17979.
78. Kresse, G.; Joubert, D., From ultrasoft pseudopotentials to the projector augmented-wave method. *Phys. Rev. B* **1999**, *59* (3), 1758-1775.

79. Dudarev, S. L.; Botton, G. A.; Savrasov, S. Y.; Humphreys, C. J.; Sutton, A. P., Electron-energy-loss spectra and the structural stability of nickel oxide: an LSDA+U study. *Phys. Rev. B* **1999**, *57* (3), 1505-1509.
80. Cococcioni, M.; de Gironcoli, S., Linear response approach to the calculation of the effective interaction parameters in the LDA+U method. *Phys. Rev. B* **2005**, *71* (3), 035105.
81. Murgida, G. E.; Ferrari, V.; Llois, A. M.; Ganduglia-Pirovano, M. V., Reduced CeO₂(111) ordered phases as bulk terminations: Introducing the structure of Ce₃O₅. *Phys. Rev. Mater.* **2018**, *2* (8), 083609.
82. Olbrich, R.; Murgida, G. E.; Ferrari, V.; Barth, C.; Llois, A. M.; Reichling, M.; Ganduglia-Pirovano, M. V., Surface stabilizes ceria in unexpected stoichiometry. *J. Phys. Chem. C* **2017**, *121* (12), 6844-6851.
83. Murgida, G. E.; Ganduglia-Pirovano, M. V., Evidence for subsurface ordering of oxygen vacancies on the reduced CeO₂(111) surface using density-functional and statistical calculations. *Phys. Rev. Lett.* **2013**, *110* (24), 246101.
84. Monkhorst, H. J.; Pack, J. D., Special points for Brillouin-zone integrations. *Phys. Rev. B* **1976**, *13* (12), 5188-5192.
85. Heyd, J.; Scuseria, G. E.; Ernzerhof, M., Hybrid functionals based on a screened Coulomb potential. *J. Chem. Phys.* **2003**, *118* (18), 8207-8215.
86. Heyd, J.; Scuseria, G. E.; Ernzerhof, M., Erratum: "Hybrid functionals based on a screened Coulomb potential" [J. Chem. Phys. 118, 8207 (2003)]. *J. Chem. Phys.* **2006**, *124*, 219906.
87. Paier, J.; Marsman, M.; Hummer, K.; Kresse, G.; Gerber, I. C.; Ángyán, J. G., Screened hybrid density functionals applied to solids. *J. Chem. Phys.* **2006**, *124* (15), 154709.

88. Köhler, L.; Kresse, G., Density functional study of CO on Rh(111). *Phys. Rev. B* **2004**, *70* (16), 165405.
89. Momma, K.; Izumi, F., VESTA: a three-dimensional visualization system for electronic and structural analysis. *J. Appl. Crystallogr.* **2008**, *41* (3), 653-658.
90. Reuter, K.; Scheffler, M., Composition, structure, and stability of RuO₂(110) as a function of oxygen pressure. *Phys. Rev. B* **2001**, *65* (3), 035406.
91. Reuter, K.; Scheffler, M., Composition and structure of the RuO₂(110) surface in an O₂ and CO environment: implications for the catalytic formation of CO₂. *Phys. Rev. B* **2003**, *68* (4), 045407.
92. Werner, K.; Weng, X.; Calaza, F.; Sterrer, M.; Kropp, T.; Paier, J.; Sauer, J.; Wilde, M.; Fukutani, K.; Shaikhutdinov, S.; Freund, H. J., Toward an understanding of selective alkyne hydrogenation on ceria: on the impact of O vacancies on H₂ interaction with CeO₂(111). *J. Am. Chem. Soc.* **2017**, *139* (48), 17608-17616.
93. Wu, Z.; Cheng, Y.; Tao, F.; Daemen, L.; Foo, G. S.; Nguyen, L.; Zhang, X.; Beste, A.; Ramirez-Cuesta, A. J., Direct neutron spectroscopy observation of cerium hydride species on a cerium oxide catalyst. *J. Am. Chem. Soc.* **2017**, *139* (28), 9721-9727.
94. Mullins, D. R.; Albrecht, P. M.; Chen, T.-L.; Calaza, F. C.; Biegalski, M. D.; Christen, H. M.; Overbury, S. H., Water dissociation on CeO₂(100) and CeO₂(111) thin films. *J. Phys. Chem. C* **2012**, *116* (36), 19419-19428.
95. Jerratsch, J.-F.; Shao, X.; Nilius, N.; Freund, H.-J.; Popa, C.; Ganduglia-Pirovano, M. V.; Burow, A. M.; Sauer, J., Electron localization in defective ceria films: a study with scanning-tunneling microscopy and density-functional theory. *Phys. Rev. Lett.* **2011**, *106* (24), 246801.

96. Fernandez-Torre, D.; Carrasco, J.; Ganduglia-Pirovano, M. V.; Perez, R., Hydrogen activation, diffusion, and clustering on CeO₂(111): a DFT+U study. *J. Chem. Phys.* **2014**, *141* (1), 014703.
97. Murgida, G. E.; Ferrari, V.; Ganduglia-Pirovano, M. V.; Llois, A. M., Ordering of oxygen vacancies and excess charge localization in bulk ceria: a DFT+U study. *Phys. Rev. B* **2014**, *90* (11), 115120.
98. Wu, X. P.; Gong, X. Q.; Lu, G. Z., Role of oxygen vacancies in the surface evolution of H at CeO₂(111): a charge modification effect. *Phys. Chem. Chem. Phys.* **2015**, *17* (5), 3544-3549.
99. Wu, X. P.; Gong, X. Q., Clustering of oxygen vacancies at CeO₂(111): critical role of hydroxyls. *Phys. Rev. Lett.* **2016**, *116* (8), 086102.
100. Wolf, M. J.; Kullgren, J.; Hermansson, K., Comment on "clustering of oxygen vacancies at CeO₂(111): critical role of hydroxyls". *Phys. Rev. Lett.* **2016**, *117* (27), 279601.
101. Wu, X. P.; Gong, X. Q., Wu and Gong reply. *Phys. Rev. Lett.* **2016**, *117* (27), 279602.
102. Piotrowski, M. J.; Piquini, P.; Da Silva, J. L., Density functional theory investigation of 3d, 4d, and 5d 13-atom metal clusters. *Phys. Rev. B* **2010**, *81* (15), 155446.
103. Feibelman, P. J.; Hammer, B.; Nørskov, J. K.; Wagner, F.; Scheffler, M.; Stumpf, R.; Watwe, R.; Dumesic, J., The CO/Pt (111) Puzzle. *J. Phys. Chem. B* **2001**, *105* (18), 4018-4025.
104. Kresse, G.; Gil, A.; Sautet, P., Significance of single-electron energies for the description of CO on Pt(111). *Phys. Rev. B* **2003**, *68* (7), 073401.
105. Mason, S. E.; Grinberg, I.; Rappe, A. M., First-principles extrapolation method for accurate CO adsorption energies on metal surfaces. *Phys. Rev. B* **2004**, *69* (16), 161401.

106. Schimka, L.; Harl, J.; Stroppa, A.; Grüneis, A.; Marsman, M.; Mittendorfer, F.; Kresse, G., Accurate surface and adsorption energies from many-body perturbation theory. *Nat. Mater.* **2010**, *9* (9), 741-744.
107. Sumaria, V.; Nguyen, L. T.; Tao, F. F.; Sautet, P., Optimal packing of CO at high coverage on Pt(100) and Pt(111) surfaces. *ACS Catal.* **2020**, *10* (16), 9533-9544.
108. Yan, G.; Tang, Y.; Li, Y.; Li, Y.; Nguyen, L.; Sakata, T.; Higashi, K.; Tao, F. F.; Sautet, P., Reaction product-driven restructuring and assisted stabilization of a highly dispersed Rh-on-ceria catalyst. *Nat. Catal.* **2022**, *5* (2), 119-127.
109. Marcella, N.; Lim, J. S.; Płonka, A. M.; Yan, G.; Owen, C. J.; van der Hoeven, J. E.; Foucher, A. C.; Ngan, H. T.; Torrisi, S. B.; Marinkovic, N. S., Decoding reactive structures in dilute alloy catalysts. *Nat. Commun.* **2022**, *13* (1), 1-9.
110. Leung, L. W. H.; He, J. W.; Goodman, D. W., Adsorption of CO on Rh (100) studied by infrared reflection-absorption spectroscopy. *J. Chem. Phys.* **1990**, *93* (11), 8328-8336.
111. Eren, B.; Zherebetsky, D.; Patera, L. L.; Wu, C. H.; Bluhm, H.; Africh, C.; Wang, L.-W.; Somorjai, G. A.; Salmeron, M., Activation of Cu (111) surface by decomposition into nanoclusters driven by CO adsorption. *Science* **2016**, *351* (6272), 475-478.
112. Sun, H.; Ang, H. M.; Tade, M. O.; Wang, S., Co₃O₄ Nanocrystals with Predominantly Exposed Facets: Synthesis, Environmental and Energy Applications. *J. Mat. Chem. A* **2013**, *1* (46), 14427-14442.
113. Zhang, S.; Shan, J.-j.; Zhu, Y.; Frenkel, A. I.; Patlolla, A.; Huang, W.; Yoon, S. J.; Wang, L.; Yoshida, H.; Takeda, S., WGS Catalysis and In Situ Studies of CoO_{1-x}, PtCo_n/Co₃O₄, and Pt_mCo_{m'}/CoO_{1-x} Nanorod Catalysts. *J. Am. Chem. Soc.* **2013**, *135* (22), 8283-8293.

114. Meng, B.; Zhao, Z.; Wang, X.; Liang, J.; Qiu, J., Selective catalytic reduction of nitrogen oxides by ammonia over Co₃O₄ nanocrystals with different shapes. *Appl. Catal. B: Environ.* **2013**, *129*, 491-500.
115. Nguyen, L.; Zhang, S.; Wang, L.; Li, Y.; Yoshida, H.; Patlolla, A.; Takeda, S.; Frenkel, A. I.; Tao, F., Reduction of Nitric Oxide with Hydrogen on Catalysts of Singly Dispersed Bimetallic Sites Pt₁Co_m and Pd₁Co_n. *ACS Catal.* **2016**, *6* (2), 840-850.
116. Tyo, E. C.; Yin, C.; Di Vece, M.; Qian, Q.; Kwon, G.; Lee, S.; Lee, B.; DeBartolo, J. E.; Seifert, S.; Winans, R. E., Oxidative dehydrogenation of cyclohexane on cobalt oxide (Co₃O₄) nanoparticles: the effect of particle size on activity and selectivity. *ACS Catal.* **2012**, *2* (11), 2409-2423.
117. Fung, V.; Tao, F. F.; Jiang, D.-e., Understanding oxidative dehydrogenation of ethane on Co₃O₄ nanorods from density functional theory. *Catal. Sci. & Technol.* **2016**, *6* (18), 6861-6869.
118. Liu, J.; Fung, V.; Wang, Y.; Du, K.; Zhang, S.; Nguyen, L.; Tang, Y.; Fan, J.; Jiang, D.-e.; Tao, F. F., Promotion of catalytic selectivity on transition metal oxide through restructuring surface lattice. *Appl. Catal. B: Environ.* **2018**, *237*, 957-969.
119. Roth, W., The magnetic structure of Co₃O₄. *J. Phys. Chem. Solids* **1964**, *25* (1), 1-10.
120. Chen, J.; Wu, X.; Selloni, A., Electronic structure and bonding properties of cobalt oxide in the spinel structure. *Phys. Rev. B* **2011**, *83* (24), 245204.
121. Zasada, F.; Piskorz, W.; Stelmachowski, P.; Kotarba, A.; Paul, J.-F.; Płociński, T.; Kurzydłowski, K. J.; Sojka, Z., Periodic DFT and HR-STEM studies of surface structure and morphology of cobalt spinel nanocrystals. Retrieving 3D shapes from 2D images. *J. Phys. Chem. C* **2011**, *115* (14), 6423-6432.

122. Meyer, W.; Biedermann, K.; Gubo, M.; Hammer, L.; Heinz, K., Surface structure of polar Co₃O₄ (111) films grown epitaxially on Ir (100)-(1×1). *J. Phys.: Condens. Mat.* **2008**, *20* (26), 265011.
123. Goniakowski, J.; Finocchi, F.; Noguera, C., Polarity of oxide surfaces and nanostructures. *Rep. Prog. Phys.* **2007**, *71* (1), 016501.
124. Xu, X.-L.; Chen, Z.-H.; Li, Y.; Chen, W.-K.; Li, J.-Q., Bulk and surface properties of spinel Co₃O₄ by density functional calculations. *Surf. Sci.* **2009**, *603* (4), 653-658.
125. Montoya, A.; Haynes, B. S., Periodic density functional study of Co₃O₄ surfaces. *Chem. Phys. Lett.* **2011**, *502* (1-3), 63-68.
126. Xie, Y.; Guo, H., Thermodynamic stability of cobalt oxide's low-index surfaces from density functional theory calculations. *Surf. Coat. Technol.* **2017**, *320*, 18-22.
127. Busca, G.; Guidetti, R.; Lorenzelli, V., Fourier-transform infrared study of the surface properties of cobalt oxides. *J. Chem. Soc., Faraday Trans.* **1990**, *86* (6), 989-994.
128. Chuang, T.; Brundle, C.; Rice, D., Interpretation of the x-ray photoemission spectra of cobalt oxides and cobalt oxide surfaces. *Surf. Sci.* **1976**, *59* (2), 413-429.
129. Nguyen, L.; Zhang, S.; Yoon, S. J.; Tao, F., Preferential Oxidation of CO in H₂ on Pure Co₃O_{4-x} and Pt/Co₃O_{4-x}. *ChemCatChem* **2015**, *7* (15), 2346-2353.
130. Faisal, F.; Bertram, M.; Stumm, C.; Cherevko, S.; Geiger, S.; Kasian, O.; Lykhach, Y.; Lytken, O.; Mayrhofer, K. J.; Brummel, O., Atomically defined Co₃O₄(111) thin films prepared in ultrahigh vacuum: stability under electrochemical conditions. *J. Phys. Chem. C* **2018**, *122* (13), 7236-7248.
131. Lukashuk, L.; Yigit, N.; Rameshan, R.; Kolar, E.; Teschner, D.; Hävecker, M.; Knop-Gericke, A.; Schlögl, R.; Föttinger, K.; Rupprechter, G. n., Operando insights into CO

- oxidation on cobalt oxide catalysts by NAP-XPS, FTIR, and XRD. *ACS Catal.* **2018**, *8* (9), 8630-8641.
132. Petitto, S. C.; Marsh, E. M.; Carson, G. A.; Langell, M. A., Cobalt oxide surface chemistry: The interaction of CoO (1 0 0), Co₃O₄ (1 1 0) and Co₃O₄ (1 1 1) with oxygen and water. *J. Mol. Catal. A: Chem.* **2008**, *281* (1-2), 49-58.
133. Schwarz, M.; Faisal, F.; Mohr, S.; Hohner, C.; Werner, K.; Xu, T.; Skála, T. s.; Tsud, N.; Prince, K. C.; Matolín, V., Structure-dependent dissociation of water on cobalt oxide. *J. Phys. Chem. Lett.* **2018**, *9* (11), 2763-2769.
134. Schwarz, M.; Mohr, S.; Hohner, C.; Werner, K.; Xu, T.; Libuda, J., Water on atomically-defined cobalt oxide surfaces studied by temperature-programmed IR reflection absorption spectroscopy and steady state isotopic exchange. *J. Phys. Chem. C* **2018**, *123* (13), 7673-7681.
135. Chen, J.; Selloni, A., Electronic states and magnetic structure at the Co₃O₄(110) surface: A first-principles study. *Phys. Rev. B* **2012**, *85* (8), 085306.
136. Plaisance, C. P.; van Santen, R. A., Structure sensitivity of the oxygen evolution reaction catalyzed by cobalt (II, III) oxide. *J. Am. Chem. Soc.* **2015**, *137* (46), 14660-14672.
137. Selcuk, S.; Selloni, A., DFT+ U study of the surface structure and stability of Co₃O₄ (110): dependence on U. *J. Phys. Chem. C* **2015**, *119* (18), 9973-9979.
138. Fung, V.; Tao, F.; Jiang, D. e., Trends of alkane activation on doped cobalt (II, III) oxide from first principles. *ChemCatChem* **2018**, *10* (1), 244-249.
139. Lu, J.; Song, J.; Niu, H.; Pan, L.; Zhang, X.; Wang, L.; Zou, J.-J., Periodic density functional theory study of ethylene hydrogenation over Co₃O₄ (1 1 1) surface: The critical role of oxygen vacancies. *Appl. Surf. Sci.* **2016**, *371*, 61-66.

140. Zasada, F.; Piskorz, W.; Cristol, S.; Paul, J.-F.; Kotarba, A.; Sojka, Z., Periodic density functional theory and atomistic thermodynamic studies of cobalt spinel nanocrystals in wet environment: Molecular interpretation of water adsorption equilibria. *J. Phys. Chem. C* **2010**, *114* (50), 22245-22253.
141. Jiang, D.-e.; Dai, S., The role of low-coordinate oxygen on Co₃O₄ (110) in catalytic CO oxidation. *Phys. Chem. Chem. Phys.* **2011**, *13* (3), 978-984.
142. Steinmann, S. N.; Corminboeuf, C., A generalized-gradient approximation exchange hole model for dispersion coefficients. *J. Chem. Phys.* **2011**, *134* (4).
143. Steinmann, S. N.; Corminboeuf, C., Comprehensive Benchmarking of a Density-Dependent Dispersion Correction. *J. Chem. Theory Comput.* **2011**, *7* (11), 3567-3577.
144. Wang, L.; Maxisch, T.; Ceder, G., Oxidation energies of transition metal oxides within the GGA+U framework. *Phys. Rev. B* **2006**, *73* (19), 195107.
145. Yan, G.; Wähler, T.; Schuster, R.; Schwarz, M.; Hohner, C.; Werner, K.; Libuda, J.; Sautet, P., Water on Oxide Surfaces: A Triqua Surface Coordination Complex on Co₃O₄(111). *J. Am. Chem. Soc.* **2019**, *141* (14), 5623-5627.
146. Allen, J. P.; Watson, G. W., Occupation matrix control of d- and f-electron localisations using DFT+U. *Phys. Chem. Chem. Phys.* **2014**, *16* (39), 21016-21031.
147. Dementyev, P.; Dostert, K. H.; Ivars-Barceló, F.; O'Brien, C. P.; Mirabella, F.; Schauermaun, S.; Li, X.; Paier, J.; Sauer, J.; Freund, H. J., Water interaction with iron oxides. *Angew. Chem.* **2015**, *127* (47), 14148-14152.
148. Liu, X.; Prewitt, C. T., High-temperature X-ray diffraction study of Co₃O₄: Transition from normal to disordered spinel. *Phys. Chem. Miner.* **1990**, *17* (2), 168-172.

149. Zasada, F.; Gryboś, J.; Piskorz, W.; Sojka, Z., Cobalt Spinel (111) Facets of Various Stoichiometry DFT+ U and Ab Initio Thermodynamic Investigations. *J. Phys. Chem. C* **2018**, *122* (5), 2866-2879.
150. Capdevila-Cortada, M.; Łodziana, Z.; López, N., Performance of DFT+U approaches in the study of catalytic materials. *ACS Catal.* **2016**, *6* (12), 8370-8379.
151. Chen, J.; Selloni, A., First Principles Study of Cobalt (Hydr)oxides under Electrochemical Conditions. *J. Phys. Chem. C* **2013**, *117* (39), 20002-20006.
152. Bajdich, M.; Garcia-Mota, M.; Vojvodic, A.; Norskov, J. K.; Bell, A. T., Theoretical investigation of the activity of cobalt oxides for the electrochemical oxidation of water. *J. Am. Chem. Soc.* **2013**, *135* (36), 13521-13530.
153. Hu, W.; Cao, X.-M.; Hu, P., DFT+ U Study on Catalysis by Co₃O₄: Influence of U Value and a Surface–Bulk Bi-U Strategy. *J. Phys. Chem. C* **2018**, *122* (34), 19593-19602.
154. Grillo, F.; Natile, M. M.; Gilisenti, A., Low temperature oxidation of carbon monoxide: the influence of water and oxygen on the reactivity of a Co₃O₄ powder surface. *Appl. Catal. B: Environ.* **2004**, *48* (4), 267-274.
155. Finocchio, E.; Busca, G.; Lorenzelli, V.; Sanchez Escribano, V., FTIR studies on the selective oxidation and combustion of light hydrocarbons at metal oxide surfaces. Part 2.— Propane and propene oxidation on Co₃O₄. *J. Chem. Soc., Faraday Trans.* **1996**, *92*, 1587-1593.
156. Tang, X.; Li, J.; Hao, J., Synthesis and characterization of spinel Co₃O₄ octahedra enclosed by the {1 1 1} facets. *Mater. Res. Bull.* **2008**, *43* (11), 2912-2918.
157. Xie, X.; Li, Y.; Liu, Z. Q.; Haruta, M.; Shen, W., Low-Temperature Oxidation of CO Catalysed by Co₃O₄ Nanorods. *Nature* **2009**, *458* (7239), 746-749.

158. Russo, N.; Fino, D.; Saracco, G.; Specchia, V., N₂O catalytic decomposition over various spinel-type oxides. *Catal. Today* **2007**, *119* (1-4), 228-232.
159. Piskorz, W.; Zasada, F.; Stelmachowski, P.; Kotarba, A.; Sojka, Z., Decomposition of N₂O over the surface of cobalt spinel: A DFT account of reactivity experiments. *Catal. Today* **2008**, *137* (2-4), 418-422.
160. Zhang, S.; Nguyen, L.; Liang, J.-X.; Shan, J.; Liu, J.; Frenkel, A. I.; Patlolla, A.; Huang, W.; Li, J.; Tao, F., Catalysis on singly dispersed bimetallic sites. *Nat. Commun.* **2015**, *6*, 7938.
161. Zasada, F.; Janas, J.; Piskorz, W.; Gorczynska, M.; Sojka, Z., Total oxidation of lean methane over cobalt spinel nanocubes controlled by the self-adjusted redox state of the catalyst: experimental and theoretical account for interplay between the Langmuir–Hinshelwood and Mars–Van Krevelen mechanisms. *ACS Catal.* **2017**, *7* (4), 2853-2867.
162. Ferstl, P.; Mehl, S.; Arman, M. A.; Schuler, M.; Toghan, A.; Laszlo, B.; Lykhach, Y.; Brummel, O.; Lundgren, E.; Knudsen, J., Adsorption and activation of CO on Co₃O₄ (111) thin films. *J. Phys. Chem. C* **2015**, *119* (29), 16688-16699.
163. Pang, X. Y.; Liu, C.; Li, D. C.; Lv, C. Q.; Wang, G. C., Structure sensitivity of CO oxidation on Co₃O₄: a DFT study. *ChemPhysChem* **2013**, *14* (1), 204-212.
164. Wang, S.; Vorotnikov, V.; Vlachos, D. G., Coverage-induced conformational effects on activity and selectivity: hydrogenation and decarbonylation of furfural on Pd(111). *ACS Catal.* **2015**, *5* (1), 104-112.
165. Rellan-Pineiro, M.; Lopez, N., One Oxygen Vacancy, Two Charge States: Characterization of Reduced alpha-MoO₃(010) through Theoretical Methods. *J. Phys. Chem. Lett.* **2018**, *9* (10), 2568-2573.

166. Henkelman, G.; Jónsson, H., Improved tangent estimate in the nudged elastic band method for finding minimum energy paths and saddle points. *J. Chem. Phys.* **2000**, *113* (22), 9978-9985.
167. Henkelman, G.; Uberuaga, B. P.; Jonsson, H., A climbing image nudged elastic band method for finding saddle points and minimum energy paths. *J. Chem. Phys.* **2000**, *113* (22), 9901-9904.
168. Henkelman, G.; Jónsson, H., A dimer method for finding saddle points on high dimensional potential surfaces using only first derivatives. *J. Chem. Phys.* **1999**, *111* (15), 7010-7022.
169. Hill, T. L., *An introduction to statistical thermodynamics*. Courier Corporation: 1986.
170. Cortright, R. D.; Dumesic, J. A., Kinetics of heterogeneous catalytic reactions: Analysis of reaction schemes. *Adv. Catal.* **2001**, *46*.
171. Campbell, C. T., The Degree of Rate Control: A Powerful Tool for Catalysis Research. *ACS Catal.* **2017**, *7* (4), 2770-2779.
172. Yan, G.; Sautet, P., Surface Structure of Co₃O₄ (111) under Reactive Gas-Phase Environments. *ACS Catal.* **2019**, *9* (7), 6380-6392.
173. Chempath, S.; Bell, A. T., A DFT study of the mechanism and kinetics of methane oxidation to formaldehyde occurring on silica-supported molybdena. *J. Catal.* **2007**, *247* (1), 119-126.
174. Prasomsri, T.; Nimmanwudipong, T.; Román-Leshkov, Y., Effective hydrodeoxygenation of biomass-derived oxygenates into unsaturated hydrocarbons by MoO₃ using low H₂ pressures. *Energy Environ. Sci.* **2013**, *6* (6), 1732-1738.

175. Mironenko, A. V.; Vlachos, D. G., Conjugation-Driven "Reverse Mars-van Krevelen"-Type Radical Mechanism for Low-Temperature C-O Bond Activation. *J. Am. Chem. Soc.* **2016**, *138* (26), 8104-8113.
176. Fu, J.; Lym, J.; Zheng, W.; Alexopoulos, K.; Mironenko, A. V.; Li, N.; Boscoboinik, J. A.; Su, D.; Weber, R. T.; Vlachos, D. G., C-O bond activation using ultralow loading of noble metal catalysts on moderately reducible oxides. *Nat. Catal.* **2020**, *3* (5), 446-453.
177. Merte, L. R.; Peng, G.; Bechstein, R.; Rieboldt, F.; Farberow, C. A.; Grabow, L. C.; Kudernatsch, W.; Wendt, S.; Lægsgaard, E.; Mavrikakis, M., Water-mediated proton hopping on an iron oxide surface. *Science* **2012**, *336* (6083), 889-893.
178. Joubert, J.; Delbecq, F.; Thieuleux, C.; Taoufik, M.; Blanc, F.; Coperet, C.; Thivolle-Cazat, J.; Basset, J.-M.; Sautet, P., Synthesis, Characterization, and Catalytic Properties of γ -Al₂O₃-Supported Zirconium Hydrides through a Combined Use of Surface Organometallic Chemistry and Periodic Calculations. *Organometallics* **2007**, *26*, 3329-3335.
179. Zhang, L.; Zhou, M.; Wang, A.; Zhang, T., Selective hydrogenation over supported metal catalysts: from nanoparticles to single atoms. *Chem. Rev.* **2019**, *120* (2), 683-733.
180. Cárdenas-Lizana, F.; Keane, M. A., The development of gold catalysts for use in hydrogenation reactions. *J. Mat. Sci.* **2013**, *48* (2), 543-564.
181. Lindlar, H., Ein neuer Katalysator für selektive Hydrierungen. *Helv. Chim. Acta* **1952**, *35* (2), 446-450.
182. Schwab, F.; Weidler, N.; Lucas, M.; Claus, P., Highly cis-selective and lead-free hydrogenation of 2-hexyne by a supported Pd catalyst with an ionic-liquid layer. *Chem. Comm.* **2014**, *50* (72), 10406-10408.

183. Studt, F.; Abild-Pedersen, F.; Bligaard, T.; Sørensen, R. Z.; Christensen, C. H.; Nørskov, J. K., Identification of non-precious metal alloy catalysts for selective hydrogenation of acetylene. *Science* **2008**, *320* (5881), 1320-1322.
184. Mei, D.; Sheth, P. A.; Neurock, M.; Smith, C. M., First-principles-based kinetic Monte Carlo simulation of the selective hydrogenation of acetylene over Pd (111). *J. Catal.* **2006**, *242* (1), 1-15.
185. Sheth, P. A.; Neurock, M.; Smith, C. M., A first-principles analysis of acetylene hydrogenation over Pd (111). *J. Phys. Chem. B* **2003**, *107* (9), 2009-2017.
186. Luneau, M.; Shirman, T.; Foucher, A. C.; Duanmu, K.; Verbart, D. M.; Sautet, P.; Stach, E. A.; Aizenberg, J.; Madix, R. J.; Friend, C. M., Achieving High Selectivity for Alkyne Hydrogenation at High Conversions with Compositionally Optimized PdAu Nanoparticle Catalysts in Raspberry Colloid-Templated SiO₂. *ACS Catal.* **2019**, *10* (1), 441-450.
187. Zaera, F., The surface chemistry of metal-based hydrogenation catalysis. *ACS Catal.* **2017**, *7* (8), 4947-4967.
188. Han, J.; Lu, J.; Wang, M.; Wang, Y.; Wang, F., Single atom alloy preparation and applications in heterogeneous catalysis. *Chin. J. Chem.* **2019**, *37* (9), 977-988.
189. Giannakakis, G.; Flytzani-Stephanopoulos, M.; Sykes, E. C. H., Single-atom alloys as a reductionist approach to the rational design of heterogeneous catalysts. *Acc. Chem. Res.* **2018**, *52* (1), 237-247.
190. Darby, M. T.; Stamatakis, M.; Michaelides, A.; Sykes, E. C. H., Lonely atoms with special gifts: breaking linear scaling relationships in heterogeneous catalysis with single-atom alloys. *J. Phys. Chem. Lett.* **2018**, *9* (18), 5636-5646.

191. Yuan, D.; Gong, X.; Wu, R., Atomic configurations of Pd atoms in PdAu (111) bimetallic surfaces investigated using the first-principles pseudopotential plane wave approach. *Phys. Rev. B* **2007**, *75* (8), 085428.
192. Thirumalai, H.; Kitchin, J. R., Investigating the reactivity of single atom alloys using density functional theory. *Top. Catal.* **2018**, *61* (5), 462-474.
193. Greiner, M. T.; Jones, T.; Beeg, S.; Zwiener, L.; Scherzer, M.; Girgsdies, F.; Piccinin, S.; Armbrüster, M.; Knop-Gericke, A.; Schlögl, R., Free-atom-like d states in single-atom alloy catalysts. *Nat. Chem.* **2018**, *10* (10), 1008-1015.
194. Fung, V.; Hu, G.; Sumpter, B., Electronic band contraction induced low temperature methane activation on metal alloys. *J. Mat. Chem. A* **2020**, *8* (12), 6057-6066.
195. Vignola, E.; Steinmann, S. N.; Al Farra, A.; Vandegehuchte, B. D.; Curulla, D.; Sautet, P., Evaluating the risk of C–C bond formation during selective hydrogenation of acetylene on palladium. *ACS Catal.* **2018**, *8* (3), 1662-1671.
196. Liu, J.; Shan, J.; Lucci, F. R.; Cao, S.; Sykes, E. C. H.; Flytzani-Stephanopoulos, M., Palladium–gold single atom alloy catalysts for liquid phase selective hydrogenation of 1-hexyne. *Catal. Sci. & Technol.* **2017**, *7* (19), 4276-4284.
197. Boucher, M. B.; Zugic, B.; Cladaras, G.; Kammert, J.; Marcinkowski, M. D.; Lawton, T. J.; Sykes, E. C. H.; Flytzani-Stephanopoulos, M., Single atom alloy surface analogs in Pd_{0.18}Cu₁₅ nanoparticles for selective hydrogenation reactions. *Phys. Chem. Chem. Phys.* **2013**, *15* (29), 12187-12196.
198. Pei, G. X.; Liu, X. Y.; Wang, A.; Li, L.; Huang, Y.; Zhang, T.; Lee, J. W.; Jang, B. W.; Mou, C.-Y., Promotional effect of Pd single atoms on Au nanoparticles supported on silica

for the selective hydrogenation of acetylene in excess ethylene. *New J. Chem.* **2014**, *38* (5), 2043-2051.

199. Pei, G. X.; Liu, X. Y.; Yang, X.; Zhang, L.; Wang, A.; Li, L.; Wang, H.; Wang, X.; Zhang, T., Performance of Cu-alloyed Pd single-atom catalyst for semihydrogenation of acetylene under simulated front-end conditions. *ACS Catal.* **2017**, *7* (2), 1491-1500.

200. Xie, W.; Xu, J.; Ding, Y.; Hu, P., Quantitative studies of the key aspects in selective acetylene hydrogenation on Pd (111) by microkinetic modeling with coverage effects and molecular dynamics. *ACS Catal.* **2021**, *11* (7), 4094-4106.

201. Liu, J.; Uhlman, M. B.; Montemore, M. M.; Trimpalis, A.; Giannakakis, G.; Shan, J.; Cao, S.; Hannagan, R. T.; Sykes, E. C. H.; Flytzani-Stephanopoulos, M., Integrated catalysis-surface science-theory approach to understand selectivity in the hydrogenation of 1-hexyne to 1-hexene on PdAu single-atom alloy catalysts. *ACS Catal.* **2019**, *9* (9), 8757-8765.

202. Methfessel, M.; Paxton, A., High-precision sampling for Brillouin-zone integration in metals. *Phys. Rev. B.* **1989**, *40* (6), 3616.

203. Gautier, S.; Steinmann, S. N.; Michel, C.; Fleurat-Lessard, P.; Sautet, P., Molecular adsorption at Pt (111). How accurate are DFT functionals? *Phys. Chem. Chem. Phys.* **2015**, *17* (43), 28921-28930.

204. Koeleman, B.; De Zwart, S.; Boers, A.; Poelsema, B.; Verhey, L., Adsorption study of hydrogen on a stepped Pt (997) surface using low energy recoil scattering. *Nucl. Instruments Methods Phys. Res.* **1983**, *218* (1-3), 225-229.

205. Norton, P.; Davies, J.; Jackman, T., Absolute coverage and isosteric heat of adsorption of deuterium on Pt (111) studied by nuclear microanalysis. *Surf. Sci.* **1982**, *121* (1), 103-110.

206. Dion, M.; Rydberg, H.; Schröder, E.; Langreth, D. C.; Lundqvist, B. I., Van der Waals density functional for general geometries. *Phys. Rev. Lett.* **2004**, *92* (24), 246401.
207. Román-Pérez, G.; Soler, J. M., Efficient implementation of a van der Waals density functional: application to double-wall carbon nanotubes. *Phys. Rev. Lett.* **2009**, *103* (9), 096102.
208. Klimeš, J.; Bowler, D. R.; Michaelides, A., Van der Waals density functionals applied to solids. *Phys. Rev. B* **2011**, *83* (19), 195131.
209. Klimeš, J.; Bowler, D. R.; Michaelides, A., Chemical accuracy for the van der Waals density functional. *J. Phys. Condens. Matter* **2009**, *22* (2), 022201.
210. Gokhale, A. A.; Kandoi, S.; Greeley, J. P.; Mavrikakis, M.; Dumesic, J. A., Molecular-level descriptions of surface chemistry in kinetic models using density functional theory. *Chem. Eng. Sci.* **2004**, *59* (22-23), 4679-4691.
211. Janthon, P.; Luo, S.; Kozlov, S. M.; Vines, F.; Limtrakul, J.; Truhlar, D. G.; Illas, F., Bulk properties of transition metals: a challenge for the design of universal density functionals. *J. Chem. Theory Comput.* **2014**, *10* (9), 3832-3839.
212. van der Hoeven, J. E.; Ngan, H. T.; Taylor, A.; Eagan, N. M.; Aizenberg, J.; Sautet, P.; Madix, R. J.; Friend, C. M., Entropic control of HD exchange rates over dilute Pd-in-Au alloy nanoparticle catalysts. *ACS Catal.* **2021**, *11* (12), 6971-6981.
213. Dong, W.; Kresse, G.; Hafner, J., Dissociative adsorption of H₂ on the Pd(111) surface. *J. Mol. Catal. A: Chem.* **1997**, *119* (1-3), 69-76.
214. Dumesic, J., Analyses of reaction schemes using De Donder relations. *J. Catal.* **1999**, *185* (2), 496-505.
215. Mao, Z.; Campbell, C. T., Apparent activation energies in complex reaction mechanisms: a simple relationship via degrees of rate control. *ACS Catal.* **2019**, *9* (10), 9465-9473.

216. Canduela-Rodriguez, G.; Sabbe, M. K.; Reyniers, M.-F.; Joly, J.-F.; Marin, G. B., Thermodynamic study of benzene and hydrogen coadsorption on Pd(111). *Phys. Chem. Chem. Phys.* **2014**, *16* (43), 23754-23768.
217. Darby, M. T.; Sykes, E. C. H.; Michaelides, A.; Stamatakis, M., Carbon monoxide poisoning resistance and structural stability of single atom alloys. *Top. Catal.* **2018**, *61* (5), 428-438.
218. Darby, M. T.; Réocreux, R.; Sykes, E. C. H.; Michaelides, A.; Stamatakis, M., Elucidating the stability and reactivity of surface intermediates on single-atom alloy catalysts. *ACS Catal.* **2018**, *8* (6), 5038-5050.
219. Li, H.; Chai, W.; Henkelman, G., Selectivity for ethanol partial oxidation: the unique chemistry of single-atom alloy catalysts on Au, Ag, and Cu (111). *J. Mat. Chem. A* **2019**, *7* (41), 23868-23877.
220. Hammer, B.; Nørskov, J. K., Why gold is the noblest of all the metals. *Nature* **1995**, *376* (6537), 238-240.
221. Xin, H.; Vojvodic, A.; Voss, J.; Nørskov, J. K.; Abild-Pedersen, F., Effects of d-band shape on the surface reactivity of transition-metal alloys. *Phys. Rev. B* **2014**, *89* (11), 115114.
222. Silvestre-Albero, J.; Rupprechter, G.; Freund, H.-J., Atmospheric pressure studies of selective 1, 3-butadiene hydrogenation on well-defined Pd/Al₂O₃/NiAl (110) model catalysts: Effect of Pd particle size. *J. Catal.* **2006**, *240* (1), 58-65.
223. van der Hoeven, J. E.; Jelic, J.; Olthof, L. A.; Totarella, G.; van Dijk-Moes, R. J.; Krafft, J.-M.; Louis, C.; Studt, F.; van Blaaderen, A.; de Jongh, P. E., Unlocking synergy in bimetallic catalysts by core-shell design. *Nat. Mater.* **2021**, *20* (9), 1216-1220.

224. El Kooli, N.; Delannoy, L.; Louis, C., Bimetallic Au–Pd catalysts for selective hydrogenation of butadiene: Influence of the preparation method on catalytic properties. *J. Catal.* **2013**, *297*, 79-92.
225. Rassolov, A.; Bragina, G.; Baeva, G.; Mashkovsky, I.; Stakheev, A. Y., Alumina-supported palladium–silver bimetallic catalysts with single-atom Pd1 sites in the liquid-phase hydrogenation of substituted alkynes. *Kinet. Catal.* **2020**, *61* (6), 869-878.
226. Duchoň, T.; Dvořák, F.; Aulická, M.; Stetsovych, V.; Vorokhta, M.; Mazur, D.; Veltruská, K.; Skála, T.; Mysliveček, J.; Matolínová, I.; Matolín, V., Ordered phases of reduced ceria as epitaxial films on Cu(111). *J. Phys. Chem. C* **2013**, *118* (1), 357-365.
227. Duchoň, T.; Dvořák, F.; Aulická, M.; Stetsovych, V.; Vorokhta, M.; Mazur, D.; Veltruská, K.; Skála, T.; Mysliveček, J.; Matolínová, I.; Matolín, V., Comment on “ordered phases of reduced ceria as epitaxial films on Cu(111)”. *J. Phys. Chem. C* **2014**, *118* (9), 5058-5059.
228. Réocreux, R.; Ould Hamou, C. A.; Michel, C.; Giorgi, J. B.; Sautet, P., Decomposition mechanism of anisole on Pt (111): combining single-crystal experiments and first-principles calculations. *ACS Catal.* **2016**, *6* (12), 8166-8178.
229. Piotrowski, M. J.; Piquini, P.; Zeng, Z.; Da Silva, J. L., Adsorption of NO on the Rh₁₃, Pd₁₃, Ir₁₃, and Pt₁₃ clusters: a density functional theory investigation. *J. Phys. Chem. C* **2012**, *116* (38), 20540-20549.
230. Balasubramanian, K.; Liao, D. W., Spectroscopic properties of low-lying electronic states of rhodium dimer. *J. Phys. Chem.* **1989**, *93* (10), 3989-3992.
231. Dai, D.; Balasubramanian, K., Potential energy surfaces for Rh–CO, Rh–OC, Ir–CO, and Ir–OC interactions. *J. Chem. Phys.* **1994**, *101* (3), 2148-2156.

232. Frisch, M.; Trucks, G.; Schlegel, H.; Scuseria, G.; Robb, M.; Cheeseman, J.; Scalmani, G.; Barone, V.; Mennucci, B.; Petersson, G., Gaussian 09, Revision D. 01. **2009**.
233. Dunning Jr., T. H., Gaussian basis sets for use in correlated molecular calculations. I. The atoms boron through neon and hydrogen. *J. Chem. Phys.* **1989**, *90* (2), 1007-1023.
234. Kendall, R. A.; Dunning Jr., T. H.; Harrison, R. J., Electron affinities of the first-row atoms revisited. Systematic basis sets and wave functions. *J. Chem. Phys.* **1992**, *96* (9), 6796-6806.
235. Peterson, K. A.; Figgen, D.; Dolg, M.; Stoll, H., Energy-consistent relativistic pseudopotentials and correlation consistent basis sets for the 4d elements Y-Pd. *J. Chem. Phys.* **2007**, *126* (12), 124101.
236. Lee, T. J.; Taylor, P. R., A diagnostic for determining the quality of single-reference electron correlation methods. *Int. J. Quantum Chem.* **1989**, *36* (S23), 199-207.
237. Allian, A. D.; Garland, M., Spectral resolution of fluxional organometallics. The observation and FTIR characterization of all-terminal [Rh₄(CO)₁₂]. *Dalton Trans.* **2005**, *11*, 1957-1965.
238. Ding, H.; Lu, Y.; Xie, Y.; Liu, H.; Schaefer III, H. F., The energy difference between the triply-bridged and all-terminal structures of Co₄(CO)₁₂, Rh₄(CO)₁₂, and Ir₄(CO)₁₂: a difficult test for conventional density functional methods. *J. Chem. Theory Comput.* **2015**, *11* (3), 940-949.
239. Herman, G. S.; Kim, Y. J.; Chambers, S. A.; Peden, C. H. F., Interaction of D₂O with CeO₂(001) investigated by temperature-programmed desorption and X-ray photoelectron spectroscopy. *Langmuir* **1999**, *15* (11), 3993-3997.

240. Shahed, S. M. F.; Hasegawa, T.; Sainoo, Y.; Watanabe, Y.; Isomura, N.; Beniya, A.; Hirata, H.; Komeda, T., STM and XPS study of CeO₂(111) reduction by atomic hydrogen. *Surf. Sci.* **2014**, *628*, 30-35.
241. Chase, M. W., *NIST-JANAF thermochemical tables*. American Chemical Society Washington, DC: 1998; Vol. 9.
242. Fulmer, G. R.; Herndon, A. N.; Kaminsky, W.; Kemp, R. A.; Goldberg, K. I., Hydrogenolysis of palladium (II) hydroxide, phenoxide, and alkoxide complexes. *J. Am. Chem. Soc.* **2011**, *133* (44), 17713-17726.
243. Wellendorff, J.; Lundgaard, K. T.; Møgelhøj, A.; Petzold, V.; Landis, D. D.; Nørskov, J. K.; Bligaard, T.; Jacobsen, K. W., Density functionals for surface science: Exchange-correlation model development with Bayesian error estimation. *Phys. Rev. B* **2012**, *85* (23), 235149.